Characterizing the Excited State Dynamics of Organic Materials for Efficient Energy Conversion: from Current to Photons and Vice-Versa

by

Ricardo Vázquez

A dissertation submitted in partial fulfillment
of the requirements for the degree of
Doctor of Philosophy
(Chemistry)
in The University of Michigan
2019

Doctoral Committee:

Professor Theodore Goodson lll, Co-Chair
Professor Jinsang Kim, Co-Chair
Professor Jay Guo
Associate Professor Dominika Zgid

"*The history of science, like the history of all human ideas, is a history of irresponsible dreams, of obstinacy, and of error. But science is one of the very few human activities - perhaps the only one - in which errors are systematically criticized and fairly often, in time, corrected. This is why we can say that, in science, we often learn from our mistakes, and why we can speak clearly and sensibly about making progress there*."

- Karl R. Popper**,** Conjectures and Refutations: The Growth of Scientific Knowledge (1963)

Ricardo Vázquez

ricbacu@umich.edu

ORCID iD: 0000-0003-3245-8123

DEDICATION

This dissertation was written thinking on those who get out of their comfort zone and go to work hard on daily basis for the sake of a better future. The world is yours. Keep thriving!

ACKNOWLEDGMENTS

To my parents, Germán Vázquez and Daisy Vázquez, for teaching me their views on how basic human interaction should be based on solidarity, empathy, patience, and respect. Also, for encouraging me to think for myself and experience the world in my own way, so I can arrive to conclusions based on my understanding and perception. I will ALWAYS appreciate that the most. Also, to my two fantastic siblings (Germán Jorge y César Augusto), with whom my patient was tested the most. To my abuela Olga, for sacrificing herself on daily basis during my undergraduate studies. Your food will always be better than any three Michelin starred restaurant. To Angel Santiago (Angelo), for his unconditional support and help in multiple situations that allow me to reach this point in my professional career. To Rebecca Escribano and Harold Bones, for their support during my allocation from Puerto Rico to Michigan. To my girlfriend Sarah Cox and to her family, for their constant support on my personal and graduate career. To my closest friends, for putting my feet on the ground whenever it was needed to be done. To Annabell C. Segarra, for mentoring me for two years while I was part of the MARC program in Puerto Rico. To Theodore Goodson and Jinsang Kim, for believing in my potential as a scientist and pushing me toward scientific excellence at every turn. To all the members of the Goodson laboratory and Kim laboratory, for their everyday stimulant conversations. To Dr. Oleg Varnavski, for his countless hours dedicated to teaching me how to properly align a laser. At last but not least important, this dissertation is mostly dedicated to Dr. José Luis Agosto (a.k.a El Profe), whose passion and will

for teaching, mentoring, training and development, or any other endeavor in which one human being seeks to support the personal and professional growth and development of another, set a standard for anyone. He was the one who scouted me while I was an undergrad, saw my potential, and encouraged me the most to pursue a Ph.D. career in science. For all your support, time, and encouraging words: THANK YOU.

TABLE OF CONTENTS

LIST OF FIGURES

LIST OF TABLES

ABSTRACT

The use of organic semiconductor (OSC) materials for optoelectronic applications such as display technologies, consumer electronics, energy-storage, and photovoltaic conversion has drawn academic and industrial interest in recent years. The OSC rise in popularity and demand is due to their multiple advantageous properties over their inorganic counterparts. Some of these OSC properties are their ease of device processability, flexibility, and cost-efficiency. In addition, their synthetic flexibility allows for subtle modifications in their structure so their optical and electrochemical properties could be systematically tuned. The molecular structure dictates their function, therefore, fundamental understanding on how modulating their chemical structures will tune their opto-electrical properties is imperative to optimize their optoelectronic performance. In this dissertation, ultrafast spectroscopy and nonlinear optical methods were used to probe the excited state dynamics of OSC materials with 1) thermally activated delayed fluorescence (TADF) characteristics, and 2) light harvesting and low-bandgap materials for bulk heterojunction (BHJ) architectures. The former is a mechanism used for enhancing the efficiency of the third-generation organic light emitting diodes (OLEDs), while the latter composed the active layer of the third generation organic photovoltaic (OPV) devices.

TADF is the idea that dark triplet excitons can be converted into emissive singlet exciton via a reverse intersystem crossing (rISC) mechanism, which the rISC is prompted by the

combination of room thermal energy with the small energy gap between the singlet-triplet manifolds (ΔE_{ST}). This mechanism has been implemented into OLEDs. However, one of the major challenges hampering their commercialization is the lack of seep understanding on the overall TADF mechanism in such systems. Throughout the course of this thesis, the photophysical properties of multiple TADF emitters are elucidated. In addition, a new optical approach for the direct characterization of the rate of rISC (k_{rISC}) is introduced. This new methodology could be used to predict their respective device performances. The k_{rISC} in TADF emitters is believed to be critical for reducing the triplet-triplet annihilation (TTA) mechanism that cause efficiency roll-off at high operational voltage.

In the case of the active materials for BHJ applications, the optical properties of light harvesting polymers and low-bandgap small molecules for non-fullerene acceptors (NFA) devices are elucidated. Specifically, the influence of heterocycles such as furan and thiophene as linkers on the photophysical properties of light harvesting polymers were probed with and emphasis in their charge transfer properties. These light harvesting polymers were based on benzodifuran (BDF) as the donor and diketopyrrolopyrrole (DPP) as the acceptor. The low-bandgap materials were designed to be acceptor-donor-acceptor ladder-type molecules based on perylene-diimide (PDI) as the acceptor and heteroacenes as the donor. These materials have also drawn interest for developing transparent solar cells. Their photophysical properties were investigated and an intense intramolecular charge-transfer character upon pi-conjugation lengthening was observed among them. In addition, fundamental investigation of the feasibility of intramolecular singlet exciton fission (iSF) and subsequent two-electron transfer from tetracyanimethylene quinoidal bithiophene (QOT2) to anthracene were investigated as well.

Chapter 1

Introduction and Background of Organic Semiconductors for Optoelectronic Applications

1.1 History of Light Emitting Diodes for Display Applications

The creation of artificial light is an essential aspect of our civilization, and improvements towards more ecofriendly lightning sources are required with urgency. Using organic light emitting diodes (OLEDs) represent an attractive way to address the current issues as organic materials can be used in ways that cannot be used by traditional fluorescent tubes, namely liquid crystal displays (LCD). Nowadays, multiple companies have commercially available displays based on OLED technologies, but their efficiencies are ways away from overcoming the LCD leading technologies. Some of the companies involved in the OLEDs technologies are Philips, LG, Konica Minolta, among others.

Artificial lightening is governed by a mechanism known as electroluminescence (EL). In EL, uncorrelated charge carriers are injected into a device that possess an emissive material. The recombination of these charges is in charge of producing light.[1–3] Nowdays, scientist are very familiarized with how the EL works, but it took decades of hard work and dedication to figured it out. The electroluminescence phenomenon was discovered by H. J. Round by accident in 1907 using a silicon carbide semiconductor material.[4] However, Round did not pay a lot of attention to this phenomena, and it was not until 1923 when Oleg Lossev systematically studied this

GaAs Alq$_3$ PVV

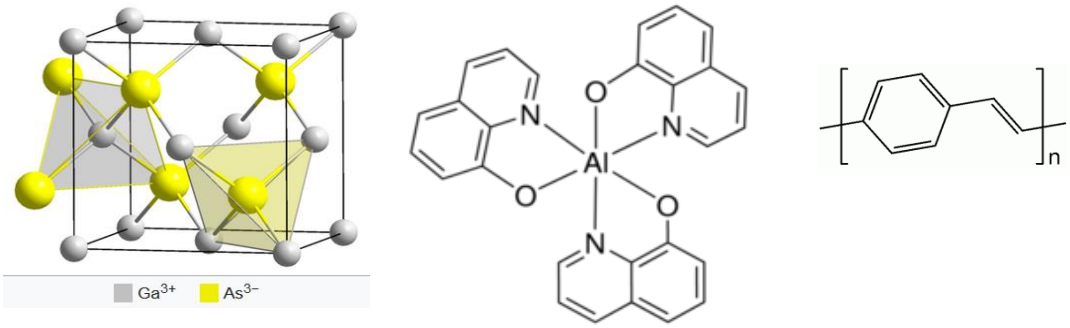

Figure 1.1.1. Molecular structure of inorganic and organic light emitting diodes.

phenomenon using silicon carbide (SiC) as the emissive material.[5] Years later (1939), Zoltán Bay patented a light emitting device based on SiC. Until this point, the mechanism of action in electroluminescence was widely unclear. Kurt Lehovec and colleagues at the Signal Corps Engineering Laboratories revolutionized the light emitting diode (LED) field by providing the first modern and correct interpretation of light emission in 1951.[6] They claimed that the luminescence came from minority carrier injection across the boundary of a p-n junction.

Slow but systematic progress with color tuning was done using Gallium derivatives up until the 1990s when Aluminum Quinolate (Alq$_3$) was discovered (**Figure 1.1.1.**).[7] Alq$_3$ was considered to be the first OLED despite its organometallic nature and despite that electroluminescence properties were already observed in anthracene.[6] Alq$_3$ displayed device performances of 1 % ηEQE, a brightness of more than 1000 cd/m^2 with a driving voltage of about 10 V. In 1990, Richard Friend's group at Cambridge University developed a poly(p-phenylenevinylene) (PPV) based OLED.[8] The color properties were in the green-yellow part of the visible spectrum, and its efficiency < 1 %. Since then, enormous progress has been made in improving the color range, efficiencies at high operating voltages, and device operational stability OLEDs. The growing interest is mostly motivated by it potential use as flexible and wearable

electronics, and large panel displays, features that are not necessary accessible for current leading technologies such as LCD.

The manufacturing interest in OLEDs as display applications can be best described and understood throughout a comparison with LCD, which is the leading display technology. LCDs have been the dominant technology for flat panel displays, but liquid crystals are not necessarily the emissive material in the device. Instead, LCDs use the light-modulating properties of liquid crystals to filtrate light and generate colored images. For that, a diffusive film with embedded LEDs are coupled with the liquid crystal technologies. The LCD device architecture requires the incorporation of thin-film transistor (TFT) backplanes, a series of polarizers, spacers, color filters, and a backlight in order to produce an image on a display (**Figure 1.1.2**).[6,9] Liquid crystals operate by a mechanism known as the twisted nematic effect. The liquid crystal molecules will rotate by 90-degrees in the layer along its axis when an electric field is not applied. As a result, light will be transmitted through an orthogonal polarizer to produce a bright pixel. Contrariwise, the liquid crystal will align parallel to the electric field when it is applied, and they will no longer polarize light to form a dark screen.[9] In a simplified version, color "tuning" is achieved by subdividing each pixel into blue, green, and red subpixels by allowing the white backlight to pass through appropriate color filters, namely liquid crystals.

Contrarily to the liquid crystal mechanism for pixel production, each OLED pixel work as the light emitting source by itself.[10] As a result, no color filters or spacers nor any diffuse backlighting source, which have a massive impact in its device architecture and flexibility, are required. OLED technologies offer advantages such as higher resolution, wide-viewing angles, wide color gamut, ultra-thin, flexible, and semitransparent devices. In addition, OLEDs most important advantages over LCD is its low energy consumption as they do not need the diffuse

A

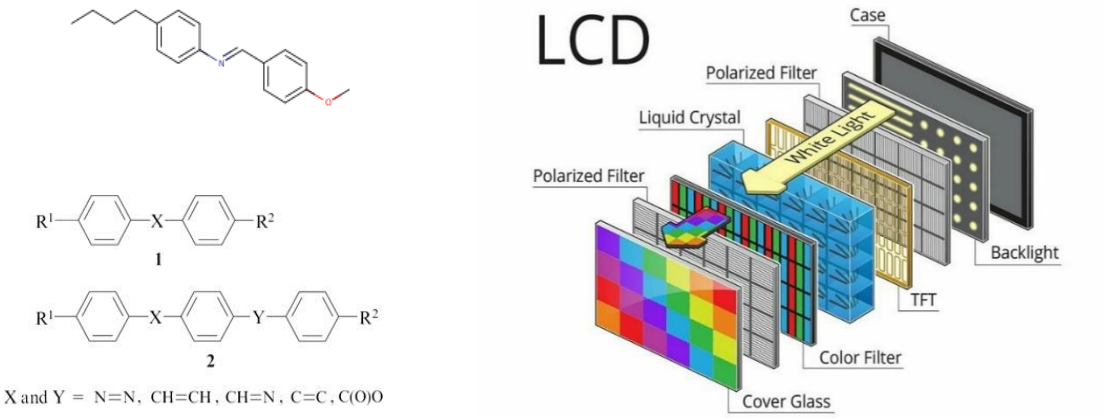

B

Figure 1.1.2 Molecular structure of some liquid crystals and general device architecture of an LCD (A). Wearable OLED and flexible OLED display (B).

backlight to operate due to their inherently emissive nature.[10] This offers the opportunity of obtaining high energy conversion efficiencies, while in the case of the LCD technologies only 10 % of the diffuse backlighting source is transmitted as a result its device architectures complexity. However, LCD technologies are still more accessible in comparison with OLED technologies. This is mostly due to the cost of OLED emitter production. Nevertheless, this gap has been narrowed in recent years thanks to the contribution from large technological companies such as Samsung, LG, Panasonic, and Apple. These companies are motivated to develop OLED devices for wearable displays and cell-phone applications. Massive improvements in the cost of big OLEDs displays have been done in the past few years and drops in OLED TV (LG EC9300) retail

prices of more than 500 % (8,000 $ to 1,500 $) has been achieved. This drastic price drops over the last 5 years is attributed to the developed of cost-efficient and highly efficient organic-based emissive materials. Further price reductions are predicted to happen in the next years upon the implementation of purely organic chromophores as the emissive materials that can harvest the dark triplet-excitons in an unconventional way; a mechanism known as thermally activated delayed fluorescence (TADF).

1.2 Organic Semiconductors Light Emitting Diodes (OLEDs) for Display Applications

1.2.1 Organic Semiconductors Fundamental Properties

Organic materials circle around having carbon and hydrogen atoms as the backbone of their molecular structure.[11] Their ability to incorporate heteroatoms (oxygen, sulfur, nitrogen) allows flexibility for the incorporation of different types of functional groups, which influences their unique properties in comparison to the inorganic counterparts. This functionalization is also critical for their synthetic flexibility and property tuning. Organic molecules are bounded by Van der Waal forces upon forming solids, which are electrostatic interactions governed by induced dipole moments in the molecule.[12] If the distance is suitable (few nm), this induced dipole moment will attract surrounding molecules and make them interact. The strength of Van der Waals interactions is significantly weaker than the strength that holds covalent bonds (electron sharing between atoms) or ionic bonds (Coulombic interactions). As a result, discrete molecular orbitals are obtained as density of states in organic materials instead of a continuous energy band as it happens in inorganic materials. This density of states controls the energy levels of the system, playing a major role in the charge transport properties of these organic semiconductors (OSC).[13]

Upon excitation, charge carriers may travel through these energy levels, and their nature dictates the efficiency of its charge mobility and energy conversion. The flow of charge carriers in

organic systems is hindered by the energy required to promote these charge carriers from the highest occupied molecular orbital (HOMO) to the lowest unoccupied molecular orbital (LUMO). The HOMO and LUMO energy levels are analogs to what is the valence band and conduction band, respectively, are in inorganic conducting materials. In the case of conducting materials, the valence band and conduction band overlaps between them so the required energy for the creation of the charge carrier is minimal (no bandgap). As a result, a strong continuous (coherent) charge carriers flow through the conducting band dominates in inorganic materials. In the case of OSC, a hopping base charge-transport mechanism (incoherent) is what dominates. Thus, the charge mobility of semiconductors is four magnitudes smaller than for inorganic materials. A value approaching to 0.1 $cm^2/(V \cdot s)$ is usually obtained for OSC while a values over 1000 $cm^2/(V \cdot s)$ can be obtained for inorganic materials.[14]

Another fundamental property of organic systems is their low dielectric constant (ε) relative to the inorganic materials. In OSC, an electron is promoted if the energy is equal or higher to the bandgap (HOMO to the LUMO) upon excitation, leaving behind an electron-hole to form a bound state (exciton) governed by strong Coulombic interactions. This bonding force depends on their separation distance according to the photon energy and the ε. As the ε of the material increases, the separation distance between the electron-hole pair gets larger and the binding energy between the electrons and holes in the excitons gets smaller. An analytical expression obtained after solving the Schrödinger's equation of the atomic electronic states illustrates the relationship between the exciton binding energy, dielectric constant, and electron-hole distances:[14]

$$E_b \frac{e^2 a_0}{\left(\frac{m^*}{m}\right)(a_0^*)^2}$$ **Equation 1.2.1.1**

$$a_0^* = \frac{m}{m^* \varepsilon a_0}$$ **Equation 1.2.1.2**

Table 1.2.1. Fundamental properties of organic and inorganic materials.

Property	Organic Materials	Inorganic Materials
Charge Transport	Incoherent	Coherent
Charge Mobility	< 0.1cm^2/V.s	> 1000 cm^2/V.s
Exciton Radius	~ 10 Å	~ 100 Å
Exciton Binding Energy	0.1-1 *eV*	< 100 *meV*

Where, *Eb* is the exciton binding energy, a_0^* is the exciton radius, *m* corresponds to the electron mass, *e* corresponds to the elementary charge, *m** is the effective reduced mass, ε is the dielectric constant, and $a_0$is the hydrogen atom Bohr radius. Typically, the a_0^* of organic materials is ~ 1 nm, which results in a large *Eb* (0.1 – 1 eV), called Frenkel excitons.[14] Excitons can also happen in inorganic materials, however they have significantly smaller *Eb*, mostly driven by its bigger exciton radius, called Wannier-Mott exciton.[15] The binding energy for inorganics materials is typically smaller than the energy available at ambient conditions (*kT* = 25.7 *meV;* where *k* is the Boltzmann constant). A summary of the fundamental properties of OSC can be observed in **Table 1.2.1**. The properties of inorganic materials were also included for comparison. This large exciton binding energy as well as the small dielectric constant plays a critical role in the energy conversion process in organic optoelectronics devices, whether from light absorption to charge carriers or vice-versa.

1.2.2 OLEDs Principles and Device Architectures

The electroluminescence process consists of injecting uncorrelated charges (electron and holes) from the electrodes to create excited states in a light emitting material. Since the spin-nature

of the injected charges (electrons and holes) are uncorrelated, spin-statistics dictate that the nature of the excited state created will result in a 25 % singlet-excitons and 75 % triplet-ecitons.[16] This means that for a traditional fluorescent organic molecule, only 25% of the charge-to-exciton created will potentially emit, wasting the other 75% of the triplet exciton created via non-radiative pathways. This explains the small external quantum efficiencies (ηEQE) that hindered the LED commercialization in the 90s. Substantial improvement of the charge-to-photon internal quantum efficiency (ηIQE) was made when organometallic iridium-based phosphorescence chromophores were developed by Thompson and Forrest, and a nearly 100 % ηIQE was reported.[17] The access to this previously non-emissive triplet state is attributed to the high spin-orbit coupling (SOC) induced by the heavy atom effect in these organometallic complexes. This huge SOC promotes an electron forbidden spin flipping process from singlet state to triplet state, arising molecules with phosphorescence nature due to the resulting faster rate of intersystem crossing (k_{ISC}) than their rate of fluorescence (k_f).[18,19] Emission from the triplet state as phosphorescence is achieved. Since then, a plethora of iridium (Ir) and platinum (Pt) based emitters have been developed, which advanced the understanding in the electroluminescence mechanism and have been able to achieved ηEQE ~ 25 % for the three main color coordinates.[20–24]

The state of the art device architecture is composed of a multilayer organic hetero-structures between two electrodes.[25] Specifically, the organic hetero-structure is designed to have a hole injection layer (HIL), a host transport layer (HTL), an electron blocking layer (EBL), an emissive layer (EML), an electron transport layer (ETL), a hole blocking layer (HBL), and an electron injection layer (EIL) as is shown in **Figure 1.2.1.1**. Each material/layer is chosen with a specific chemical potential gradient to reduce the energetic barrier between the electrodes and the recombination zone (EML) and also to improve the charge carrier balance in the device. This

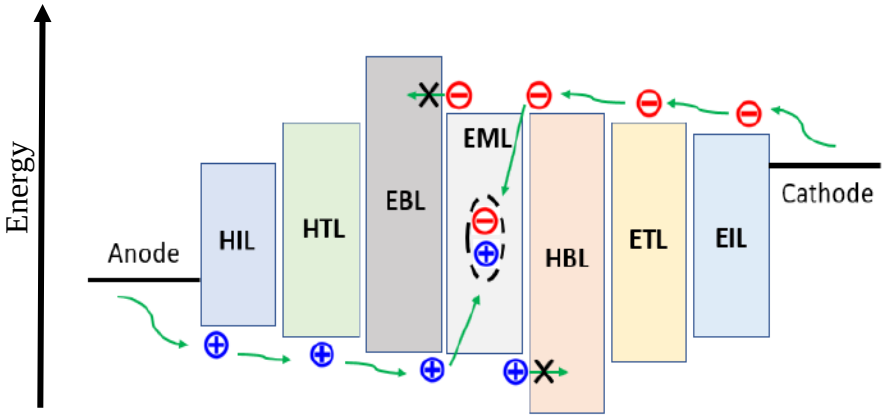

Figure 1.2.1.1 Standard OLED device structure with the required chemical potential energy levels for superior performance.

architectural design based on the chemical potential gradient is critical for developing devices with high efficiencies at low operational voltages. The EIL and the HIL are in charge facilitating the injection of charge carriers, namely electron and holes, from the cathode and anode, respectively. The charge transport layers (HTL, ETL) are responsible of transporting their respective charge carriers from each injection layer to the recombination zone (EML), their chemical potential helps to confine the formation of excitons within the EML. The LUMO level of the EBL needs to be equal or slightly shallower than the one of the EML to prevent electrons to escape the recombination zone. Conversely, the HOMO level of HBL needs to be at least equal or deeper than that of EML to prevent holes escaping from the recombination zone.

The EML is designed to have two different organic materials to optimize the OLEDs efficiency. This designed is best explained by using the terminology of guest-host system.[26] The guest material is in charge of the emissive process while the host material plays an integral role in the energy transferring processes (the charge carriers transfer) that leads to the creation of the exciton in the emissive material. In order to achieve optimal device efficiencies, the host material must meet several key properties.[27,28] The first is that the host must have a higher triplet energy

level than the guest. The second is that the host must have suitable energy levels to match the ones from the electrodes for efficient charge injection. Finally, the third is that the host most ensure a balanced charge distribution across the recombination zone. If these requirements are meet, two types of energy transfer mechanisms govern the exciton formation in the EML. The first one is the Förster resonant energy transfer (FRET) mechanism, which is a long-range electromagnetic dipole-dipole coupling between the guest and host materials.[29,30] As a consequence of the pure dipole-dipole interaction, conservation of spin of each molecule occurs during the energy transfer process. Consequently, triplet transfer from donor (host) to acceptor (guest) is forbidden in this mechanism. The efficiency of this energy transfer mechanism is inversely proportional to the sixth power of the distance between host and guest, which makes FRET very sensitive to small changes in distance. The FRET rate is expressed in **Equation 1.2.1A**:

$$k_{FRET} = \frac{1}{t_D} * (\frac{R_0}{R})^2 \qquad \textbf{Equation 1.2.1A}$$

$$R_0^6 = 8.77 \cdot \Phi_D \kappa^2 \int I_D(\lambda)\varepsilon_A(\lambda)\lambda^4 d\lambda \qquad \textbf{Equation 1.2.1B}$$

where t_D is the emissive lifetime of the host molecule, R is the distance between the host and the guest molecules, and R_0 is the Förster radius, which is defined in **Equation 1.2.1B.** Here, the Φ_D is the fluorescence quantum yield of the host, k^2 is the orientation factor, I_D is the emission intensity of the host, and the E_a is the absorption coefficient of the guest. A qualitative perspective will show that the FRET efficiency can be estimated by the spectral overlap between the emission spectra of the donor (host) and the absorption spectra of the acceptor (guest).

The second energy transfer mechanism is called Dexter energy transfer (DET). This mechanism requires a molecular orbital overlap between the guest-host materials, thus, it is more efficient at distance < 10 Å.[31] Contrarily to the FRET, the DET is an electron transfer mechanism that

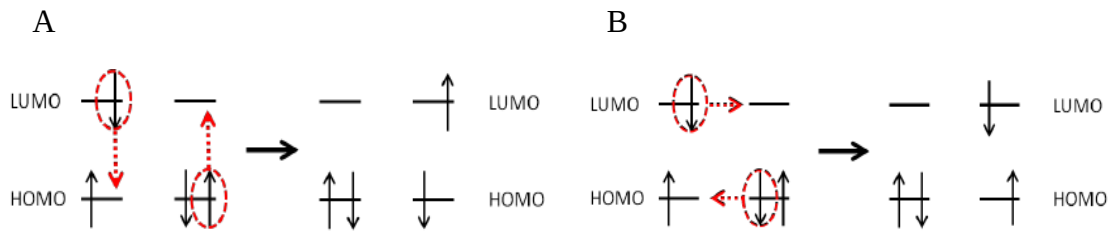

Figure 1.2.1.2. Graphical illustration of FRET (A) and DET (B) mechanism.

allows electron migration with both singlet and triplet character.[32–34] Dexter transfer rate is given by **Equation 1.2.2A**.

$$k_{Dexter} = \frac{2\pi}{\hbar} \Gamma^2 \int I_D(\lambda)\varepsilon_A(\lambda)\, d\lambda \qquad \textbf{Equation 1.2.2A}$$

$$\Gamma^2 = < \Phi_D(1)\Phi_A^*(2)|\frac{1}{4\pi\varepsilon_r\varepsilon_0 R}|\Phi_D^*(1)\Phi_A(2) >< \sigma_D(2)|\sigma_A(2) >< \sigma_D^*(1)|\sigma_A^*(1) > \qquad \textbf{Equation 1.2.2B}$$

Here, Φ_D is the spatial component and σ is the spin component of the molecule ground state wavefunction (* implies excited state). As it can be observed in **Equation 1.2.2B**, transition matrix element Γ becomes non-zero only if two molecular wave functions overlap with the same multiplicity in both the ground state and excited state. It needs to be reiterated the importance of proximity and bandgap energy level matching between the host and the guest in the EML to ensure an energy efficient and exothermic transfer of exciton from the host to the guest.[35,36] A schematic representation of the FRET and DET energy processes can be observed in **Figure 1.2.1.2**.

The efficiency of these energy transfer processes dictates the device performances of the OLED such as its external quantum efficiency (ηEQE) and its internal quantum efficiency (ηIQE). The ηEQE is one of the most important parameters in OLEDs, which quantify the number of extracted photons per charge carrier injected into the device. It is defined as follows:

A B

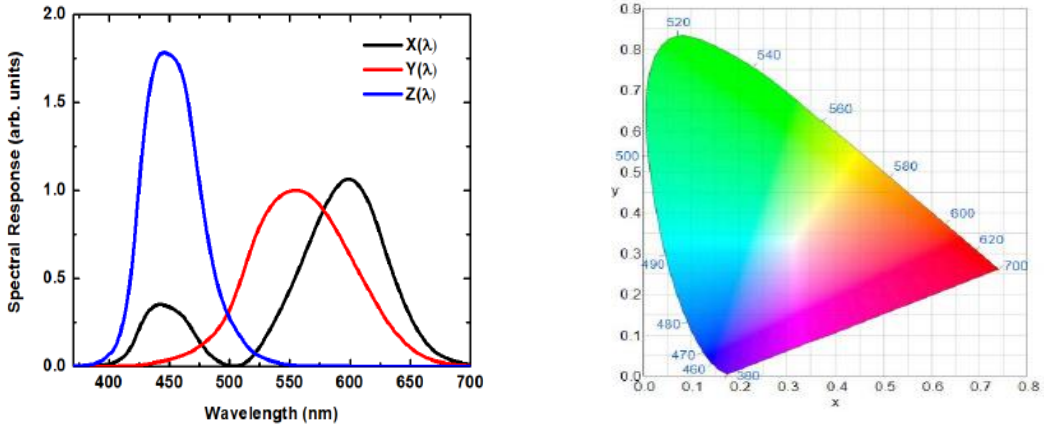

Figure 1.2.1.3. Spectral response of the three color-sensitive photoreceptors cell (A). CIE color space (x, y) diagram for conversion from monochromatic light (B).

Equation 1.2.3

$$EQE = \frac{number\ of\ photons\ extracted}{number\ of\ electrons\ injected}$$

$$= \frac{number\ of\ photons\ generated}{number\ of\ electrons\ injected} \times \frac{number\ of\ photons\ extracted}{number\ of\ photons\ generated}$$

$$= \eta_C \eta_E \eta_{PLQY} \times \eta_{out}$$

were the η_C is the charge balance factor, η_E is the ratio of emissive excitons, η_{PL} is the photoluminescence quantum yield, and ηOUT is the external out-coupling efficiency. The η_C, η_E, and η_{PL} are parameters intrinsic to the photophysical properties of the emitter. Contrarily, the ηOUT is limited to a 20-30 % due to a combination of factors such as total internal reflection (TIR) and surface plasmon resonance (SPR).[37–39] Emission is a radial process and therefore, the TIR happens when the emitted photons from the EML fails to meet the critical angle of incidence, preventing it escape the device. As a result, a high percentage of photons do not escape the device and are reflected within the OLED electrodes. Consequently, the SPR mechanism is more probable to happen. In this case, an energy transfer happens between a photon and the electrodes happens

if their frequency matches the natural frequency of surface valence electrons.[40] Efforts have been made to control the molecular alignment of the emitter in the EML to enhance the extracted photons from the OLED device and ηEQE > 30 % has been reported.[41] The *Commision Internationale de l'Éclairage* (CIE) have modeled specific color coordinate system based on the spectral responsivity of ρ, γ, β cones in the retina (**Equation 1.2.4A** and **Equation 1.2.4A)**.[42,43] In **Equation 1.2.4A**, the *Φp* represent the photon flux from the emissive chromophore, while the X(λ), Y(λ), Z(λ) is a standardized response of the three color-sensitive photoreceptors in the human eye as shown in **Figure 1.2.1.3A**. The **Equation 1.2.4A** is fundamental for understanding how obtaining monochromatic photons translate to the retina detection color coordinates as observed in **Figure 1.2.1.3B**. Researchers have developed emissive chromophores based on these color coordinates, with red, green, and blue being the fundamental colors to create images.

$$x = \int \Phi_p(\lambda)X(\lambda)d\lambda,\ y = \int \Phi_p(\lambda)Y(\lambda)d\lambda,\ z = \int \Phi_p(\lambda)Z(\lambda)d\lambda \qquad \textbf{Equation 1.2.4A}$$

$$\bar{x} = x / (x + y + z),\ \bar{y} = y / (x + y + z) \qquad \textbf{Equation 1.2.4B}$$

1.2.3 Organic Semiconductors Emissive Materials for High-Performance OLEDs

In the electroluminescence mechanism, uncorrelated charge carriers are injected to electrically excite an emissive material with the purpose of extracting photons. Sophisticated engineering of OLEDs has led to unprecedented device efficiencies that have narrowed their commercialization gap, making them to compete with traditional displays. One of the most critical interactions in the OLEDs happens in the emissive layer (EML), which is governed by the energy transfer efficiency from the host material to the guest emissive material. These energy transfer processes, namely FRET and DET, are highly dependent on favorable energetic alignment and

distances between the host material and the guest material. Because of these energetic features, green-emitting OLEDs are often defined as the state-of-the art performance in OLEDs.[44]

The first high-performance green emitter was reported by *Baldo et al.* in 1998, when he used tris(2-phenylpyridine)iridium(III) (Ir(ppy)3) doped in 4,4′-Bis(N-carbazolyl)-1,1′-biphenyl (CBP) at a 6% concentration, which obtained an 8 % ηEQE with a power efficiency of 31 lm/W.[18] Since then, a plethora of green phosphors have been developed based on this chromophore, to form the second generation of OLEDs. However, CBP has stayed as the elite host material for its favorable energetics, specifically its triplet energy.[45] Ligand and morphology modifications have allowed the efficiency of these devices to go up to ~ 30 %. *Wang et al*. in 2011 reported a green-emitting OLEDs that produced an ηEQE > 28 %. This was possible by controlling the orientation in the EML. Specifically, an horizontally oriented approach using bis(2-phenylpyridine) (acetylacetonate)iridium(III) (Ir(ppy)2(acac)), doped in a CBP was used with an ETL composed of 2,2',2'' -(1,3,5-benzinetriyl)-tris(1- phenyl-1-H-benzimidazole) (TPBi).[44] Further improvements in the ηEQE was achieved by electrodes modification and an out-coupling lens array was included in the OLED. *Kim et al*. achieved ηEQE > 30 % by using Ir(ppy)2(acac) green phosphor as the guest and by modifying the HOST via exciplex-forming co-host system with [4,4′,4″-tri(N-carbazolyl)triphenylamine] (TCTA) and [bis-4,6-(3,5-di-3-pyridylphenyl)-2-methylpyrimidine] (B3PYMPM).[41] These advances in green phosphors and EML design has led to device operational half lifetimes (LT_{50}) of ~ 400,000 h, which is defined by how much time it takes to arrive to half of its original device performance. These performances have allowed green phosphor OLEDs to compete with traditional displays such as LCD. However, the case is different for blue phosphor emitters. Examples of organic phosphors emitters for OLEDs applications can be observed in **Figure 1.2.2.1**.

Ir(ppy)$_3$ Ir(ppy)$_2$(acac) FIrpic

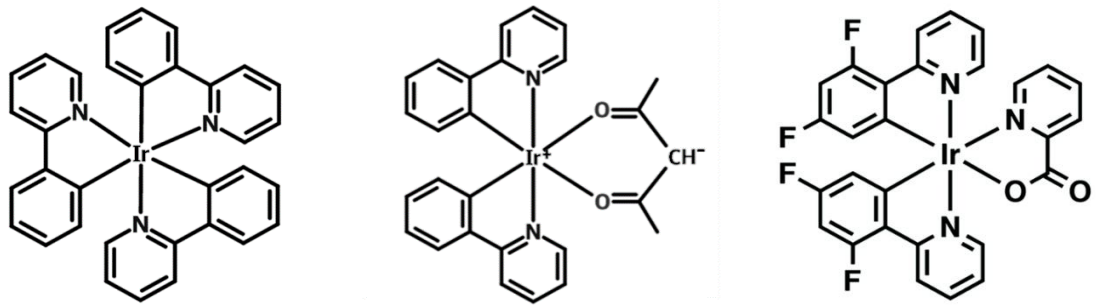

Figure 1.2.2.1. Organic phosphors for OLEDs applications.

Adachi et al. reported the first EML with a blue fluorescence emitter back in the 1990.[46] A decade later, he reported the first OLEDs device with a blue phosphor emitter in the EML and it yielded 5.7 % ηEQE using a power efficiency of 6.3 lm/W.[47] This discovery represented a significant advance in the blue OLEDs field. However, the triplet energy of the CBP was lower than the one for the blue phosphor, namely iridium (III)bi[(4,6-di-fluorophenyl)-pyridinato-N,C2']picolinate (FIrpic). Because of the endothermic nature of the energy transfer process, the Dexter energy transfer was hampered. Improvements in the device ηEQE (7.5 %) and power efficacy (8.9 lm/W) was made when CBP was replaced by N,N'-dicarbazolyl-3,5-benzene (mCP). This was possible due to its higher lying triplet energy level in comparison with CBP and in comparison with the blue phosphor FIrpic.[48] Further ηEQE improvements were reported by *Liu et al*.,[49] however, the development of blue phosphors for OLEDs applications have been very limited since then. Unfortunately, the organometallic nature of the blue phosphors induces synthetic constraint, making it difficult to tune their photophysical properties. In addition, the high lying triplet energy levels require for host materials with even higher lying triplet energy levels for efficient exothermic energy transfer. Both issues with blue-emitting devices contributes to the very high device efficiency roll-off at high brightness levels that hampers their commercialization

current densities. The efficiency roll-off at high brightness levels is attributed to a mechanism known as triplet-triplet annihilation (TTA).[49] When the density of triplets excitons in the EML is high, the probability of triplet-triplet encounters is higher. As a result, two triplets of the same energy can collide and as a result get up-converted to produce a singlet of twice the energy of the colliding triplets. When that mechanism happens in blue phosphors, singlets with energies higher than 5.8 eV can occur. Resulting in molecules carrying energies high enough to break their fundamental C-C, C-H, and C-N bonds that compose the ligands in organometallic phosphor emitter.[50] As a result, massive degradation of the emitter results in very short device operational lifetimes. In addition, a complex tri-layer EML with several different host materials are used to maximize carrier injection and recombination. These features play a major role in impeding their commercialization.

While phosphors emitters can provide device efficiencies as high as the theoretical predicted value, they must overcome some challenges to outcompete LCDs. First, their cost of fabrication is too high. This is mostly attributed due to their need of a rare earth metal such as Ir and Pt to have access to their emissive triplet state. By incorporating these transition metals, the cost of synthesizing is 2-3 times higher than typical fluorescence chromophores.[16] Second is their poor device stability, specifically with blue phosphorescent emitters. The efficiency roll-off of blue OLEDs makes their device operational lifetimes to be around 20,000 h.[49] The massive blue phosphor OLED degradation is due to a combination of the TTA mechanism at high triplet densities and their intrinsic high lying triplet energy levels relative to the most common host materials. As a result of these high lying triplet energy level, blue-emitting phosphors are less efficient at confining excitons in the OLED recombination zone, making them to have smaller device operational lifetimes compared to green and red phosphors.[51] This disparity in device

operational lifetimes between the blue, green, and red phosphors became relevant in display applications, where blue-emitting OLEDs degrade much quicker than the green and red phosphors counterparts, causing image distortion.[27] Scientist have suggested that this problems may be addressed by developing an universal host material with triplet energy level > 2.9 eV. Reports on universal hosts with high lying triplet energy and ambipolar charge carrier mobility have recently surfaced, and it is believe that it could contribute to the device operational lifetime and stability of phosphors emitters.[52–54] In recent years, lots of effort has been made in developing blue chromophores for triplets harvesting from purely organic materials via an unusual mechanism named thermally activated delayed fluorescence (TADF). This mechanism represents the third generation of OLEDs and it will be described in detail in sections to come.

1.2.4 Thermally Activated Delayed Fluorescence (TADF) for High-Performance OLEDs

Thermally activated delayed fluorescence (TADF) is the idea that non-emissive triplets can be converted into emissive singlets ($T_1 \rightarrow S_1$) by a reverse intersystem crossing mechanism (rISC).[26,55–60] This rISC mechanism is prompted by the combination of thermal energy with the small energy gap between the singlet-triplet manifolds (ΔE_{ST}).[16,61] This phenomena was first observed in eosin (e-type fluorescence) and it was also observed in copper-based systems, but little to no information on how to design chromophores with a small ΔE_{ST} was known.[62–64] In 2012, Chihaya Adachi first published a design rule on how to achieve a small ΔE_{ST} in purely organic chromophores.[16] The molecular structure was composed by carbazole and benzonitrile subunits, and their superior ηEQE (> 10 %) over traditional organic chromophores quickly solidified the TADF technology as the third generation of OLEDs.[65,66] The design rule consists on synthesizing a charge transfer complex with a C-N bond connecting the donor and acceptor that will partially

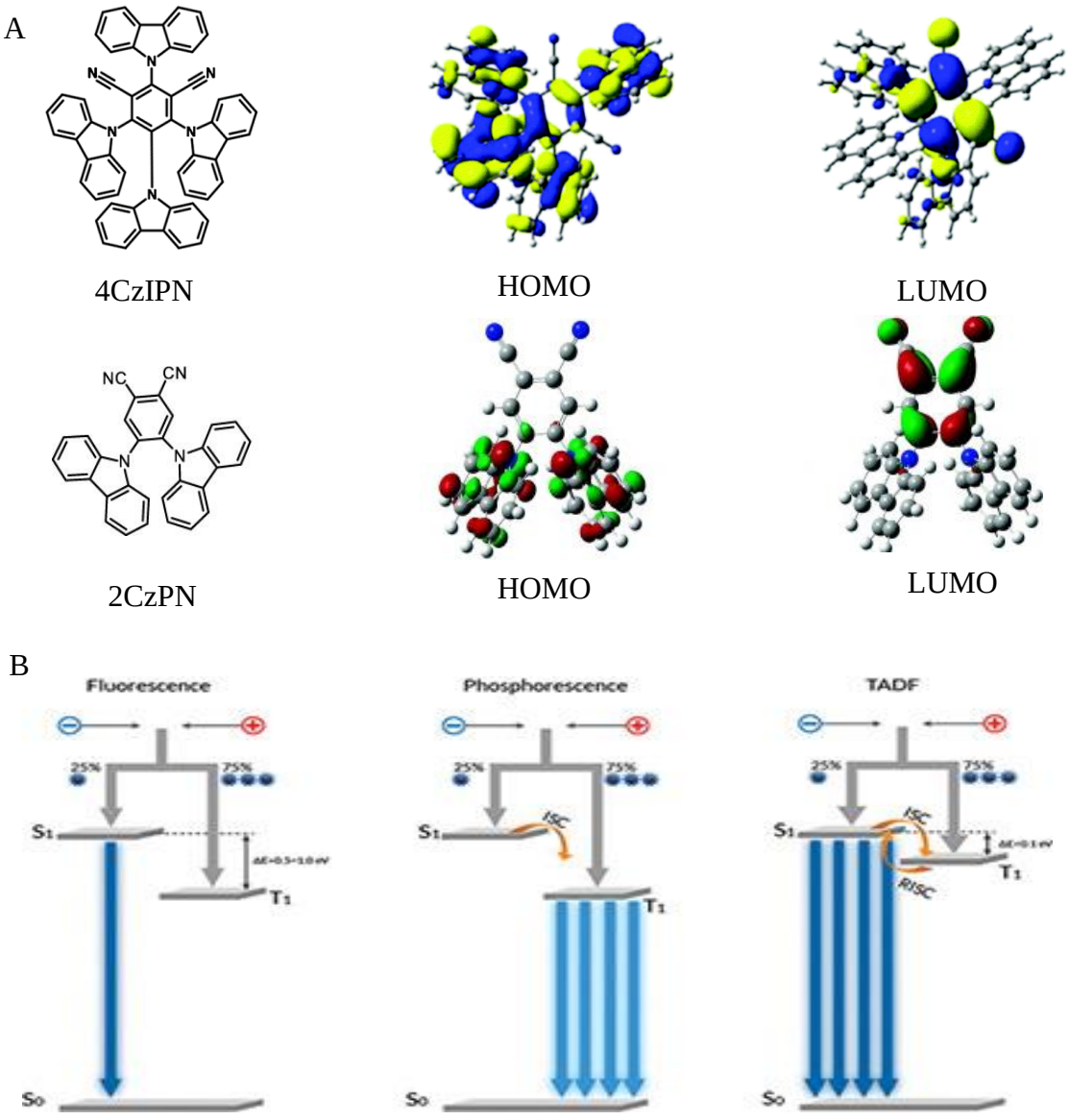

Figure 1.2.3.1. Molecular structure and the molecular orbitals of highly efficient TADF chromophores (A). Electroluminescence mechanism of the first, second, and third generations OLEDs (B).

$$E_{S_1} = h_H + h_L + J_{HL} + K_{HL}$$

$$E_{T_1} = h_H + h_L + J_{HL} - K_{HL}$$

$$\Delta E_{ST} = 2K_{HL}$$

$$J_{HL} = \int\int d\vec{r}_1\, d\vec{r}_2\, H(\vec{r}_1)H(\vec{r}_1)\frac{1}{r_{12}}L(\vec{r}_2)L(\vec{r}_2)$$

$$K_{HL} = \int\int d\vec{r}_1\, d\vec{r}_2\, H(\vec{r}_1)L(\vec{r}_1)\frac{1}{r_{12}}H(\vec{r}_2)L(\vec{r}_2)$$

Equation 1.2.3.1

break the pi-conjugation length between the donor-acceptor junctions (**Figure 1.2.3.1**). This partial break in its conjugation length will result in a dihedral angle that will spatially separate the HOMO and the LUMO orbitals in different moieties of the chromophores. The correlation between the singlet-triplet manifolds energy proximity (ΔE_{ST}) and the spatial separation of the HOMO and LUMO can be obtained from **Equation 1.2.3.1.**

In such charge transfer system, the singlet and triplet energy splitting can be obtained by the one-electron energy of the HOMO and LUMO orbitals overlap (h_H and h_L), the Coulomb repulsion energy (J_{HL}) between the electron 1 on the HOMO and electron 2 on the LUMO, and the electron exchange energy (K_{HL}). Emphasis on how the K_{HL} depends greatly on the spatial overlap between the molecular orbitals.[57,67,68] In synthesis, ΔE_{ST} is proportional to K, which is closely related to the frontier molecular orbital overlap extent and separation distance. Consequently, a significant area of the TADF development is attributed to the use of inexpensive quantum chemical simulations (QCS) to explore their singlet-triplet state energy gap to demarcate if the chromophores is synthesized or not.[57,67,68] It is widely accepted that by maximizing the dihedral angle between the donor-acceptor junctions of these TADF chromophores a small ΔE_{ST} should be obtained.[65] However, recent reports have disproved this synthetic approach, and have further highlighted that having a small ΔE_{ST} may not be a sufficient feature to ensure effective communication between the singlet-triplet manifolds. *Samanta et al*. reported that designing a TADF chromophore with either a significant charge-transfer (CT) contribution to the T_1 state or having a minimal energy difference between the local-excited triplet state and charge-transfer triplet states is required to achieve a small ΔE_{ST}.[69] In addition, they showed that having a TADF chromophore with an S_1 with charge transfer character and T_1 states with local-excited nature could enhance the chromophore spin-orbit coupling (SOC) and facilitate the communication

between the singlet-triplet manifolds. The structure of the material dictates its function. Therefore, understanding how the physio-organic aspects of these chromophores modulate their excited state electronic transition (such as the ISC and rISC) is one of the focal points under intense investigation today.[56,68,69]

Many improvements in the device performances of TADF-OLEDs have been made since Adachi published its breakthrough paper in 2012. Recent work has shown that the efficiencies of these devices can be further improved if a universal ambiopolar material is used to replace CBP as the host in the EML, with reported TADF-OLEDS ηEQEs > 25%.[70,71] In 2015, *Hirata et al.* achieved a major breakthrough in TADF technology and OLEDs reporting blue emitters with ηIQE ~ 100 %.[72] In this case, carbazole subunits were used as donor moieties and triazine derivatives were used as the acceptor moiety. In that study, the importance of obtaining a high rISC rate (k_{rISC}) for optimal device performances is emphasized. Since then, lots of studies have focused on understanding the molecular parameters that control the rISC rate in rational designed TADF emitters under the premise that the k_{rISC} may help to predict their device performance.[57,69,72–78] Specifically, it is believed that obtaining a high k_{rISC} is critical for reducing the triplet-triplet annihilation (TTA) mechanism that cause ηEQE roll-off.[73,79,80] However, a combination of selected tools are needed to experimentally measure the k_{rISC}. These approaches do not exclude the parallel coexistence of phosphorescence in the chromophore nor the influence of the host material if the measurements are conducted in solid state.[68,77,79,81–83]

The effect of having a host in the EML with TADF properties has been also explored with promising results.[45] It is believed that having a universal host with efficient rISC process could further help to reduce the TTA mechanism that preclude the devices efficiencies of OLEDs. In addition, the synthetic flexibility of organic TADF may facilitate tuning of the optical and

photophysical properties so desired triplet energy level for optimal Förster and Dexter energy transfer processes are obtained.[84,85] The TADF technology offers several advantages over organometallic technologies such as device flexibility and cost-efficiency. However, as with the phosphors OLEDs counterparts, their device efficiency abruptly decrease at high brightness levels, which affects its device operational lifetime.[45,73,86] When the TADF material is used as the host and phosphors emitters are used, device operational lifetimes as high as 20,000 h have been reported. When blue TADF are used as the emitters, device operational lifetimes < 1,000 h have been reported.[45] These device performance lifetimes are well below those of the second generation OLEDs, which makes them to be ways away from being commercially available. Therefore, enhancing the device operational lifetimes by 1) exploring different device architectures and 2) understanding how the molecular structure governs the excited state electronic transitions in these systems are the focal point of research in this technology.[45,73]

1.3 The Fundamental Properties Behind the TADF Mechanism.

1.3.1 Electronic Transition and the Jablonski Diagram

In the photoluminescence (PL) process, an electron is excited from the ground state to the excited singlet state ($S_0 \rightarrow S_n$). This electronic transition usually happens in sub femtosecond timescale ($k_A > 10^{15}$ s^{-1}) and is the fundamental first step of the PL process. Following the photon absorption, several excited state processes can occur in order to dissipate the excess of energy induced by the photon absorption. The most favorable one is called internal conversion (^{1}IC). The ^{1}IC is a non-radiative vibrational relaxation process usually occurring in sub picosecond timescales ($k_{IC} > 10^{12}$ s^{-1}) that dissipate the excess of energy into the surrounding of the molecule. As a result, the molecule will relax until it arrives to the S_1 state ($S_n \rightarrow S_1$). From the S_1 state, the molecule can dissipate its energy via-radiative, namely fluorescence, or non-radiative decay ($S_1 \rightarrow S_0$). The

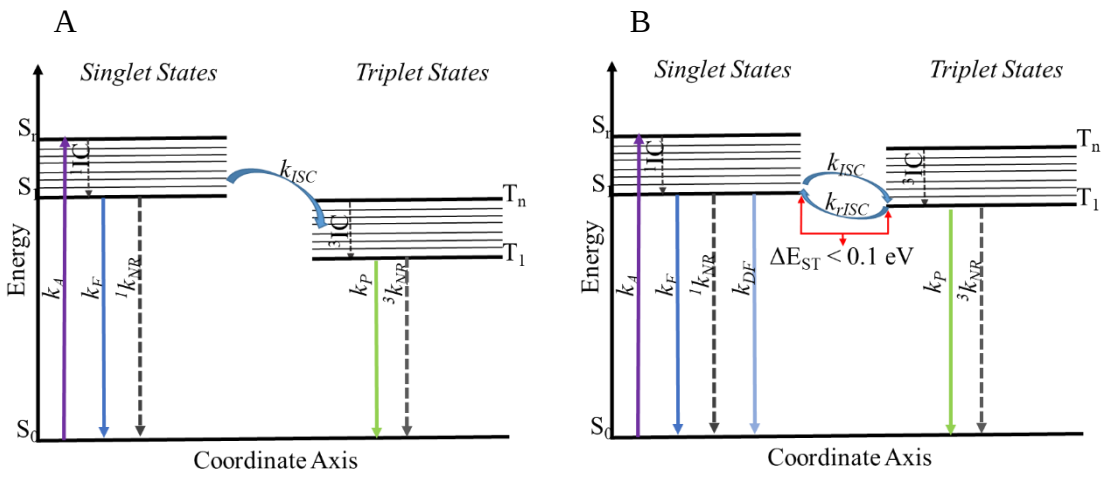

Figure 1.3.1.1. Jablonski diagram depicting the excited state electronic transition of typical fluorescence and phosphorescence chromophores (A) and chromophores with TADF characteristics (B).

fluorescence from the S_1 state is typically in the nanosecond timescales or faster ($k_F > 10^9$ s^{-1}) and it is best explained by Kasha's rule, which states that photonic emission occur in substantial yield only from the lowest excited state of a specific multiplicity.[87] The multiplicity concept, which explains the singlet and triplet nature of molecules, will be expanded in following sections.

One of the most important concepts for chromophores with TADF characteristics is the intersystem crossing (ISC), which is a non-emissive electronic transition that changes the multiplicity of the system. As a result, a transition between singlet states and the triplet states occur via a spin flipping process. In photoluminescence, the ISC first occurs from the singlet state to the triplet state ($S_n \rightarrow T_n$), and it could happen in timescales slower than nanoseconds for typical fluorescence chromophores ($k_{ISC} < 10^9$ s^{-1}). However, it could happen in the sub picosecond timescale for phosphorescence chromophores.[19,23] The ISC mechanism will be further expanded in sections below. If the triplet state is accessed, another IC process from a higher triplet state to the lowest triplet state could happen ($T_n \rightarrow T_1$) as an energy dissipation process, which is also explained by Kasha's rule. From the lowest triplet state (T_1), the system can dissipate its energy

via a radiative pathway, namely phosphorescence, or via non-radiative pathways ($T_1 \rightarrow S_0$). Both energy dissipation processes are typically in timescales slower than milliseconds (k_P and ${}^3k_{NR} < 10^6\ s^{-1}$). The probability of photonic emission from the triplet state is forbidden, but it becomes probable by the spin-orbit coupling interactions (SOC) in the system.[88] The SOC will be further explained in coming sections.

In the case of materials with TADF characteristics (**Figure 1.3.1.1B**), the energy difference between the lowest singlet and lowest triplet states (ΔE_{ST}) is so small that room thermal energy may facilitate a multiplicity change in these systems. This is true for the ISC mechanism and for the reverse intersystem crossing mechanism (rISC) ($T_1 \rightarrow S_1$). The latter mechanism usually happens in the millisecond timescales ($k_{rISC} \sim 10^6\ s^{-1}$) for purely organic chromophores and in sub-nanosecond timescales for copper-based TADF systems.[69,77,89] It is important to highlight that in order to have an efficient long-lived delayed fluorescence component the k_{rISC} needs to be orders of magnitudes larger than the k_P and the ${}^3k_{NR}$. In this way, the density of triplet state is converted into singlets for photonic emission rather than dissipating its energy via non-emissive transition from the triplet state.[90] As a result, emission from the S_1 state with lifetimes similar to those for phosphorescence are obtained. However, a multi-exponential decay is usually obtained as a result of the prompt fluorescence (PF: $S_0 \rightarrow S_n \rightarrow S_1 \rightarrow S_0$) and the delayed fluorescence (DF: $S_0 \rightarrow S_n \rightarrow S_1 \rightarrow T_1 \rightarrow S_1 \rightarrow S_0$), which is a characteristic feature of organic TADF materials. There is a fundamental difference between the photoluminescence and the electroluminescence excitation process, as it has been discussed in previous sections. However, the excitation process may not affect the excited state dynamics and their probability to happen. The Jablonski diagram depicting the excited state transitions of fluorescence, phosphorescence, and TADF chromophores can be observed in **Figure 1.3.1.1**.

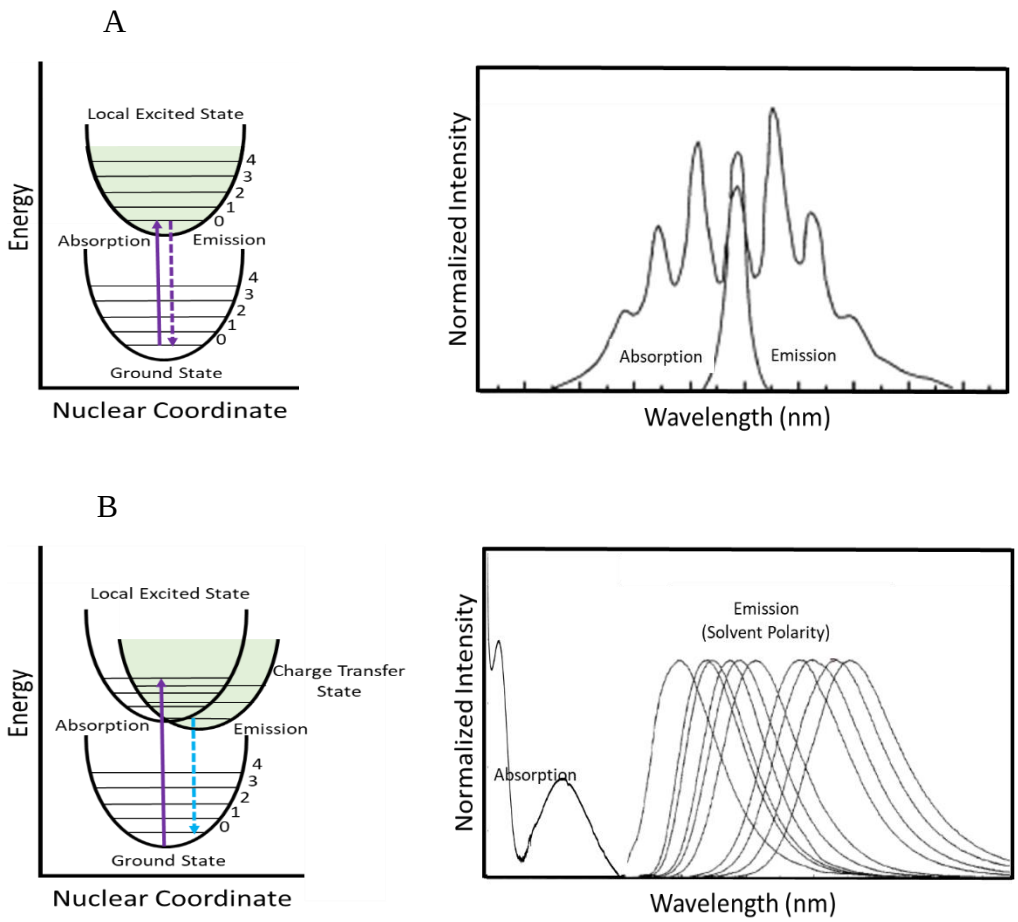

Figure 1.3.2.1. General schematic representation of local excited (A) and charge transfer (B) states optical transitions and its steady state absorption and emission representation.

1.3.2 Franck-Condon Principle for Local Excited and Charge Transfer States

The Franck-Condon principle (FCP) is a rule in spectroscopy and in quantum mechanics that explains the intensity of vibronic transitions in a photoluminescence process. Vibronic transitions are the simultaneous changes in vibrational and electronic energy levels of a molecule because of the photonic absorption and subsequent emission. Specifically, the FCP states that the relative velocity between the photo-excited electrons, which happens in sub femtosecond timescales, and the nuclei is so big that one can assume that the nuclei is in stationary position during the photon absorption process.[91–93] The nuclei does not readjust during the excitation

process, but rather must readjust while the electrons are in the excited state, which accounts for the loss of energy (internal conversions) due to vibrational motions. The relative geometry of the molecule between the ground and excited state plays a major role in these transitions. If the molecule has almost identical geometries between the ground and excited states, the absorption and emission transitions could be expected to be very similar. As a result, a mirror image between the absorption and emission transitions is obtained.[94] This behavior is known as the Franck-Condon states or local excited states (LE) of the system. This optical behavior is mostly observed in solvents with very low polarity.[95] A schematic representation of the LE transitions can be observed in **Figure 1.3.2.1A.**

Contrarily to the LE transitions, an emission displacement towards lower energy wavelengths could be obtained when the geometry between the ground state and the excited state differs among them, as is explained by the Stokes shift principle.[96,97] The slight shift in equilibrium geometry of the excited states is due to a reorganization process, which results in energy dissipation into the surroundings of the molecules. This process is much more pronounced in systems with high dipole moments, and is best observed in solvents with high polarity.[98] The state in which the geometry between the ground state and the excited state differs greatly is known as the charge transfer state (CT). In the CT state, the excited state dipole moment is larger than the one for the ground state. As a result, the solvent dipole greatly influences the energy dissipation pathways of the excited chromophore. After excitation, the dipole of the solvent interacts with the dipole moment of the excited molecule to induce an energy reorganization to the lowest CT energy state. Solvents with strong dipole moments also leads to the broadening of the emission spectra.[99] A schematic representation of the CT transitions can be observed in **Figure 1.3.2.1B**. It is important to highlight that, contrarily to the LE excitations, excitations to a higher vibrational state is often

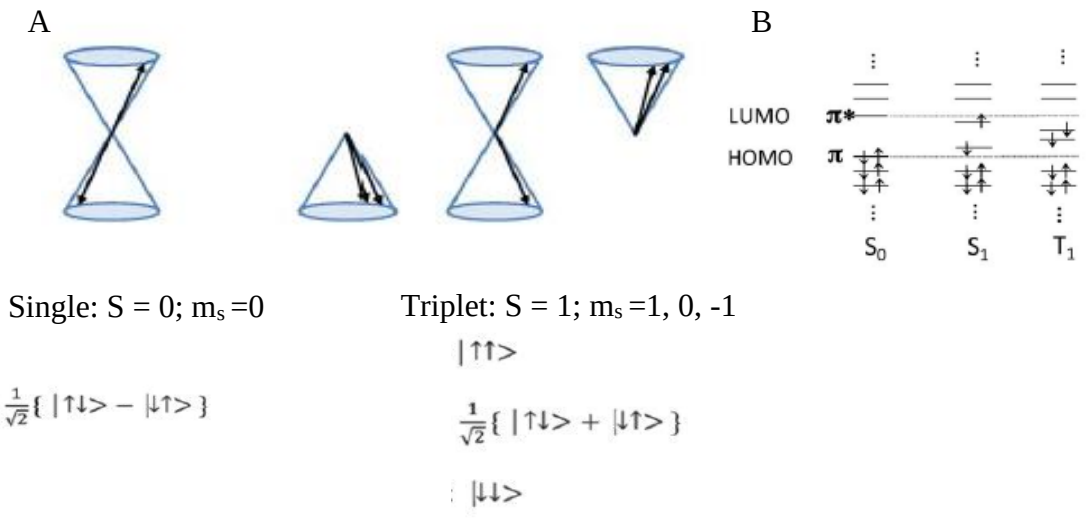

Figure 1.3.3.1. Vectorial representation illustration the spatial orientation of singlets and triplets, and their respective spin wavefunctions for the four eigenstates in a two-particle system (A). Singlet and triplet state configuration relative to the molecular orbitals of semiconductor.

favored in systems with CT character.[100] As a result, the most intense absorption peak does not necessarily correspond to the lowest energy transitions. As expected, the emission process of the systems with divergence in their ground state and excited state geometries comes from the CT states. The LE and CT states plays an important role in the excited state dynamics of chromophores with TADF characteristics, and they will be further discussed in sections to come.

1.3.3 Singlet and Triplet States

In quantum mechanics, the spin nature of the system is invoked to conceptualize the electron angular momentum, which is a fundamental property along with the electron charge and mass. Electrons are fermions with a half spin angular momentum, S, where S = ± ½. The spin angular momentum is a vectorial quantity that can be best described by a two-electron system, the multiplicity equation (m; where m = 2S + 1), and by the Pauli Exclusion Principle (PEP).[101,102] For convenience and due to the vectorial nature of the angular momentum, we can denote each electron spin as either "up; ↑" and "down; ↓". The PEP states that no two-electrons in a system can possess

the same electronic quantum numbers, ergo they must not possess the same eigenvalue. A two-electron system has four potential electron spin vectorial configurations (↑↑, ↑↓, ↓↑, ↓↓), with opposite spins (singlet) being the most probable multiplicity, while having the same spins (triplet) being the less probable multiplicity. In order to account for the multiplicity of all the potential electronic configurations and still satisfying the PEP, the wavefunction that describes these systems is written as a product of wavefunctions. Specifically, their wavefunction will be a combination of the electron spatial coordinates and the spin wavefunction.[103] As a result, different eigenstate values, which satisfy the PEP, are obtained if the symmetric spin wavefunction of the triplet state is combined with an antisymmetric spatial wavefunction; conversely, wavefunction construction is employed for the singlet state. Specifically, the first spin wavefunction has an S = zero, which results in a spin multiplicity equals to 1; ergo, singlet. The next three wavefunction have an S = one, which results in a triplet multiplicity. However, the eigenstate differs in the z-component of the spin, which results in three different eigenvalues, namely m_s = -1, 0, 1, and satisfying the PEP. A vectorial representation and singlet triplet multiplicity can be observed in **Figure 1.3.3.1A**.

The ground state of organic semiconductors is generally a singlet sate. This means that two-electrons with opposite spins are occupying the same HOMO. Upon photoexcitation, one electron is promoted from the HOMO to the LUMO, which are analogs to the S_0 and S_n states, respectively, and are explained in detail in previous sections. This electronic transition conserved the spin nature of the molecule from the ground state, which result in a singlet excited state (S_n). In occasion, a spin flipping process via an intersystem crossing (ISC) mechanism can occur in the excited state. Excited state singlets can be converted into excited state triplets by an intersystem crossing mechanism ($S_n \rightarrow T_n$), and triplets can be converted into singlet ($T_n \rightarrow S_n$) in a reverse

ISC (rISC) mechanism. The fundamental properties for both processes, namely the ISC and the rISC, will be discussed in a further section.

1.3.4 Intersystem-Crossing (ISC) and Reverse Intersystem-Crossing (rISC)

As mentioned in previous sections, the ISC is a radiation-less transition that plays a major role in the excited state dynamics of phosphorescence and TADF emissive materials.[45] In essence, the ISC is an adiabatic process that occurs between states of different multiplicity. Specifically, a change in the electronic spin-angular momentum between the two-electrons in an orbital could change while in the excited state. This electronic transition is strictly forbidden ($\Delta S = 0$), based on the Fermi's golden rule.[104] However, this transition could become non-zero if the angular spin of the electrons is coupled with the orbital angular momentum, namely the spin-orbit coupling (SOC). Because of the SOC, systems can achieve a spin flipping process and change their multiplicity, from singlet to triplets and vice-versa.

Since a large SOC is critical for the change in multiplicity, it is worth expanding on factors that influence the SOC in a system. Success in achieving efficient ISC have been observed when heavy atoms are introduced into a system. This is because the magnetic field from the nucleus of the heavy atom is large enough that is capable of influencing the velocity the electron pair and the spatial orientation of both the electrons pair and the orbital.[104] This phenomena is known as the "heavy atom effect".[105,106] The SOC can be large; however, this electronic transition must be conserved in order to diverge from being non-zero. Thus, the multiplicity change in the electronic spin angular momentum is compensated with a change in the orbital angular momentum. Specifically, if the orbital p has an angular momentum 1, its transitions to an orbital with angular momentum 0 is achieved to compensate for the spin flipping process. This spin-orbit angular conservation is best explained by the El-Sayed rule, which states that the probability of electronic

multiplicity changing, namely the ISC, diverge from being non-zero if a simultaneous change in the molecular orbital type is involved.[88,107] The orbital nature change favors the ISC process in this order: $^1(\pi, \pi*) \rightarrow {}^3(n,\pi*) > {}^1(\pi, \pi*) \rightarrow {}^3(\pi, \pi*)$. Consequently, $^1(n, \pi*) \rightarrow {}^3(\pi, \pi*) > {}^1(n, \pi*) \rightarrow {}^3(n, \pi*)$. Extensive theoretical and experimental work has been conducted in order to understand the ISC process. The experimental work consists of using spectroscopy to characterize the triplet state, while the theoretical work is comprised of construction operators to evaluate the probability of this transition.[108–110] A quantum mechanical representation of the ISC probability can be is observed in **Equation 1.3.4.1**.

$$k_{ISC} = | < \Psi_1 | H_{SO} | \Psi_3 > |^2 \qquad \textbf{Equation 1.3.4.1}$$

In **Equation 1.3.4.1**, the k_{ISC} represents the rate of ISC, the Ψ_1 represents the wavefunction of the singlet state, the Ψ_3 represents the wavefunction of the triplet state, and the H_{SO} is the SOC operator, which accounts for the overall angular momentum conservation.[88]

Similar principles in terms of conservation of spin-orbital angular momentum are needed for the reverse intersystem-crossing (rISC) mechanism. However, the small exchange energy that yields a small ΔE_{ST} is considered to be critical for obtaining a sizable rISC.[77] It has been widely accepted that by spatially separating the HOMO-LUMO orbitals in materials with TADF characteristics a small ΔE_{ST} could be achieved,[65,111] and how to obtained it was described in previous sections. However, recent theoretical findings by *Samanta et al*. showed that enhancing the dihedral angle between the donor-acceptor junctions might not be an effective method to decrease the exchange energy. Instead, they found that having a significant charge-transfer (CT) contribution to the T_1 state or a minimal energy difference between the local-excitation and charge-

transfer triplet states is required to achieve a small ΔE_{ST}. In addition, having S_1 and T_1 states of a different nature is found to strongly enhance SOC, which is consistent with the El-Sayed rule for ISC rates.[69] They further give theoretical insight into the rate of rISC in chromophores with TADF characteristics, as it can be observed in **Equation 1.3.4.2**.

$$k_{rISC} = \frac{2\pi}{\hbar} p_{FC} | < \Psi_1 | H_{SO} | \Psi_3 > |^2 \qquad \textbf{Equation 1.3.4.2}$$

In **Equation 1.3.4.2**, the k_{ISC} represent the rate of rISC, the $| < \Psi_1 | H_{SO} | \Psi_3 > |^2$ is analogous to the in **Equation 1.3.4.1**, and the p_{FC} is the denotes the Franck-Condon weighted density of states. The p_{FC} terms were evaluated in the framework of Marcus-Levich-Jortner theory and is further expanded in **Equation 1.3.4.3.**

$$\rho_{\mathrm{FC}} = \frac{1}{\sqrt{4\pi\lambda_{\mathrm{M}} k_{\mathrm{B}} T}} \sum_{n=0}^{\infty} \exp(-S) \frac{S^n}{n!} \exp\left[-\frac{(\Delta E_{\mathrm{ST}} + n\hbar\omega_{\mathrm{eff}} + \lambda_{\mathrm{M}})^2}{4\lambda_{\mathrm{M}} k_{\mathrm{B}} T} \right] \qquad \textbf{Equation 1.3.4.3}$$

In **equation 1.3.4.3**, the λ_M denotes the Marcus reorganization energy associated with the intermolecular and intramolecular low-frequency vibrations, k_B is the Boltzmann constant, T is the temperature; $\hbar\omega_{\mathrm{eff}}$ is the effective energy of a mode representing the non-classical high-frequency intramolecular vibrations ($\frac{\hbar\omega_{eff}}{k_b T} \gg 1$), and S is the effective Huang-Rhys factor associated with this mode.[69,112,113] Emphasis on how the rISC rate is inversely proportional to the ΔE_{ST}. Therefore, the k_{rISC} is proportional to the SOC and inversely proportional to the ΔE_{ST} ($k_{rISC} = \frac{SOC}{\Delta E_{ST}}$). Since then, this theoretical approach has been instrumental for the k_{rISC} determination of chromophores with TADF characteristics.

In line with this work, experimental studies have combined steady state and time resolved spectroscopy to characterize the nature of the excited states involved in the rISC process. These studies suggested that obtaining a high k_{rISC} might depend on minimizing the energy difference between the triplet local excited state (^{3}LE), and both, the triplet and singlet charge transfer state, ^{3}CT and ^{1}CT, respectively.[73,114] The small energy difference between the aforementioned states may help to facilitate the rISC process in these systems due to a second-order vibronic coupling among these states, as it has been proposed by *Gibson et al*.[115,116] *Hosokai et al*. was able to identify transient states consistent with ^{3}LE and charge resonance (CR) states, which they linked to the delocalized charge transfer state ^{de}(CT), to be integral to obtaining TADF chromophores with a large k_{rISC} even when ΔE_{ST} is not close to zero.[114] However, how subtle chemical structure modifications to the ^{3}LE, ^{3}CT, and ^{1}CT states are systematically modified in order for the k_{rISC} to be modulated is still far from being fully understood. Consequently, understanding the molecular parameters that control the rISC in molecules with TADF characteristics and developing methods for the efficient k_{rISC} determination has drawn lots of interest in recent years. These days, the focal point lies in the experimental determination of the k_{rISC} of the system.[45,117] It is believe that the k_{rISC} may help in reducing the TTA mechanism that limits their device operational lifetimes and hampers their commercialization. The current methods for the experimental k_{rISC} determination will be discussed in further sections and the development of a new optical methodology for determining the k_{rISC} is one of the focal points of this dissertation.

1.3.5 Experimental Methods for Estimating the rISC rate in TADF Emitters

Until this point, the key challenge hampering the TADF-OLEDs commercialization is their poor device efficiency at high brightness levels, an effect known as efficiency roll-off.[45,118] The efficiency roll-off at high brightness levels is mostly attributed to a TTA mechanism when a high

density of triplets is present in the EML, as described previously. It is believed that obtaining a high k_{rISC} is critical for reducing the TTA mechanism that cause this efficiency roll-off.[73,79,80] Therefore, understanding the intersystem crossing mechanism between the singlet and triplet manifolds in chromophores with TADF characteristics is pivotal if one wants to achieve superior device operational lifetimes. The field has primarily used steady-state measurements and microsecond spectroscopy to illustrate and calculate the k_{rISC}. However, these indirect methods require a combination of selected tools and do not exclude the parallel coexistence of phosphorescence in the chromophore nor the influence of the host material if the measurements are conducted in solid state.[68,77,79,81–83]

Currently, there are two main methods for the k_{rISC} determination, and both of them lies in characterizing the fluorescence quantum yield before and after purging oxygen from the solution, and characterizing the multi-exponential emissive lifetime of these TADF chromophores.[82,90] The first one was developed by *Masui et al*. back in 2013.[82] The k_{rISC} determination with the Masui method can be observed in **Equation 1.3.5.1**.

$$k_{rISC} = \frac{k_p k_d \phi_{TADF}}{k_{ISC} \phi_F} \qquad \textbf{Equation 1.3.5.1}$$

In **Equation 1.3.5.1**, the ϕ_F represents the quantum yield of the chromophore at oxygen rich atmospheres, the ϕ_{TADF} represents the delayed fluorescence quantum yield of the chromophore, which is calculated by the difference in quantum yield before and after removing oxygen from the solution ($\phi_{OxygenFree} - \phi_F$). The k_p represents the rate of fluorescence, which is calculated by obtaining the inverse of the fluorescence lifetime ($k_P = \frac{1}{t_F}$). The k_d represents the rate of delayed fluorescence and it is determined by the inverse of the delayed fluorescence lifetime ($k_{DF} = \frac{1}{t_{DF}}$).

The k_{ISC} is the rate of intersystem crossing, and it is determined by determining the non-radiative quantum yield and multiplying it by the rate of fluorescence ($(1- \phi_F)*k_p$).[82] Also, the triplet non-radiative decay ($^3k_{NR}$) can be determined by multiplying the fluorescence quantum yield by the rate of rISC and subtracting this product to the rate of delayed fluorescence ($^3k_{NR} = k_D - \phi_F*k_{rISC}$). This contribution has been integral for the indirect determination of the rISC rate in TADF chromophores. However, this method does not exclude the parallel coexistence of phosphorescence in the chromophore nor the influence of the host material if the measurements are conducted in solid state.[68,77,79,81–83] Additionally, it does not take into consideration the non-emissive triplet dynamics of the TADF chromophores.

Dias et al. developed a methodology for the estimation of the reverse intersystem crossing rate back in 2016.[119,120] Similar to the Masui method, the Dias method estimates k_{rISC} from the photoluminescence quantum yields (PLQY) and the exponential lifetimes of the prompt fluorescence and the delayed fluorescence, as it can be observed in **Equation 1.3.5.2.**

$$k_{rISC} = \frac{1}{t_{DF}} * \frac{\phi_F + \phi_{DF}}{\phi_F} \qquad \textbf{Equation 1.3.5.2}$$

In **Equation 1.3.5.2**, the t_{DF} represents the delayed fluorescence lifetime of the TADF chromophore. The ϕ_F represents the quantum yield of the chromophore at oxygen rich atmospheres, and the ϕ_{DF} represents the delayed fluorescence quantum yield of the chromophore. The ϕ_{DF} is calculated by the difference in quantum yield before and after removing oxygen from the solution, as is calculated in the Masui method. However, this equation is based on the assumption that non-radiative processes from the triplet state are suppressed such that all of the triplet state density is converted into singlet density.[119] This assumption may hold when PLQY are

approaching to one in oxygen free atmospheres. However, this assumption is not valid when the PLQY is not close to 1. As a result, inaccurate k_{rISC} estimations may be obtained. The same is true for the Masui indirect method for determining the k_{rISC} of chromophores with TADF characteristics. Consequently, there is a need for the direct determination of the k_{rISC} so the device performances can be estimated with more accuracy.[45] Finding a new optical methodology for the direct determination of the k_{rISC} in chromophores with TADF characteristics is one of the focal points of this dissertation and will be discussed in further chapters.

1.4 Energy Sources for Electricity Production and their Conversion Processes

Humanity has exploited fossil fuels as their primary source of energy since the industrial revolution happened in the 18th century. Since their discovery, their demand has continued to increase exponentially. This is mainly attributed to the current world population, which is projected to reach 8 billion in the coming years and is expected to reach the 10-billion mark in 40 years from now (2059).[121] With that growth, the energy demand and consumption will grow accordingly. It is projected that a 28 % rise in energy consumption will happen by 2040, as it is observed in **Figure 1.4.1**.[121] However, using fossil fuels as the main energy source to meet humanity demands has intrinsic inevitable repercussions. Fossil fuels are the product of long years of gradual flora and fauna decomposition under specific conditions such as high pressure and temperature. Ergo, they are a nonrenewable source over human timescales. In addition, fossil fuel extraction, processing, and combustion have immediate detrimental effects on the environment.[121] Their harmful emissions are responsible for environmental pollutants such as sulfur dioxides, nitrous oxides, and carbon dioxide, which all together are protagonists of the devastating climate change that we are currently experiencing.[122] These circumstances have prompted the search for sustainable and clean energy technologies that can fulfil the fossil fuel energy demands. Interest has been given to

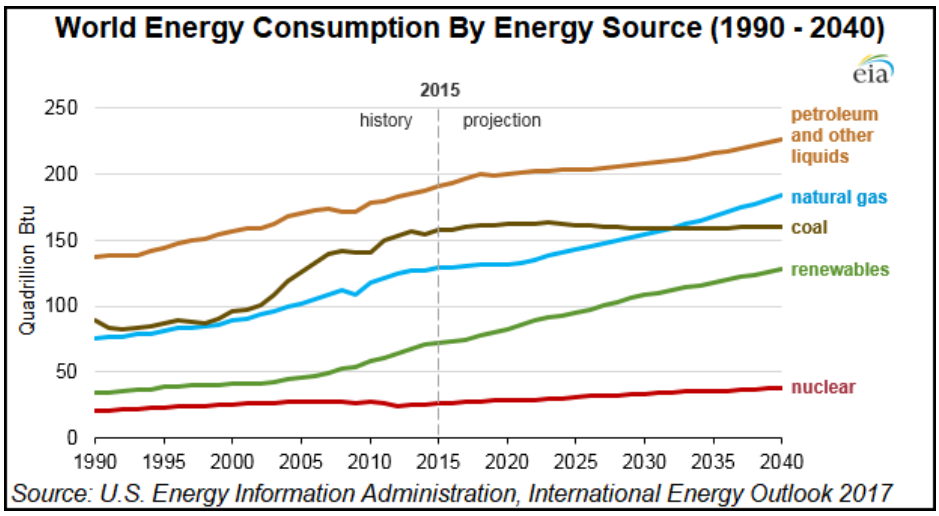

Figure 1.4.1. World energy consumption projections by energy source.

alternative energies such hydroelectric, wind, nuclear, geothermal, biofuels, and solar (**Figure 1.4.2**).

Hydroelectric power generation is the idea of using water current as mechanical energy to prompt turbines and produce electrical current. This technique has shown some promise; however, its potential use is limited to areas with strong water flows. In addition, this technology is highly reliable in energy storage devices, which make them reliant and entangled to the development of energy storage technologies.[123] The Eolic energy has seen a massive increase in production capacity in the past years.[124] The principle of this form of energy generation is to use air current flows as mechanical energy to drive large rotating blades that prompt turbines for electricity generation. However, this technology is also limited to areas with high air current flows and highly depend on energy storage technologies.[123,124] Nuclear power is the idea of fusing radioactive atoms to heat up water, so the steam produced by the water heating will prompt turbines.[125] This technology offers a high-energy production to weight ratio. However, it depends on rare earth metals, which makes the waste generated to require sophisticated

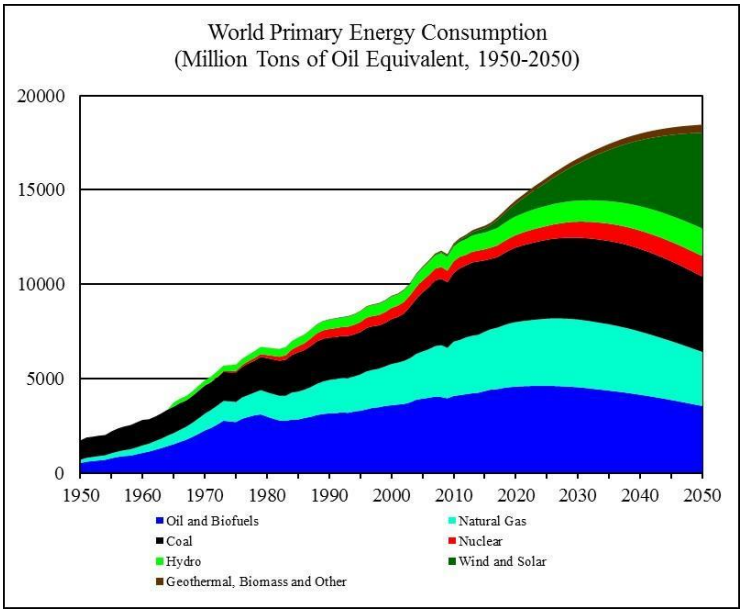

Figure 1.4.2. World primary energy consumption projections.

storage facilities for treatment. In addition, previous accidents have risen awareness on how hazard to humanity this technology may be if the proper safety requirements are not followed (Chernobyl disaster).[125] Geothermal energy involves the conversion of thermal energy from the crust to of the earth to useful energy.[126] Its similar to the nuclear energy, but we can think of this technology as the earth's crust being a natural reactor for the decay of radioactive materials such as uranium to produce heat. However, this energy source can be hazardous to the environments due to potential migration of harmful gasses from the crust of the earth. Biofuels have recently drawn tremendous attention. This technology circles around the idea of using living organisms such as plants and micro-organism to extract energy.[127] However, one major disadvantage is that some of the plants that are often used to generate biofuels also serves as a food sources, and the processing of biofuels can lead to the production of unwanted pollutants. In addition, its dependence on plant consumption may have an immediate impact on the food prices.

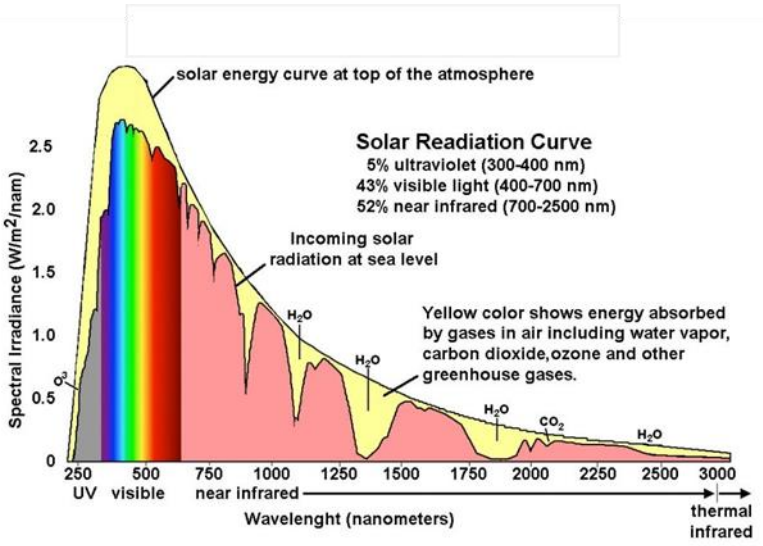

Figure 1.4.3. Solar electromagnetic energy distribution.

One of the most promising energy sources comes from the sun. The sun represents a stable and quasi-infinite energy source for our entire solar system. It produces 3.828x 10^{26} J of energy every second in the form of electromagnetic radiation as it can be observed in **Figure 1.4.3**.[128] This high-energy flux implies that the sun releases more energy from its core in one second than what we will need to meet the world demands for one decade.[129] Some of that energy is lost because of absorption by the air mass in the atmosphere. However, the earth still receives over 100,000 TW of energy from the sun annually.[122,128] This implies that an hour of electromagnetic radiation harvesting from the sun can supply enough energy to fulfill the world demands for one year. The energy from the sun could be harvested by using solar thermal electricity, solar architecture, artificial photosynthesis, and solar photovoltaics.[130–135] However, solar energy is one of the most neglected energy sources due to a significant lack of knowledge in harvesting its electromagnetic radiation.

The solar photovoltaic (PV) process is the most common and versatile method of harvesting electromagnetic radiation in the form of photons from the sun. This process offers the

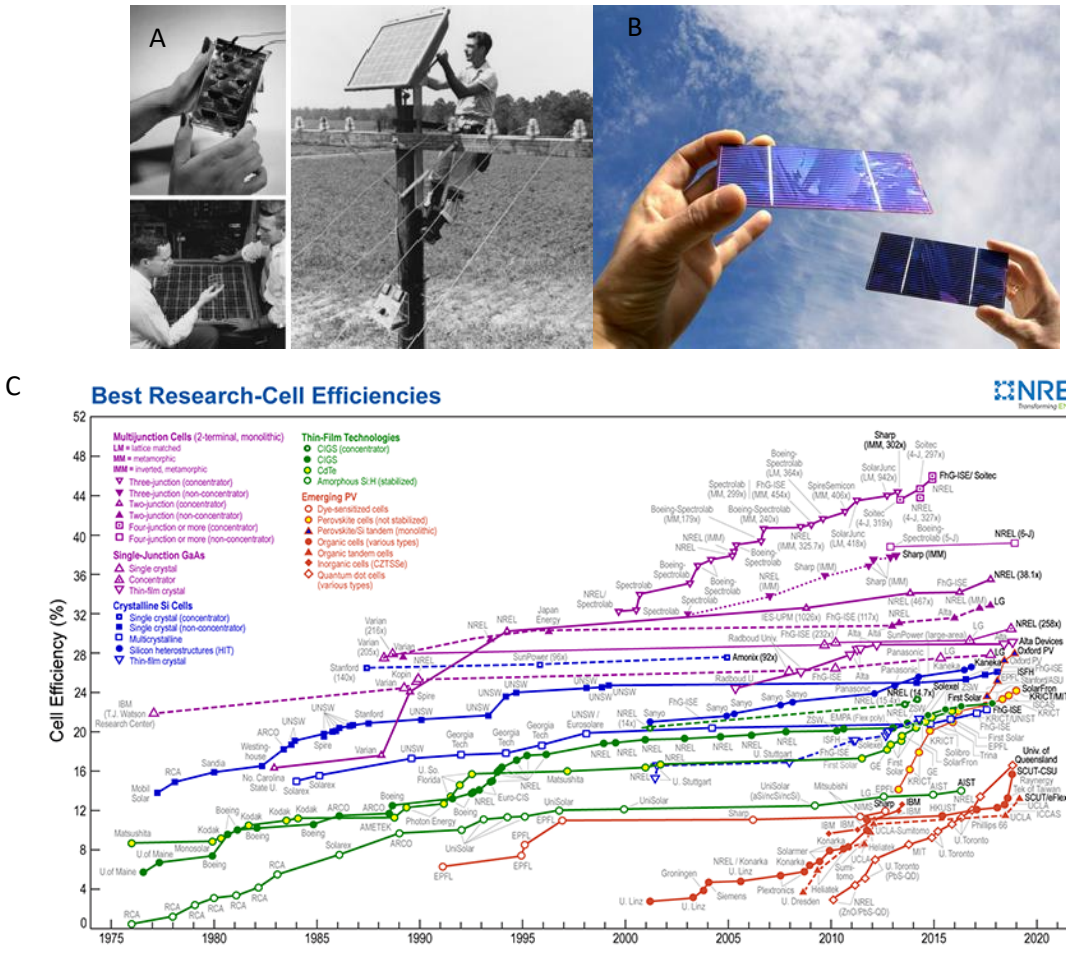

Figure 1.4.4. Advantages of PV technologies: Ease of space installation (A); Flexible and portable PV based on organic active layers (B). Timeline of the history of solar cells (C). (Extracted from www.nrel.gov)

ability to directly convert solar energy into electrical current, which facilitates its usage in every place on Earth. Consequently, it offers flexibility for space installation (**Figure 1.4.4A**). Further flexibility and portability can be adopted if organic materials are used as the active layer in the PV process (**Figure 1.4.4B**).[136] However, harvesting solar photons and converting them into useful energy such as electricity (photovoltaic) is not an easy task, as it can be observed in the timeline in **Figure 1.4.4C**. The PV was first reported back in the 19th century and it was not until the end of that same century that it was scientifically investigated.[137] Albert Einstein revolutionized the

20th century when he was able to described the photoelectric effect.[138] Over 50 years later, the first silicon solar cell was developed in Bell Labs with an unprecedented 6% energy conversion efficiency.[139] From that point forward, the possibility of converting electromagnetic radiation from the sun into electrical current became a possibility. However, materials with promising features for solar applications must meet some essential properties before they can be used for photovoltaics. We can divide these essential properties in two main categories; (1) The photovoltaic properties, namely the (a) light absorption process over the solar flux spectral range, (b) good charge carrier generators, and (c) stability over time when subjected to illumination and (2) the fabrication properties, namely (a) cost-efficient, (b) high abundance of source materials, and (c) environmentally friendly technology.

The first step in the semiconducting photovoltaic process is the absorption of solar electromagnetic radiation, usually in the visible region. Therefore, the semiconductor materials must have excellent absorbing properties where the solar flux is.[11,140] When the active layer absorbs a photon, an electron is excited to form a bound electron-hole state known as exciton. Organic semiconductors could possess absorption coefficients ($10^{5\text{-}6}$ M^{-1} cm^{-1}) two orders of magnitude bigger than the ones for silicon ($10^{2\text{-}3}$ M^{-1} cm^{-1}).[141] After the exciton splits, generated charge carriers diffuse through the active layer to reach their respective electrodes. The holes diffuse to the anode while the electrons diffuse to the cathode. The active layer thickness plays an important role in the charge carrier generation and collection properties of the photovoltaic devices.[11,141–143] In the case of silicon, its high dielectric constant allows it to have active layer thickness two magnitudes larger than the ones for organic semiconductors. In the case of organic semiconductors, the small dielectric constant hampers its exciton mobility and subsequent generation of charge carriers. As a result, active layers with thickness < 20 nm are required in

organic semiconductors solar cells technologies to have optimal charge mobility and collection. Hence, the architectural approach of designing thicker active layers in organic semiconductors solar cells to harvest more photons have detrimental effects in the device short-circuit current. Tuning its absorption properties via chemical structure modulation is a better approach to take advantage of the solar flux.[129,144,145] It needs to be highlighted that a solar cell device must be stable over time upon constant illumination for real life applications. Presently, the silicon semiconductors are more durable than organic solar cells. This is mostly due to organic semiconductors oxidation when exposed to air and humidity and reactions with electrode material.[146] The cost of production plays a major role on the commercial availability of solar cells. At the end, the $/watt should be comparable with those obtained from traditional fossil fuels. Silicon is abundant, but the need of extremely pure silicon sparks the cost of its device fabrication. Contrarily, organic semiconductors are soluble in most organic solvents. Thus, versatile techniques such as spin-coating, ink-jet printing, and roll-to-roll processing can be employed for its device fabrication. As a result, the device fabrication of organic photovoltaics is cost-effective relative to the one for silicon.

1.5 Principles of Solar Energy Harvesting in Semiconductors

The photovoltaic mechanism is an energy conversion process in where electromagnetic radiation from the sun is transformed into electrical current. To understand this conversion process, it is important to define the fundamental terminologies and parameters that governs it. The first step is the light harvesting process. The solar harvesting material must have strong absorption properties where the solar flux is.[147] After a photon with the appropriate energy is absorbed, an electron-hole bound state will be formed (exciton). The next step involves the exciton ti diffuse throughout the light harvesting backbone for potential charge carrier generation via exciton

splitting, which this splitting will be the last fundamental step of the photovoltaic mechanism corresponding to the light harvesting material. The exciton binding energy and dielectric constant of the material plays a major role in both process.[14] If the energy holding together the electron and hole is too high, they will recombine and no current will be generated. The fourth step involves the charge carrier's diffusion through the active layer of the device. For these processes to be efficient, inhomogeneities in the active layer must not be present. Inhomogeneities in the material have a detrimental effect in the exciton migration distance of the material, trapping them and enhancing its probability of recombination. As a result, no useful current will be generated. The final and fifth step involves the charge collection. The cathode collects the electrons and the anodes collects the holes. All together, these steps control the photovoltaic process in semiconductors. Several factors dictate the conversion efficiency of the photovoltaic process, including the solar cell reflectance efficiency, thermodynamic efficiency, charge carrier separation and collection efficiency, and conduction efficiency.[143,147,148] These parameters may be difficult to measure directly. Therefore, other parameters that account for them all together are measured instead. These parameters are the quantum efficiencies, open-circuit voltage (V_{OC}), and fill-factor (FF).[149]

The quantum efficiency of the device is a parameter used to characterize the conversion of incident photons into electrical current. The quantum efficiency can be split into two categories: external quantum efficiency (ηEQE) and internal quantum efficiency (ηIQE). In solar cells, the ηEQE measurement is the ratio of the charge carriers generated to the numbers of incident photons. In general, the number of absorbed photons by the material are less than the number of incident photons. Therefore, the ηIQE quantifies the amount of charge carriers generated by absorbed photons. Given that the ηEQE accounts for all the incident photons (**Equation 1.5.1A**), the ηIQE

is a good indicator of the number of charge carriers collected by the solar cells per the number of photons absorbed (**Equation 1.5.1B**).

$$EQE = \frac{charge\ carriers\ generated\ per\ unit\ time}{numbers\ of\ incident\ photons\ per\ unit\ time}$$ **Equation 1.5.1A**

$$IQE = \frac{charge\ carriers\ generated\ per\ unit\ time}{numbers\ of\ photons\ absorbed\ per\ unit\ time}$$ **Equation 1.5.1B**

These efficiencies are useful to calculate the amount of current that the photovoltaic device will produce upon solar irradiation by integrating the whole ηEQE of the solar cell at standard solar cell illuminations.[150,151] The short-circuit current (J_{SC}) is the current generated by collection of the light-generated charge carriers and occurs when the voltage across the solar cell device is zero. Thus, the J_{SC} is the maximum amount of current that can be obtained from a device and its measured in terms of current density. The short-circuit current could be limited by the absorption properties of the material. Photons that are not absorbed and instead are reflected are converted into heat and do not participate in the photovoltaic mechanism. In addition, the J_{SC} may be affected by the charge carriers diffusion properties and mobility of the material.[152]

The solar cell device efficiency is often characterized by considering the short circuit current density (J_{SC}) per open circuit voltage curve (V_{OC}).[153] By definition, the V_{OC} is the highest amount of voltage obtained by a solar cell device when there is not net current flow through the device. As it can be observed in **Equation 1.5.2**, the V_{OC} is defined in terms of the temperature (T) in Kelvin, the ideality factor (n) which accounts for the recombination process, the Boltzmann's constant (k) in C/K, the absolute value of charge (q) in Coulombs, the dark saturation current (I_0), which tells you about the maximum current that can be generated without illumination, and the

A B

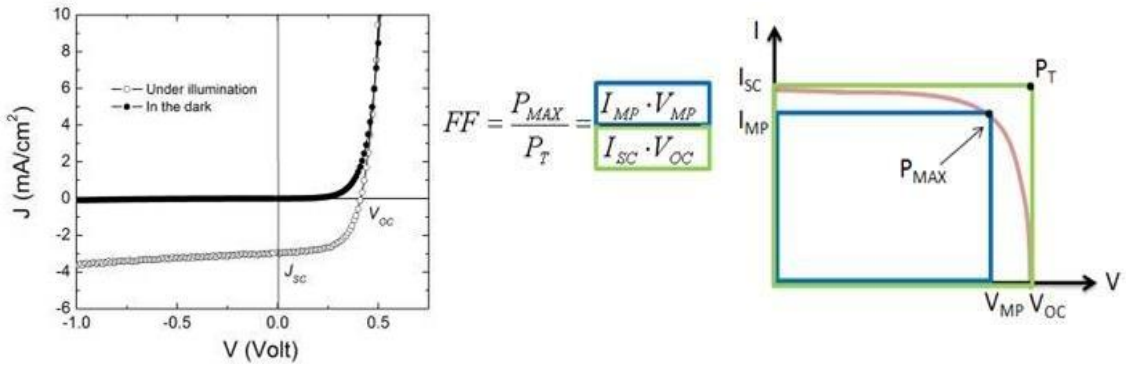

Figure 1.5.1. Current density vs open-circuit voltage plot (A). Quality of the photovoltaic device determined by the fill-factor (B).

photo-generated current (I_L). Thus, the open-circuit voltage is determined by the thermal voltage (*nkT/q*), the maximum current that can be generated, I_0, and the observed current generated by illumination, I_L.[154] The I_0 is equivalent to the $J_{SC,}$ after small loss mechanism are adapted for J_{SC}**.**

.

$$V_{OC} = \frac{nkT}{q} \ln \left(\frac{I_L}{I_0} + 1\right) \qquad \textbf{Equation 1.5.2}$$

The J_{SC} vs V_{OC} plot (**Figure 1.5.1A**) can simultaneously tell you the highest amount of current density that can be generated from the solar cell when the voltage is zero, and the maximum open-circuit voltage when the short-circuit current is zero.[154] Ergo, when no energy conversion is occurring. This implies that the maximum theoretical power is compromised and cannot be achieved at simultaneous optimal J_{SC} and V_{OC}. However, it helps you realize the optimal power achievable by the photovoltaic device. The level of quality of the theoretical power extraction from the photovoltaic device is measured by the fill factor (*FF*).[155] The *FF* is defined by the experimental power (J_{SC}*V_{OC}) extracted from the photovoltaic device divided by the available power at the maximum power point (theoretical P_{max}). These parameters can be obtained from the

J_{SC} vs V_{OC} plot (**Figure 1.5.1B**). The quality of the solar cell, namely the FF, is mostly affected by the resistance of the photovoltaic device.[156] Specifically, by the shunt (R_{SH}) and series (R_{SR}) resistances. The R_{SR} is attributed most of the time to the semiconductors charge carrier properties. The R_{SH} is mostly due to the inhomogeneities of the solar cell. Because of the inhomogeneities in the active layer, the charge carriers must travel higher distances, which will eventually result in energy loss. Therefore, having high crystallinity in the active layer will reduce the R_{SH}. Shunt resistance is mostly characterized at lower illuminations because it is highly dependent to the light-generated current.

The end goal of characterizing the J_{SC}, V_{OC}, and FF is to obtain the power conversion efficiency (PCE) of the solar cell (**Equation 1.5.3**). These factors will tell you the output power (P_{out}) of the solar cell. The PCE is the performance metric to evaluate the photovoltaic devices, and it is the percentage of the incident radiant energy from the sun that is converted into useful current. The input power (P_{in}) is determined by the intensity of the energy from the sun (E) in W/m^2 and the surface area (s) in m^2.[157,158] This methodology is universal for all photovoltaic devices. Therefore, the PCE need to be measured under standard test conditions (STC) for the sake of comparison. The STC are: temperature of 25 ^{o}C, irradiance of 1000 W/m^2, and an air mass of 1.5 (AM1.5) spectrum.[157,159–161] Ideally, the PCE of the solar cell should be 100 %. However, current materials have not been able to meet such a high efficiency. Further opportunities in enhancing the PCE % may be available by optimizing the photophysical and charge transport properties of the light absorbing materials, and optimize the architecture design of photovoltaic devices.[162]

$$PCE = \frac{P_{out}}{P_{in}} = \frac{J_{SC} * V_{OC} * FF}{E * s} \qquad \textbf{Equation 1.5.3}$$

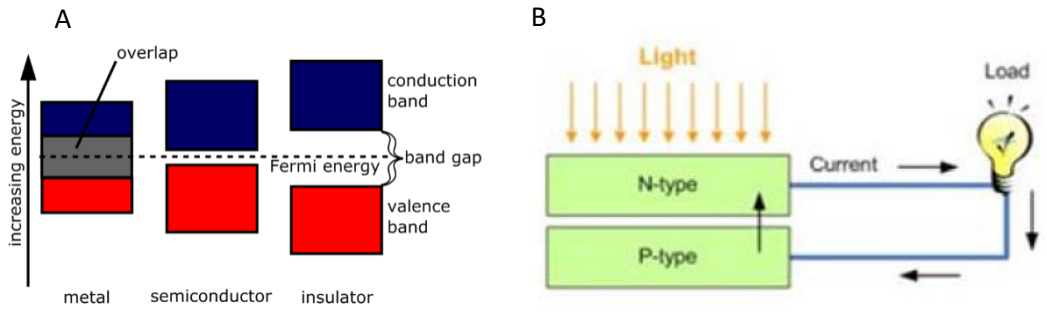

Figure 1.6.1. Valence band and conducting band comparison diagram metals, semiconductors, and insulators materials (A). Basic device architecture of a silicon solar cell (B).

1.6 Silicon-Based Photovoltaics Solar Cells

The inorganic semiconductor materials for solar harvesting (such as silicon) presently have efficiencies (~ 25 %)[142] almost as twice as the efficiencies for the organic semiconductor materials (14 %).[163,164] The combination of the silicon higher efficiencies with its abundant silicon supply as a raw material makes the silicon-based solar cells to dominate the PV technologies and its market. Such high efficiency is possible due to the optimization of the semiconducting properties of silicone by a process called doping.[165,166] Silicon has four electron in its valence shell, but upon adding small "impurities" (doping) of elements with 3 electrons (Group III) in their valence shell, the conductivity of the crystal is greatly increased. This type of doping is referred as p-type doping, and is the result of creating a vacant orbital in the crystal lattice that can hold electrons (electron deficient; hole).[166] As a result, the p-type silicon is responsible for the conduction of holes as its predominant charge carriers.[167] Contrarily, n-type doping is when impurities of elements with five electrons (Group V) in their valence shell are added to silicon. In this case, an excess of electrons is introduced into the crystal lattice. As a result, n-type doping of silicon is responsible for the conduction of electrons as its predominant charge carriers.[139,142,167] Both of these doping processes play a major role in the fermi levels of silicon, which is the chemical potential for electrons in a

body.[167] As a result, the fermi level comes closer to the conduction band so visible light can promote an electron from the fermi level to the conduction band easier, making silicone to have conductivity "like" metals (**Figure 1.6.1A).**

For metallic materials, the massive overlap between their valence band and conduction bands explains their conductivity. The bandgap of semiconducting materials (< 3 eV) lies between that of conducting materials (neglectable) and insulators (3 eV).[168] However, silicon represents a semi-conductive material with an indirect bandgap. This feature has massive implications in its absorbing and emissive properties. The indirect bandgaps nature is a solid-state phenomenon in were the crystal momentum (k-vector) in the minimum energy state of the conduction band differs from the one at the maximum energy state in the valence band. As a result, materials with an indirect bandgap nature can only emit photons via an intermediate state. These dynamics make the recombination process long, which results in enhanced exciton diffusion lengths. However, this indirect bandgap nature also implies that light must penetrate deeper in order to promote an electronic transition from the ground state to the excited state. As a result, thick active layers (>100μm) are required as active layers for solar cell applications.[142] A typical active layer of silicon solar cells consist of an n-type layer together with a p-type layer to form a n-p junction (**Figure1.6.1B**). The different doping effect in these layers induce a gradient in which the electrons in the n-type layer migrate to the holes in the p-type layers, and vice-versa. This gradient causes a positive region in the n-type silicon and a negative region in the p-type silicon, resulting in an electric field. Eventually, this electric field induced by the massive migration of electron and holes will result in a depleted zone. Now, the photons with the appropriate energy are absorbed by the active layer to disassociate an electron-hole pair. After this disassociation happens, the created electric field will promote migration of the electrons and holes to their respective parent layers. If

a wire is connected between the n-type layer and p-type layer, the massive charge carrier migration will generate current (**Figure 1.6.1B**).

To achieve optimal efficiencies, the silicon crystal needs to be extremely pure. Unfortunately, the purification process of pure silica is a time consuming and not cost-effective effort. In addition, silicon is brittle, which limit its application. All the above-mentioned features can be addressed by using amorphous silicon, but the efficiencies are ~ 14 %. In addition, silicon solar cells with n-p junction as it active layers are near the maximum theoretical efficiency of 30%. This efficiency is predicted by the Shockley-Queisser limit and it hampers further improvements in silicon PV cost due to its very limited synthetic flexibility.[169,170] Therefore, emerging market of thin-film materials for solar cell applications diverging from silicon have been explored with quantum dots, perovskites, and organic materials showing promising results.

1.7 Organic Semiconductors for Photovoltaic Applications

1.7.1 Organic Semiconductors for Solar Cell Applications and its Device Architecture

The potential use of organic semiconductors as active materials for photovoltaics was first unlocked by Kallmann and Pope about 60 years ago by using a single layer of anthracene that was placed between the electrodes.[162] The electron and hole would be drawn to the cathode and anode respectively, but the strong Coulombic interactions holding the exciton together prevented the exciton to split, and as a result, the PCE reported was ~0.1%. A one magnitude higher PCE % was reported almost 30 years later when Tang used a bilayer of p-type copper phthalocyanine (CuPc) and n-type 3,4,9,10-perylene tetracarboxylic-bis-benzimidazole (PTCBI) as the active layer of the photovoltaic process, which showed a 1 % PCE.[171] Tang's contribution was

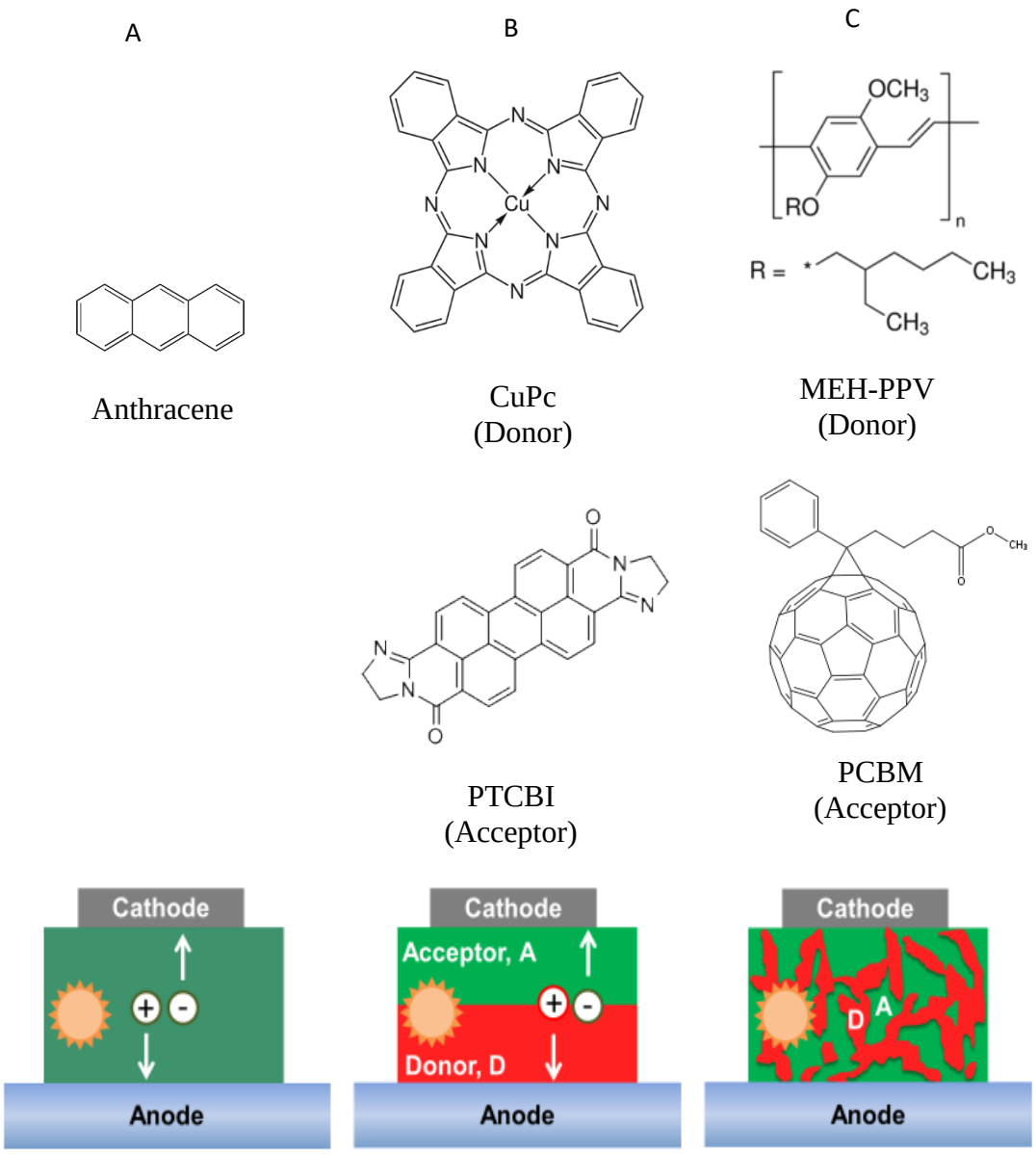

Figure 1.7.1. Fundamental device architectures of organic semiconductors solar cells with their respective breakthrough active materials. Monolayer (A), bilayer (B), and bulk-heterojunction (C).

fundamental from a device architectural standpoint and since that point, the second generation of solar cell architecture was developed and regarded as a bilayers active layer. This design improved the charge separation in organic active layers with a reported short-circuit density of 2.3 mA/cm^2, open-circuit voltage of 0.24 V and fill factor of 0.65. However, the active layer of this architectural

design was 100 nm, while the exciton diffusion length of organic materials is ~ 10-20 nm. As a result, massive exciton recombination due to its inability to arrive to the bilayer interface hampered the charge carrier generation.

Almost a decade later, the third generation solar cells were discovered when Alan Heeger introduced the bulk heterojunction (BHJ) architecture as an active layer in organic solar cells using a polymer, namely poly[2-methoxy-5-(2-ethylhexyloxy)-1,4-phenylenevinylene] (MEH-PVV), as the donor and phenyl-C61-butyric acid methyl ester (PCBM) as the acceptor.[172] In the BHJ, the electron rich (donor) and electron deficient (acceptor) materials are mixed to form interpenetrating networks. This design architecture limited the active layer thickness to ~20nm. This thickness will ensure that the generated exciton arrives to the donor-acceptor interface to generate charge carriers before the exciton recombines. Until this day, this design is the most common active layer used when constructing organic solar cells. This architectural design offers the flexibility of bandgap engineering between the light harvesting materials and acceptor material for complementary offset matching. Recent progress in BHJ has shown that these bandgaps offset matching may control the short-circuit current and open-circuit voltage of the photovoltaic device. Since then, a plethora of light harvesting materials, as well as acceptor materials, for active layer BHJ applications have been synthesized. The evolution of OSC active layer for photovoltaic applications can be observed in **Figure 1.7.1**.

1.7.2 Organic Semiconductors as Light Harvesting Materials (donors)

When organic semiconductors absorb light, an electron is promoted from the highest unoccupied molecular orbital (HOMO) to the lowest unoccupied molecular orbital (LUMO) to form a bound state called exciton.[163,173–175] The HOMO and LUMO orbitals represent the region

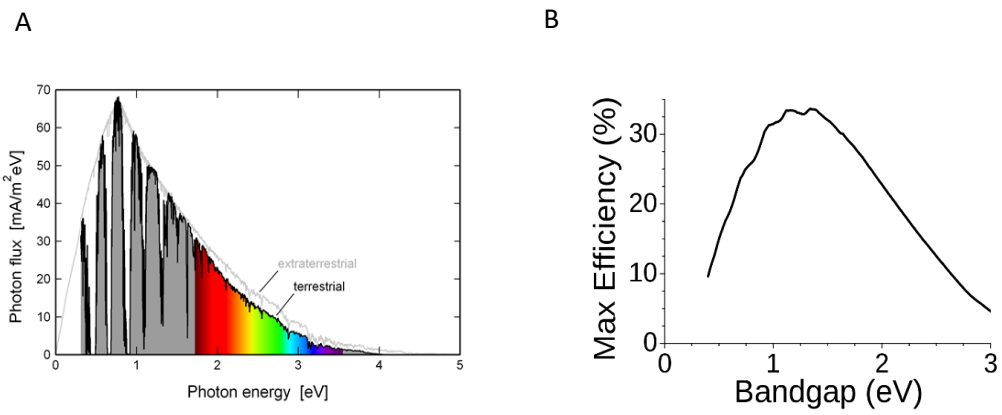

Figure 1.7.2.1. Solar photon flux in electron volts (A). Shockley-Queisser efficiency limit for a p-n junction solar cell (B).

in the molecule were the probability of finding an electron is highest. The former is equivalent to the valence band and the latter is equivalent to the conduction band of inorganic semiconductors. In organic systems, these molecular orbitals are formed by the hybridization of independent orbitals (σ and π-orbitals) between the atoms that forms the molecule, with the π-orbitals playing a major role in the photovoltaic process.[11,140,164,176] The energy between the HOMO and LUMO is called the bandgap energy and is defined as the minimum energy required to promote an electronic transition from the ground state to the excited state. Systematic modifications of the independent atoms plays a role in tuning the HOMO and LUMO energy levels, which is usually given in electron volts (eV) and it has to be in the region of 1.1-1.5 eV for taking maximum advantages of the solar flux.[177,178] This bandgap energy will allow for photons from the near infrared and higher energies to promote the electronic transition and create an exciton. In addition, it will match the bandgap energy that is needed to satisfy the Shockley-Queisser efficiency limit, which predicts the maximum theoretical efficiency of a solar cell (**Figure 1.7.2.1B**)[170,179]

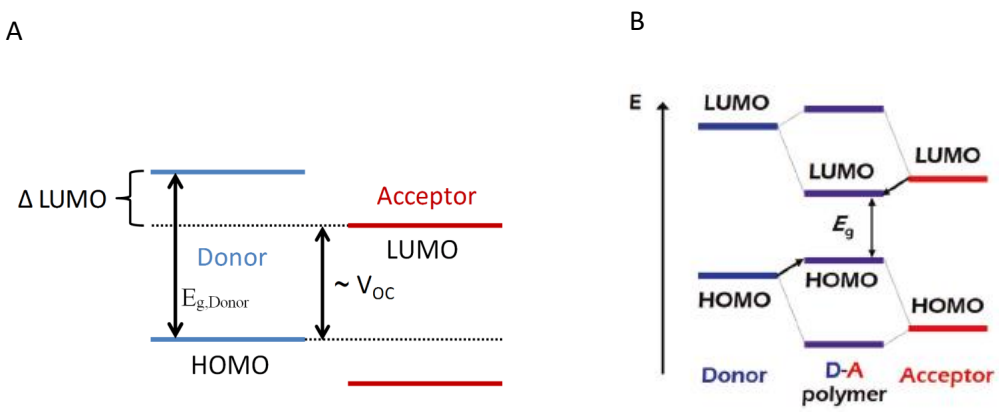

Figure 1.7.2.2 Open-circuit voltage dependence on the donor-HOMO and the acceptor-LUMO energy level offset in the BHJ active layer(A).[188] Energy bandgap hybridization of the donor-acceptor light harvesting polymer (B).[221]

Since Alan Heeger's BHJ discovery over 20 years ago, the development of suitable light harvesting polymers to couple with PCMB has been a focal point in the OSC photovoltaics mechanism, with poly(3-hexylthiophene) (P3HT) homo-polymer being one of the most investigated systems.[180–182] Studies conducted in P3HT revealed how the systematic addition of π-orbitals simultaneously enhance the light absorbing properties of the materials and reduce its bandgap.[183] This served as a synthetic strategy for the fine-tuning of the energy bandgap of light absorbing materials. In addition, P3HT showed enhanced crystallinity, which resulted in higher conductivity and light harvesting properties than the previous homo-polymers, mostly attributed to the influence of the sulfur heteroatom to the photochemistry of the polymer.[184] However, the bandgap modulation of P3HT plateaus at ~1.9 eV, which limits its ability to absorb photons in the near-infrared region.[185,186] In addition, its high HOMO level (-5.19 eV) makes P3HT susceptible to oxidation.[187] *Scharber et al*. contributes in the fundamental understanding of how the bandgap offsets between the materials in the BHJ (donor-acceptor) may play a role in the power conversion efficiency of the devices.[188] Specifically, how the energy difference between the HOMO energy level of the polymer and the LUMO energy level of the PCBM may control the open-circuit of the

OSC photovoltaic device (**Figure 1.7.2.2A**). Despite that these seminal findings provided fundamental understanding on the importance of the energy levels offset in the BHJ, the homo-polymers faces similar limitations as the P3HT homopolymer.[187,188]

An advance in the energy gap modulation was made when electron rich moieties were coupled with electron deficient moieties to produce donor-acceptor conjugated polymers for light harvesting applications.[189,190] These new class of light harvesting materials offers the ability to further modulate the energy bandgap depending on the electron donating or electron accepting strength of the independent moieties. The energy levels of the donor monomer and the acceptor monomer will be hybridized, with the HOMO of the new polymer closely resembling the HOMO energy level of the donor monomer and the LUMO energy level of the new polymer closely resembling the LUMO of the acceptor monomer (**Figure 1.7.2.2B**).[129,177,191,192] This energy modulation allows for deeper understanding of how the LUMO offsets between the light harvesting polymer and the acceptor materials may play a role in the photovoltaic process. It is imperative that the LUMO-LUMO energy levels offset lies in the range of 0.1-0.5 eV between the active materials in the BHJ. In this way, the electrochemical potential gradient created in the BHJ will be sufficient to overcome the exciton binding energy of the light harvesting polymer and prevent its exciton recombination.[193,194]

A breakthrough in the search for light harvesting polymers for photovoltaic applications was made when symmetric benzodithiophene (BDT) were synthesized to rapidly became one of the most successful donor building blocks in the synthesis of highly efficient light harvesting polymers.[195] Properties such as its rigid and planar conjugated structure, makes BDT an attractive building block for achieving highly tunable molecular energy levels and optical band gaps, high crystallinity, and high hole motilities.[196] *Yu et al*. was able to achieve PCE over 7 % when BDT

was coupled with thieno[3,4-b] thiophene (TT) subunits to develop the class of light harvesting polymers known as the PTB series.[136] TT can support the quinoidal structure of the BDT subunit, resulting in enhanced crystallinity and reduced bandgaps. Side-chain engineering focused in introducing alkoxy group were explored for the BDT subunits while fluorination of the TT resulted in polymers with bandgap reduction down to 1.6 eV and hole mobilities between 2.6×10^{-4} and 7.7×10^{-4} cm^2/ (V s). The best performing polymer out of the PTB series is still poly[[4,8-bis[(2-ethylhexyl)oxy]benzo[1,2-b:4,5-b′]dithiophene-2,6-diyl][3-fluoro-2-[(2-ethylhexyl) carbonyl] thieno[3,4-b]thiophenediyl]] (PTB7), which once held the world record for PCE % at 7.4 %.

Promising OSC device performances have been achieved by developing BDT derivatives with periphery and sidechain modifications, and by exploring electron withdrawing candidates to couple with the BDT derivatives**.** [197–202] Specifically, thiophene subunits have been located in places were alkoxy groups used to dominate under the premise that enhancing the conjugation length of the donor subunit may further stabilize the HOMO energy level of the polymer.[203] It needs to be highlighted that the rational design of acceptor moieties to couple with the BDT derivatives has been instrumental in the development of conjugated polymers for light harvesting applications with thiophene acceptor derivatives showing superior performances.[204–206] Other promising electron withdrawing subunits includes diketopyrrolopyrole (DPP), benzothiadiazole (BT), isoindigo (II), and naphthalene-diimide (NDI) with DPP being one the most promising moieties among them. DPP's fused planar structure improves conjugations along the polymer backbone while exhibiting excellent photochemical, mechanical, and thermal stability over time. In addition, light harvesting polymers that have incorporated DPP into their backbones has been able to achieve PDCE > 10%.[207,208] Example of light harvesting polymers based on BDT with different acceptors units can be observed in **Figure 1.7.2.3**. It is important to note that these

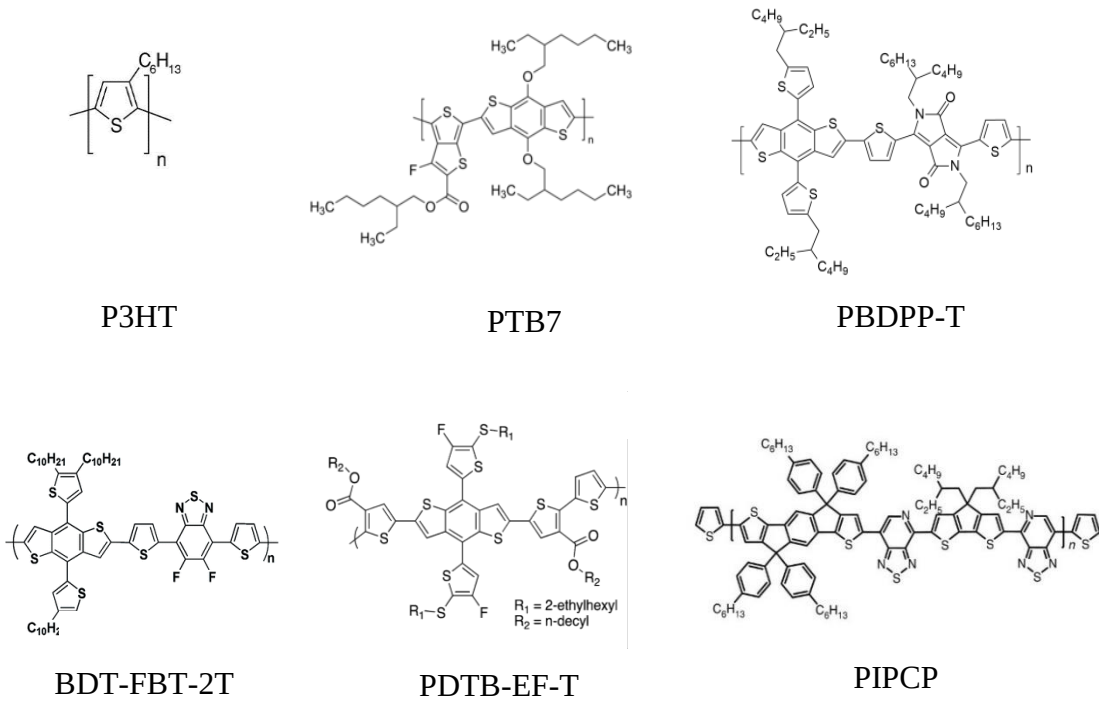

Figure 1.7.2.3. Molecular structure of highly efficient donor-acceptor conjugated light harvesting polymers.

advances in light harvesting conjugated polymers have been done by bandgap engineering of the polymer with respect to the bandgap of PCBM (fullerene).[136,151,209] However, recent progress in photovoltaic device performances using a BHJ architecture as the active layers have been made by replacing fullerene derivatives in the active layer, which are called low-bandgap materials.[164] This field is known as the fullerene-free organic solar cells and it has attracted lots of attention in the past 5 years.[210,211]

1.7.3 Organic Semiconductors Acceptor Materials

The bulk heterojunction architecture for organic photovoltaic applications is still the most used active layer for device fabrication. For years, light harvesting polymers were engineered to meet the bandgap energy levels of different fullerene derivatives.[150,176,212] These high-performing acceptor materials (n-type semiconductors) offers attractive properties such as photochemistry

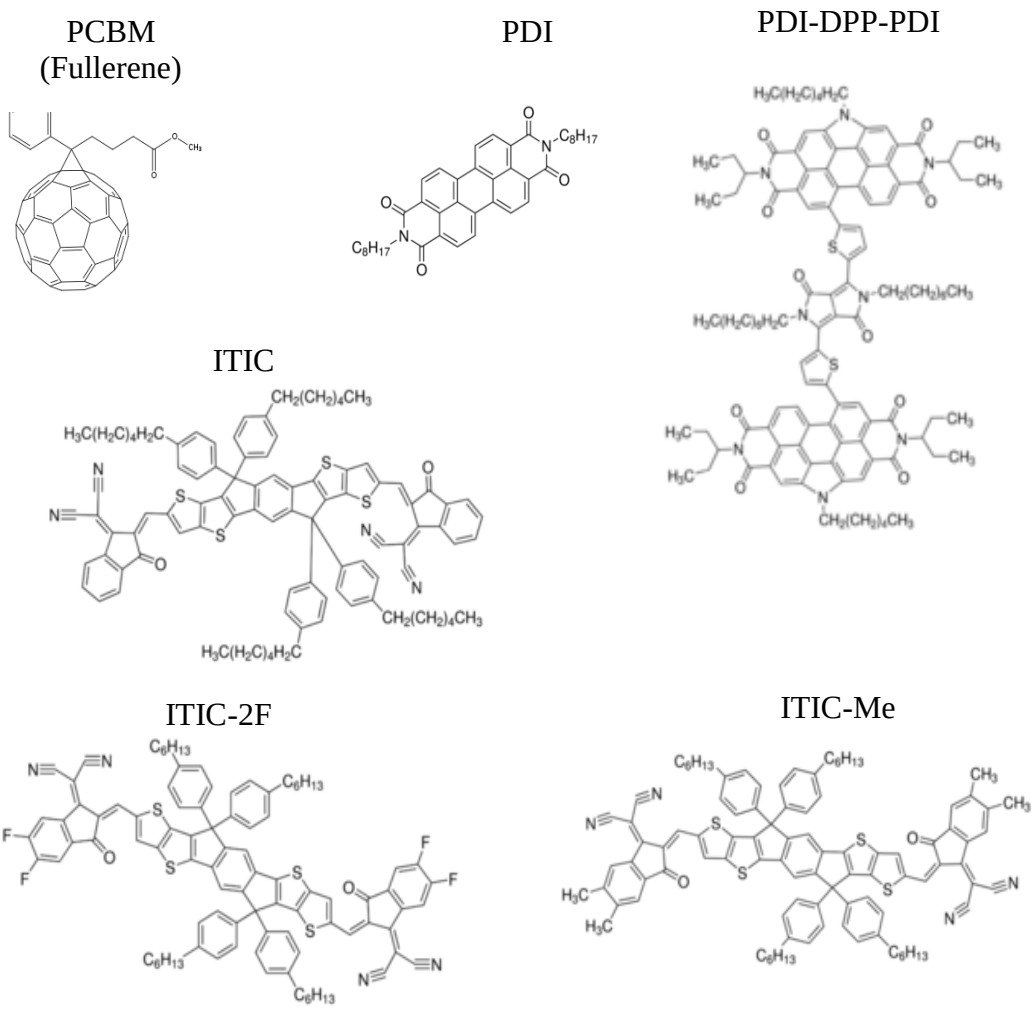

Figure 1.7.3. Molecular structure of high-performance acceptor materials for bulk-heterojunctions active layers.

stability[213,214], low-lying LUMO levels (-3.5 to -4.5 eV)[209,215], and fast charge transfer rates with low exciton binding energy.[215] In addition, its absorption properties complement well those for the light harvesting polymers. However, fullerenes tends to forms crystal domains between themselves over time.[216] As a result, the bulk heterojunction charge separation zone is reduced by a process called phase separation, which have a detrimental effect in the power conversion efficiency of the photovoltaic solar cell.[216] Consequently, suitable candidates to replace fullerene derivatives in the BHJ have been explored.

Non-fullerene acceptors (NFA) offer superior synthetic flexibility than the one that fullerene derivatives have. As a result, tunable absorption properties, tunable electron mobility, tunable solubility to enhance phase mixing between the donor and acceptor material can be achieved while lowering manufacturing costs.[164,210,211,217] Derivatives of perylene-diimides (PDI) and naphthalene-diimides (NDI) have been explored as acceptor materials in the BHJ due to their high electron affinity.[218] In addition, PDI units have been conjugated with ladder-type thienoacenes for enhancing their charge transfer properties.[219] However, more work has been done in the development of other small molecules as suitable acceptor materials because the efficiency offered by the PDI derivatives is presently low. Recently, small molecules that significantly outperform fullerene-based photovoltaics with respect to the power-conversion efficiency was demonstrated for the first time.[210] Since then, exploring 3,9-bis(2-methylene-(3-(1,1-dicyanomethylene)-indanone))-5,5,11,11-tetrakis(4-hexylphenyl)-dithieno[2,3-d:2',3'-d']-s-indaceno[1,2-b:5,6-b']dithiophene) (ITIC) derivatives for superior organic photovoltaic performances has been the focal point of the field. Furthermore, the indanone derivatives as the electro-windrowing group have been coupled to other thiophene derivatives to unlock bandgap narrowing below 1.35 eV, which is highly desirable for transparent solar cells applications.[220] This feature, coupled with their high photovoltaic performances, represent the harvesting of photons in the NIR region, which is almost 50 % of the solar flux. Examples of high-performance acceptors materials for BHJ applications can be observed in **Figure 1.7.3**.

1.8 Big Picture of the Dissertation and Outline

The fundamental aspects of organic semiconductors (OSC) and their application to the electroluminescence and photovoltaic mechanisms has been explained in detail throughout this chapter. Their properties, active-layer development, and device architectures were discussed and

compared with the current leading technologies. There have been extensive improvements in the synthetic approaches and device architecture knowledge for developing highly efficient OSC for both energy conversion processes. In the case of organic photovoltaics, the bulk-heterojunction approach using light harvesting polymers and non-fullerene acceptors (NFA) as the active-layer is regarded as one of the most promising technologies for competing with traditional energy sources. This is because their efficiencies are approaching the 15 % PCE mark.[163,206] In the case of OLEDs, which are governed by the electroluminescence mechanism, using purely organic emitters with thermally activated delayed fluorescence (TADF) characteristics have shown promising efficiency while concurrently decreasing the cost by 2-3 times in comparison with phosphors emitters. In addition, the color display and device flexibility are superior to those offered by the liquid crystal display technologies. However, continuous design and energy conversion probing to optimize the efficiencies of these new organic materials requires significant efforts. Therefore, it is essential to elucidate the fundamental properties that photovoltaic and electroluminescence materials need in order to be able to fulfill their energy conversion process with high efficiency.

In this dissertation, the work on the use of multiple spectroscopic techniques to elucidate the excited state dynamics governing materials for energy conversion process will be presented. Specifically, the excited state electronic transition of light harvesting polymers, low-band gap small molecules, intermolecular singlet fission (iSF) materials, and materials with TADF properties were investigated. Techniques such as steady-state spectroscopy, ultrafast time-resolved fluorescence spectroscopy, ultrafast two-photon absorption spectroscopy, ultrafast femtosecond and nanosecond transient absorption spectroscopy, as well as quantum mechanical simulations (QCS), were used to elucidate the optical and electric properties of materials for energy conversion with the hopes of giving insight into their structural-optoelectic property relationships. The steady-

state spectroscopy gives insight into the time-independent absorption and emissive properties of the inquired systems. The two-photon absorption spectroscopy gives insight into the two-photon absorption (TPA) capabilities of the chromophores. These capabilities are expressed in terms of their TPA cross-section, which is proportional to the transition dipole moment and give insight into the charge transfer nature of the investigated materials. The ultrafast time-resolved fluorescence spectroscopy gives insight into the emissive decay and energy transfer dynamics using fluorescence emission as the analytical signal for detection. The nanosecond time-resolved fluorescence spectroscopy gives insight into longer timescale emissive decay processes in the investigated systems. The ultrafast femtosecond transient absorption spectroscopy can give insight into the emissive and non-emissive electronic transitions happening within one nanosecond after photoexcitation. The nanosecond transient absorption spectroscopy can give insight about the emissive and non-emissive electronic transitions happening in the long-lived excited state dynamics of the materials. The QCS were correlated with the experimental results. They were also used to have insight into the molecular structures responsible for the experimental results.

In Chapter 2, the experimental techniques used to investigate the energy conversion processes in the investigated materials and described above will be discussed in detail. The theory of each technique as well as the practical aspects of these techniques will be discussed.

In Chapter 3, the excited state dynamics of a highly efficient thermally activated delayed fluorescence (TADF) chromophore were probed. Its dynamics were compared with those for well-known fluorescence and phosphorescence standards. The fluorescence up conversion, the time-correlated single photon counting (TCSPC), and the ns transient absorption spectroscopy were the integral techniques for the excited state elucidation and comparison among the investigated

fluorescence, phosphorescence, and TADF chromophores. This work was accepted and published by the *Journal of Material Science C* (JMC C).

In Chapter 4, a new optical methodology for the direct determination of the rate of reverse intersystem crossing (k_{rISC}) of organic materials with TADF characteristics is introduced. We focused in using the ns TAS to directly characterize the triplet state dynamics of TADF chromophores to get fundamental information about the rISC mechanism. Techniques such as the TCSPC are used in a complementary manner to validate this technique, but the ns TAS is the fundamental technique for the k_{rISC} determination.

In Chapter 5, the influence of thiophene and/or furan as linkers on the optical and electronic properties of light harvesting donor-acceptor conjugated polymers was investigated. The exciton emissive lifetime and the two-photon absorption capabilities in respect to the heteroatoms were also explored. QCSs to understand how the heteroatom may affect the planarity of the polymers was also included. The light harvesting polymers presented in this chapter were synthesized by the group of Malika Jeffries-EL, who is a faculty at Boston University. The synthesis of the compounds was briefly summarized, and the photovoltaic studies were presented. This work was accepted and published by *The Journal of Physical Chemistry C* (JPC C).

In Chapter 6, the synthesis, optical, and electronic properties of low-bandgap ladder-type non-fullerene acceptors (NFA) materials were investigated. Quantum mechanical calculations were used to offer further insight into the electronic structures responsible for the optical properties. The photophysical properties were investigated and an intense intramolecular charge-transfer was observed proportional to the pi-conjugation length of the ladder-type NFA. The journal *Chemistry of Materials* (Chem. Mater.) accepted and published this work.

In Chapter 7, the feasibility of intramolecular singlet fission (iSF) and subsequent electron transfer mechanism to a suitable acceptor was investigated. Quantum chemical simulations as well as ultrafast spectroscopy such as fluorescence up-conversion and femtosecond transient absorption was used to characterize the electron transfer reactions and intermediates conformers present in the iSF mechanism. The *Journal of American Chemical Association* (JACS) accepted and published this work.

In chapter 8, an overall summary of the research presented in this dissertation is presented and suggestions for future research endeavors on the investigated organic semiconductors for opto-electric applications are suggested.

References

(1) Thornton, W. A. Electroluminescence at Low Voltages. *Phys. Rev.* **1959**, *116* (4), 893–894. https://doi.org/10.1103/PhysRev.116.893.

(2) Friend, R. H.; Gymer, R. W.; Holmes, A. B.; Burroughes, J. H.; Marks, R. N.; Taliani, C.; Bradley, D. D. C.; Dos Santos, D. A.; Brédas, J. L.; Lögdlund, M.; et al. Electroluminescence in Conjugated Polymers. *Nature* **1999**, *397* (6715), 121–128. https://doi.org/10.1038/16393.

(3) Brander, R. W. A Review of the Merits of Direct and Indirect Gap Semiconductors for Electroluminescence Devices. *Rev. Phys. Technol.* **1972**, *3* (3), 145–194. https://doi.org/10.1088/0034-6683/3/3/I01.

(4) Schubert, F.; Kim, J. K. *Light-Emitting Diodes Hit the Centenary Milestone*; 2007.

(5) Daukantas, P. Fifty Years of Visible LEDs. *Opt. Photonics News* **2012**, *23* (11), 32. https://doi.org/10.1364/opn.23.11.000032.

(6) Lehovec, K. New Photoelectric Devices Utilizing Carrier Injection. *Proc. IRE* **1952**, *40* (11), 1407–1409. https://doi.org/10.1109/JRPROC.1952.273970.

(7) Tang, C. W.; Vanslyke, S. A. Organic Electroluminescent Diodes. *Appl. Phys. Lett.* **1987**, *51* (12), 913–915. https://doi.org/10.1063/1.98799.

(8) Burroughes, J. H.; Bradley, D. D. C.; Brown, A. R.; Marks, R. N.; Mackay, K.; Friend, R. H.; Burns, P. L.; Holmes, A. B. Light-Emitting Diodes Based on Conjugated Polymers. *Nature* **1990**, *347* (6293), 539–541. https://doi.org/10.1038/347539a0.

(9) Schadt, M. Liquid Crystal Materials and Liquid Crystal Displays. *Annu. Rev. Mater. Sci.* **2002**, *27* (1), 305–379. https://doi.org/10.1146/annurev.matsci.27.1.305.

(10) Thejo Kalyani, N.; Dhoble, S. J. Organic Light Emitting Diodes: Energy Saving Lighting Technology - A Review. *Renew. Sustain. Energy Rev.* **2012**, *16* (5), 2696–2723. https://doi.org/10.1016/j.rser.2012.02.021.

(11) Alonso, M. I.; Campoy-Quiles, M. Organic Solar Cells. *Springer Ser. Opt. Sci.* **2018**, *212* (3), 439–461. https://doi.org/10.1007/978-3-319-75377-5_15.

(12) Liu, Y.; Weiss, N. O.; Duan, X.; Cheng, H. C.; Huang, Y.; Duan, X. Van Der Waals Heterostructures and Devices. *Nat. Rev. Mater.* **2016**, *1* (9). https://doi.org/10.1038/natrevmats.2016.42.

(13) Oehzelt, M.; Koch, N.; Heimel, G. Organic Semiconductor Density of States Controls the Energy Level Alignment at Electrode Interfaces. *Nat. Commun.* **2014**, *5* (1), 4174. https://doi.org/10.1038/ncomms5174.

(14) Pope, M.; Swenberg, C. Electronic Processes in Organic Crystals and Polymers. **1999**.

(15) Kittel, C.; McEuen, P.; McEuen, P. *Introduction to Solid State Physics*; 1976.

(16) Uoyama, H.; Goushi, K.; Shizu, K.; Nomura, H.; Adachi, C. Highly Efficient Organic Light-Emitting Diodes from Delayed Fluorescence. *Nature* **2012**, *492* (7428), 234–238. https://doi.org/10.1038/nature11687.

(17) Adachi, C.; Baldo, M. A.; Thompson, M. E.; Forrest, S. R. Nearly 100% Internal Phosphorescence Efficiency in an Organic Light-Emitting Device ARTICLES YOU MAY BE INTERESTED IN Electroluminescence in Organic Crystals. *J. Chem. Phys.* **2001**, *90* (10), 2042. https://doi.org/10.1063/1.1409582.

(18) Baldo, M. A.; O'Brien, D. F.; You, Y.; Shoustikov, A.; Sibley, S.; Thompson, M. E.; Forrest, S. R. Highly Efficient Phosphorescent Emission from Organic Electroluminescent Devices. *Nature* **1998**, *395* (6698), 151–154. https://doi.org/10.1038/25954.

(19) Kleinschmidt, M.; Van Wüllen, C.; Marian, C. M. Intersystem-Crossing and Phosphorescence Rates in Fac-IrIII(Ppy)3: A Theoretical Study Involving Multi-Reference Configuration Interaction Wavefunctions. *J. Chem. Phys.* **2015**, *142* (9), 094301. https://doi.org/10.1063/1.4913513.

(20) Lamansky, S.; Djurovich, P.; Murphy, D.; Abdel-Razzaq, F.; Kwong, R.; Tsyba, I.; Bortz, M.; Mui, B.; Bau, R.; Thompson, M. E. Synthesis and Characterization of Phosphorescent Cyclometalated Iridium Complexes. *Inorg. Chem.* **2001**, *40* (7), 1704–1711. https://doi.org/10.1021/ic0008969.

(21) Baldo, M. A.; Lamansky, S.; Burrows, P. E.; Thompson, M. E.; Forrest, S. R. Very High-Efficiency Green Organic Light-Emitting Devices Based on Electrophosphorescence. *Appl. Phys. Lett.* **1999**, *75* (1), 4–6. https://doi.org/10.1063/1.124258.

(22) Lamansky, S.; Djurovich, P.; Murphy, D.; Abdel-Razzaq, F.; Lee, H. E.; Adachi, C.; Burrows, P. E.; Forrest, S. R.; Thompson, M. E. Highly Phosphorescent Bis-Cyclometalated Iridium Complexes: Synthesis, Photophysical Characterization, and Use in Organic Light Emitting Diodes. *J. Am. Chem. Soc.* **2001**, *123* (18), 4304–4312. https://doi.org/10.1021/ja003693s.

(23) Lamansky, S.; Djurovich, P. I.; Abdel-Razzaq, F.; Garon, S.; Murphy, D. L.; Thompson, M. E. Cyclometalated Ir Complexes in Polymer Organic Light-Emitting Devices. *J. Appl. Phys.* **2002**, *92* (3), 1570–1575. https://doi.org/10.1063/1.1491587.

(24) Adachi, C.; Baldo, M. A.; Forrest, S. R.; Lamansky, S.; Thompson, M. E.; Kwong, R. C. High-Efficiency Red Electrophosphorescence Devices. *Appl. Phys. Lett.* **2001**, *78* (11), 1622–1624. https://doi.org/10.1063/1.1355007.

(25) Hung, L. S.; Chen, C. H. Recent Progress of Molecular Organic Electroluminescent Materials and Devices. *Mater. Sci. Eng. R Reports* **2002**, *39* (5–6), 143–222. https://doi.org/10.1016/S0927-796X(02)00093-1.

(26) Dos Santos, P. L.; Ward, J. S.; Bryce, M. R.; Monkman, A. P. Using Guest-Host Interactions

to Optimize the Efficiency of TADF OLEDs. *J. Phys. Chem. Lett.* **2016**, *7* (17), 3341–3346. https://doi.org/10.1021/acs.jpclett.6b01542.

(27) Murawski, C.; Leo, K.; Gather, M. C. Efficiency Roll-off in Organic Light-Emitting Diodes. *Advanced Materials*. December 2013, pp 6801–6827. https://doi.org/10.1002/adma.201301603.

(28) Kondakov, D. Y.; Pawlik, T. D.; Hatwar, T. K.; Spindler, J. P. Triplet Annihilation Exceeding Spin Statistical Limit in Highly Efficient Fluorescent Organic Light-Emitting Diodes. *J. Appl. Phys.* **2009**, *106* (12), 124510. https://doi.org/10.1063/1.3273407.

(29) Sapsford, K. E.; Berti, L.; Medintz, I. L. Materials for Fluorescence Resonance Energy Transfer Analysis: Beyond Traditional Donor-Acceptor Combinations. *Angewandte Chemie - International Edition*. Wiley-Blackwell July 10, 2006, pp 4562–4588. https://doi.org/10.1002/anie.200503873.

(30) Selvin, P. R. The Renaissance of Fluorescence Resonance Energy Transfer. *Nature Structural & Molecular Biology*. 2000, pp 730–734. https://doi.org/10.1038/78948.

(31) Kandada, A. R. S.; Grancini, G.; Petrozza, A.; Perissinotto, S.; Fazzi, D.; Raavi, S. S. K.; Lanzani, G. Ultrafast Energy Transfer in Ultrathin Organic Donor/Acceptor Blend. *Sci. Rep.* **2013**, *3* (1), 2073. https://doi.org/10.1038/srep02073.

(32) Lin, S. H.; Xiao, W. Z.; Dietz, W. *Generalized Forster-Dexter Theory of Photoinduced Intramolecular Energy Transfer*; 1993; Vol. 47.

(33) Murphy, C. B.; Zhang, Y.; Troxler, T.; Ferry, V.; Martin, J. J.; Jones, W. E. Probing Förster and Dexter Energy-Transfer Mechanisms in Fluorescent Conjugated Polymer Chemosensors. *J. Phys. Chem. B* **2004**, *108* (5), 1537–1543. https://doi.org/10.1021/jp0301406.

(34) Monguzzi, A.; Tubino, R.; Meinardi, F. Upconversion-Induced Delayed Fluorescence in Multicomponent Organic Systems: Role of Dexter Energy Transfer. *Phys. Rev. B - Condens. Matter Mater. Phys.* **2008**, *77* (15). https://doi.org/10.1103/PhysRevB.77.155122.

(35) Giovanella, U.; Leone, G.; Galeotti, F.; Mróz, W.; Meinardi, F.; Botta, C. FRET-Assisted Deep-Blue Electroluminescence in Intercalated Polymer Hybrids. *Chem. Mater.* **2014**, *26* (15), 4572–4578. https://doi.org/10.1021/cm501870e.

(36) Kim, Y.-H.; Young Kim, W.; Moon, C.-B. Energy Transfer between Host and Dopant Molecules in Blue Organic Light-Emitting Devices. *J. Appl. Phys.* **2011**, *110* (3), 034501. https://doi.org/10.1063/1.3614493.

(37) Furno, M.; Meerheim, R.; Thomschke, M.; Hofmann, S.; Lüssem, B.; Leo, K. Outcoupling Efficiency in Small-Molecule OLEDs: From Theory to Experiment. In *Light-Emitting Diodes: Materials, Devices, and Applications for Solid State Lighting XIV*; Streubel, K. P., Jeon, H., Tu, L.-W., Linder, N., Eds.; International Society for Optics and Photonics, 2009; Vol. 7617, p 761716. https://doi.org/10.1117/12.840043.

(38) Singh Mehta, D.; Saxena, K. *Light Out-Coupling Strategies in Organic Light Emitting Devices*; 2006.

(39) Xiao, Y.; Yang, J. P.; Cheng, P. P.; Zhu, J. J.; Xu, Z. Q.; Deng, Y. H.; Lee, S. T.; Li, Y. Q.; Tang, J. X. Surface Plasmon-Enhanced Electroluminescence in Organic Light-Emitting Diodes Incorporating Au Nanoparticles. *Appl. Phys. Lett.* **2012**, *100* (1), 013308. https://doi.org/10.1063/1.3675970.

(40) Jeong, S. H.; Choi, H.; Kim, J. Y.; Lee, T. W. Silver-Based Nanoparticles for Surface Plasmon Resonance in Organic Optoelectronics. *Part. Part. Syst. Charact.* **2015**, *32* (2), 164–175. https://doi.org/10.1002/ppsc.201400117.

(41) Kim, S. Y.; Jeong, W. I.; Mayr, C.; Park, Y. S.; Kim, K. H.; Lee, J. H.; Moon, C. K.; Brütting, W.; Kim, J. J. Organic Light-Emitting Diodes with 30% External Quantum Efficiency Based on a Horizontally Oriented Emitter. *Adv. Funct. Mater.* **2013**, *23* (31), 3896–3900. https://doi.org/10.1002/adfm.201300104.

(42) Ishii, H.; Kudo, K.; Nakayama, T.; Ueno, N. *Electronic Processes in Organic Electronics*; Ishii, H., Kudo, K., Nakayama, T., Ueno, N., Eds.; Springer Series in Materials Science; Springer Japan: Tokyo, 2015; Vol. 209. https://doi.org/10.1007/978-4-431-55206-2.

(43) Adachi, C.; Baldo, M. A.; Thompson, M. E.; Forrest, S. R. Nearly 100% Internal Phosphorescence Efficiency in an Organic Light Emitting Device. *J. Appl. Phys.* **2001**, *90* (10), 5048–5051. https://doi.org/10.1063/1.1409582.

(44) Helander, M. G.; Wang, Z. B.; Qiu, J.; Greiner, M. T.; Puzzo, D. P.; Liu, Z. W.; Lu, Z. H. Chlorinated Indium Tin Oxide Electrodes with High Work Function for Organic Device Compatibility. *Science (80-.).* **2011**, *332* (6032), 944–947. https://doi.org/10.1126/science.1202992.

(45) Jeon, S. K.; Lee, H. L.; Yook, K. S.; Lee, J. Y. Recent Progress of the Lifetime of Organic Light-Emitting Diodes Based on Thermally Activated Delayed Fluorescent Material. *Adv. Mater.* **2019**, 1803524. https://doi.org/10.1002/adma.201803524.

(46) Adachi, C.; Tsutsui, T.; Saito, S. Blue Light-Emitting Organic Electroluminescent Devices. *Appl. Phys. Lett.* **1990**, *56* (9), 799–801. https://doi.org/10.1063/1.103177.

(47) Adachi, C.; Kwong, R. C.; Djurovich, P.; Adamovich, V.; Baldo, M. A.; Thompson, M. E.; Forrest, S. R. Endothermic Energy Transfer: A Mechanism for Generating Very Efficient High-Energy Phosphorescent Emission in Organic Materials. *Appl. Phys. Lett.* **2001**, *79* (13), 2082–2084. https://doi.org/10.1063/1.1400076.

(48) Holmes, R. J.; Forrest, S. R.; Tung, Y.-J.; Kwong, R. C.; Brown, J. J.; Garon, S.; Thompson, M. E. Blue Organic Electrophosphorescence Using Exothermic Host–Guest Energy Transfer. *Appl. Phys. Lett.* **2003**, *82* (15), 2422–2424. https://doi.org/10.1063/1.1568146.

(49) Song, W.; Lee, J. Y. Degradation Mechanism and Lifetime Improvement Strategy for Blue Phosphorescent Organic Light-Emitting Diodes. *Adv. Opt. Mater.* **2017**, *5* (9), 1600901.

https://doi.org/10.1002/adom.201600901.

(50) Brédas, J.-L.; Beljonne, D.; Coropceanu, V.; Cornil, J. Charge-Transfer and Energy-Transfer Processes in Pi-Conjugated Oligomers and Polymers: A Molecular Picture. *Chem. Rev.* **2004**, *104* (11), 4971–5004. https://doi.org/10.1021/cr040084k.

(51) Tao, Y.; Yang, C.; Qin, J. Organic Host Materials for Phosphorescent Organic Light-Emitting Diodes. *Chem. Soc. Rev.* **2011**, *40* (5), 2943–2970. https://doi.org/10.1039/c0cs00160k.

(52) Lai, M. Y.; Chen, C. H.; Huang, W. S.; Lin, J. T.; Ke, T. H.; Chen, L. Y.; Tsai, M. H.; Wu, C. C. Benzimidazole/Amine-Based Compounds Capable of Ambipolar Transport for Application in Single-Layer Blue-Emitting OLEDs and as Hosts for Phosphorescent Emitters. *Angew. Chemie - Int. Ed.* **2008**, *47* (3), 581–585. https://doi.org/10.1002/anie.200704113.

(53) Zheng, C. J.; Ye, J.; Lo, M. F.; Fung, M. K.; Ou, X. M.; Zhang, X. H.; Lee, C. S. New Ambipolar Hosts Based on Carbazole and 4,5-Diazafluorene Units for Highly Efficient Blue Phosphorescent Oleds with Low Efficiency Roll-Off. *Chem. Mater.* **2012**, *24* (4), 643–650. https://doi.org/10.1021/cm2036647.

(54) Kondrasenko, I.; Tsai, Z. H.; Chung, K. Y.; Chen, Y. T.; Ershova, Y. Y.; Doménech-Carbó, A.; Hung, W. Y.; Chou, P. T.; Karttunen, A. J.; Koshevoy, I. O. Ambipolar Phosphine Derivatives to Attain True Blue OLEDs with 6.5% EQE. *ACS Appl. Mater. Interfaces* **2016**, *8* (17), 10968–10976. https://doi.org/10.1021/acsami.6b01041.

(55) Mewes, J. M. Modeling TADF in Organic Emitters Requires a Careful Consideration of the Environment and Going beyond the Franck-Condon Approximation. *Phys. Chem. Chem. Phys.* **2018**, *20* (18), 12454–12469. https://doi.org/10.1039/c8cp01792a.

(56) Chen, X. K.; Kim, D.; Brédas, J. L. Thermally Activated Delayed Fluorescence (TADF) Path toward Efficient Electroluminescence in Purely Organic Materials: Molecular Level Insight. *Acc. Chem. Res.* **2018**, *51* (9), 2215–2224. https://doi.org/10.1021/acs.accounts.8b00174.

(57) Bui, T. T.; Goubard, F.; Ibrahim-Ouali, M.; Gigmes, D.; Dumur, F. Recent Advances on Organic Blue Thermally Activated Delayed Fluorescence (TADF) Emitters for Organic Light-Emitting Diodes (OLEDs). *Beilstein Journal of Organic Chemistry*. Beilstein-Institut January 30, 2018, pp 282–308. https://doi.org/10.3762/bjoc.14.18.

(58) Nobuyasu, R. S.; Ren, Z.; Griffiths, G. C.; Batsanov, A. S.; Data, P.; Yan, S.; Monkman, A. P.; Bryce, M. R.; Dias, F. B. Rational Design of TADF Polymers Using a Donor-Acceptor Monomer with Enhanced TADF Efficiency Induced by the Energy Alignment of Charge Transfer and Local Triplet Excited States. *Adv. Opt. Mater.* **2016**, *4* (4), 597–607. https://doi.org/10.1002/adom.201500689.

(59) Huang, T.; Jiang, W.; Duan, L. Recent Progress in Solution Processable TADF Materials for Organic Light-Emitting Diodes. *Journal of Materials Chemistry C*. Royal Society of

Chemistry May 31, 2018, pp 5577–5596. https://doi.org/10.1039/c8tc01139g.

(60) Hosokai, T.; Matsuzaki, H.; Furube, A.; Tokumaru, K.; Tsutsui, T.; Nakanotani, H.; Yahiro, M.; Adachi, C. Role of Intermediate State in the Excited State Dynamics of Highly Efficient TADF Molecules. In *Organic Light Emitting Materials and Devices XX*; So, F., Adachi, C., Kim, J.-J., Eds.; International Society for Optics and Photonics, 2016; Vol. 9941, p 994107. https://doi.org/10.1117/12.2236248.

(61) Youn Lee, S.; Yasuda, T.; Nomura, H.; Adachi, C. High-Efficiency Organic Light-Emitting Diodes Utilizing Thermally Activated Delayed Fluorescence from Triazine-Based Donor-Acceptor Hybrid Molecules. *Appl. Phys. Lett.* **2012**, *101* (9), 093306. https://doi.org/10.1063/1.4749285.

(62) Jankus, V.; Chiang, C. J.; Dias, F.; Monkman, A. P. Deep Blue Exciplex Organic Light-Emitting Diodes with Enhanced Efficiency; P-Type or E-Type Triplet Conversion to Singlet Excitons? *Adv. Mater.* **2013**, *25* (10), 1455–1459. https://doi.org/10.1002/adma.201203615.

(63) Greinert, R.; Staerk, H.; Stier, A.; Weller, A. E-Type Delayed Fluorescence Depolarization, a Technique to Probe Rotational Motion in the Microsecond Range. *J. Biochem. Biophys. Methods* **1979**, *1* (2), 77–83. https://doi.org/10.1016/0165-022X(79)90014-9.

(64) Kirchhoff, J. R.; Gamache, R. E.; Blaskie, M. W.; Paggio, A. A. D.; Lengel, R. K.; Mcmillin, D. R. Temperature Dependence of Luminescence from Cu(NN)2+ Systems in Fluid Solution. Evidence for the Participation of Two Excited States. *Inorg. Chem.* **1983**, *22* (17), 2380–2384. https://doi.org/10.1021/ic00159a008.

(65) Tao, Y.; Yuan, K.; Chen, T.; Xu, P.; Li, H.; Chen, R.; Zheng, C.; Zhang, L.; Huang, W. Thermally Activated Delayed Fluorescence Materials towards the Breakthrough of Organoelectronics. *Adv. Mater.* **2014**, *26* (47), 7931–7958. https://doi.org/10.1002/adma.201402532.

(66) Adachi, C. Third-Generation Organic Electroluminescence Materials. *Jpn. J. Appl. Phys.* **2014**, *53* (6). https://doi.org/10.7567/JJAP.53.060101.

(67) Rajamalli, P.; Senthilkumar, N.; Gandeepan, P.; Ren-Wu, C. C.; Lin, H. W.; Cheng, C. H. A Method for Reducing the Singlet-Triplet Energy Gaps of TADF Materials for Improving the Blue OLED Efficiency. *ACS Appl. Mater. Interfaces* **2016**, *8* (40), 27026–27034. https://doi.org/10.1021/acsami.6b10678.

(68) Chen, X. K.; Tsuchiya, Y.; Ishikawa, Y.; Zhong, C.; Adachi, C.; Brédas, J. L. A New Design Strategy for Efficient Thermally Activated Delayed Fluorescence Organic Emitters: From Twisted to Planar Structures. *Adv. Mater.* **2017**, *29* (46), 1702767. https://doi.org/10.1002/adma.201702767.

(69) Samanta, P. K.; Kim, D.; Coropceanu, V.; Brédas, J. L. Up-Conversion Intersystem Crossing Rates in Organic Emitters for Thermally Activated Delayed Fluorescence: Impact of the Nature of Singlet vs Triplet Excited States. *J. Am. Chem. Soc.* **2017**, *139* (11), 4042–4051. https://doi.org/10.1021/jacs.6b12124.

(70) Nakanotani, H.; Higuchi, T.; Furukawa, T.; Masui, K.; Morimoto, K.; Numata, M.; Tanaka, H.; Sagara, Y.; Yasuda, T.; Adachi, C. High-Efficiency Organic Light-Emitting Diodes with Fluorescent Emitters. *Nat. Commun.* **2014**, *5* (1), 1–7. https://doi.org/10.1038/ncomms5016.

(71) Cho, Y. J.; Yook, K. S.; Lee, J. Y. A Universal Host Material for High External Quantum Efficiency Close to 25% and Long Lifetime in Green Fluorescent and Phosphorescent OLEDs. *Adv. Mater.* **2014**, *26* (24), 4050–4055. https://doi.org/10.1002/adma.201400347.

(72) Hirata, S.; Sakai, Y.; Masui, K.; Tanaka, H.; Lee, S. Y.; Nomura, H.; Nakamura, N.; Yasumatsu, M.; Nakanotani, H.; Zhang, Q.; et al. Highly Efficient Blue Electroluminescence Based on Thermally Activated Delayed Fluorescence. *Nat. Mater.* **2015**, *14* (3), 330–336. https://doi.org/10.1038/nmat4154.

(73) Noda, H.; Nakanotani, H.; Adachi, C. Excited State Engineering for Efficient Reverse Intersystem Crossing. *Sci. Adv.* **2018**, *4* (6), eaao6910. https://doi.org/10.1126/sciadv.aao6910.

(74) Kaji, H.; Suzuki, H.; Fukushima, T.; Shizu, K.; Suzuki, K.; Kubo, S.; Komino, T.; Oiwa, H.; Suzuki, F.; Wakamiya, A.; et al. Purely Organic Electroluminescent Material Realizing 100% Conversion from Electricity to Light. *Nat. Commun.* **2015**, *6*, 8476. https://doi.org/10.1038/ncomms9476.

(75) Nakanotani, H.; Masui, K.; Nishide, J.; Shibata, T.; Adachi, C. Promising Operational Stability of High-Efficiency Organic Light-Emitting Diodes Based on Thermally Activated Delayed Fluorescence. *Sci. Rep.* **2013**, *3* (1), 2127. https://doi.org/10.1038/srep02127.

(76) Liu, Y.; Li, C.; Ren, Z.; Yan, S.; Bryce, M. R. All-Organic Thermally Activated Delayed Fluorescence Materials for Organic Light-Emitting Diodes. *Nature Reviews Materials*. Nature Publishing Group April 10, 2018, p 18020. https://doi.org/10.1038/natrevmats.2018.20.

(77) Yang, Z.; Mao, Z.; Xie, Z.; Zhang, Y.; Liu, S.; Zhao, J.; Xu, J.; Chi, Z.; Aldred, M. P. Recent Advances in Organic Thermally Activated Delayed Fluorescence Materials. *Chemical Society Reviews*. The Royal Society of Chemistry February 6, 2017, pp 915–1016. https://doi.org/10.1039/c6cs00368k.

(78) Liang, X.; Tu, Z. L.; Zheng, Y. X. Thermally Activated Delayed Fluorescence Materials: Towards Realization of High Efficiency through Strategic Small Molecular Design. *Chemistry - A European Journal*. John Wiley & Sons, Ltd April 17, 2019, pp 5623–5642. https://doi.org/10.1002/chem.201805952.

(79) Dias, F. B.; Bourdakos, K. N.; Jankus, V.; Moss, K. C.; Kamtekar, K. T.; Bhalla, V.; Santos, J.; Bryce, M. R.; Monkman, A. P. Triplet Harvesting with 100% Efficiency by Way of Thermally Activated Delayed Fluorescence in Charge Transfer OLED Emitters. *Adv. Mater.* **2013**, *25* (27), 3707–3714. https://doi.org/10.1002/adma.201300753.

(80) Inoue, M.; Serevičius, T.; Nakanotani, H.; Yoshida, K.; Matsushima, T.; Juršenas, S.;

Adachi, C. Effect of Reverse Intersystem Crossing Rate to Suppress Efficiency Roll-off in Organic Light-Emitting Diodes with Thermally Activated Delayed Fluorescence Emitters. *Chem. Phys. Lett.* **2016**, *644*, 62–67. https://doi.org/10.1016/j.cplett.2015.11.042.

(81) Jankus, V.; Data, P.; Graves, D.; McGuinness, C.; Santos, J.; Bryce, M. R.; Dias, F. B.; Monkman, A. P. Highly Efficient TADF OLEDs: How the Emitter-Host Interaction Controls Both the Excited State Species and Electrical Properties of the Devices to Achieve Near 100% Triplet Harvesting and High Efficiency. *Adv. Funct. Mater.* **2014**, *24* (39), 6178–6186. https://doi.org/10.1002/adfm.201400948.

(82) Masui, K.; Nakanotani, H.; Adachi, C. Analysis of Exciton Annihilation in High-Efficiency Sky-Blue Organic Light-Emitting Diodes with Thermally Activated Delayed Fluorescence. *Org. Electron. physics, Mater. Appl.* **2013**, *14* (11), 2721–2726. https://doi.org/10.1016/j.orgel.2013.07.010.

(83) Serevičius, T.; Bučiūnas, T.; Bucevičius, J.; Dodonova, J.; Tumkevičius, S.; Kazlauskas, K.; Juršėnas, S. Room Temperature Phosphorescence vs. Thermally Activated Delayed Fluorescence in Carbazole-Pyrimidine Cored Compounds. *J. Mater. Chem. C* **2018**, *6* (41), 11128–11136. https://doi.org/10.1039/c8tc02554a.

(84) Liu, X. Y.; Liang, F.; Yuan, Y.; Cui, L. S.; Jiang, Z. Q.; Liao, L. S. An Effective Host Material with Thermally Activated Delayed Fluorescence Formed by Confined Conjugation for Red Phosphorescent Organic Light-Emitting Diodes. *Chem. Commun.* **2016**, *52* (52), 8149–8151. https://doi.org/10.1039/c6cc02856j.

(85) Wex, B.; Kaafarani, B. R. Perspective on Carbazole-Based Organic Compounds as Emitters and Hosts in TADF Applications. *J. Mater. Chem. C* **2017**, *5* (34), 8622–8653. https://doi.org/10.1039/c7tc02156a.

(86) Tsang, D. P. K.; Adachi, C. Operational Stability Enhancement in Organic Light-Emitting Diodes with Ultrathin Liq Interlayers. *Sci. Rep.* **2016**, *6*. https://doi.org/10.1038/srep22463.

(87) Michael Kasha. Characterization of Electronic Transitions in Complex Molecules. *Discuss. Faraday Soc.* **1950**, *9*, 14–19.

(88) Marian, C. M. Spin-Orbit Coupling and Intersystem Crossing in Molecules. *Wiley Interdiscip. Rev. Comput. Mol. Sci.* **2012**, *2* (2), 187–203. https://doi.org/10.1002/wcms.83.

(89) Bergmann, L.; Hedley, G. J.; Baumann, T.; Bräse, S.; Samuel, I. D. W. Direct Observation of Intersystem Crossing in a Thermally Activated Delayed Fluorescence Copper Complex in the Solid State. *Sci. Adv.* **2016**, *2* (1), e1500889. https://doi.org/10.1126/sciadv.1500889.

(90) Dias, F. B.; Penfold, T. J.; Monkman, A. P. Photophysics of Thermally Activated Delayed Fluorescence Molecules. *Methods Appl. Fluoresc.* **2017**, *5* (1), 012001. https://doi.org/10.1088/2050-6120/aa537e.

(91) Coolidge, A. S.; James, H. M.; Present, R. D. A Study of the Franck-Condon Principle. *J. Chem. Phys.* **1936**, *4* (3), 193–211. https://doi.org/10.1063/1.1749818.

(92) Lax, M. The Franck-Condon Principle and Its Application to Crystals. *J. Chem. Phys.* **1952**, *20* (11), 1752–1760. https://doi.org/10.1063/1.1700283.

(93) Condon, E. U. The Franck-Condon Principle and Related Topics. *Am. J. Phys.* **2005**, *15* (5), 365–374. https://doi.org/10.1119/1.1990977.

(94) Heimel, G.; Daghofer, M.; Gierschner, J.; List, E. J. W.; Grimsdale, A. C.; Müllen, K.; Beljonne, D.; Brédas, J. L.; Zojer, E. Breakdown of the Mirror Image Symmetry in the Optical Absorption/Emission Spectra of Oligo(Para-Phenylene)S. *J. Chem. Phys.* **2005**, *122* (5), 4775. https://doi.org/10.1063/1.1839574.

(95) Hosokai, T.; Noda, H.; Nakanotani, H.; Nawata, T.; Nakayama, Y.; Matsuzaki, H.; Adachi, C. Solvent-Dependent Investigation of Carbazole Benzonitrile Derivatives: Does the LE3−CT1 Energy Gap Facilitate Thermally Activated Delayed Fluorescence? *J. Photonics Energy* **2018**, *8* (03), 1. https://doi.org/10.1117/1.JPE.8.032102.

(96) Mataga, N.; Kaifu, Y.; Koizumi, M. The Solvent Effect on Fluorescence Spectrum, Change of Solute-Solvent Interaction during the Lifetime of Excited Solute Molecule. *Bull. Chem. Soc. Jpn.* **2006**, *28* (9), 690–691. https://doi.org/10.1246/bcsj.28.690.

(97) Kash, J. A. *Comment on "Origin of the Stokes Shift: A Geometrical Model of Exciton Spectra in 2D Semiconductors";* 1993; Vol. 71. https://doi.org/10.1103/PhysRevLett.71.1286.

(98) Mataga, N.; Kaifu, Y.; Koizumi, M. Solvent Effects upon Fluorescence Spectra and the Dipolemoments of Excited Molecules. *Bull. Chem. Soc. Jpn.* **1956**, *29* (4), 465–470. https://doi.org/10.1246/bcsj.29.465.

(99) Ishimatsu, R.; Matsunami, S.; Shizu, K.; Adachi, C.; Nakano, K.; Imato, T. Solvent Effect on Thermally Activated Delayed Fluorescence by 1,2,3,5-Tetrakis(Carbazol-9-Yl)-4,6-Dicyanobenzene. *J. Phys. Chem. A* **2013**, *117* (27), 5607–5612. https://doi.org/10.1021/jp404120s.

(100) Bayliss, N. S.; Mcrae, E. G. Solvent Effects in Organic Spectra: Dipole Forces and the Franck-Condon Principle. *J. Phys. Chem.* **1954**, *58* (11), 1002–1006. https://doi.org/10.1021/j150521a017.

(101) Bolton, H. C.; Edmonds, A. R. *Angular Momentum in Quantum Mechanics*; 1959; Vol. 43. https://doi.org/10.2307/3610250.

(102) Allen, L.; Beijersbergen, M. W.; Spreeuw, R. J. C.; Woerdman, J. P. Orbital Angular Momentum of Light and the Transformation of Laguerre-Gaussian Laser Modes. *Phys. Rev. A* **1992**, *45* (11), 8185–8189. https://doi.org/10.1103/PhysRevA.45.8185.

(103) Lawdin, P. O. Angular Momentum Wavefunctions Constructed by Projector Operators. *Rev. Mod. Phys.* **1964**, *36* (4), 966–976. https://doi.org/10.1103/RevModPhys.36.966.

(104) Penfold, T. J.; Gindensperger, E.; Daniel, C.; Marian, C. M. Spin-Vibronic Mechanism for

Intersystem Crossing. *Chem. Rev.* **2018**, *118* (15), 6975–7025. https://doi.org/10.1021/acs.chemrev.7b00617.

(105) Mac, M.; Najbar, J.; Wirz, J. Fluorescence and Intersystem Crossing from the Twisted Intramolecular Charge Transfer (TICT) State of Bianthryl in the Presence of Inorganic Ions in Polar Solvents. *J. Photochem. Photobiol. A Chem.* **1995**, *88* (2–3), 93–104. https://doi.org/10.1016/1010-6030(94)04008-P.

(106) Gan, S.; Hu, S.; Li, X. L.; Zeng, J.; Zhang, D.; Huang, T.; Luo, W.; Zhao, Z.; Duan, L.; Su, S. J.; et al. Heavy Atom Effect of Bromine Significantly Enhances Exciton Utilization of Delayed Fluorescence Luminogens. *ACS Appl. Mater. Interfaces* **2018**, *10* (20), 17327–17334. https://doi.org/10.1021/acsami.8b05389.

(107) Bañares, L. Unexpected Intersystem Crossing. *Nat. Chem.* **2019**, *11* (2), 103–104. https://doi.org/10.1038/s41557-018-0207-4.

(108) Tang, K. C.; Liu, K. L.; Chen, I. C. Rapid Intersystem Crossing in Highly Phosphorescent Iridium Complexes. *Chem. Phys. Lett.* **2004**, *386* (4–6), 437–441. https://doi.org/10.1016/j.cplett.2004.01.098.

(109) Kleinschmidt, M.; Van Wüllen, C.; Marian, C. M. Intersystem-Crossing and Phosphorescence Rates in Fac-IrIII(Ppy)3: A Theoretical Study Involving Multi-Reference Configuration Interaction Wavefunctions. *J. Chem. Phys.* **2015**, *142* (9), 094301. https://doi.org/10.1063/1.4913513.

(110) McLean, A. J.; McGarvey, D. J.; Truscott, T. G.; Lambert, C. R.; Land, E. J. Effect of Oxygen-Enhanced Intersystem Crossing on the Observed Efficiency of Formation of Singlet Oxygen. *J. Chem. Soc. Faraday Trans.* **1990**, *86* (18), 3075. https://doi.org/10.1039/ft9908603075.

(111) Penfold, T. J.; Dias, F. B.; Monkman, A. P. The Theory of Thermally Activated Delayed Fluorescence for Organic Light Emitting Diodes. *Chemical Communications*. 2018, pp 3926–3935. https://doi.org/10.1039/c7cc09612g.

(112) Schmidt, K.; Brovelli, S.; Coropceanu, V.; Beljonne, D.; Cornil, J.; Bazzini, C.; Caronna, T.; Tubino, R.; Meinardi, F.; Shuai, Z.; et al. Intersystem Crossing Processes in Nonplanar Aromatic Heterocyclic Molecules. *J. Phys. Chem. A* **2007**, *111* (42), 10490–10499. https://doi.org/10.1021/jp075248q.

(113) Brédas, J.-L.; Beljonne, D.; Coropceanu, V.; Cornil, J. Charge-Transfer and Energy-Transfer Processes in π-Conjugated Oligomers and Polymers: A Molecular Picture. *Chem. Rev.* **2004**, *104* (11), 4971–5004. https://doi.org/10.1021/cr040084k.

(114) Hosokai, T.; Matsuzaki, H.; Nakanotani, H.; Tokumaru, K.; Tsutsui, T.; Furube, A.; Nasu, K.; Nomura, H.; Yahiro, M.; Adachi, C. Evidence and Mechanism of Efficient Thermally Activated Delayed Fluorescence Promoted by Delocalized Excited States. *Sci. Adv.* **2017**, *3* (5), e1603282. https://doi.org/10.1126/sciadv.1603282.

(115) Etherington, M. K.; Gibson, J.; Higginbotham, H. F.; Penfold, T. J.; Monkman, A. P. Revealing the Spin-Vibronic Coupling Mechanism of Thermally Activated Delayed Fluorescence. *Nat. Commun.* **2016**, *7* (1), 13680. https://doi.org/10.1038/ncomms13680.

(116) Gibson, J.; Monkman, A. P.; Penfold, T. J. The Importance of Vibronic Coupling for Efficient Reverse Intersystem Crossing in Thermally Activated Delayed Fluorescence Molecules. *ChemPhysChem* **2016**, *17* (19), 2956–2961. https://doi.org/10.1002/cphc.201600662.

(117) Im, Y.; Kim, M.; Cho, Y. J.; Seo, J. A.; Yook, K. S.; Lee, J. Y. Molecular Design Strategy of Organic Thermally Activated Delayed Fluorescence Emitters. *Chemistry of Materials*. 2017, pp 1946–1963. https://doi.org/10.1021/acs.chemmater.6b05324.

(118) Cui, L. S.; Ruan, S. Bin; Bencheikh, F.; Nagata, R.; Zhang, L.; Inada, K.; Nakanotani, H.; Liao, L. S.; Adachi, C. Long-Lived Efficient Delayed Fluorescence Organic Light-Emitting Diodes Using n-Type Hosts. *Nat. Commun.* **2017**, *8* (1), 2250. https://doi.org/10.1038/s41467-017-02419-x.

(119) Haase, N.; Danos, A.; Pflumm, C.; Morherr, A.; Stachelek, P.; Mekic, A.; Brütting, W.; Monkman, A. P. Kinetic Modeling of Transient Photoluminescence from Thermally Activated Delayed Fluorescence. *J. Phys. Chem. C* **2018**, *122* (51), 29173–29179. https://doi.org/10.1021/acs.jpcc.8b11020.

(120) Dias, F. B.; Santos, J.; Graves, D. R.; Data, P.; Nobuyasu, R. S.; Fox, M. A.; Batsanov, A. S.; Palmeira, T.; Berberan-Santos, M. N.; Bryce, M. R.; et al. The Role of Local Triplet Excited States and D-A Relative Orientation in Thermally Activated Delayed Fluorescence: Photophysics and Devices. *Adv. Sci.* **2016**, *3* (12), 1600080. https://doi.org/10.1002/advs.201600080.

(121) Speidel, J. J.; Weiss, D. C.; Ethelston, S. A.; Gilbert, S. M. Population Policies, Programmes and the Environment. *Philos. Trans. R. Soc. B Biol. Sci.* **2009**, *364* (1532), 3049–3065. https://doi.org/10.1098/rstb.2009.0162.

(122) Jacobson, M. Z. Powerpoint of Review of Energy Solutions to Global Warming , Air Pollution , and Energy Security Comparison of Energy Solutions to Global Warming. *pubs.rsc.org* **2009**.

(123) Deane, P.; Gallachóir, B. Ó. Pumped Hydro Energy Storage. *Handb. Clean Energy Syst.* **2015**, *44*, 1–16. https://doi.org/10.1002/9781118991978.hces137.

(124) Cherubini, A.; Papini, A.; Vertechy, R.; Fontana, M. Airborne Wind Energy Systems: A Review of the Technologies. *Renew. Sustain. Energy Rev.* **2015**, *51*, 1461–1476. https://doi.org/10.1016/j.rser.2015.07.053.

(125) Jenkins, K.; Heffron, R. J.; McCauley, D. The Political Economy of Energy Justice: A Nuclear Energy Perspective. In *The Palgrave Handbook of the International Political Economy of Energy*; Palgrave Macmillan UK: London, 2016; pp 661–682. https://doi.org/10.1057/978-1-137-55631-8_27.

(126) Lund, J. W.; Boyd, T. L. Direct Utilization of Geothermal Energy 2015 Worldwide Review. *Geothermics* **2016**, *60*, 66–93. https://doi.org/10.1016/j.geothermics.2015.11.004.

(127) Gaurav, N.; Sivasankari, S.; Kiran, G.; Ninawe, A.; Selvin, J. Utilization of Bioresources for Sustainable Biofuels: A Review. *Renew. Sustain. Energy Rev.* **2017**, *73*, 205–214. https://doi.org/10.1016/j.rser.2017.01.070.

(128) Dincer, I.; Acar, C. A Review on Clean Energy Solutions for Better Sustainability. *Int. J. Energy Res.* **2015**, *39* (5), 585–606. https://doi.org/10.1002/er.3329.

(129) Kannan, N.; Vakeesan, D. Solar Energy for Future World: - A Review. *Renew. Sustain. Energy Rev.* **2016**, *62*, 1092–1105. https://doi.org/10.1016/j.rser.2016.05.022.

(130) Vigil-Galán, O.; Courel, M.; Andrade-Arvizu, J. A.; Sánchez, Y.; Espíndola-Rodríguez, M.; Saucedo, E.; Seuret-Jiménez, D.; Titsworth, M. Route towards Low Cost-High Efficiency Second Generation Solar Cells: Current Status and Perspectives. *J. Mater. Sci. Mater. Electron.* **2015**, *26* (8), 5562–5573. https://doi.org/10.1007/s10854-014-2196-4.

(131) Peer, A.; Biswas, R. Nanophotonic Organic Solar Cell Architecture for Advanced Light Trapping with Dual Photonic Crystals. *ACS Photonics* **2014**, *1* (9), 840–847. https://doi.org/10.1021/ph500124q.

(132) Berardi, S.; Drouet, S.; Francàs, L.; Gimbert-Suriñach, C.; Guttentag, M.; Richmond, C.; Stoll, T.; Llobet, A. Molecular Artificial Photosynthesis. *Chem. Soc. Rev.* **2014**, *43* (22), 7501–7519. https://doi.org/10.1039/c3cs60405e.

(133) Romero, M.; González-Aguilar, J. Solar Thermal CSP Technology. *Wiley Interdiscip. Rev. Energy Environ.* **2014**, *3* (1), 42–59. https://doi.org/10.1002/wene.79.

(134) Kribus, A. A High-Efficiency Triple Cycle for Solar Power Generation. *Sol. Energy* **2002**, *72* (1), 1–11. https://doi.org/10.1016/S0038-092X(01)00070-6.

(135) Ekechukwu, O.; management, B. N.-E. conversion and; 1999, undefined. 99/02111 Review of Solar-Energy Drying Systems II: An Overview of Solar Drying Technology. *Fuel Energy Abstr.* **2003**, *40* (3), 216. https://doi.org/10.1016/s0140-6701(99)97881-5.

(136) Liang, Y.; Xu, Z.; Xia, J.; Tsai, S.-T.; Wu, Y.; Li, G.; Ray, C.; Yu, L. For the Bright Future-Bulk Heterojunction Polymer Solar Cells with Power Conversion Efficiency of 7.4%. *Adv. Mater.* **2010**, *22* (20), E135-8. https://doi.org/10.1002/adma.200903528.

(137) On the Action of Light on Selenium. *Nature* **1876**, *13* (334), 407–408. https://doi.org/10.1038/013407a0.

(138) Einstein, A. Über Einen Die Erzeugung Und Verwandlung Des Lichtes Betreffenden Heuristischen Gesichtspunkt. *Ann. Phys.* **1905**, *322* (6), 132–148. https://doi.org/10.1002/andp.19053220607.

(139) Chapin, D. M.; Fuller, C. S.; Pearson, G. L. A New Silicon P-n Junction Photocell for

Converting Solar Radiation into Electrical Power [3]. *J. Appl. Phys.* **1954**, *25* (5), 676–677. https://doi.org/10.1063/1.1721711.

(140) Hoppe, H.; Sariciftci, N. S. Organic Solar Cells: An Overview. *J. Mater. Res.* **2011**, *19* (07), 1924–1945. https://doi.org/10.1557/JMR.2004.0252.

(141) Kaur, N.; Singh, M.; Pathak, D.; Wagner, T.; Nunzi, J. M. Organic Materials for Photovoltaic Applications: Review and Mechanism. *Synth. Met.* **2014**, *190*, 20–26. https://doi.org/10.1016/j.synthmet.2014.01.022.

(142) Green, M. A. Silicon Photovoltaic Modules: A Brief History of the First 50 Years. *Prog. Photovoltaics Res. Appl.* **2005**, *13* (5), 447–455. https://doi.org/10.1002/pip.612.

(143) Kaltenbrunner, M.; White, M. S.; Głowacki, E. D.; Sekitani, T.; Someya, T.; Sariciftci, N. S.; Bauer, S. Ultrathin and Lightweight Organic Solar Cells with High Flexibility. *Nat. Commun.* **2012**, *3* (1), 770. https://doi.org/10.1038/ncomms1772.

(144) Green, M. A.; Emery, K.; Hishikawa, Y.; Warta, W.; Dunlop, E. D.; Levi, D. H.; Ho-Baillie, A. W. Y. Solar Cell Efficiency Tables (Version 49). *Prog. Photovoltaics Res. Appl.* **2017**, *25* (1), 3–13. https://doi.org/10.1002/pip.2855.

(145) Dou, L.; Liu, Y.; Hong, Z.; Li, G.; Yang, Y. Low-Bandgap Near-IR Conjugated Polymers/Molecules for Organic Electronics. *Chem. Rev.* **2015**, *115* (23), 12633–12665. https://doi.org/10.1021/acs.chemrev.5b00165.

(146) Mikkel Jørgensen; Kion Norrman; Frederik C. Krebs. Stability/Degradation of Polymer Solar Cells. *Sol. Energy Mater. Sol. Cells* **2008**, *92* (7), 686–714.

(147) Etxebarria, I.; Ajuria, J.; Pacios, R. Solution-Processable Polymeric Solar Cells: A Review on Materials, Strategies and Cell Architectures to Overcome 10%. *Org. Electron. physics, Mater. Appl.* **2015**, *19*, 34–60. https://doi.org/10.1016/j.orgel.2015.01.014.

(148) Siddiki, M. K.; Li, J.; Galipeau, D.; Qiao, Q. A Review of Polymer Multijunction Solar Cells. *Energy Environ. Sci.* **2010**, *3* (7), 867–883. https://doi.org/10.1039/b926255p.

(149) He, Z.; Zhong, C.; Su, S.; Xu, M.; Wu, H.; Cao, Y. Enhanced Power-Conversion Efficiency in Polymer Solar Cells Using an Inverted Device Structure. *Nat. Photonics* **2012**, *6* (9), 591–595. https://doi.org/10.1038/nphoton.2012.190.

(150) Lenes, M.; Wetzelaer, G.-J. A. H.; Kooistra, F. B.; Veenstra, S. C.; Hummelen, J. C.; Blom, P. W. M. Fullerene Bisadducts for Enhanced Open-Circuit Voltages and Efficiencies in Polymer Solar Cells. *Adv. Mater.* **2008**, *20* (11), 2116–2119. https://doi.org/10.1002/adma.200702438.

(151) Slooff, L. H.; Veenstra, S. C.; Kroon, J. M.; Moet, D. J. D.; Sweelssen, J.; Koetse, M. M. Determining the Internal Quantum Efficiency of Highly Efficient Polymer Solar Cells through Optical Modeling. *Appl. Phys. Lett.* **2007**, *90* (14), 143506. https://doi.org/10.1063/1.2718488.

(152) Ohkita, H.; Cook, S.; Astuti, Y.; Duffy, W.; Tierney, S.; Zhang, W.; Heeney, M.; McCulloch, I.; Nelson, J.; Bradley, D. D. C.; et al. Charge Carrier Formation in Polythiophene/Fullerene Blend Films Studied by Transient Absorption Spectroscopy. *J. Am. Chem. Soc.* **2008**, *130* (10), 3030–3042. https://doi.org/10.1021/ja076568q.

(153) He, Z.; Zhong, C.; Huang, X.; Wong, W. Y.; Wu, H.; Chen, L.; Su, S.; Cao, Y. Simultaneous Enhancement of Open-Circuit Voltage, Short-Circuit Current Density, and Fill Factor in Polymer Solar Cells. *Adv. Mater.* **2011**, *23* (40), 4636–4643. https://doi.org/10.1002/adma.201103006.

(154) Shaheen, S. E.; Brabec, C. J.; Sariciftci, N. S.; Padinger, F.; Fromherz, T.; Hummelen, J. C. 2.5% Efficient Organic Plastic Solar Cells. *Appl. Phys. Lett.* **2001**, *78* (6), 841–843. https://doi.org/10.1063/1.1345834.

(155) Bouzidi, K.; Chegaar, M.; Bouhemadou, A. Solar Cells Parameters Evaluation Considering the Series and Shunt Resistance. *Sol. Energy Mater. Sol. Cells* **2007**, *91* (18), 1647–1651. https://doi.org/10.1016/j.solmat.2007.05.019.

(156) El-Adawi, M. K.; Al-Nuaim, I. A. A Method to Determine the Solar Cell Series Resistance from a Single I-V. Characteristic Curve Considering Its Shunt Resistance - New Approach. *Vacuum* **2001**, *64* (1), 33–36. https://doi.org/10.1016/S0042-207X(01)00370-0.

(157) Li, G.; Zhu, R.; Yang, Y. Polymer Solar Cells. *Nat. Photonics* **2012**, *6* (3), 153–161. https://doi.org/10.1038/nphoton.2012.11.

(158) Green MA. PV Modules: Operating Principles, Technology and System Applications. *Englewood Cliffs, NJ, Prentice-Hall, Inc., 1982. 288 p.* **1982**, 79–117.

(159) Green, M. A.; Blakers, A. W.; Shi, J.; Keller, E. M.; Wenham, S. R. 19.1% Efficient Silicon Solar Cell. *Appl. Phys. Lett.* **1984**, *44* (12), 1163–1164. https://doi.org/10.1063/1.94678.

(160) Burschka, J.; Pellet, N.; Moon, S. J.; Humphry-Baker, R.; Gao, P.; Nazeeruddin, M. K.; Grätzel, M. Sequential Deposition as a Route to High-Performance Perovskite-Sensitized Solar Cells. *Nature* **2013**, *499* (7458), 316–319. https://doi.org/10.1038/nature12340.

(161) Wang, A.; Zhao, J.; Green, M. A. 24% Efficient Silicon Solar Cells. *Appl. Phys. Lett.* **1990**, *57* (6), 602–604. https://doi.org/10.1063/1.103610.

(162) Forrest, S. R. The Limits to Organic Photovoltaic Cell Efficiency. *MRS Bull.* **2005**, *30* (1), 28–32. https://doi.org/10.1557/mrs2005.5.

(163) Yan, C.; Barlow, S.; Wang, Z.; Yan, H.; Jen, A. K. Y.; Marder, S. R.; Zhan, X. Non-Fullerene Acceptors for Organic Solar Cells. *Nat. Rev. Mater.* **2018**, *3* (3), 18003. https://doi.org/10.1038/natrevmats.2018.3.

(164) Zhang, S.; Qin, Y.; Zhu, J.; Hou, J. Over 14% Efficiency in Polymer Solar Cells Enabled by a Chlorinated Polymer Donor. *Adv. Mater.* **2018**, *30* (20), 1800868. https://doi.org/10.1002/adma.201800868.

(165) Ristein, J.; Mammadov, S.; Seyller, T. Origin of Doping in Quasi-Free-Standing Graphene on Silicon Carbide. *Phys. Rev. Lett.* **2012**, *108* (24), 246104. https://doi.org/10.1103/PhysRevLett.108.246104.

(166) Demichelis, F.; Pirri, C. F.; Tresso, E. Influence of Doping on the Structural and Optoelectronic Properties of Amorphous and Microcrystalline Silicon Carbide. *J. Appl. Phys.* **1992**, *72* (4), 1327–1333. https://doi.org/10.1063/1.351742.

(167) Spear, W. E.; Le Comber, P. G. Substitutional Doping of Amorphous Silicon. *Solid State Commun.* **1993**, *88* (11–12), 1015–1018. https://doi.org/10.1016/0038-1098(93)90286-V.

(168) Chiu, F. C. A Review on Conduction Mechanisms in Dielectric Films. *Adv. Mater. Sci. Eng.* **2014**, *2014*, 1–18. https://doi.org/10.1155/2014/578168.

(169) Yoshikawa, K.; Kawasaki, H.; Yoshida, W.; Irie, T.; Konishi, K.; Nakano, K.; Uto, T.; Adachi, D.; Kanematsu, M.; Uzu, H.; et al. Silicon Heterojunction Solar Cell with Interdigitated Back Contacts for a Photoconversion Efficiency over 26%. *Nat. Energy* **2017**, *2* (5), 17032. https://doi.org/10.1038/nenergy.2017.32.

(170) Krogstrup, P.; Jørgensen, H. I.; Heiss, M.; Demichel, O.; Holm, J. V.; Aagesen, M.; Nygard, J.; Fontcuberta I Morral, A. Single-Nanowire Solar Cells beyond the Shockley-Queisser Limit. *Nat. Photonics* **2013**, *7* (4), 306–310. https://doi.org/10.1038/nphoton.2013.32.

(171) Tang, C. W. Two-Layer Organic Photovoltaic Cell. *Appl. Phys. Lett.* **1986**, *48* (2), 183–185. https://doi.org/10.1063/1.96937.

(172) Yu, G.; Gao, J.; Hummelen, J. C.; Wudl, F.; Heeger, A. J. Polymer Photovoltaic Cells: Enhanced Efficiencies via a Network of Internal Donor-Acceptor Heterojunctions. *Science (80-.).* **1995**, *270* (5243), 1789. https://doi.org/10.1126/science.270.5243.1789.

(173) Son, H. J.; Wang, W.; Xu, T.; Liang, Y.; Wu, Y.; Li, G.; Yu, L. Synthesis of Fluorinated Polythienothiophene- Co -Benzodithiophenes and Effect of Fluorination on the Photovoltaic Properties. *J. Am. Chem. Soc.* **2011**, *133* (6), 1885–1894. https://doi.org/10.1021/ja108601g.

(174) Kobilka, B. M.; Hale, B. J.; Ewan, M. D.; Dubrovskiy, A. V.; Nelson, T. L.; Duzhko, V.; Jeffries-EL, M. Influence of Heteroatoms on Photovoltaic Performance of Donor–Acceptor Copolymers Based on 2,6-Di(Thiophen-2-Yl)Benzo[1,2-b:4,5-B′]Difurans and Diketopyrrolopyrrole. *Polym. Chem.* **2013**, *4* (20), 5329. https://doi.org/10.1039/c3py00138e.

(175) Günes, S.; Neugebauer, H.; Sariciftci, N. S. Conjugated Polymer-Based Organic Solar Cells. *Chem. Rev.* **2007**, *107* (4), 1324–1338. https://doi.org/10.1021/cr050149z.

(176) Polymer:Fullerene Bulk Heterojunction Solar Cells. *Mater. Today* **2011**, *14* (10), 462–470. https://doi.org/10.1016/S1369-7021(11)70210-3.

(177) Xu, T.; Yu, L. How to Design Low Bandgap Polymers for Highly Efficient Organic Solar

Cells. *Mater. Today* **2014**, *17* (1), 11–15. https://doi.org/10.1016/j.mattod.2013.12.005.

(178) Zheng, Z.; Zhang, S.; Zhang, J.; Qin, Y.; Li, W.; Yu, R.; Wei, Z.; Hou, J. Over 11% Efficiency in Tandem Polymer Solar Cells Featured by a Low-Band-Gap Polymer with Fine-Tuned Properties. *Adv. Mater.* **2016**, *28* (25), 5133–5138. https://doi.org/10.1002/adma.201600373.

(179) Scharber, M. C.; Sariciftci, N. S. Efficiency of Bulk-Heterojunction Organic Solar Cells. *Prog. Polym. Sci.* **2013**, *38* (12), 1929–1940. https://doi.org/10.1016/j.progpolymsci.2013.05.001.

(180) Dang, M.; Hirsch, L.; Materials, G. W.-A.; 2011, undefined. P3HT: PCBM, Best Seller in Polymer Photovoltaic Research. *Wiley Online Libr.*

(181) Chen, D.; Nakahara, A.; Wei, D.; Nordlund, D.; Russell, T. P. P3HT/PCBM Bulk Heterojunction Organic Photovoltaics: Correlating Efficiency and Morphology. *Nano Lett.* **2011**, *11* (2), 561–567. https://doi.org/10.1021/nl103482n.

(182) Shang, Z.; Dimitrov, S. D.; Yousaf, S. A.; Ashraf, R. S.; Durrant, J. R.; Tan, C.-H.; Gasparini, N.; Alamoudi, M.; Holliday, S.; Wadsworth, A.; et al. High-Efficiency and Air-Stable P3HT-Based Polymer Solar Cells with a New Non-Fullerene Acceptor. *Nat. Commun.* **2016**, *7* (1), 1–11. https://doi.org/10.1038/ncomms11585.

(183) Chu, T. Y.; Lu, J.; Beaupré, S.; Zhang, Y.; Pouliot, J. R.; Wakim, S.; Zhou, J.; Leclerc, M.; Li, Z.; Ding, J.; et al. Bulk Heterojunction Solar Cells Using Thieno[3,4- c]Pyrrole-4,6-Dione and Dithieno[3,2- b:2′,3′- d]Silole Copolymer with a Power Conversion Efficiency of 7.3%. *J. Am. Chem. Soc.* **2011**, *133* (12), 4250–4253. https://doi.org/10.1021/ja200314m.

(184) Manceau, M.; Chambon, S.; Rivaton, A.; Gardette, J. L.; Guillerez, S.; Lematre, N. Effects of Long-Term UVvisible Light Irradiation in the Absence of Oxygen on P3HT and P3HT: PCBM Blend. *Sol. Energy Mater. Sol. Cells* **2010**, *94* (10), 1572–1577. https://doi.org/10.1016/j.solmat.2010.03.012.

(185) Glatthaar, M.; Riede, M.; Keegan, N.; Sylvester-Hvid, K.; Zimmermann, B.; Niggemann, M.; Hinsch, A.; Gombert, A. Efficiency Limiting Factors of Organic Bulk Heterojunction Solar Cells Identified by Electrical Impedance Spectroscopy. *Sol. Energy Mater. Sol. Cells* **2007**, *91* (5), 390–393. https://doi.org/10.1016/j.solmat.2006.10.020.

(186) Krebs, F. C.; Monestier, F.; Simon, J.-J.; Torchio, P.; Escoubas, L.; Flory, F.; Bailly, S.; de Bettignies, R.; Guillerez, S.; Defranoux, C. Modeling the Short-Circuit Current Density of Polymer Solar Cells Based on P3HT:PCBM Blend. *Sol. Energy Mater. Sol. Cells* **2007**, *91* (5), 405–410.

(187) Acevedo-Peña, P.; Baray-Calderón, A.; Hu, H.; González, I.; Ugalde-Saldivar, V. M. Measurements of HOMO-LUMO Levels of Poly(3-Hexylthiophene) Thin Films by a Simple Electrochemical Method. *J. Solid State Electrochem.* **2017**, *21* (8), 2407–2414. https://doi.org/10.1007/s10008-017-3587-2.

(188) Scharber, M. C.; Mühlbacher, D.; Koppe, M.; Denk, P.; Waldauf, C.; Heeger, A. J.; Brabec, C. J. Design Rules for Donors in Bulk-Heterojunction Solar Cells - Towards 10 % Energy-Conversion Efficiency. *Adv. Mater.* **2006**, *18* (6), 789–794. https://doi.org/10.1002/adma.200501717.

(189) Zhu, Z.; Waller, D.; Gaudiana, R.; Morana, M.; Mühlbacher, D.; Scharber, M.; Brabec, C. Panchromatic Conjugated Polymers Containing Alternating Donor/ Acceptor Units for Photovoltaic Applications. *Macromolecules* **2007**, *40* (6), 1981–1986. https://doi.org/10.1021/ma062376o.

(190) Siddiki, M. K.; Li, J.; Galipeau, D.; Qiao, Q. A Review of Polymer Multijunction Solar Cells. *Energy Environ. Sci.* **2010**, *3* (7), 867–883. https://doi.org/10.1039/b926255p.

(191) Huo, L.; Hou, J.; Chen, H.-Y.; Zhang, S.; Jiang, Y.; Chen, T. L.; Yang, Y. Bandgap and Molecular Level Control of the Low-Bandgap Polymers Based on 3,6-Dithiophen-2-Yl-2,5-Dihydropyrrolo[3,4- c]Pyrrole-1,4-Dione toward Highly Efficient Polymer Solar Cells. *Macromolecules* **2009**, *42* (17), 6564–6571. https://doi.org/10.1021/ma9012972.

(192) Elumalai, N. K.; Uddin, A. Open Circuit Voltage of Organic Solar Cells: An in-Depth Review. *Energy Environ. Sci.* **2016**, *9* (2), 391–410. https://doi.org/10.1039/c5ee02871j.

(193) Eftaiha, A. F.; Sun, J. P.; Hill, I. G.; Welch, G. C. Recent Advances of Non-Fullerene, Small Molecular Acceptors for Solution Processed Bulk Heterojunction Solar Cells. *J. Mater. Chem. A* **2014**, *2* (5), 1201–1213. https://doi.org/10.1039/c3ta14236a.

(194) Rand, B. P.; Burk, D. P.; Forrest, S. R. Offset Energies at Organic Semiconductor Heterojunctions and Their Influence on the Open-Circuit Voltage of Thin-Film Solar Cells. *Phys. Rev. B - Condens. Matter Mater. Phys.* **2007**, *75* (11), 115327. https://doi.org/10.1103/PhysRevB.75.115327.

(195) Li, Y. Molecular Design of Photovoltaic Materials for Polymer Solar Cells: Toward Suitable Electronic Energy Levels and Broad Absorption. *Acc. Chem. Res.* **2012**, *45* (5), 723–733. https://doi.org/10.1021/ar2002446.

(196) Liang, Y.; Feng, D.; Wu, Y.; Tsai, S. T.; Li, G.; Ray, C.; Yu, L. Highly Efficient Solar Cell Polymers Developed via Fine-Tuning of Structural and Electronic Properties. *J. Am. Chem. Soc.* **2009**, *131* (22), 7792–7799. https://doi.org/10.1021/ja901545q.

(197) Dou, L.; Gao, J.; Richard, E.; You, J.; Chen, C. C.; Cha, K. C.; He, Y.; Li, G.; Yang, Y. Systematic Investigation of Benzodithiophene- and Diketopyrrolopyrrole- Based Low-Bandgap Polymers Designed for Single Junction and Tandem Polymer Solar Cells. *J. Am. Chem. Soc.* **2012**, *134* (24), 10071–10079. https://doi.org/10.1021/ja301460s.

(198) Ye, L.; Zhang, S.; Huo, L.; Zhang, M.; Hou, J. Molecular Design toward Highly Efficient Photovoltaic Polymers Based on Two-Dimensional Conjugated Benzodithiophene. *Acc. Chem. Res.* **2014**, *47* (5), 1595–1603. https://doi.org/10.1021/ar5000743.

(199) Kan, B.; Zhang, Q.; Li, M.; Wan, X.; Ni, W.; Long, G.; Wang, Y.; Yang, X.; Feng, H.;

Chen, Y. Solution-Processed Organic Solar Cells Based on Dialkylthiol-Substituted Benzodithiophene Unit with Efficiency near 10%. *J. Am. Chem. Soc.* **2014**, *136* (44), 15529–15532. https://doi.org/10.1021/ja509703k.

(200) Zhou, J.; Zuo, Y.; Wan, X.; Long, G.; Zhang, Q.; Ni, W.; Liu, Y.; Li, Z.; He, G.; Li, C.; et al. Solution-Processed and High-Performance Organic Solar Cells Using Small Molecules with a Benzodithiophene Unit. *J. Am. Chem. Soc.* **2013**, *135* (23), 8484–8487. https://doi.org/10.1021/ja403318y.

(201) Zhang, Z. G.; Li, Y. Side-Chain Engineering of High-Efficiency Conjugated Polymer Photovoltaic Materials. *Sci. China Chem.* **2015**, *58* (2), 192–209. https://doi.org/10.1007/s11426-014-5260-2.

(202) Ye, L.; Jiao, X.; Zhang, H.; Li, S.; Yao, H.; Ade, H.; Hou, J. 2D-Conjugated Benzodithiophene-Based Polymer Acceptor: Design, Synthesis, Nanomorphology, and Photovoltaic Performance. *Macromolecules* **2015**, *48* (19), 7156–7163. https://doi.org/10.1021/acs.macromol.5b01537.

(203) Huang, Y.; Guo, X.; Liu, F.; Huo, L.; Chen, Y.; Russell, T. P.; Han, C. C.; Li, Y.; Hou, J. Improving the Ordering and Photovoltaic Properties by Extending π-Conjugated Area of Electron-Donating Units in Polymers with D-A Structure. *Adv. Mater.* **2012**, *24* (25), 3383–3389. https://doi.org/10.1002/adma.201200995.

(204) Keller, B.; McLean, A.; Kim, B. G.; Chung, K.; Kim, J.; Goodson, T. Ultrafast Spectroscopic Study of Donor-Acceptor Benzodithiophene Light Harvesting Organic Conjugated Polymers. *J. Phys. Chem. C* **2016**, *120* (17), 9088–9096. https://doi.org/10.1021/acs.jpcc.6b01727.

(205) Liu, C.; Dong, S.; Cai, P.; Liu, P.; Liu, S.; Chen, J.; Liu, F.; Ying, L.; Russell, T. P.; Huang, F.; et al. Donor-Acceptor Copolymers Based on Thermally Cleavable Indigo, Isoindigo, and DPP Units: Synthesis, Field Effect Transistors, and Polymer Solar Cells. *ACS Appl. Mater. Interfaces* **2015**, *7* (17), 9038–9051. https://doi.org/10.1021/am5089956.

(206) Li, S.; Ye, L.; Zhao, W.; Yan, H.; Yang, B.; Liu, D.; Li, W.; Ade, H.; Hou, J. A Wide Band Gap Polymer with a Deep Highest Occupied Molecular Orbital Level Enables 14.2% Efficiency in Polymer Solar Cells. *J. Am. Chem. Soc.* **2018**, *140* (23), 7159–7167. https://doi.org/10.1021/jacs.8b02695.

(207) Li, M.; Gao, K.; Wan, X.; Zhang, Q.; Kan, B.; Xia, R.; Liu, F.; Yang, X.; Feng, H.; Ni, W.; et al. Solution-Processed Organic Tandem Solar Cells with Power Conversion Efficiencies >12%. *Nat. Photonics* **2017**, *11* (2), 85–90. https://doi.org/10.1038/nphoton.2016.240.

(208) Etxebarria, I.; Ajuria, J.; Pacios, R. Polymer:Fullerene Solar Cells: Materials, Processing Issues, and Cell Layouts to Reach Power Conversion Efficiency over 10%, a Review. *J. Photonics Energy* **2015**, *5* (1), 057214. https://doi.org/10.1117/1.jpe.5.057214.

(209) Pivrikas, A.; Sariciftci, N. S.; Juška, G.; Österbacka, R. A Review of Charge Transport and Recombination in Polymer/Fullerene Organic Solar Cells. *Prog. Photovoltaics Res. Appl.*

2007, *15* (8), 677–696. https://doi.org/10.1002/pip.791.

(210) Zhao, W.; Qian, D.; Zhang, S.; Li, S.; Inganäs, O.; Gao, F.; Hou, J. Fullerene-Free Polymer Solar Cells with over 11% Efficiency and Excellent Thermal Stability. *Adv. Mater.* **2016**, *28* (23), 4734–4739. https://doi.org/10.1002/adma.201600281.

(211) Cnops, K.; Rand, B. P.; Cheyns, D.; Verreet, B.; Empl, M. A.; Heremans, P. 8.4% Efficient Fullerene-Free Organic Solar Cells Exploiting Long-Range Exciton Energy Transfer. *Nat. Commun.* **2014**, *5* (1), 3406. https://doi.org/10.1038/ncomms4406.

(212) Collavini, S.; Delgado, J. L. Fullerenes: The Stars of Photovoltaics. *Sustain. Energy Fuels* **2018**, *2* (11), 2480–2493. https://doi.org/10.1039/c8se00254a.

(213) Yanilkin, V. V.; Gubskaya, V. P.; Morozov, V. I.; Nastapova, N. V.; Zverev, V. V.; Berdnikov, E. A.; Nuretdinov, I. A. Electrochemistry of Fullerenes and Their Derivatives. *Russ. J. Electrochem.* **2003**, *39* (11), 1147–1165. https://doi.org/10.1023/B:RUEL.0000003442.51938.5f.

(214) Xie, Q.; Pérez-Cordero, E.; Echegoyen, L. Electrochemical Detection of C606- and C706-: Enhanced Stability of Fullerides in Solution. *Journal of the American Chemical Society*. May 1, 1992, pp 3978–3980. https://doi.org/10.1021/ja00036a056.

(215) Nelson, J. Polymer: Fullerene Bulk Heterojunction Solar Cells. *Mater. Today* **2011**, *14* (10), 462–470. https://doi.org/10.1016/S1369-7021(11)70210-3.

(216) Jamieson, F. C.; Domingo, E. B.; McCarthy-Ward, T.; Heeney, M.; Stingelin, N.; Durrant, J. R. Fullerene Crystallisation as a Key Driver of Charge Separation in Polymer/Fullerene Bulk Heterojunction Solar Cells. *Chem. Sci.* **2012**, *3* (2), 485–492. https://doi.org/10.1039/c1sc00674f.

(217) Cui, Y.; Yao, H.; Gao, B.; Qin, Y.; Zhang, S.; Yang, B.; He, C.; Xu, B.; Hou, J. Fine-Tuned Photoactive and Interconnection Layers for Achieving over 13% Efficiency in a Fullerene-Free Tandem Organic Solar Cell. *J. Am. Chem. Soc.* **2017**, *139* (21), 7302–7309. https://doi.org/10.1021/jacs.7b01493.

(218) Zhan, X.; Tan, Z.; Domercq, B.; An, Z.; Zhang, X.; Barlow, S.; Li, Y.; Zhu, D.; Kippelen, B.; Marder, S. R. A High-Mobility Electron-Transport Polymer with Broad Absorption and Its Use in Field-Effect Transistors and All-Polymer Solar Cells. *J. Am. Chem. Soc.* **2007**, *129* (23), 7246–7247. https://doi.org/10.1021/ja071760d.

(219) Zheng, T.; Cai, Z.; Ho-Wu, R.; Yau, S. H.; Shaparov, V.; Goodson, T.; Yu, L. Synthesis of Ladder-Type Thienoacenes and Their Electronic and Optical Properties. *J. Am. Chem. Soc.* **2016**, *138* (3), 868–875. https://doi.org/10.1021/jacs.5b10175.

(220) Lee, J.; Ko, S. J.; Seifrid, M.; Lee, H.; Luginbuhl, B. R.; Karki, A.; Ford, M.; Rosenthal, K.; Cho, K.; Nguyen, T. Q.; et al. Bandgap Narrowing in Non-Fullerene Acceptors: Single Atom Substitution Leads to High Optoelectronic Response Beyond 1000 Nm. *Adv. Energy Mater.* **2018**, *8* (24), 1801212. https://doi.org/10.1002/aenm.201801212.

(221) Mori, H.; Nishihara, Y. Low-Bandgap Semiconducting Polymers Based on Sulfur-Containing Phenacene-Type Molecules for Transistor and Solar Cell Applications. *Polym. J.* **2018**, *50* (8), 615–625. https://doi.org/10.1038/s41428-018-0072-4.

Chapter 2

Experimental Techniques and Methods

2.1 Overview

The experimental techniques and methods utilized in the studies enclosed in this dissertation are discussed in this section. These techniques were used to probe the excited state dynamics of light harvesting polymers, low-bandgap small molecules, intramolecular singlet exciton fission (iSF) mechanism, and chromophores with thermally activated delayed fluorescence (TADF) characteristics. Understanding the theoretical background of the instrumentation will help in the elucidation and better understanding of the obtained optical properties of the investigated systems. In addition, the details are described such that the reader does not need to consult other sources of information for further clarification of the techniques discussed in here.

2.2 Steady-State Spectroscopy

Two fundamental steady-state spectroscopic techniques were used to investigate the basic light-mater interaction of the investigated materials. These techniques are UV-visible absorption spectroscopy and fluorescence spectroscopy. The steady-state spectroscopic approach investigated the basic light mater interaction in function of a range of frequencies/wavelengths. The UV-Visible absorption is a technique that involves the measurements of absorbed electromagnetic radiation in function of its incident wavelength or frequency.[1] This measurement can be carried out in solution or in film. Matter can absorb electromagnetic radiation in the form of discrete pockets known as

photon. For the sake of this study, we will focus this discussion in the visible electromagnetic radiation known as light. An electronic transition from the ground state to the excited state is promoted if a photon with the proper energy interact with the absorbing materials, a characteristic proper of the quantized nature of light-mater interactions.[1,2] The electronic transition from the ground state to the excited state is a very fast process, it occurs over in sub femtoseconds timescale, which is much faster than the detector can resolve.[3] This electronic transition is what measure the steady state absorption and is better explained by Beer-Lambert's law.[2] This law stated that the light absorbance (A) of a sample at a given wavelength is directly proportional to the concentration (*C*) of the sample for a given path length (*L*) and the molar absorptivity coefficient (*E*) that is intrinsic for each material and is measured in $M^{-1}cm^{-1}$ (**Equation 2.2.1**).

$$A = \log(\frac{I_0}{I}) = E \,.\, L \,.\, C \qquad \textbf{Equation 2.2.1}$$

As it can be observed from **Equation 2.2.1**, the obtained absorption is highly dependent on the conditions that the measurement is taken, with the concentration (C) and the path-length (L) of the cuvette or film playing an integral role in the obtained optical density (A). However, it is imperative to explain how the instruments makes the absorption measurements. In practice, the spectrophotometer measures the ratio between the amount of input light (l_0) before passing through the absorbing media and the attenuated light (l) after it passed through the absorbing media. The spectrophotometer is not able to distinguish between all the potential light-matter interaction such as diffraction, reflection, refraction, and scattering.[2] Therefore, it is important to run a background measurement of the matrix (the medium in which the measurements is going to take place) to account for these other potential light mater interactions. In the case of the absorption

measurements in solution, concentration homogeneities are assumed within the cuvette dimension due to uniform dispersion of the sample throughout the solution. The case might be different when the measurement is taken in solid state. Therefore, the absorption at solid state are usually obtained for qualitative purpose only. Contrarily, the absorption measurement in solution is a quantitative method that gives you the molar absorptivity coefficient (*E*), which is a critical parameter for describing the absorption characteristics of organic light harvesting materials. The *E* represents the absorbing capabilities of a molecule at a given wavelength,[4] with a typical molar absorptivity coefficients between $10^{6\text{-}3}$ $M^{-1}cm^{-1}$ for conjugated light harvesting organic molecules are obtained.[5] Another important parameter that is intrinsic of a material and can be obtained from the *E* is the one photon absorption cross-section, σ in cm^2, which is a measurement for the one photon absorption process and can be described by **Equation 2.2.2**

$$\sigma = \frac{2.303\ .\ E\ .\ C}{n} \qquad \textbf{Equation 2.2.2}$$

In **Equation 2.2.2**, the n is the number of absorbing molecules per cm^2, *E* is the molar absorptivity coefficient obtained from **Equation 2.2.1**, and *C* is the concentration in mol/L. Analogous terminology will be employed to describe the two-photon absorption process in later sections.

All the absorption measurements in this dissertation were carried out by an Agilent 8453 UV-visible spectroscopic system and the data was collected with Agilent Chemstation software that was connected to the spectrophotometer. The incident light is produced by a combination of deuterium-discharge lamp and a tungsten lamp, which will result in electromagnetic radiation from the ultraviolet wavelength range (190 nm) to the short wave near-infrared region (1100nm).

A

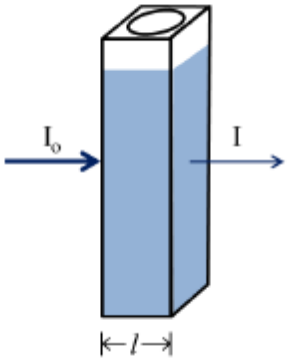

B

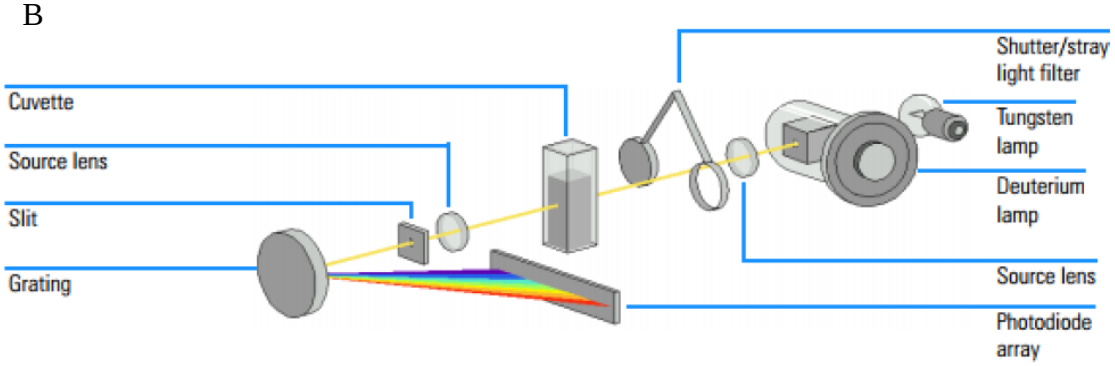

Figure 2.2.1. Light-mater interaction in a sample (A). Agilent 8453 UV-Vis spectrophotometer schematic (Agilent 8453 UV-visible Spectroscopy System Service Manual) (B).

Optical elements are used to collimate the light from the two lamps and direct it to pass through the shutter or stray light filter into the sample. Quartz cuvettes manufactures by Starna (1 cm x 0.4 cm) were used to hold the solution samples. Optical lens is used once again to collimate the transmitted and attenuated light to pass through a slit. The light is then dispersed onto the diode array via a holographic grating. The Agilent 8453 UV-Vis spectrophotometer schematic can be seen in **Figure 2.2.1B.**

The second fundamental steady-state technique measures the emission spectra of the investigated materials, which is obtained with a fluorimeter. The steady-state emission is mostly used to investigate the quantum efficiency of an emissive materials, which is the ratio of absorbed

photons to emitted photons at a wavelength. In addition, by knowing the quantum efficiency, or as it better known, the quantum yield (Φ), one can have insight into other non-emissive photophysical processes that may be taking place.[6–8] The fluorescence intensity is given by **Equation 2.2.3**.

$$\boldsymbol{I_{flu} = I_0 . \Phi . l . E . c} \qquad \textbf{Equation 2.2.3}$$

In **Equation 2.2.3**, $\boldsymbol{I_{flu}}$ is the measured fluorescence intensity, which depends on the incident light intensity (I_0), the quantum yield (Φ), the path length of the medium (l), the molar absorptivity coefficient (E), and the concentration (c) in mol/L. The timescales in where the fluorescence process happens are usually magnitudes longer than the timescales in where the absorption process happens. The lifetimes of typical fluorescence chromophores can vary from hundreds of picoseconds to a couple of nanoseconds. Thus, the steady-state fluorescence can be explained and understood by its fluorescence lifetime.[9]

The fluorescence intensity is highly dependent on the Φ, which serves as a quantitative method of the chromophore's emissive efficiency. However, the excited state energy dissipations in materials can happens via radiative or non-radiative deactivation process. The quantum yield of a material is governed by **Equation 2.2.4.**

$$\Phi = \frac{k_f}{k_f + k_{isc} + k_{ec} + k_{ic} + k_{pd} + k_d} \qquad \textbf{Equation 2.2.4}$$

In **Equation 2.2.4**, the Where k_f is the fluorescence rate constant, k_i is the intersystem rate constant, k_{ec} is the external conversion rate constant, k_{ic} is the internal conversion rate, k_{pd} is the pre-

dissociation rate constant, and k_d is the dissociation rate constant. As mentioned before, the quantum yield can quantify the emissive and the non-emissive processes.[10,11] The fluorescence quantum yield was determined by using the Williams comparative methods, which required the use of a well-known and highly emissive standards with very similar steady state properties than the ones under investigation. In this way, the limitations of the instrumentation are neglected. In order to minimize re-absorption effects, the optical densities of investigated systems and the standard were kept below 0.1 OD. Some of the standards used for these studies are Rhodamine B,[12] Zinc Phtalocyanine,[13] and Coumarin 307.[14] The fluorescence quantum yield is calculated by **Equation 2.2.5.**

$$\phi_x = \phi_{STD} \frac{Grad_x \eta_x^2}{Grad_{STD}\, \eta_{STD}^2} \qquad \textbf{Equation 2.2.5}$$

In **Equation 2.2.5**, the Φ_x is the inquired quantum yield, η is the refractive index of the solvent, and $Grad$ is the slope obtained from plotting the fluorescence area vs the optical density (OD).

The fluorescence spectra measurements were carried out by a Spex Fluoromax-2 and Spex Fluoromax-4 spectrophotometer, which a representative diagram can be observed in **Figure 2.2.2.** The excitation source in the spectrophotometer is a xenon lamp that can produce light from 190 nm to 2000 nm. The excitation beam is focused on the entrance slit of an excitation monochromator with an elliptical mirror. The excitation and collection slits are adjustable in units of bandwidth that can go from 0 nm to over 20 nm and are determined mostly by the intensity of the investigated materials. Diffraction gratings in the excitation monochromator is responsible for enabling single wavelength excitation of samples placed in the sample chamber. Due to the radial nature of the fluorescence, the photomultiplier tube (PMT) detector is placed with a 90^o angle relative to the

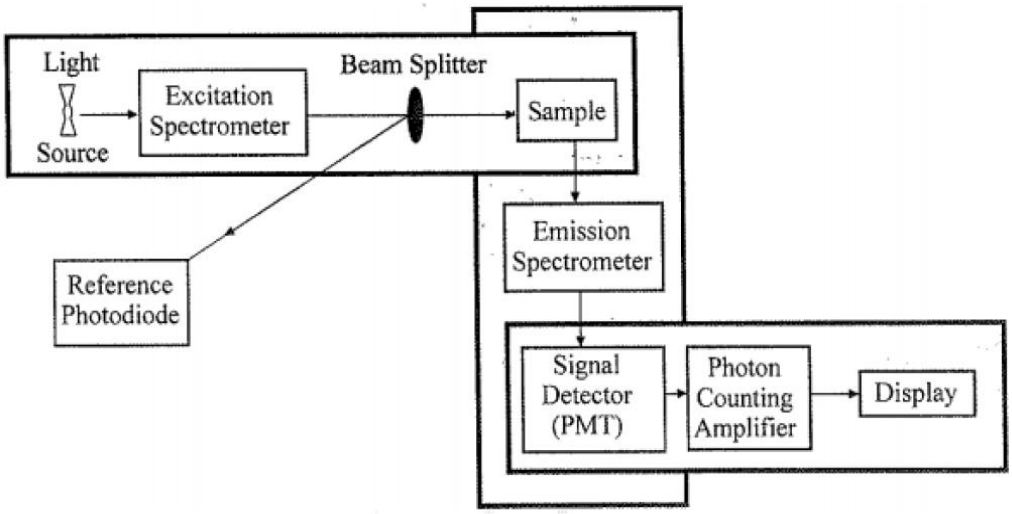

Figure 2.2.2. Genera schematic for a Fluoromax-2 and Fluoromax-4.

excitation source to eliminate background signal and minimize noise due to stray light. The radial fluorescence from the samples enters the slits to an emission spectrometer. These slits can be controlled in order to prevent saturating the detector. Gratings are also placed in front of the emission spectrometer to ensure efficient collection of each emission wavelength. The signal is then amplified by a photon counting amplifier which is then recorded by a computer. Similar cuvettes than those used for the absorption measurements were used for the emission spectra and quantum yield characterization.

2.3 Two-Photon Absorption Spectroscopy

It is possible that a two-photon light-matter interaction promotes an analogous electronic transition from the ground state to the exited than those described in the previous section by linear absorption. Two-photon absorption (TPA) is a non-linear phenomenon that happens when two photons with supplemental frequency than the one for the one photon in linear absorption are absorbed. In synthesis, the difference between the energy of the ground and excited states is the

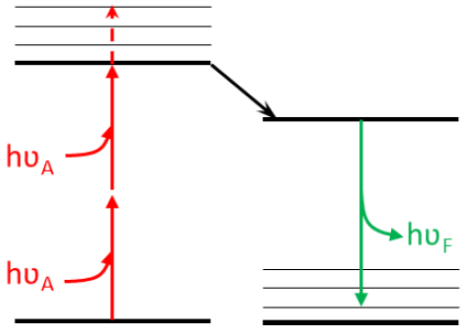

Figure 2.3.1. Jablonski diagram for two-photon absorption and fluorescence processes.

sum of the energy of the two photons that are absorbed almost simultaneously (**Figure 2.3.1**).[15,16] The TPA phenomenon was originally predicted by Maria Goeppert-Mayer in 1931,[10] but the it was first reported experimentally until the invention of lasers thirty years later from its prediction.[17]

The non-linear nature of this technique is better understood by the two-photon excited fluorescence (TPEF) method, in which the polarization density (P) of the absorbing material have a non-linear response to the electric field (E) induced by two-photons.[18] This technique use the TPA-fluorescence, which have a square dependence on the incident power of the laser, to determine the TPA cross-section of the material. The TPEF set up use spectra physics mode-locked Ti:Sapphire laser, which is tunable from 700 to 900 nm delivering 110 fs output pulses at a repetition rate of 80 MHz and pumps an OPAL optical parametric oscillator (OPO) lithium borate (LBO) crystal which allows for 1.3 and 1.5 μm output excitations with output power of 200 mW. Emission scans can be performed at the preferred excitation wavelength, while the emission is collected in the visible region. After optimizing the excitation and determining the right detection wavelength, the beam is directed to a variable neutral density wheel by using set of mirrors in the set-up. The variable neutral density wheel will control of the power of the excitation beam. An optical glass is used to reflect a very small portion of the excitation source into a high-speed silicon photodiode connected to a multimeter, which monitors the excitation beam power. The

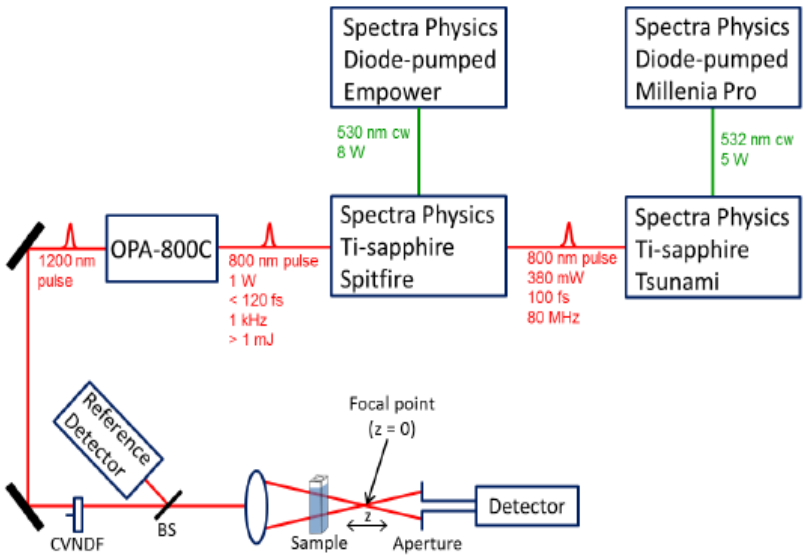

Figure 2.3.2. Nonlinear optical set-up for the two-photon absorption measurements.

fluorescence is collected at right angle to the excitation beam to avoid the excitation beam finding its way into the photomultiplier tube (PMT). A monochromator is used to select the fluorescence wavelength of interest which is then detected by a photomultiplier tube (R152P, Hamamatsu, Hamamatsu City, Japan) connected to a computer via a photo-counting unit.

The TPA cross-section were calculated by the fluorescence method by using well-known two-photon active standards such as Coumarin 307 and Rhodamine B.[19] Input power from the laser was varied using a variable neutral density filter. Two-photon power-dependent fluorescence intensity was utilized to determine the two-photon absorption cross section through the TPEF method described in **Equation 2.3.1**.

$$F(t) = \frac{1}{2}\eta\delta[c]n \cdot \frac{g_p}{\pi\lambda f\tau}\phi\left\langle P(t)\right\rangle^2 \qquad \textbf{Equation 2.3.1}$$

In **Equation 2.3.1**, the *F(t)* is the emissive photons collected per second, η **i**s the quantum yield of the material, δ **i**s the TPA cross-section of the sample, *[c]* is the concentration, *n* is the refractive

index of the solvent, g_p is the shape factor of the pulsed laser (0.66 for Gaussian shape), f is the frequency of the laser, λ is the excitation wavelength, τ is the pulse durations, ϕ is the collection efficiency, and $\langle P(t) \rangle$ is the input intensity. Some of the parameters that dictate **Equation 2.3.1** are associated with the laser, therefore, can be assumed to be constant between measurements if the excitation wavelength remains the same. Consequently, it is possible to establish a comparative method between a well-known standard and the inquired sample by knowing the standards quantum yields, the concentrations, and the refractive index of the solvents in where the measurements are conducted. By taking the logarithm of **Equation 2.3.1**, it is possible to express the equation as a linear regression (y = mx + b) as given in **Equation 2.3.2**.

$$\log(F(t)) = 2\log < P(t) > + \log(\frac{1}{2}\eta\delta[c]n \cdot \frac{g_p}{\pi\lambda f\tau}\phi) \qquad \textbf{Equation 2.3.2}$$

In **Equation 2.3.2**, the logarithmic approach of the data sets of the fluorescence intensity and the power dependence of the incident excitation source to have a quadratic response (slope of 2), which corroborate the two-photon activity of the investigated system. For logarithmic plots of fluorescence intensity versus the input power for both the sample and the standard having slopes of 2, **Equation 2.3.2** will hold for the same input power for both the sample and the standard as it can be observed in **Equation 2.3.3.**

$$\log[F(t)_{sample}] - b_{sample} = \log[F(t)_{std}] - b_{std} \qquad \textbf{Equation 2.3.3}$$

In **Equation 2.3.3**, b represents the intercept on the vertical axis but is defined as observed in **Equation 2.3.4**. Further manipulation of **Equation 2.3.4** will result in an exponential relationship

between the fluorescence intensity of the compared chromophores and their respective intercept, as it can be observed in **Equation 2.3.5**

$$b = \log\left[\frac{1}{2}\eta\delta[c]n \cdot \frac{g_p}{\pi\lambda f\tau}\phi\right] \qquad \textbf{Equation 2.3.4}$$

$$\frac{F(t)_{sample}}{F(t)_{std}} = 10^{(b_{sample} - b_{std})} \qquad \textbf{Equation 2.3.5}$$

If the logarithmic of input power for both investigated samples are assumed to be zero, **Equation 2.3.1** simplifies, and **Equation 2.3.5** turns into **Equation 2.3.6**. As mentioned before, the laser parameters are independent of the sample and therefore they cancel out in **Equation 2.3.7**.

$$\frac{\frac{1}{2}\eta_{sample}\delta_{sample}[c]_{sample}n_{sample} \cdot \frac{g_p}{\pi\lambda f\tau}\phi}{\frac{1}{2}\eta_{std}\delta_{std}[c]_{std}n_{std} \cdot \frac{g_p}{\pi\lambda f\tau}\phi} = 10^{(b_{sample} - b_{std})} \qquad \textbf{Equation 2.3.6}$$

$$\delta_{sample} = \frac{10^{(b_{sample} - b_{std})} \cdot \eta_{std}\delta_{std}[c]_{std}n_{std}}{\eta_{sample}[c]_{sample}n_{sample}} \qquad \textbf{Equation 2.3.7}$$

With **Equation 2.3.7**, the TPA cross section of an inquired material can be investigated via a comparative method that relies in the quantum yield of the systems (η), the cross-section of the standard (δ_{STD}), the concentration [c] of the samples, the slope (b) obtained from the Keithley plot (Log (power) vs log (Counts)), and the refractive index of the solvents (n).

2.4 Time-Resolved Fluorescence Up-Conversion (UpC)

The time-resolved fluorescence up-conversion (UpC) technique is a well-known approach used to characterize the emissive lifetime of chromophores from hundreds of femtoseconds to

hundreds of picosecond.[15] This technique can also help to investigate energy transfer process using fluorescence as the analytical signal.[20] To understand how the time-resolved fluorescence emission is detected, we need to understand the instrumentation that build the UpC setup. The UpC setup comprises two lasers, the Spectra Physics Millennia and Spectra Physics Tsunami lasers systems. The Spectra Physics Millennia laser is powered by a continuous wave laser diode, which can deliver up to 5 W CW power at 532 nm. This laser has a gain medium of neodymium-doped yttrium vanadate (Nd:YVO_4), and the 532 nm CW is generated through frequency doubling by the nonlinear optics in the Millennia laser. This beam serves as input to the Spectra Physics Tsunami, which has a Ti-Sapphire gain medium.

The Tsunami laser is capable of generating < 80 fs pulses at wavelengths between 780 and 820 nm at a repetition rate of 82 MHz. The output of this laser has a power that fluctuates between 680-720 mW at optimal performance. The sub 80 fs pulsed photons are generated through a process called mode-locking, which is a technique in optics used to generate pulses of sub picosecond durations.[21] The optimal operating wavelength of the Tsunami laser is 800 nm, and was the excitation wavelength used for the measurements enclosed in this dissertation. The 800 nm beam is passed through a series of focusing elements on to a second harmonic generation made of β–barium borate (BBO) crystal to convert part of the 800 nm fundamental beam into a 400 nm beam.[22] A dichronic mirror splits the fundamental beam and the 400 nm beam. The residual fundamental 800 nm beam that pass through the dichroic mirror goes into an optical delay line with step size of 6.25 fs. The 400 nm beam is reflected towards the sample by the dichroic mirror. A berek compensator is used to control the polarization of the beam so that the beam exciting the sample is plane-polarized (parallel). The sample is placed in a 1 mm cuvette that rotates to eliminate and minimize the potential photo-degradation and damage of the sample. The

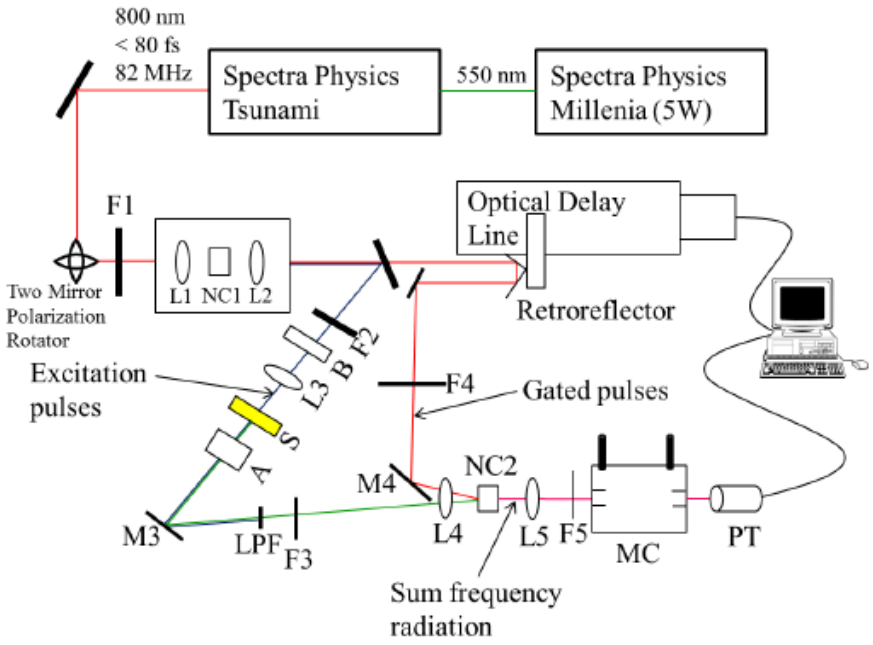

Figure 2.4.1. Fluorescence up-conversion set up diagram.

fluorescence from the sample is collected by an achromat and directed through several focusing elements and mirrors into a nonlinear sum-frequency generator crystal made of β–barium borate, where it is recombined with the fundamental beam gate pulse. The fundamental beam gate pulse and the fluorescence must overlap in space and time for maximum and efficient fluorescence up-conversion detection.[23]

The overlapping arrangement of the fluorescence beam and the gate pulse is optimized to be collinear between them by focusing elements and subtle mirror alignments in the upconversion set up. The sum frequency beam generated from the combination of the fluorescence beam and the gate pulse fundamental beam is usually in the wavelength range of 300-400 nm. The gate pulse has a step size of 6.25 fs; therefore, the sum-frequency generation intensity will be dependent on the steps (each step 6.25 fs) that the detection is taken. As a result, intensity in function of steps is obtained. The sum frequency beam pass through focusing lens and is directed into the

monochromator, which picks out the desired wavelength from the up-converted beam and then send it into the photomultiplier tube (R152P, Hamamatsu, Hamamatsu City, Japan) for detection. The excitation beam used for the study varied between 20 mW and 30 mW. Standard dyes of Coumarin 30, and cresyl violet were used in the process of alignment of the laser systems. The choice of which standard to use for alignments depends on the operating fluorescence wavelength. The absorption spectrum of the sample is measured before and after conducting the experiments to confirm that there is no photo-degradation in the course of the fluorescence measurement, especially for long experimental scans. In cases where photo-stability is a concern, fresh samples are used for each experimental run. The fluorescence lifetimes characterization of the investigated systems is obtained by fitting the experimentally determined fluorescence decay curve to the best exponential function fit using the fitting function in Origin 8. If needed, more rigorous deconvolution fitting procedure in an in-house developed program on the platform of MATLAB is used for extremely small fluorescence lifetimes in the order of femtosecond.

2.5 Time Correlated Single Photon Counting (TCSPC)

Our time-correlated single photon counting (TCSPC) technique is a common method to characterize the time-resolved emission of materials. This setup used for this dissertation is able to characterize the emissive lifetime of chromophores from the nanosecond to the microsecond timescale. The TCSPC sample excitation approach is like the one for the UpC technique in terms of how a second harmonic generator is needed to convert 800 nm to 400 nm. The TCSPC setup consists of a Kapteyn Murnane (KM) Laboratories Ti-sapphire femtosecond laser pumped by a Millenia V Nd:YVO_4 (Spectra Physics). The pump beam is a 4W continuous green light at 532 nm, but its power is adapted to optimize the mode-lock procedure. The output from the KM laser is capable of being tuned between 780 to 830 nm. For the experiment conducted in this study, the

output from the KM laser was set at 800 nm wavelength with pulse duration of ~ 30 fs and a repetition rate of 90 MHz. As with the UpC technique, the fundamental beam from the KM laser was frequency-doubled through the second harmonic generation by using a β-barium borate crystal to obtain a 400 nm pulsed beam. However, the rest of the 800 nm bean is not used in this experimental technique. In addition, the time-resolved emission collection is very different.

The time-resolved emission measurement using the TCSPC setup is unique because of the method of collection of the fluorescence beams. The principle of TCSPC is creating a histogram by detecting and resolving for the arrival time of single photons in respect to a triggering signal, which is usually the excitation source. Therefore, the TCSPC requires a high repetitive light source to accumulate a enough photonic events for the creation of the high precision histogram. After the chromophore is excited, the emissive signal is passed through a constant function discriminator (CFD), which accurately correlate the arrival time of the beam with the triggering signal. Then, the emissive signal is passed to a time-to-amplitude converter (TAC) which converts the signal to a voltage ramp. The voltage ramp continues to increase until the emission pulse arrives at the detector and stops the ramp-up process. Therefore, this technique is considered an electrical technique. The voltage signal is amplified (by a programmable gain amplifier) and converted to a numerical value by an analog-to-digital converter (ADC), thanks to the bin numerical value which depends on the time delay between the excitation beam and the emission.

The time-resolved emission of the chromophores is collected perpendicular to the excitation source to avoid electrical interference. A monochromator is placed in front of the photomultiplier (PMT) to filter any potential external photon that can be converted into signal. The PMT detect the signal and send it to the computer through an interface card, namely TimeHarp200. The computer displays the created histogram using PicoQuant, a specialized software. The IRF is

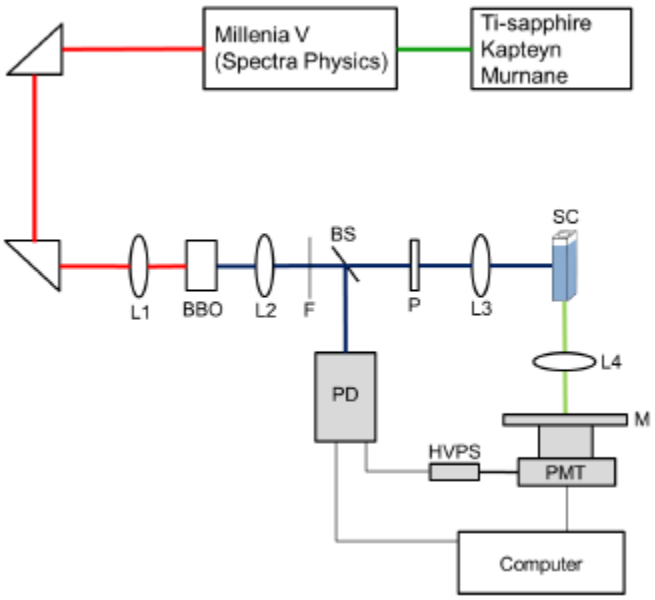

Figure 2.5.1. Time-correlated single photon counting (TCSPC) setup. L1-4 corresponds to focusing lenses.

measured using the Rayleigh scattering of a scattering medium and is used on the decay function in order to verify the significance of the decay process. The IRF has a full width at half maximum (FWHM) of 330 ps. The experimental fitting process is carried out in Origin 8, using the best mono/multi-exponential decay fitting. To ensure that the sample is stable in the course of the fluorescence measurements, the absorbance of the sample is measured before and after each measurement. The TCSPC set-up is shown in **Figure 2.5.1**.

2.6 Transient Absorption Spectroscopy (TAS)

Transient absorption spectroscopy (TAS) is arguably one of the most powerful time-resolved spectroscopic techniques. It offers you the opportunity to characterize the photoinduced emissive and non-emissive excited state electronic transitions of materials.[24–26] It also can be utilize to elucidate electron transfer reactions, chemical species involved in transitions, vibrational cooling, bleach recovery, and singlet to triplet conversion.[27,28] For this dissertation, two different

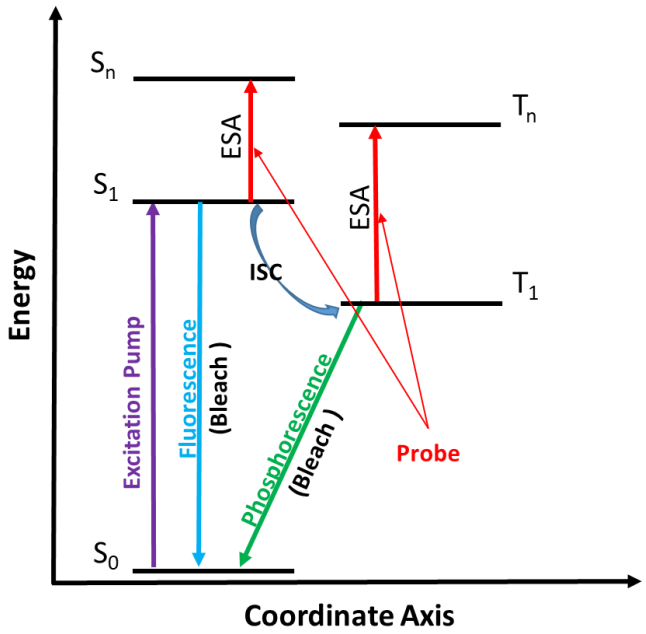

Figure 2.6.1. Diagram for the occurring excited state transition that the TAS can probe.

setups were used. One with resolution from femtosecond to nanosecond timescales (fs TAS) and the other with resolution from the nanosecond to the millisecond timescales (ns TAS).

The transient absorption is a pump-probe set-up. That means that a fundamental beam, the pump, oversees exciting the chromophores to the excited state, while the probe beam (usually white light) is used to characterize the molecule while it is at its excited state. In this way, we create multiple absorption snapshots of the investigated system while is in its excited state. These absorption snapshots are compared to the initial absorption snapshot measurements of the probe, which is analog to the system steady state absorption spectrum. As a result, the TAS technique produces a spectrum of the change in absorption ΔA in function of wavelengths. The electronic transition relating the chromophores steady-state properties, such as absorption and emission (including stimulated emission), will be detected as a $-\Delta A$ bands, while the transient intermediates states will be detected as a $+\Delta A$ bands. In **Figure 2.6.1**, a schematic representation of the transient absorption process can be observed. The pump excites the inquired sample from the ground state

(S_0) to the excited state (S_n). From the S_n, the molecule can dissipate its energy via multiple non-emissive process such as such as: internal conversion ($S_n \rightarrow S_1 \rightarrow S_0$), intersystem crossing ($S_1 \rightarrow T_1$), 3), and internal conversion from the triplet ($T_1 \rightarrow S_1$). As mentioned before, other processes of energy dissipation may occur, and its excited state characterization depends on the time resolution capabilities of the systems.

The fs TAS setups uses a diode pumped neodymium-doped yttrium vanadate (Nd:YVO_4) Millennia (Spectra Physics) CW laser to generate a 532 nm beam of up to 4.2W of power. This CW laser pumps a Ti-Sapphire Tsunami (Spectra Physics) which produces laser pulses of 20 fs between 790 to 810 nm of up to 300 mW with a repetition rate of 100 MHz. The Ti-sapphire pumped by the CW laser generates the ultrafast pulses through a technique called passive mode-locking, which produced an 800 nm fundamental beam used for the experiments in this dissertation. The pulse energy of the seed beam is a few *nJ*. These pulses are amplified inside a regenerative amplifier (Spitfire Pro, Spectra Physics) in three stages. The first stage stretches the seed pulse. A retro-reflecting mirror assembly slows the shorter end (blue) of the spectral pulse relative to the longer part of the spectral pulse (red), which results in a negative Group Velocity Dispersion (GVD) stretching the pulse temporally. Then the temporally stretched pulse is regenerative amplified. A Ti:Sapphire crystal is pumped by a 532 nm Nd: YLF laser (Empower, Spectra Physics) at power > 7.5W to cause a population inversion of the gain medium. The stretched seed pulse then is injected into resonator via a Pockels cell. After a single pass through the crystal, the pulse energy of the seed is amplified by a factor in the 3 to 4 range. But in order to get enough gain for the stretched pulse, the pulse is oscillated through the gain to elevate the pulse energy level until they are high enough to eliminate the population inversion of the gain medium. Another Pockels cell allows the amplified stretched pulse to exit the resonator. The pulse

compression constituted the final step inside the amplifier. A retro-reflecting mirror assembly slows the long end (red) of the spectral pulse relative to the shorter part of the spectral pulse (blue), which compress the pulse back into a 130-fs pulse. The resulting output from the amplifier is a red beam (800nm) with properties of 1 kHz and ~100 fs pulse width, with an average power of 1 W and a pulse energy on the order of μJ.

A beam splitter splits the resulting output from the amplifier with a 20% of the pulse directed into the Helios box (for white beam probe generation), while 80% of the beam is directed into the Optical Parametric Amplifier (OPA) for pump generation. The OPA uses multiple sum-frequency generation crystal and processes to modulate frequency and achieve a spectral range from 350 nm to 2000 nm. The white light in the Helios box is generated by a Ti:Sapphire plate and is focused onto the main BBO Crystal (BBO_1). The optical parametric generation (OPG) is coupled to amplify the specific wavelengths of the white light inside BBO_1. The preamp beam passes through a delay stage before arriving at BBO_1, which eventually will modulate the time gap between the pump and probe. The preamp beam is spatial and temporally overlapping the white light on BBO_1 and will result in having a signal and idler beam. The signal is removed using dichroic mirrors and the idler beam is aligned to be collinear in space and time with remaining 85% of the fundamental red beam. The idler beam is then passed through BBO_2 and BBO_3, where a spectral range of 300 nm to 2000 nm could be generated as will by controlling the angles of the BBOs.

The Helios box uses the output beam from the amplifier and directed into the optical delay line. The pulse is focused onto a Ti:Sapphire plate after the delay line to generate the probe (440 nm to 750 nm). The white light is then aligned to be collinear in space with the pump in a cuvette with the inquired sample, but the time in where it overlaps with the pump is controlled with a

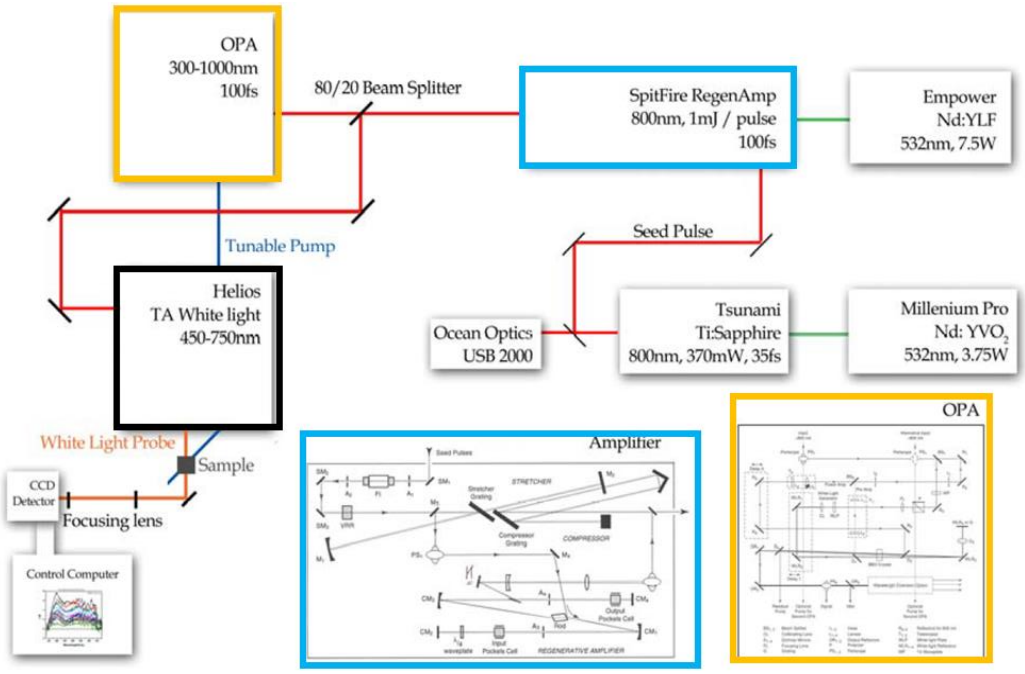

Figure 2.6.2. Ultrafast fs transient absorption diagram.

delayed line. The cuvette is a made of quartz and have dimension of 1 cm x 0.2xm. A CCD detector (Ocean optics 2000) collects the change in absorption of the probe beam. The software from Ultrafast Systems Inc oversees collecting the data. The typical operational powers are ~ 10 Jcm^{-1} and 1000 Jcm^{-1} for the probe beam and pump beam, respectively. A magic angle polarization is maintained between the pump and probe beam using a wave-plate. In this way, potential anisotropy contributions due to polarization will be avoided. The sample is stirred with a rotating magnetic stirrer to prevent degradation. In addition, the absorption spectra are measured before and after carrying out the experiments to prevent degradation of the sample.

For the ns transient absorption set-up, A LP980 (Edinburgh) system, which contains the photomultiplier (PMT-LP), was coupled with a Spectra-Physics QuantaRay Nd:YAG nanosecond (*ns*) pulsed laser and a GWU Optical Parametric Oscillator (OPO) tunable from 250 nm to 2600 nm for the excitation source. The probe source comes from a xenon lamp within the/ The 150 W

ozone-free, xenon arc lamp produces 6 ms pulses of a continuous spectrum from 190 nm to 2000 nm. The probe pulse excites the sample perpendicular to the laser excitation which maximizes the change in absorption while minimizing scattering and fluorescence. As with the fs TAS, the excited state probing only when the pump and probe are overlapping among them. After passing through the sample at a right angle to the excitation beam, the light is directed to a monochromator. Eventually, the selected wavelength will be measured by a PMT (Hamamatsu R928) with a spectral range from 185 to 870 nm. Other detectors may be adapted to take advantage of the long-range probe lamp. The transmission response of the sample before, during, and after the excitation pulse is converted by the PMT into electrical signals that are measured by a TDS3052B Model oscilloscope, while the Edinburgh supplied software converts the electrical signal into change of optical density. The kinetic analysis was conducted in Origin 8.

2.7 Quantum Chemical Simulations (QCS)

Correlating experimental and theoretical results have been proven to be a powerful technique for the elucidation of the electronic properties of materials. In addition, carrying out quantum chemical simulations (QCS) are rapidly becoming more popular for solving more complex due to advantages such as computer memory, speed, multiprocessing, threading, and recent improvements in computer theory.[29] We used multiple computational methods to investigate electronic properties such as molecular orbital distribution, energy levels, excited state structures and their electronic transitions, and dipole moments.

For the light harvesting polymers, the ground state geometry of each monomer was obtained by computations using density functional theory (DFT). The ωB97X-D functional basis sets are employed. The ground state calculations were conducted using Q-Chem 4.0. Excited state simulations using time-dependent DFT (TD-DFT) were performed to analyze the trend of lifetime.

The same functional used in the ground state calculations and smaller basis sets, 3-21G*, were employed for the geometry optimization of the first singlet excited state (S_1) in the gas phase. Single-point energy calculations to evaluate the electronic property (Fluorescence emission energy and corresponding transition dipole moment) were performed using 6-31G* basis sets, and the medium effect is included using polarizable continuum. The dielectric constant of dichloromethane is 8.91. All excited state calculations were conducted using Q-Chem 4.0.

For the chromophores with thermally activated delayed fluorescence (TADF) characteristics, the ground state (S_0) geometries were optimized using density functional theory (DFT). The B3LYP functional, which has successfully predicted the ΔE_{ST} of a variety of TADF materials, was used along with the 6-31G* basis set.[30] The first excited singlet state (S_1) geometry of BCC-TPTA was obtained with a restricted open-shell Kohn-Sham (ROKS) approach and 6-31G* basis sets. ROKS is known to improve the deficiency of semilocal linear response time-dependent DFT (LR−TD−DFT) and offers a good alternative for investigating charge transfer states.[31–35] The first triplet (T_1) geometry was predicted with spin unrestricted DFT. Single point energy calculations to evaluate the fluorescence emission energies, spin−orbit coupling elements, and adiabatic energy gap ($\Delta E_{ST} = E_{\text{TDDFT } S1 \text{ at min } S1} - E_{\text{UDFT } T1 \text{ at min } T1}$) were conducted, and the solvent environment effect is treated using a polarizable continuum model. The dielectric constant of chloroform of. All quantum chemical calculations were performed using Q−Chem 5.0.[29] The rate constant of ISC and rISC, were estimated via Fermi's Golden rule, as described in **Equation 2.7.1**[36,37]

$$k_{\text{ISC}} = \frac{2\pi}{\hbar}\rho_{\text{FC}}|\langle S_1|H_{SO}|T_1\rangle|^2 \qquad \textbf{Equation 2.7.1}$$

where $\langle S_1|H_{SO}|T_1\rangle$ is the spin−orbit coupling element between S_1 and T_1, ρ_{FC} denotes the Franck−Condon weighted density of states, and $\hbar$ is the reduced Planck constant of 6.582×10^{-16} eVs. ρ_{FC} is evaluated with Marcus−Levich−Jortner theory, as described in **Equation 2.7.2** [38,39]

$$\rho_{FC} = \frac{1}{\sqrt{4\pi\lambda_M k_B T}} \sum_{n=0}^{\infty} \exp(-S) \frac{S^n}{n!} \exp\left[-\frac{(\Delta E_{ST} + n\hbar\omega_{eff} + \lambda_M)^2}{4\pi\lambda_M k_B T}\right] \quad \textbf{Equation 2.7.2}$$

where λ_M is the Marcus reorganization energy associated with the intermolecular and intramolecular low−frequency vibrations, k_B is for Boltzmann constant of 8.6173×10^{-5} eV/K, T is the temperature (in this study, 298.15 K), $\hbar\omega_{eff}$ represents the effective energy of a mode representing the non-classical high−frequency intramolecular vibrations. Huang−Rhys factor associated with these modes are given as *S*. The rate constant of the rISC process was described by parameters generated at the T_1 geometry, and the k_{ISC} estimation with parameters relevant to the S_1 geometry.

One recent computational study on TADF mechanism discussed the rate of rISC within the same framework used in this work.[40] They computed the contribution of non-classical intramolecular vibrations and estimated the Marcus reorganization energy due to low frequency intramolecular vibrations and the medium-induced relaxation effects to be in the range of ~0.1-0.2 eV.[39–41] Also, they assumed the Huang-Rhys factors can be neglected without significant changes to the results for large molecules. The approximation setting λ_M to 0.1 or 0.2 eV reproduced available experimental k_{RISC} values on the same order of magnitude. The close examination revealed that use λ_M value of 0.2 eV gave better quantitative agreement with the available experimental k_{RISC} dta. Therefore, λ_M value is set to 0.2 eV in this study.

The fluorescence emission rate (k_F) was approximated by the product of the oscillator strength and the square of the wavenumber.[42] The observed k_F values of anthraquinone-based intramolecular charge transfer compounds, one class of TADF materials reported by the Adachi group, could be reproduced with this simple calculation.[42]

References

(1) Kuhn, H. A Quantum-Mechanical Theory of Light Absorption of Organic Dyes and Similar Compounds. *J. Chem. Phys.* **1949**, *17* (12), 1198–1212. https://doi.org/10.1063/1.1747143.

(2) Swinehart, D. F. The Beer-Lambert Law. *J. Chem. Educ.* **1962**, *39* (7), 333. https://doi.org/10.1021/ed039p333.

(3) Strickler, S. J.; Berg, R. A. Relationship between Absorption Intensity and Fluorescence Lifetime of Molecules. *J. Chem. Phys.* **1962**, *37* (4), 814–822. https://doi.org/10.1063/1.1733166.

(4) Shalhoub, G. M. Visible Spectra Conjugated Dyes: Integrating Quantum Chemical Concepts with Experimental Data. *J. Chem. Educ.* **1997**, *74* (11), 1317. https://doi.org/10.1021/ed074p1317.

(5) Lee, Y.; Jo, A.; Park, S. B. Rational Improvement of Molar Absorptivity Guided by Oscillator Strength: A Case Study with Furoindolizine-Based Core Skeleton. *Angew. Chemie - Int. Ed.* **2015**, *54* (52), 15689–15693. https://doi.org/10.1002/anie.201506429.

(6) Weber, G.; Teale, F. W. J. *Determination of the Absolute Quantum Yield of Fluorescent Solutions*; 1957; Vol. 53. https://doi.org/10.1039/tf9575300646.

(7) Hedley, G. J.; Ruseckas, A.; Samuel, I. D. W. Light Harvesting for Organic Photovoltaics. *Chem. Rev.* **2017**, *117* (2), 796–837. https://doi.org/10.1021/acs.chemrev.6b00215.

(8) Ware, W. R.; Baldwin, B. A. Absorption Intensity and Fluorescence Lifetimes of Molecules. *J. Chem. Phys.* **1964**, *40* (6), 1703–1705. https://doi.org/10.1063/1.1725384.

(9) Albani, J. R. *Principles and Applications of Fluorescence Spectroscopy*; Blackwell Publishing Ltd: Oxford, UK, 2008. https://doi.org/10.1002/9780470692059.

(10) Resch-Genger, U.; Rurack, K. Determination of the Photoluminescence Quantum Yield of Dilute Dye Solutions (IUPAC Technical Report). *Pure Appl. Chem.* **2013**, *85* (10), 2005–2013. https://doi.org/10.1351/pac-rep-12-03-03.

(11) Birks, J. B. Fluorescence Quantum Yield Measurements. *J. Res. Natl. Bur. Stand. Sect. A Phys. Chem.* **2012**, *80A* (3), 389. https://doi.org/10.6028/jres.080a.038.

(12) Karstens, T.; Kobs, K. Rhodamine B and Rhodamine 101 as Reference Substances for Fluorescence Quantum Yield Measurements. **2002**.

(13) Adegoke, O. O.; Ince, M.; Mishra, A.; Green, A.; Varnavski, O.; Martínez-Díaz, M. V.; Bäuerle, P.; Torres, T.; Goodson, T. Synthesis and Ultrafast Time Resolved Spectroscopy of Peripherally Functionalized Zinc Phthalocyanine Bearing Oligothienylene-Ethynylene Subunits. *J. Phys. Chem. C* **2013**, *117* (40), 20912–20918. https://doi.org/10.1021/jp404406b.

(14) Doan, P. H.; Pitter, D. R. G.; Kocher, A.; Wilson, J. N.; Goodson, T. Two-Photon Spectroscopy as a New Sensitive Method for Determining the DNA Binding Mode of Fluorescent Nuclear Dyes. *J. Am. Chem. Soc.* **2015**, *137* (29), 9198–9201. https://doi.org/10.1021/jacs.5b02674.

(15) Guo, M.; Varnavski, O.; Narayanan, A.; Mongin, O.; Majoral, J.-P.; Blanchard-Desce, M.; Theodore Goodson, I. Investigations of Energy Migration in an Organic Dendrimer Macromolecule for Sensory Signal Amplification†. **2009**.

(16) Ramakrishna, G.; Bhaskar, A.; Goodson, T. Ultrafast Excited State Relaxation Dynamics of Branched Donor-Pi-Acceptor Chromophore: Evidence of a Charge-Delocalized State. *J. Phys. Chem. B* **2006**, *110* (42), 20872–20878. https://doi.org/10.1021/jp063262h.

(17) Kaiser, W.; Garrett, C. G. B. Two-Photon Excitation in CaF2:Eu2+. *Phys. Rev. Lett.* **1961**, *7* (6), 229–231. https://doi.org/10.1103/PhysRevLett.7.229.

(18) Chemla, D. S. *Nonlinear Optical Properties of Organic Molecules and Crystals*; Elsevier Science, 2016. https://doi.org/10.1016/b978-0-12-170612-8.x5001-9.

(19) Xu, C.; Webb, W. W. Measurement of Two-Photon Excitation Cross Sections of Molecular Fluorophores with Data from 690 to 1050 Nm. *J. Opt. Soc. Am. B* **1996**, *13* (3), 481. https://doi.org/10.1364/JOSAB.13.000481.

(20) Taylor, E. L.; Metcalf, K. J.; Carlotti, B.; Lai, C. T.; Modica, J. A.; Schatz, G. C.; Mrksich, M.; Goodson, T. Long-Range Energy Transfer in Protein Megamolecules. *J. Am. Chem. Soc.* **2018**, *140* (46), 15731–15743. https://doi.org/10.1021/jacs.8b08208.

(21) Ramakrishna, G.; Varnavski, O.; Kim, J.; Lee, D.; Goodson, T. Quantum-Sized Gold Clusters as Efficient Two-Photon Absorbers. **2008**.

(22) Keller, B.; Cai, Z.; Muthike, A. K.; Sahu, P. K.; Kim, H.; Eshun, A.; Zimmerman, P. M.; Zhang, D.; Goodson, T. Investigating the Optical Properties of Thiophene Additions to S-Indacene Donors with Diketopyrrolopyrrole, Isoindigo, and Thienothiophene Acceptors. *J. Phys. Chem. C* **2018**, *122* (48), 27713–27733. https://doi.org/10.1021/acs.jpcc.8b08567.

(23) Zhao, L.; Lustres, J. L. P.; Farztdinov, V.; Ernsting, N. P. Femtosecond Fluorescence Spectroscopy by Upconversion with Tilted Gate Pulses. *Phys. Chem. Chem. Phys.* **2005**, *7* (8), 1716–1725. https://doi.org/10.1039/b500108k.

(24) Gustavsson, T.; Coto, P. B.; Serrano-Andŕs, L.; Fujiwara, T.; Lim, E. C. Do Fluorescence and Transient Absorption Probe the Same Intramolecular Charge Transfer State of 4-(Dimethylamino)Benzonitrile? *J. Chem. Phys.* **2009**, *131* (3), 31101. https://doi.org/10.1063/1.3173609.

(25) Kim, D.; Holten, D.; Gouterman, M. Evidence from Picosecond Transient Absorption and Kinetic Studies of Charge-Transfer States in Copper(II) Porphyrins. *J. Am. Chem. Soc.* **1984**, *106* (10), 2793–2798. https://doi.org/10.1021/ja00322a012.

(26) Varnavski, O.; Goodson, T.; Sukhomlinova, L.; Twieg, R. Ultrafast Exciton Dynamics in a Branched Molecule Investigated by Time-Resolved Fluorescence, Transient Absorption, and Three-Pulse Photon Echo Peak Shift Measurements. *J. Phys. Chem. B* **2004**, *108* (29), 10484–10492. https://doi.org/10.1021/jp0495996.

(27) Fron, E.; Pilot, R.; Schweitzer, G.; Qu, J.; Herrmann, A.; Müllen, K.; Hofkens, J.; Van Der Auweraer, M.; De Schryver, F. C. Photoinduced Electron-Transfer in Perylenediimide Triphenylamine-Based Dendrimers: Single Photon Timing and Femtosecond Transient Absorption Spectroscopy. *Photochem. Photobiol. Sci.* **2008**, *7* (5), 597–604. https://doi.org/10.1039/b718479d.

(28) Berera, R.; van Grondelle, R.; Kennis, J. T. M. Ultrafast Transient Absorption Spectroscopy: Principles and Application to Photosynthetic Systems. *Photosynth. Res.* **2009**, *101* (2–3), 105–118. https://doi.org/10.1007/s11120-009-9454-y.

(29) Shao, Y.; Gan, Z.; Epifanovsky, E.; Gilbert, A. T. B.; Wormit, M.; Kussmann, J.; Lange, A. W.; Behn, A.; Deng, J.; Feng, X.; et al. Advances in Molecular Quantum Chemistry Contained in the Q-Chem 4 Program Package. *Mol. Phys.* **2015**, *113* (2), 184–215. https://doi.org/10.1080/00268976.2014.952696.

(30) Hirata, S.; Sakai, Y.; Masui, K.; Tanaka, H.; Lee, S. Y.; Nomura, H.; Nakamura, N.; Yasumatsu, M.; Nakanotani, H.; Zhang, Q.; et al. Highly Efficient Blue Electroluminescence Based on Thermally Activated Delayed Fluorescence. *Nat. Mater.* **2015**, *14* (3), 330–336. https://doi.org/10.1038/nmat4154.

(31) Kowalczyk, T.; Tsuchimochi, T.; Chen, P. T.; Top, L.; Van Voorhis, T. Excitation Energies and Stokes Shifts from a Restricted Open-Shell Kohn-Sham Approach. *J. Chem. Phys.* **2013**, *138* (16), 164101. https://doi.org/10.1063/1.4801790.

(32) Hait, D.; Zhu, T.; McMahon, D. P.; Van Voorhis, T. Prediction of Excited-State Energies and Singlet-Triplet Gaps of Charge-Transfer States Using a Restricted Open-Shell Kohn-Sham Approach. *J. Chem. Theory Comput.* **2016**, *12* (7), 3353–3359. https://doi.org/10.1021/acs.jctc.6b00426.

(33) Frank, I.; Hutter, J.; Marx, D.; Parrinello, M. Molecular Dynamics in Low-Spin Excited States. *J. Chem. Phys.* **1998**, *108* (10), 4060–4069. https://doi.org/10.1063/1.475804.

(34) Okazaki, I.; Sato, F.; Yoshihiro, T.; Ueno, T.; Kashiwagi, H. Development of a Restricted Open Shell Kohn-Sham Program and Its Application to a Model Heme Complex. *J. Mol. Struct. THEOCHEM* **1998**, *451* (1–2), 109–119. https://doi.org/10.1016/S0166-1280(98)00164-X.

(35) Filatov, M.; Shaik, S. A Spin-Restricted Ensemble-Referenced Kohn–Sham Method and Its Application to Diradicaloid Situations. *Chem. Phys. Lett.* **1999**, *304* (5–6), 429–437. https://doi.org/10.1016/S0009-2614(99)00336-X.

(36) Robinson, G. W.; Frosch, R. P. Electronic Excitation Transfer and Relaxation. *J. Chem. Phys.* **1963**, *38* (5), 1187–1203. https://doi.org/10.1063/1.1733823.

(37) Lawetz, V.; Orlandi, G.; Siebrand, W. Theory of Intersystem Crossing in Aromatic Hydrocarbons. *J. Chem. Phys.* **1972**, *56* (8), 4058–4072. https://doi.org/10.1063/1.1677816.

(38) Brédas, J. L.; Beljonne, D.; Coropceanu, V.; Cornil, J. Charge-Transfer and Energy-Transfer Processes in π-Conjugated Oligomers and Polymers: A Molecular Picture. *Chem. Rev.* **2004**, *104* (11), 4971–5003. https://doi.org/10.1021/cr040084k.

(39) Schmidt, K.; Brovelli, S.; Coropceanu, V.; Beljonne, D.; Cornil, J.; Bazzini, C.; Caronna, T.; Tubino, R.; Meinardi, F.; Shuai, Z.; et al. Intersystem Crossing Processes in Nonplanar Aromatic Heterocyclic Molecules. *J. Phys. Chem. A* **2007**, *111* (42), 10490–10499. https://doi.org/10.1021/jp075248q.

(40) Samanta, P. K.; Kim, D.; Coropceanu, V.; Brédas, J. L. Up-Conversion Intersystem Crossing Rates in Organic Emitters for Thermally Activated Delayed Fluorescence: Impact of the Nature of Singlet vs Triplet Excited States. *J. Am. Chem. Soc.* **2017**, *139* (11), 4042–4051. https://doi.org/10.1021/jacs.6b12124.

(41) Beljonne, D.; Shuai, Z.; Pourtois, G.; Bredas, J. L. Spin-Orbit Coupling and Intersystem Crossing in Conjugated Polymers: A Configuration Interaction Description. *J. Phys. Chem. A* **2001**, *105* (15), 3899–3907. https://doi.org/10.1021/jp010187w.

(42) Zhang, Q.; Kuwabara, H.; Potscavage, W. J.; Huang, S.; Hatae, Y.; Shibata, T.; Adachi, C. Anthraquinone-Based Intramolecular Charge-Transfer Compounds: Computational Molecular Design, Thermally Activated Delayed Fluorescence, and Highly Efficient Red Electroluminescence. *J. Am. Chem. Soc.* **2014**, *136* (52), 18070–18081. https://doi.org/10.1021/ja510144h.

Chapter 3

Using ultra-fast spectroscopy to probe the excited state dynamics of a reported highly efficient thermally activated delayed fluorescence chromophore

3.1 Original Publication Information

The work in this chapter was accepted by *The Journal of Material Chemistry C (JMC C)* with the title:

"Using ultra-fast spectroscopy to probe the excited state dynamics of a reported highly efficient thermally activated delayed fluorescence chromophore" Ricardo Javier Vazquez, Hyungjun Kim, Paul M. Zimmerman, and Theodore Goodson III. *J. Mater. Chem. C,* **2019**,***7***, 4210-4221

Modifications were conducted to the manuscript to adapt it to the style of the content of this dissertation. References and supporting information of the manuscript are included in this chapter.

3.2 Abstract

Multiple ultrafast spectroscopic techniques and quantum chemical simulations (QCS) were used to investigate the excited state dynamics of BCC-TPTA. This organic chromophore is believed to possess excited state dynamics governed by a thermally activated delayed fluorescence (TADF) mechanism with a reported internal quantum efficiency (η_{IQE}) of 84 %. In addition, a significant enhancement in its quantum yield ($\boldsymbol{\Phi}$) in solution after purging oxygen has been reported. This $\boldsymbol{\Phi}$ enhancement has been widely accepted as due to a delayed fluorescence process occurring in the *μs* time-scale. The spectroscopic measurements were carried out both in solution and blended films, and from *fs* to *μs* time-scales. The excited state dynamics of Rhodamine B and $Ir(BT)_2(acac)$ were also probed for comparison. Investigations in the absence of oxygen were also carried out. Our time-correlated single photon counting (TCSPC) measurements revealed a lack of long-lived emissive lifetime for BCC-TPTA in any of the medium tested. Our *ns* transient absorption spectroscopy (*ns* TAS) experiments revealed that BCC-TPTA does not possess triplet transient states that could be linked to a delayed fluorescence process. Instead, the evidence obtained from our spectroscopic tools suggest that BCC-TPTA has excited state dynamics that of a typical fluorescence chromophore and that just comparing the $\boldsymbol{\Phi}$ difference before and after purging oxygen from the solution is not an accurate method to claim excited state dynamics governed by a delayed fluorescence mechanism. Consequently, we believe that previous studies, in which the photo-physics of organic chromophores with TADF characteristics are reported, may have overlooked the influence of the host materials on the obtained optical properties in blended films.

3.3 Introduction

There is still a great need for more efficient green and blue organic materials for light emitting diode (OLEDs) applications.[1,2] While phosphorescent materials have shown some success, their short lived lifetimes, high cost, and poor stability, impart several limitations.[3,4] The thermally activated delayed fluorescence (TADF) mechanism has been proposed as a cost-efficient alternative to get higher efficiencies and longer device lifetimes and there has been great success regarding the synthesis of novel TADF chromophores. Some of these materials have reported internal quantum efficiency (η_{IQE}) values approaching 100 %.[2,5–7] This very high internal quantum efficiency was suggested as due to the harvesting of triplets in the chromophore in a reverse intersystem crossing process (rISC).[3,8–10] Unfortunately, the high turnover of new TADF scaffolds has not allowed for the necessary and intricate spectroscopic measurements for each new molecule to be elucidated individually in order to fully understand the mechanism. The previous reports have utilized primarily steady-state and μs spectroscopy to illustrate the thermally activated rISC process,[11] however, these time-resolved measurements can be convoluted with the parallel existing phosphorescence in the chromophore.[2,6,11] One of the best TADF chromophores, 9'-[4-(4,6-diphenyl-1,3,5-triazin-2-yl)phenyl]-9,3':6',9"-ter-9H-carbazole (BCC-TPTA), was reported to have an η_{IQE} of ~ 84 %.[2] This material is believed to represent the basic motif of an impressive TADF system and its efficiency sets a standard as to what other materials seek to attain. However, the details of its excited state dynamics have not been elucidated with the proper spectroscopic tools.

One way to characterize the contribution between singlet or triplet emission is to carry out time-resolved measurements with the appropriate time-resolution, as well as oxygen quenching measurements to distinguish between the contributions of the singlet and triplet emission.[6,12–14] It

is interesting to note that while there have been reports of studies investigating the emission of highly efficient and very well-known TADF structures, there have not been any detailed time-resolved fluorescence and time-resolved fluorescence lifetime quenching studies of these promising materials.[15] Moreover, many previous studies were conducted in the solid state using TADF chromophores as the guest material in blended films. Recent publications have highlighted the potential influence of exciplex formation of the guest, and between the host and the guest materials (host:guest) on the obtained solid state photoluminescence decay lifetime of chromophores with TADF charasteristics.[16–19] Aditionally, the steady state optical properties of the most common materials used as hosts overlaps with ones of the materials used as guests, which could give rise to Föster resonance energy transfer (FRET) and Dexter energy transfer (DET) mechanisms among the chromophores.[18,19] Therefore, optically inert hosts should be used to elucidate the photoluminescence decay lifetime and excited state dynamics in film of chromophores with TADF character.

In this report, ultrafast spectroscopic methods, with an emphasis in the *ns* TAS, are coupled with quantum chemical simulations (QCS) to elucidate the excited state dynamics in the well-known BCC-TPTA chromophore. For the measurements conducted in film, we selected poly methyl methacrylate (PMMA) as the host material. PMMA possess high transmission properties in the range of wavelengths used in this study and is also highly impermeable to oxygen.[20] Specifically, PMMA is optically inert, and cannot be excited by any of the excitation wavelengths used in this study, unlike most of the common hosts used in previous studies.[18,19,21] This prevented any convolution between the host and the guests excited state dynamics. In addition, previous studies conducted with similar organic chromophores with TADF characteristics doped in PMMA films have reported emissive lifetimes in the μs regime. The long-lived emissive lifetime in these

chromophores has been ascribed to a delayed fluorescence process.[15,19] As a comparison, we investigated a metal-containing primary phosphorescence chromophore $Ir(BT)_2(acac)$ and a well-known fluorescence chromophore Rhodamine B. Also, we investigated the emissive dynamics of these systems in a range of temperatures. In all cases, emission quenching from purging oxygen from the solution was carried out.

3.4 Experimental Techniques

3.4.1 Steady-State Measurements

The absorption spectra were measured on an Agilent 8341 spectrophotometer. The emission spectra were collected on a Fluoromax-4 fluorimeter with slits set at 1 nm and an integration time of 0.100 s. Quartz cells with 10 mm path lengths were used for all the steady-state measurements. All optical measurements were carried out at ambient conditions. The fluorescence quantum yields ($\boldsymbol{\Phi}$**)** measurements were conducted by using the Williams comparative method. The optical density was set to be ~ 0.10 or below to avoid reabsorption and internal filter effects. The absorption and fluorescence were measured for four samples with decreasing concentrations. The $\boldsymbol{\Phi}$ for BCC-TPTA dissolved in toluene and for Ir(BT)2(acac) dissolved in THF were measured using Coumarin 30 ($\boldsymbol{\Phi}$ = 0.67)[22] dissolved in acetonitrile as the standard. The same is true for the $\boldsymbol{\Phi}$ measurements after purging out oxygen (10 minutes). Rhodamine B is a well-known standard and the $\boldsymbol{\Phi}$ value can be found elsewhere. The $\boldsymbol{\Phi}$ of Rhodamine B after purging out oxygen (10 minutes) were measured as well and compared to itself ($\boldsymbol{\Phi}$ = 0.67)[23] before purging. The low temperature emission (phosphorescence) spectrum were obtained by using a Photon Technologies International (PTI), QuantaMaster 400 scanning spectrofluorimeter. The emission spectrum of the samples at low temperature (77K) were obtained after a delay of $> 100\ \mu s$ between the excitation beam and emission detection.

3.4.2 Time-Resolved Fluorescence and Phosphorescence Measurements

The ultra-fast fluorescence upconversion (UpC) setup was used to measure the fluorescence with *ps* time resolution as it has been previously described.[14] A mode-locked Ti-sapphire femtosecond laser (Spectra-Physics Tsunami) was used to generate 80 fs pulses at 800 nm with a repetition rate of 82 MHz. This Ti-sapphire mode-locked laser was pumped by a 532 nm CW laser (Spectra-Physics Millennia), which has a gain medium of neodymium-doped yttrium vanadate (Nd:YVO4). After the 800 nm pulsed beam is generated, a second harmonic (β- barium borate crystal) generates a 400 nm excitation pulse. The residual 800 nm beam was directed to pass through a computer-controlled motorized optical delay line. A Berek compensator controlled the polarization of the 800 nm excitation beam power varied between 33 to 40 mW. The fluorescence emitted by the sample was upconverted by the residual 800 nm beam by a nonlinear crystal of β-barium borate. It is important to mention that the 800 nm beam is passed by the optical delay line with a minimum gate step of 6.25 fs. The monochromator is used to select the wavelength of the up-converted beam of interest, and the selected beam is detected by a photomultiplier tube (R152P, Hamamatsu, Hamamatsu City, Japan). The photomultiplier tube (PMT) converts the detected beam into photon counts, which can be read from a computer. Coumarin 30 was used for calibrating the laser for the range of emission wavelengths in this study. The instrument response function (IRF) has been determined from the Raman signal of water to have a width of 110 fs.[24] Lifetimes of fluorescence decay were obtained by fitting the fluorescence decay profile to the most accurate fit. *The time-correlated single photon counting (TCSPC)* technique, which has been described previously,[14] was used to study the fluorescence and phosphorescence of the investigated chromophores. The laser used for the TCSPC measurement was a Kapteyn Murnane (KM) mode-locked Ti-sapphire laser. The output beam from the KM laser

was at 800 nm wavelength has a pulse duration of ~30 fs. The 800 nm output beam was frequency-doubled using a nonlinear barium borate crystal to obtain a 400 nm beam. Focus on the sample cell (quartz cuvette, 0.4 cm path length) was ensured using a lens of focal length 11.5 cm. Collection of fluorescence was done in a direction perpendicular to the incident beam into a monochromator, and the output from the monochromator was coupled to a photomultiplier tube, which converted the photons into counts.

3.4.3 Nanosecond Transient Absorption Spectroscopy Measurements

The absorption and lifetime of emissive and non-emissive transient species can be probed by using transient absorption spectroscopy, which has been previously described.[25,26] These measurements were done in diluted solutions and in the same solvents in which the other photophysical characterization were carried out. A LP980 (Edinburgh) system, which contains the photomultiplier (PMT-LP), was coupled with a Spectra-Physics QuantaRay Nd:YAG nanosecond (*ns*) pulsed laser and a GWU Optical Parametric Oscillator (OPO) tunable from 250 nm to 2600 nm for the excitation source. For this investigation, a 415 nm excitation beam was used to pump the molecules and a pulsed xenon lamp white light continuum was used for probing the excited state.

3.4.4 Quantum Chemical Simulation

The ground state (S_0) geometries of BCC-TPTA and Rhodamine B were optimized using density functional theory (DFT). The B3LYP functional, which has successfully predicted the ΔE_{ST} of a variety of TADF materials, was used along with the 6-31G* basis set.[2] The first excited singlet state (S_1) geometry of BCC-TPTA was obtained with a restricted open-shell Kohn-Sham (ROKS) approach and 6-31G* basis sets. ROKS is known to improve the deficiency of semilocal linear response time-dependent DFT (LR−TD−DFT) and offers a good alternative for

investigating charge transfer states.[27–31] Rhodamine B is a symmetric molecule and has a positive unit charge on one nitrogen atom. Due to a closed manifold of low lying states, however, excited state geometry optimization of Rhodamine B using TDDFT and ROKS did not easily lead to a symmetry broken state. Therefore, S_1 of Rhodamine B was targeted using configuration interaction single (CIS) geometry optimization, which had no issue distinguishing the two states. The single point energy of S_1 is refined using TD-DFT based on ROKS BCC-TPTA geometry and CIS Rhodamine B geometry.

The first triplet (T_1) geometry was predicted with spin unrestricted DFT. Single point energy calculations to evaluate the fluorescence emission energies, spin−orbit coupling elements, and adiabatic energy gap ($\Delta E_{ST} = E_{\text{TDDFT } S1 \text{ at min } S1} - E_{\text{UDFT } T1 \text{ at min } T1}$) were conducted, and the solvent environment effect is treated using a polarizable continuum model. The dielectric constant of chloroform and ethanol of 4.31 and 24.3 is used to describe the solvent medium of BCC-TPTA solution and Rhodamine B solution, respectively. All quantum chemical calculations were performed using Q−Chem 5.0.[32] The rate constant of ISC and rISC, were estimated via Fermi's Golden rule,[33,34]

$$k_{\text{ISC}} = \frac{2\pi}{\hbar}\rho_{\text{FC}}|\langle S_1|H_{SO}|T_1\rangle|^2$$

where $\langle S_1|H_{SO}|T_1\rangle$ is the spin−orbit coupling element between S_1 and T_1, ρ_{FC} denotes the Franck−Condon weighted density of states, and $\hbar$ is the reduced Planck constant of 6.582×10^{-16} eVs. ρ_{FC} is evaluated with Marcus−Levich−Jortner theory, [35,36]

$$\rho_{\text{FC}} = \frac{1}{\sqrt{4\pi\lambda_{\text{M}}k_BT}}\sum_{n=0}^{\infty}\exp(-S)\frac{S^n}{n!}\exp\left[-\frac{(\Delta E_{\text{ST}} + n\hbar\omega_{\text{eff}} + \lambda_{\text{M}})^2}{4\pi\lambda_{\text{M}}k_BT}\right]$$

where λ_{M} is the Marcus reorganization energy associated with the intermolecular and intramolecular low−frequency vibrations, k_{B} is for Boltzmann constant of 8.6173×10^{-5} eV/K, T is

the temperature (in this study, 298.15 K), $\hbar\omega_{eff}$ represents the effective energy of a mode representing the nonclassical high−frequency intramolecular vibrations. Huang−Rhys factor associated with these modes are given as *S*. The rate constant of the rISC process was described by parameters generated at the T_1 geometry, and the k_{ISC} estimation with parameters relevant to the S_1 geometry.

One recent computational study on TADF mechanism discussed the rate of rISC within the same framework used in this work. They computed the contribution of non-classical intramolecular vibrations and estimated the Marcus reorganization energy due to low frequency intramolecular vibrations and the medium-induced relaxation effects to be in the range of ~0.1-0.2 eV.[36–38] Also, they assumed the Huang-Rhys factors can be neglected without significant changes to the results for large molecules. The approximation setting λ_M to 0.1 or 0.2 eV reproduced available experimental k_{RISC} values on the same order of magnitude. The close examination revealed that use λ_M value of 0.2 eV gave better quantitative agreement with the available experimental k_{RISC} dta. Therefore, λ_M value is set to 0.2 eV in this study.

The fluorescence emission rate (k_F) was approximated by the product of the oscillator strength and the square of the wavenumber.[39] The observed k_F values of anthraquinone-based intramolecular charge transfer compounds, one class of TADF materials reported by the Adachi group, could be reproduced with this simple calculation.[39]

3.5 Results

3.5.1. Steady-State Measurements: UV-Vis Absorption

The UV-Vis (steady-state absorption) spectra at ambient conditions for Rhodamine B, $Ir(BT)_2(acac)$, and BCC-TPTA were taken in a diluted solution of ethanol, tetrahydrofuran (THF),

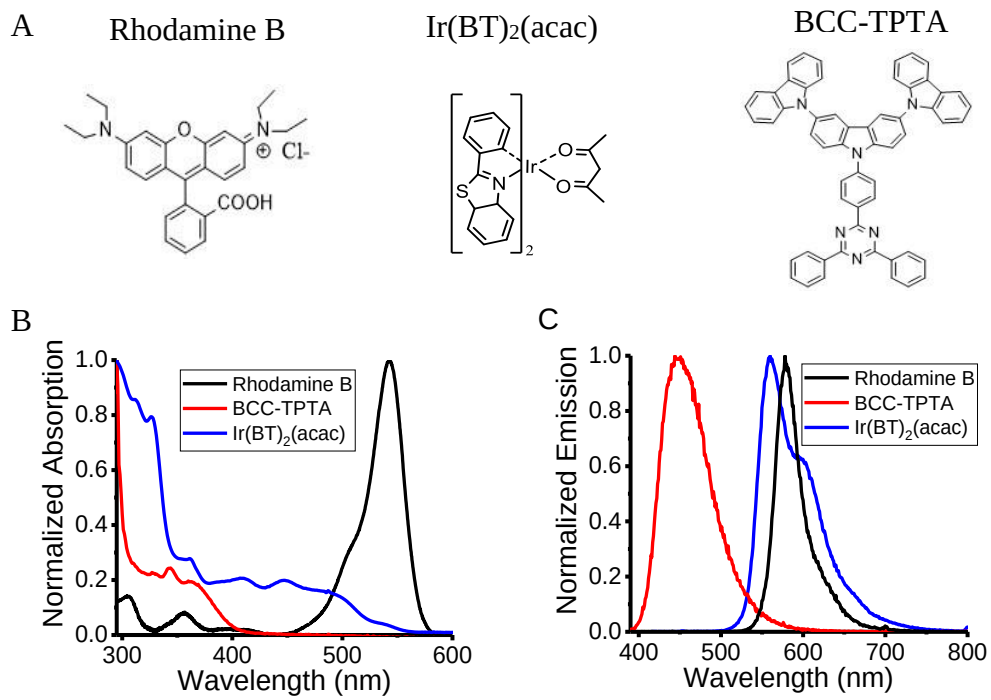

Figure 3.5.1.1 (A) Molecular structure of the investigated chromophores; steady-state absorption (B) and emission (C) of the investigated chromophores. All measurements were carried out in solution.

and toluene, respectively. Their absorption spectra are shown in **Figure 3.5.1.1B** and data is summarized in **Table 3.5.2.1**. All the investigated chromophores absorb in the visible region. The absorption spectra of Rhodamine B is perfectly in agreement with what is previously reported in the literature as well as is the absorption spectra of the $Ir(BT)_2(acac)$ complex.[40,41] For BCC-TPTA, two main absorption bands are present as is typical for chromophores with donor-acceptor configuration.[14] The high-energy band (<300 nm) is attributed to the localized excitations of the chromophore, while the lower energy band (300-400 nm) is consistence with absorption of the charge transfer state of BCC-TPTA.[14]

Table 3.5.1.1. Steady state measurements relevant data. (*) This molecule has a $\Delta E_{st} > 0.3$ eV.

Chromophores	Extinction Coefficient	λ_{maxEm}	Φ %	Φ % Purged	ΔE_{st} (eV) Theo	ΔE_{st} (eV) Exp	Stern-Volmer Quenching Rates $M^{-1}s^{-1}$
Rhodamine B (Fluorescence)	105,000 $cm^{-1}M^{-1}$ at 545 nm	575 nm	67 [40]	69	*	*	1.4×10^{10}
$Ir(BT)_2(acac)$ (Phosphorescence)	51,000 $cm^{-1}M^{-1}$ at 328 nm	560 nm	1	15	*	*	2.31×10^{9}
BCC-TPTA (TADF)	17,362 $cm^{-1}M^{-1}$ at 342 nm	450 nm	58	67	0.114[2]	0.34	2.82 10^{8}

3.5.2. Steady-State Measurements: Fluorescence and Phosphorescence Spectra

The emission spectrum under ambient conditions of Rhodamine B, $Ir(BT)_2(acac)$, and BCC-TPTA were taken in diluted solutions of ethanol, tetrahydrofuran (THF), and toluene, respectively. The emission spectra are shown in **Figure 3.5.2.1C** while the data is summarized in **Table 3.5.2.1.** All the investigated chromophores emit in the visible region and their emission spectra are in agreement with the ones previously reported in the literature. The quantum yield (Φ) of the investigated chromophores was measured before and after the oxygen purging process (**Table 3.5.2.1**). This allowed us to evaluate the potential contribution from the triplet state to the emissive characteristics of the investigated chromophores. There was a very small difference in the Φ of Rhodamine B after the solution was purged of oxygen (67 % to 69 %) that is within the margin of error for the Williams method.[42] As expected for phosphorescence chromophores, the Φ measured for the $Ir(BT)_2(acac)$ complex increased from 1% to 15 % after oxygen purging.[11,43] For BCC-TPTA, our measurements showed a 15 % Φ enhancement (from 58 % to 67 %) after the solution was purged of oxygen. This Φ enhancement after the oxygen purging process has been widely ascribed to a delayed fluorescence process occurring somewhere in the μs timescale.[2,6,15]

Moreover, we investigated the influence of the temperature and the solvent polarity on the emission spectra of BCC-TPTA. As can be observed in **Figure 3.8.5.1**, the emission intensity of BCC-TPTA is inverse proportional to the temperature. Similar behavior was obtained for Rhodamine B and for the $Ir(BT)_2(acac)$ complex. According to the Lippert-Mataga model, the charge transfer character of emitting species can be probed by evaluating how the emission λ_{max} changes due to solvent polarity (f).[44,45] As could be observed from the plot of the Stokes shift ($\nu_a - \nu_f$) in function of the (f), we obtained a linear relationship between $\nu_a - \nu_f$ and f with a large slope of 15,360 cm^{-1} (**Figure 3.8.5.14**). This implies that the emission dynamics of BCC-TPTA is highly sensitive to the solvent polarity while its absorption spectra is unaffected. The large slope obtained from the Lippert-Mataga model correlates well with the charge transfer state assignment from the steady state absorption of BCC-TPTA (**Figure 3.5.2.1B**). Therefore, we can rule out the possibility of any exciplex formations in this study.

In order to evaluate the differences in energy levels between the S_1 and T_1 state (ΔE_{st}), the phosphorescence spectrum of the investigated chromophores was also probed. Their spectra are shown in **Figure 3.8.5.2** and the data is summarized in **Table 3.5.2.1.** For Rhodamine B, we were not able to get a phosphorescence spectrum at any of the concentrations tested. Likely, the phosphorescence emission of the Rhodamine B was too low to be detected.[46] A sharper emission spectrum at 77 K than the one taken at RT was obtained for the $Ir(BT)_2(acac)$ complex. This sharpening in the emission spectrum can be explained by to the lack of molecular vibrations promoted by room thermal energy.[47,48] A red-shift in the phosphorescence spectrum of BCC-TPTA at 77 K was observed relative to its fluorescence spectrum taken at the same temperature (**Figure 3.8.5.12)** We noticed that the fluorescence spectrum of BCC-TPTA at 77 K was blue shifted relative to the one obtained at RT (**Figure 3.8.5.3**). We calculated the ΔE_{st} to be 0.34 eV from the

fluorescence and phosphorescence spectrums obtained at 77 K. A slightly smaller value was obtained if the fluorescence spectrum at RT was used for the calculation.[2,15] These small ΔE_{st} give hints of a potential excited state mixing between the S_1 and T_1 state, and if correct, it should be observed as long-lived emissive lifetime in the μs timescale.[6,18,19]

3.5.3. Time-Resolved Emissive Lifetime Measurements

The time-correlated single photon counting (TCSPC) technique were carried out to evaluate the emissive lifetime from the *ns* to the μs timescales of the investigated chromophores. Measurements were done before and after the oxygen purging process, at low temperature (77 K), and in doped film and are shown in **Figure 3.5.3.1** while the data is summarized in **Table 3.5.3.1**. In **Figure 3.5.3.1A**, the fluorescence decay profile for the Rhodamine B chromophore at ambient conditions can be observed. The decay profiles were obtained with a 400 nm excitation and emission detection at 575 nm. A mono-exponential fit to the decay profile illustrates the 2.92 *ns* relaxation time. This relaxation time matches previously reported fluorescence lifetimes of Rhodamine B in the literature.[40] Also shown in **Figure 3.5.3.1A** is the result of purging the solution of oxygen. As can be observed, the oxygen removal has no effect on the fluorescence decay profile of Rhodamine B. A longer fluorescence lifetime at low temperature and in film was obtained for Rhodamine B. This lengthening in the fluorescence lifetime of xanthene derivatives at low temperatures and in PMMA matrixes has been previously documented and can be ascribed to the lack of energy dissipation via chromophore-solvent interaction and by the massive molecular motion suppression induced by the PMMA matrix, respectivly.[49–51]

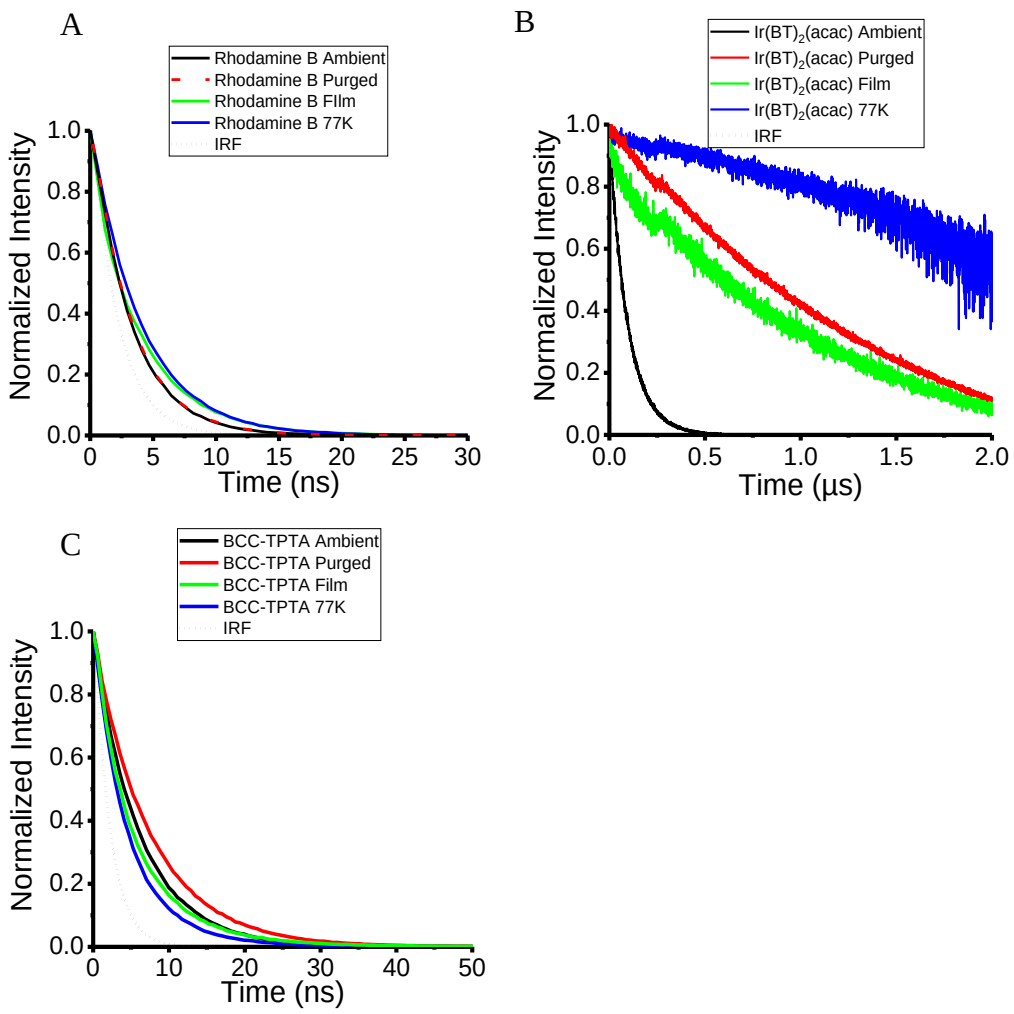

Figure 3.5.3.1. The emissive lifetime of the chromophores was investigated by using the Time Correlated Single Photon Counting (TCSPC) technique: (A) Rhodamine B, (B) $Ir(BT)_2(acac)$, and (C) BCC-TPTA. Measurements were taken at different temperatures and matrixes.

Shown in **Figure 3.5.3.1*B*** are the emissive characteristics of the $Ir(BT)_2(acac)$ complex excited at 400 nm and the emission was detected at 560 nm. The phosphorescence decay profiles for the $Ir(BT)_2(acac)$ complex at RT could be fitted to a mono-exponential expression, with a decay time of 97 *ns*. Also notable in **Figure 3.5.3.1*B*** is the decay profile of emission after purging oxygen from the $Ir(BT)_2(acac)$ solution. As can be seen from the curve, the decay is drastically lengthened

Table 3.5.3.1. Summary of the emissive lifetime measurements of the investigated chromophores. These measurements were taken with the Time-Correlated Single Photon Counting (TCSPC) technique.

Chromophores	Emissive lifetime (Ambient)	Emissive lifetime (Purged)	Emissive lifetime (77K)	Emissive lifetime (Film)
Rhodamine B	2.92 *ns*	2.96 *ns*	3.97 *ns*	3.78 *ns*
$Ir(BT)_2(acac)$	97 *ns*	1.62 μs	4 μs	1.25 μs
BCC-TPTA	6.4 *ns*	7.8 *ns*	4.66 *ns*	5.47 *ns*

and a mono-exponential expression yielded a phosphorescence lifetime of 1.62 μs. This lengthening in the phosphorescence lifetime of $Ir(BT)_2(acac)$ explains its $\boldsymbol{\Phi}$ enhancement after the oxygen purging process. This value is in agreement with reported values by Lamansky and others.[41] For such materials with a heavy metal atom in the core, the intersystem crossing (ISC) is expected to be on the order of *ps*.[11,43]

Also shown in **Figure 3.5.3.1*B*** is the phosphorescence lifetime of the $Ir(BT)_2(acac)$ complex at low temperature and in film. As can also be observed, the phosphorescence lifetime of the $Ir(BT)_2(acac)$ complex is drastically lengthened at low temperature (4 μs) and in film (1.25 μs). Sajoto and others have previously documented this lengthening in the phosphorescence lifetime at low temperatures for similar iridium-based complex, and it has been attributed to the lack of thermally activated non-radiative decay channels at low temperatures.[52] Kwon and others have reported a lengthening in the phosphorescence lifetime in chromophores when they are doped into PMMA films, which has been ascribed to the suppression of molecular motions induced by the PMMA matrix.[49]

Shown in **Figure 3.5.3.1*C*** are the emissive dynamics for the BCC-TPTA chromophore. The decay profiles were obtained with 400 nm excitation and 450 nm emission detection wavelength. As can be seen from the curve, a mono-exponential fluorescence decay on the order of 6.4 *ns* was

detected at ambient conditions which corresponds well to a singlet (S_1) decay profile. The decay of 6.4 *ns* suggests a relatively efficient fluorescence process in BCC-TPTA. Also noted in **Figure 3.5.3.1*C*** is the result of the oxygen quenching experiment with the BCC-TPTA chromophore. One observes a slightly longer fluorescence decay (7.8 *ns*) after the removal of oxygen from the solution. Interestingly, no long-lived emissive lifetime in the μs region was detected for BCC-TPTA after the oxygen purging process (**Figure 3.5.3.1*C*** and **Figure 3.8.5.10**). This was also true in all the solvents in which the emissive lifetime of BCC-TPTA was investigated (**Figure 3.8.5.6**, **Table 3.8.5.1**). The emissive lifetime characterization of BCC-TPTA was also probed with the ns TAS technique (**Figure 3.8.5.11**). The decay profiles were obtained with 415 nm excitation and 450 nm emission detection wavelength. Our ns TAS emissive characterization results are in agreement with the ones obtained by the TCSPC technique and no long-lived emission component in the μs timescale was observed. Measurements were conducted up to 5 μs. The lack of a long-lived emissive lifetime is intriguing. For a reported TADF chromophore with $\boldsymbol{\Phi}$ enhancement of ~ 15 % (from 58 % to 67 %) after the oxygen purging, one would expect to observe a long-lived emissive lifetime spanning the μs timescale as evidence of delayed fluorescence.[53]

Also shown in **Figure 3.5.3.1*C*** is the emissive lifetime of BCC-TPTA at 77 K (4.66 *ns*) and in film (5.47 *ns*). In both cases, a shorter fluorescence lifetime was obtained for BCC-TPTA relative to the ones taken in solution. However, the phosphorescence spectrum of BCC-TPTA taken at 77 K suggests triplet emission at detection wavelengths higher than 470 nm (**Figure 3.8.5.2**). We detected a long-lived emissive component for BCC-TPTA at 77 K when the emission lifetime characterization was conducted at detection wavelengths > 470 nm (**Figure 3.8.5.5**). This long-lived emission component vanished when the temperature was raised, and no long-lived emission component was detected at any other temperatures tested (**Figure 3.8.5.4**and **Figure**

3.8.5.5). Consequently, this long-lived emissive component at 77 K is attributed to the phosphorescence shown in **Figure 3.8.5.2**. Interestingly, we did not observe a long-lived emissive lifetime at the *μs* timescale in film (**Figure 3.5.3.1** and **Figure 3.8.5.10**). A previous study reported a long-lived photoluminescence decay for BCC-TPTA in blended film. This long-lived emissive lifetime was ascribed to a delayed fluorescence process owing to the excited state dynamics of BCC-TPTA.[2] We did not observe long-lived emissive lifetimes indicative of a delayed fluorescence process for BCC-TPTA at any of the medium tested. Therefore, further spectroscopic techniques were used to characterize the excited state dynamics of BCC-TPTA.

The fluorescence up-conversion (UpC) is a high-time resolution technique with high sensitivity from the *fs* to the *ps* regime.[14] We performed it to evaluate the faster emissive characteristics that could not be investigated by the TCSPC technique. The measurements were done before and after the removal of oxygen from the solution and are shown in **Figure 3.5.3.2**. The data is summarized in **Table 3.5.3**. In **Figure 3.5.3.2*A***, the fluorescence lifetimes of Rhodamine B before and after oxygen purging can be observed. As expected, there is no effect on the fluorescence lifetime after oxygen purging. In **Figure 3.5.3.2*B***, a rise time in the *ps* regime was observed for the $Ir(BT)_2(acac)$ chromophore. Similar behavior was previously observed for iridium-based phosphorescence chromophores and it was attributed to the ISC process.[43] Interestingly, our data shows that the rise-time is sensitive to O_2. The idea of $[O_2]$ affecting the k_{isc} of chromophores has been suggested.[54] These results illustrate a very long lifetime for $Ir(BT)_2(acac)$.

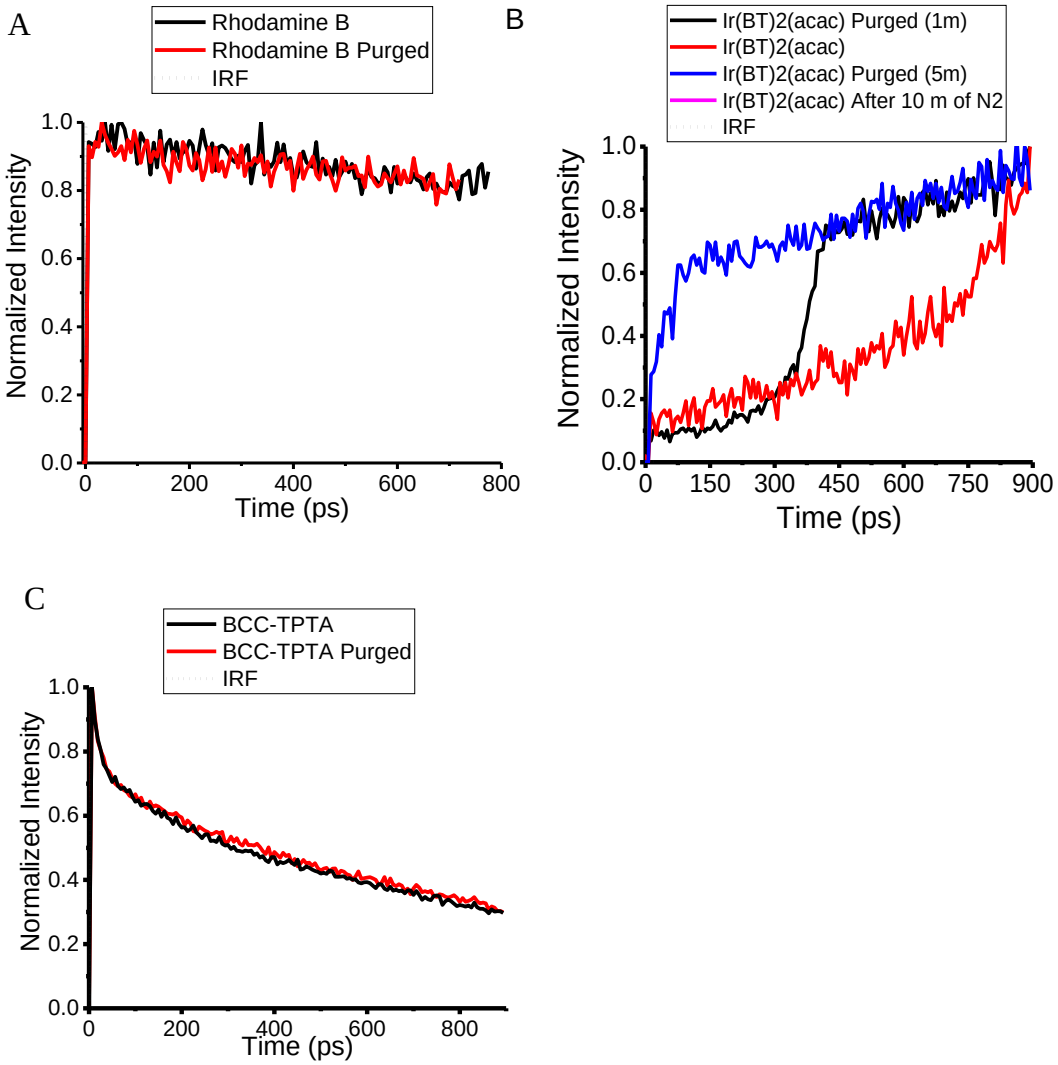

Figure 3.5.3.2. Emissive lifetime of the investigated chromophores probed with the Fluorescence up-conversion technique. All the measurements were done in solution, and before and after the oxygen purging process.

In **Figure 3.5.3.2*C***, the fluorescence lifetime of BCC-TPTA can be observed. In contrast to Rhodamine B, the fluorescence lifetime of BCC-TPTA shows a bi-exponential decay profile. We ascribed this behavior to the donor-acceptor charge transfer nature of BCC-TPTA. Similar multi-exponential behavior has been observed at this timescale in other donor-acceptor chromophores with charger transfer charasteristics.[14,55] The multi-exponential behavior by BCC-TPTA observed by the UpC also suggests that the lifetime measured by the TCSPC is the second and long

component of its fluorescence decay (τ_2). If we compare the UpC of the BCC-TPTA to the $Ir(BT)_2(acac)$ chromophore, the UpC measurements suggest no ISC occurring for BCC-TPTA in the *ps* regime. This was expected. The spin-orbit coupling (SOC) of similar organic chromophores with TADF characteristics are three orders of magnitude smaller than the ones reported for Iridium-based phosphorescence chromophores or copper-based TADF chromophores.[38,41] Given that no evidence of ISC was observed by the UpC, the *ns* TAS was carried out to evaluate if BCC-TPTA possesses triplet transient states that are characteristic of excited stated dynamics governed by a delayed fluorescence mechanism.

3.5.4. Nanosecond Transient Absorption Spectroscopy

In order to further investigate the dynamics governing the excited state of BCC-TPTA, the *ns* TAS technique was also done (**Figure 3.5.4.1**), and the data is summarized in **Table 3.8.5.2**. Our system possesses the ability and sensitivity to see any non-emissive transient states from the *ns* to the *μs* regime.[26,56] In **Figure 3.5.4.1*A***, we observed the time-resolved absorption spectrum of Rhodamine B in ethanol at ambient conditions. We only obtained one negative optical density (OD) signal from the *ns* TAS measurement. This negative OD band overlaps with the emission spectrum of Rhodamine B (**Figure 3.5.2.1C**). As expected, the kinetic traces of the negative OD band for Rhodamine B correlates well with its fluorescence lifetime obtained by the TCSPC (**Table 3.8.5.2**). Therefore, this negative OD signal is due to the overwhelming fluorescence of Rhodamine B ($S_1 \rightarrow S_0$) detected as has been previously reported.[40] As is typical for fluorescence chromophores, no significant change or evidence of a transient triplet states was observed before or after oxygen purging at the investigated timescales (**Figure 3.8.5.7**).

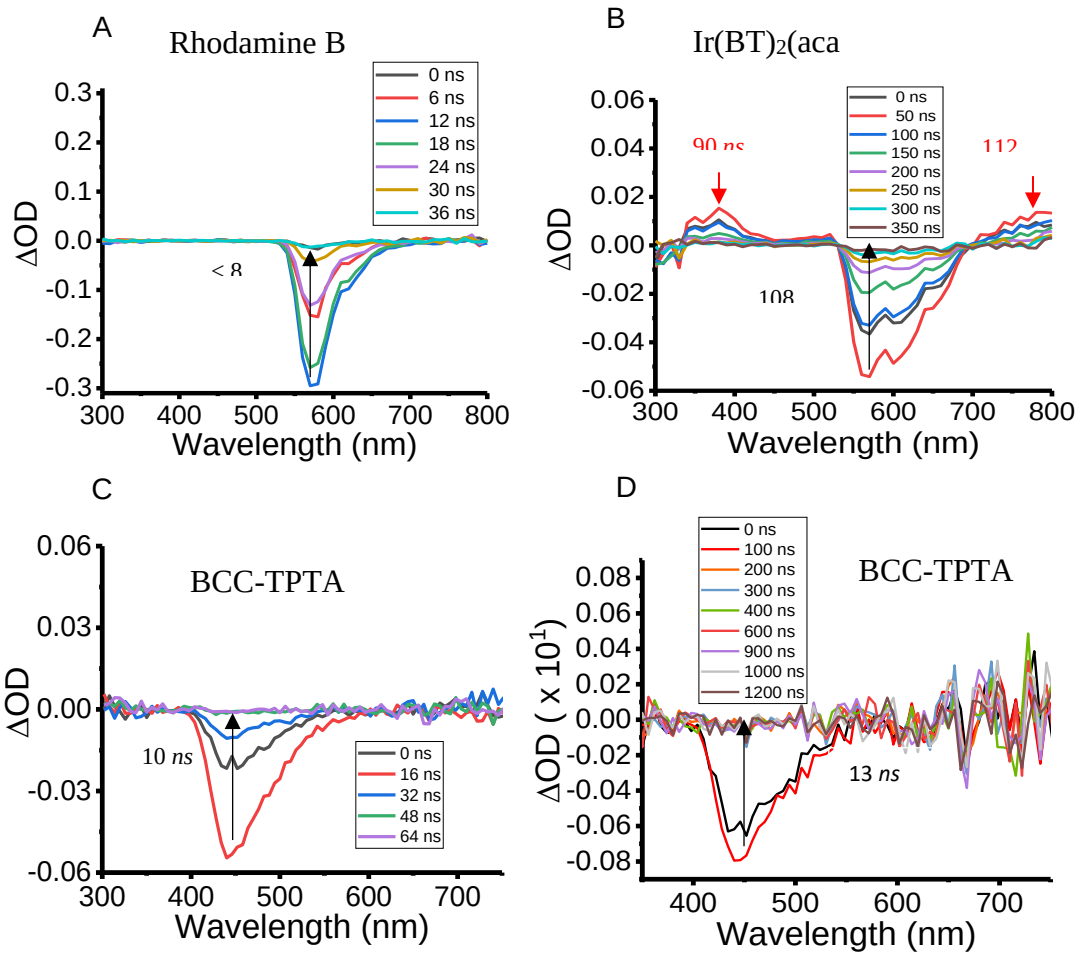

Figure 3.5.4.1. Time-resolved absorption spectra of Rhodamine B (A), $Ir(BT)_2(acac)$ (B), and BCC-TPTA (C), obtained by *ns* TAS. These measurements were conducted in solution and at ambient conditions.

In **Figure 3.5.4.1*B***, we observed the time-resolved absorption spectrum of the $Ir(BT)_2(acac)$ complex in THF at ambient conditions. For the $Ir(BT)_2(acac)$ complex we detected both, positive (excited state absorption, ESA) and negative OD signals, which is in agreement with previous reported time-resolved absorption spectrums for similar iridium-based chromophores.[57] These transient ESA signals detected by the TAS technique in iridium-based complexes have been previously attributed to spin-forbidden metal-to-ligand charge transfer (MLCT) processes and ligand centered (LC) transitions, which are all related to spin-orbit interactions and singlet to triplet electronic transitions.[43,57] As expected, the kinetic traces obtained from the observed negative OD

band correlates well with the $Ir(BT)_2(acac)$ complex phosphorescence lifetime obtained by the TCSPC (**Table 3.8.5.2**). Therefore, this negative OD signal can be attributed to its overwhelming phosphorescence ($T_1 \rightarrow S_0$) detected as has been previously reported for similar iridium-based chromophores.[43,57] The time-resolved absorption spectrum of the $Ir(BT)_2(acac)$ complex and the kinetic traces of its bands before and after the oxygen purging process can be observed in **Figure 3.7.5.8.** As observed, the time-resolved absorption spectrums of the $Ir(BT)_2(acac)$ complex is highly sensitive to the removal of oxygen. As a result, longer kinetic traces of the time-resolved absorption bands are obtained after oxygen removal. This sensitivity to oxygen is in agreement with the emissive profile obtained by the TCSPC technique and is indicative of $Ir(BT)_2(acac)$ excited state triplet nature.

In **Figure 3.5.4.1C** and **Figure 3.5.4.1D**, we observed the time-resolved absorption spectra of BCC-TPTA in toluene at ambient conditions for the *ns* and *μs* timescales, respectively. Interestingly, we detected only one signal as a negative OD band for BCC-TPTA at any of the investigated timescales. This band perfectly overlaps with the emission spectrum of BCC-TPTA. In addition, its kinetic trace correlates well with the fluorescence lifetime obtained by the TCSPC (**Table 3.8.5.2**). Therefore, as with the Rhodamine B, the only signal obtained for BCC-TPTA is attributed to its overwhelming fluorescence ($S_1 \rightarrow S_0$) detected. No significant effect in the time-resolved absorption spectrum of BCC-TPTA was observed after the removal of oxygen from the solution at any of the investigated timescales (**Figure 3.8.5.9**). This was intriguing. Given the 15% (58 % to 67 %) $\boldsymbol{\Phi}$ enhancement after the removal of oxygen from the solution, we expected to see triplet transient signals in the form of ESA bands for BCC-TPTA. These ESA bands should be observed from the *ns* to the *μs* timescale, as it has been documented in similar organic chromophores with TADF characteristics.[53]

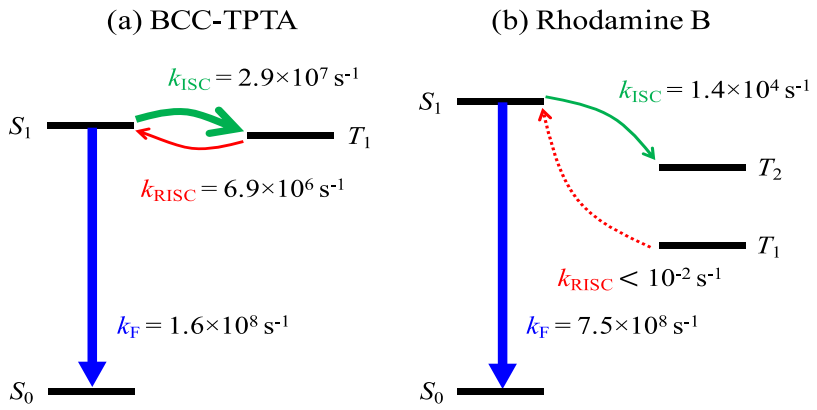

Figure 3.5.5.1. Energy diagram of the fluorescence, intersystem crossing, and reverse intersystem crossing rates for (a) BCC-TPTA and (b) Rhodamine B.

Table 3.5.5.1. Calculated rate constants of fluorescence (k_F), ISC (k_{ISC}), and rISC (k_{rISC}), and available experimental values. (The ratio of the quantity to k_F is given in the parenthesis)

Dynamic Process	BCC-TPTA			Rhodamine B		
	Calc k (s^{-1})	Calc τ (ns)	Expt.[2]	Calc k (s^{-1})	Calc τ (ns)	Expt.[58]
Fluorescence	1.6×10^{8} (1.00)	6	9.6×10^{7}	7.5×10^{8} (1.00)	1	N/A
ISC	2.9×10^{7} (0.18)	34	4.2×10^{7}	1.4×10^{4} (1.9×10^{-5})	~ 10^{5}	5.3×10^{5}
RISC	6.9×10^{6} (0.04)	146	N/A	< 0.01 (10^{-11})	> 10^{11}	N/A

3.5.5. Quantum Chemical Simulations.

Quantum chemical simulations (QCS) were carried out to gain a deeper understanding of the key differences between BCC-TPTA and Rhodamine B. Specifically, the rate of fluorescence (k_F), the rate of intersystem crossing (k_{ISC}), and the rate of reverse intersystem crossing (k_{rISC}) of these chromophores were determined by using a Fermi-Golden rule rate based on spin-orbital couplings from time-dependent density functional theory and are reported in **Table 3.5.5.1**.[32,59] BCC-TPTA has k_{ISC} and k_{rISC} values that are significantly larger than those for Rhodamine B, and these are comparable with the rate constant for fluorescence decay. The large k_{ISC} and k_{rISC} of BCC-TPTA

originated from small ΔE_{ST} (0.34 eV) and indicate efficient population transfer between singlet and triplet, which is a distinct property of BCC-TPTA. On the other hand, for Rhodamine B, a typical fluorescent chromophore, the relevant rate constants follow the pattern: $k_F >> k_{ISC} >> k_{rISC}$. The k_F of Rhodamine B is four orders of magnitude larger than its k_{ISC} and ten orders of magnitude larger than its k_{rISC}. For BCC-TPTA chromophore, the calculated rate constants suggest that the fluorescence, ISC, and rISC processes all occur on a *ns* timescale. With these findings, it is suggested that this system exhibits a dynamic equilibrium between the k_f, the k_{ISC}, and the k_{rISC}, which is important for a delayed fluorescence process. Yet, no experimental evidence of a delayed fluorescence process was observed for BCC-TPTA with any of our spectroscopic tools before or after the purging of oxygen experiments nor in film.

3.6 Discussion

In this study, we used high-time resolution ultrafast spectroscopy, with an emphasis on the *ns* TAS, to probe the excited state dynamic of a TADF chromophores with a reported η_{IQE} of 84 %.[2] Also, two well-known fluorescence and phosphorescence standards, Rhodamine B and $Ir(BT)_2(acac)$, respectively, were used for comparison. The steady state measurements showed optical activity in the UV-Vis region for all the investigated chromophores. The Φ measurements showed that BCC-TPTA has a higher sensitivity to oxygen than Rhodamine B but not as much sensitivity as the $Ir(BT)_2(acac)$ complex. This BCC-TPTA sensitivity to oxygen was observed as an enhancement in the Φ after the removal of oxygen from the solution, and has been ascribed due to a delayed fluorescence process happening in the μs timescale.[2,6,11,38,60,61] This delayed fluorescence process implies multiple electronic transitions in the excited states that are quantum mechanically forbidden. The probability of these transitions happening has been ascribed to the nature of their spin-orbit coupling (SOC), their small exchange energy (ΔE_{st}), and the existence of

locally excited triplet state (^{3}LE).[38,53] Therefore, several ultrafast spectroscopic techniques were coupled with QCS to evaluate the excited state dynamics governing in BCC-TPTA.

Our emissive lifetime characterization measurements showed a lengthening in the fluorescence lifetime for BCC-TPTA after the removal of oxygen, which correlates well with its $\boldsymbol{\Phi}$ enhancement. However, this lengthening was only about ~ 2 *ns* and no evidence of a long-lived emissive lifetime characteristic from a chromophore with excited state dynamics governed by a TADF mechanism was observed by any our spectroscopic tools (**Figure 3.5.3.2*C*, Figure 3.8.5.6, Figure 3.8.5.10*, and* Figure 3.8.5.11**). Literature shows extensive evidence of studies trying to understand the molecular oxygen quenching mechanism in a repertoire of organic chromophores with similar fluorescence lifetimes to the ones reported in this study.[12,62] Those studies have highlighted the fluorescence (S_1) sensitivity to oxygen even at ambient conditions.[62] The Stern-Volmer equation was used to evaluate the quenching mechanism in which oxygen affects the excited state dynamics of the investigated chromophores. This equation would help us to calculate the emissive quenching rates of the investigated chromophores. After solving the equation (**Table 3.5.3.1**), it showed that the quenching rate constant for BCC-TPTA in toluene is about the oxygen diffusion limit in toluene.[62] This implies that oxygen can significantly quench the fluorescence (S_1) of BCC-TPTA via a collisional mechanism. This explains the lengthening in the fluorescence lifetime and the $\boldsymbol{\Phi}$ enhancement of BCC-TPTA after the removal of oxygen from the solution. This oxygen quenching effect was not observed for Rhodamine B. This is due to its significantly faster fluorescence lifetime compared to the ones obtained for BCC-TPTA. In the case of the $Ir(BT)_2(acac)$ complex, it is well known that the robust lengthening in the phosphorescence lifetime after the removal of oxygen is due to the triplet emissive nature of its excited state.[41,62] In addition, the fluorescence UpC measurements suggests that the emission detected by the TCSPC

comes from BCC-TPTA second and long component of its fluorescence decay (**Figure 3.8.3.2C**). The comprehensive study on the emissive lifetimes obtained from the UpC and the TCSPC techniques suggests that BCC-TPTA have emissive dynamics as that of a typical fluorescence chromophore with charge transfer nature.

Studies have highlighted the effect of the dielectric constant of the medium and polarity of the solvent on the ΔE_{st} of molecules with TADF character.[63,64] Therefore, we probed the emissive lifetime of BCC-TPTA in different solvents to evaluate if the long-lived emissive lifetime was characteristic of a particular environment. As can be observed in **Figure 3.8.5.6**, no long-lived emissive lifetime was obtained in any of the solvents tested. In **Table 3.8.5.1**, we observed a proportional relationship between the fluorescence lifetime of BCC-TPTA and the solvent polarity in which the measurement was done. When we conducted the emissive lifetime characterization of BCC-TPTA at 77 K, we thought that the low temperature would prevent energy dissipation via non-radiative pathways, which should result in a longer fluorescence lifetime. Interestingly, we observed a faster fluorescence lifetime at 77 K relative to the one taken at RT. We also detected a long-lived phosphorescence emission for BCC-TPTA at detection wavelengths > 470 nm. This long-lived emissive component vanished when the temperature was raised (**Figure 3.8.5.14** and **Figure 3.8.5.5**). These observations highlighted the lack of a long-lived emissive components for BCC-TPTA at higher temperatures than 77 K. This lack of a long-lived emissive component at high temperatures is not consistent with excited state dynamics governed by a TADF mechanism.[2,6,9,53] In **Figure 3.8.5.3**, the fluorescence spectra at 77 K showed a blue-shift relative to the one taken at RT. A blue-shift in the emission spectra and faster fluorescence lifetimes in film relative to the one taken in solution were also observed for BCC-TPTA (**Figure 3.8.5.13**). In all cases, a lower energy in the emission spectra of BCC-TPTA was correlated with a longer

fluorescence lifetime.[63,64] These results shows the effect of the medium on the S_1 stabilization of BCC-TPTA, which implies that the molecular conformation of BCC-TPTA is highly dependent on the medium. Yet, no evidence of a long-lived emissive lifetime for BCC-TPTA was observed at RT in any of the medium tested.

We would like to reiterate that we did not observe any long-lived emissive lifetime spanning the μs timescale for BCC-TPTA at any of the conditions tested with any of our spectroscopic tools. This lack of long-lived emissive lifetime was intriguing. A previous study reported a long-lived emissive lifetime in the μs timescale for BCC-TPTA in blended film, which was ascribed to a delayed fluorescence process owing to the excited state properties of BCC-TPTA.[2] We noticed that the emissive decay reported in solid state was conducted by using bis[2-(diphenylphosphino)phenyl] ether oxide (DPEPO) as the host material. The problem with using DPEPO as the host material is that it has steady-state optical properties in the same range of wavelengths that BCC-TPTA does.[2,21,65] Furthermore, emissive lifetime in the μs timescale has been reported for DPEPO and its derivatives.[21] This overlap in the steady-state optical properties and the long-lived emissive character of DPEPO could give rise to excited state mechanisms such as FRET transfer and DET among the chromophores.[2,21,65] In contrast to the electroluminescence process, the excited state and bandgap optimization between the guest:host is detrimental for the photoluminescence process. This is due to the ambitious nature of deconvoluting and quantifying the influence of the host in the obtained emissive properties of the film.[65–67] In this study, the selection of an optically inert host such as PMMA showed that BCC-TPTA seems to have emissive lifetimes characteristics of a fluorescence chromophore.

We carried out the *ns* TAS technique to further investigate and compare the excited state dynamics of the investigated chromophores. Correctly, we were probing for triplet transient state

signals that could be linked to a delayed fluorescence mechanism in BCC-TPTA. Previous studies have reported transient absorption measurements for similar organic chromophores with TADF characteristics.[15,53,68] Specifically, they have reported ESA between 500-700 nm in blue and light-blue TADF chromophores.[53,68] This ESA has been linked to the ^{3}LE state, which is believed to be an integral state for the rISC facilitation.[38,53] Interestingly, the time-resolved absorption spectrum of BCC-TPTA behaves similar to the one obtained for Rhodamine B and no ESA was detected by the *ns* TAS techniques at any of the investigated timescales. Long-lived ESA was observed for the $Ir(BT)_2(acac)$ complex at the investigated timescales. These transient species detected on the $Ir(BT)_2(acac)$ complex have been linked to MLCT and LC transitions, which are all related to spin-forbidden electronic transitions.[43,57] In contrast to the ESA observed for the $Ir(BT)_2(acac)$ complex and with similar *ns* TAS conducted in similar organic chromophores with TADF characteristic, no evidence of the ^{3}LE state nor any triplet transient state at all was observed for BCC-TPTA. Studies conducted in similar organic chromophores with TADF characteristics have been able to correlate the presence of this ^{3}LE state with their observable long-lived *μs* emissive lifetimes after photoexcitation.[15,53] Furthermore, Kuang et al reported the detection of robust long-lived triplet transient states in chromophores with TADF characteristics despite of their limited long-lived emissive profile in solution.[68] Still, that study highlighted the transient triplet state as the focal point of the TADF mechanism.[53,68] Despite our quantum chemical simulations suggesting a dynamic equilibrium between the k_F, the k_{ISC}, and the k_{rISC} in the *ns* timescale for BCC-TPTA, our transient absorption experiments are highlighted by the lack of the ^{3}LE state or any triplet transient state. This lack of the ^{3}LE state could also explains why we do not observe long-lived emissive lifetime at in any of the medium tested by our multiple spectroscopic tools. Herein, the experimental evidence presented in this report suggests that BCC-TPTA has excited state

dynamics of a typical fluorescence chromophore. As a result, we believe the influence of the electronic and optical properties of the host materials has been overlooked in previous studies intended to report the photophysical properties of organic chromophores with TADF characteristics.

6.7 Conclusions

Herein, we report the first study in which multiple time-resolved spectroscopic techniques, with an emphasis in the *ns* TAS, were coupled with QCS to elucidate the excited state dynamics of a reported chromophore (BCC-TPTA) with highly efficient blue TADF characteristics. We carried out a comparison of this chromophore with two well-known fluorescent and phosphorescent chromophores. The BCC-TPTA chromophore showed some sensitivity to the removal of oxygen but not as strong as the phosphorescent $Ir(BT)_2(acac)$ chromophore and not as small as the fluorescent Rhodamine B chromophore. The sensitivity to oxygen from BCC-TPTA was observed as an enhancement in the $\boldsymbol{\Phi}$ after purging oxygen from the solution, which has been previously attributed to a delayed fluorescence process occurring in the μs timescale.[2] The evidence obtained by our spectroscopic tools showed that: (1) BCC-TPTA does not have a long-lived emissive lifetime that could be linked to a delayed fluorescence mechanism in any of the medium tested; (2) BCC-TPTA does not have any triplet transient state that could be linked to an excited state dynamic governed by a delayed fluorescence process. Therefore, the $\boldsymbol{\Phi}$ enhancement of BCC-TPTA after the oxygen purging process is ascribed to the lack of oxygen-collisional quenching of the fluorescence (S_1) rather than due to a delayed fluorescence process. These results imply that just comparing the $\boldsymbol{\Phi}$ difference before and after purging oxygen from the solution is not an accurate method to claim excited state dynamics governed by a delayed fluorescence mechanism. Consequently, the development of a better and more accurate method with a focus in

probing and characterizing the triplet state is in need. We believed that the *ns* TAS technique should be integral in the triplet characterization of rational designed chromophores with TADF characteristics.

Despite that the phosphorescence spectrum measurements on BCC-TPTA may have showed hints of a small ΔE_{ST}, our study suggests that BCC-TPTA has excited state dynamics such as typical fluorescence chromophores. Furthermore, this study suggests that previous studies in which the optical properties of organic chromophores with TADF characteristics are reported may have overlooked the influence and impact of the host electronic transitions on the obtained optical properties.

References

1) M. Hong, M. K. Ravva, P. Winget and J. L. Brédas, *Chem. Mater.*, 2016, **28**, 5791–5798.

2) S. Hirata, Y. Sakai, K. Masui, H. Tanaka, S. Y. Lee, H. Nomura, N. Nakamura, M. Yasumatsu, H. Nakanotani, Q. Zhang, K. Shizu, H. Miyazaki and C. Adachi, *Nat. Mater.*, 2015, **14**, 330–336.

3) F. B. Dias, K. N. Bourdakos, V. Jankus, K. C. Moss, K. T. Kamtekar, V. Bhalla, J. Santos, M. R. Bryce and A. P. Monkman, *Adv. Mater.*, 2013, **25**, 3707–14.

4) H. Nakanotani, K. Masui, J. Nishide, T. Shibata and C. Adachi, *Sci. Rep.*, 2013, **3**, 2127.

5) Y. J. Shiu, Y. C. Cheng, W. L. Tsai, C. C. Wu, C. T. Chao, C. W. Lu, Y. Chi, Y. T. Chen, S. H. Liu and P. T. Chou, *Angew. Chemie - Int. Ed.*, 2016, **55**, 3017–3021.

6) Y. Tao, K. Yuan, T. Chen, P. Xu, H. Li, R. Chen, C. Zheng, L. Zhang and W. Huang, *Adv. Mater.*, 2014, **26**, 7931–58.

7) H. Kaji, H. Suzuki, T. Fukushima, K. Shizu, K. Suzuki, S. Kubo, T. Komino, H. Oiwa, F. Suzuki, A. Wakamiya, Y. Murata and C. Adachi, *Nat. Commun.*, 2015, **6**, 8476.

8) S. Youn Lee, T. Yasuda, H. Nomura and C. Adachi, *Appl. Phys. Lett.*, 2012, **101**, 093306.

9) H. Uoyama, K. Goushi, K. Shizu, H. Nomura and C. Adachi, *Nature*, 2012, **492**, 234–238.

10) A. Endo, M. Ogasawara, A. Takahashi, D. Yokoyama, Y. Kato and C. Adachi, *Adv. Mater.*, 2009, **21**, 4802–6.

11) L. Bergmann, G. J. Hedley, T. Baumann, S. Bräse and I. D. W. Samuel, *Sci. Adv.* 2016, **2**, DOI:10.1126/sciadv.1500889.

12) F. Wilkinson and A. A. Abdel-Shafi, *J. Phys. Chem. A*, 1997, **101**, 5509–5516.

13) C. Grewer and H. D. Brauer, *J. Phys. Chem.*, 1994, **98**, 4230–4235.

14) R. J. Vázquez, H. Kim, B. M. Kobilka, B. J. Hale, M. Jeffries-El, P. Zimmerman and T. Goodson, *J. Phys. Chem. C*, 2017, **121**, 14382–14392.

15) Z. Yang, Z. Mao, Z. Xie, Y. Zhang, S. Liu, J. Zhao, J. Xu, Z. Chi and M. P. Aldred, *Chem. Soc. Rev.*, 2017, **46**, 915–1016.

16) P. L. Dos Santos, J. S. Ward, M. R. Bryce and A. P. Monkman, *J. Phys. Chem. Lett.*, 2016, **7**, 3341–3346.

17) J. B. Birks, *Nature*, 1967, **214**, 1187–1190.

18) D. H. Kim, A. D'Aléo, X. K. Chen, A. D. S. Sandanayaka, D. Yao, L. Zhao, T. Komino, E. Zaborova, G. Canard, Y. Tsuchiya, E. Choi, J. W. Wu, F. Fages, J. L. Brédas, J. C. Ribierre

and C. Adachi, *Nat. Photonics*, 2018, **12**, 98–104.

19) X.-K. Chen, Y. Tsuchiya, Y. Ishikawa, C. Zhong, C. Adachi and J.-L. Brédas, *Adv. Mater.*, 2017, **29**, 1702767.

20) H. M. Zidan and M. Abu-Elnader, *Phys. B Condens. Matter*, 2005, **355**, 308–317.

21) J. Zhang, D. Ding, Y. Wei, F. Han, H. Xu and W. Huang, *Adv. Mater.*, 2016, **28**, 479–485.

22) G. Jones, W. R. Jackson, C. Y. Choi and W. R. Bergmark, *J. Phys. Chem.*, 1985, **89**, 294–300.

23) R. F. Kubin and A. N. Fletcher, *J. Lumin.*, 1982, **27**, 455–462.

24) B. Keller, A. McLean, B. G. Kim, K. Chung, J. Kim and T. Goodson, *J. Phys. Chem. C*, 2016, **120**, 9088–9096.

(25) O. Varnavski, T. Goodson, L. Sukhomlinova and R. Twieg, *J. Phys. Chem. B*, 2004, **108**, 10484–10492.

(26) H. Kim, B. Keller, R. Ho-Wu, N. Abeyasinghe, R. J. Vázquez, T. Goodson and P. M. Zimmerman, *J. Am. Chem. Soc.*, 2018, **140**, 7760–7763.

(27) T. Kowalczyk, T. Tsuchimochi, P. T. Chen, L. Top and T. Van Voorhis, *J. Chem. Phys.*, 2013, **138**, 164101.

(28) D. Hait, T. Zhu, D. P. McMahon and T. Van Voorhis, *J. Chem. Theory Comput.*, 2016, **12**, 3353–3359.

(29) I. Frank, J. Hutter, D. Marx and M. Parrinello, *J. Chem. Phys.*, 1998, **108**, 4060–4069.

(30) I. Okazaki, F. Sato, T. Yoshihiro, T. Ueno and H. Kashiwagi, *J. Mol. Struct. THEOCHEM*, 1998, **451**, 109–119.

(31) M. Filatov and S. Shaik, *Chem. Phys. Lett.*, 1999, **304**, 429–437.

(32) Y. Shao, Z. Gan, E. Epifanovsky, A. T. B. Gilbert, M. Wormit, J. Kussmann, A. W. Lange, A. Behn, J. Deng, X. Feng, D. Ghosh, M. Goldey, P. R. Horn, L. D. Jacobson, I. Kaliman, R. Z. Khaliullin, T. Kuś, A. Landau, J. Liu, E. I. Proynov, Y. M. Rhee, R. M. Richard, M. A. Rohrdanz, R. P. Steele, E. J. Sundstrom, H. L. Woodcock, P. M. Zimmerman, D. Zuev, B. Albrecht, E. Alguire, B. Austin, G. J. O. O. Beran, Y. A. Bernard, E. Berquist, K. Brandhorst, K. B. Bravaya, S. T. Brown, D. Casanova, C.-M. M. Chang, Y. Chen, S. H. Chien, K. D. Closser, D. L. Crittenden, M. Diedenhofen, R. A. Distasio, H. Do, A. D. Dutoi, R. G. Edgar, S. Fatehi, L. Fusti-Molnar, A. Ghysels, A. Golubeva-Zadorozhnaya, J. Gomes, M. W. D. Hanson-Heine, P. H. P. Harbach, A. W. Hauser, E. G. Hohenstein, Z. C. Holden, T.-C. C. Jagau, H. Ji, B. Kaduk, K. Khistyaev, J. J. Kim, J. J. Kim, R. A. King, P. Klunzinger, D. Kosenkov, T. Kowalczyk, C. M. Krauter, K. U. Lao, A. D. Laurent, K. V. Lawler, S. V. Levchenko, C. Y. Lin, F. Liu, E. Livshits, R. C. Lochan, A. Luenser, P.

Manohar, S. F. Manzer, S.-P. P. Mao, N. Mardirossian, A. V. Marenich, S. A. Maurer, N. J. Mayhall, E. Neuscamman, C. M. Oana, R. Olivares-Amaya, D. P. O'Neill, J. A. Parkhill, T. M. Perrine, R. Peverati, A. Prociuk, D. R. Rehn, E. Rosta, N. J. Russ, S. M. Sharada, S. Sharma, D. W. Small, A. Sodt, T. Stein, D. Stück, Y.-C. C. Su, A. J. W. Thom, T. Tsuchimochi, V. Vanovschi, L. Vogt, O. Vydrov, T. Wang, M. A. Watson, J. Wenzel, A. White, C. F. Williams, J. Yang, S. Yeganeh, S. R. Yost, Z.-Q. Q. You, I. Y. Zhang, X. Zhang, Y. Zhao, B. R. Brooks, G. K. L. Chan, D. M. Chipman, C. J. Cramer, W. A. Goddard, M. S. Gordon, W. J. Hehre, A. Klamt, H. F. Schaefer, M. W. Schmidt, C. D. Sherrill, D. G. Truhlar, A. Warshel, X. Xu, A. Aspuru-Guzik, R. Baer, A. T. Bell, N. A. Besley, J.-D. Da Chai, A. Dreuw, B. D. Dunietz, T. R. Furlani, S. R. Gwaltney, C.-P. P. Hsu, Y. Jung, J. Kong, D. S. Lambrecht, W. Liang, C. Ochsenfeld, V. A. Rassolov, L. V. Slipchenko, J. E. Subotnik, T. Van Voorhis, J. M. Herbert, A. I. Krylov, P. M. W. Gill, M. Head-Gordon, T. Kuš, A. Landau, J. Liu, E. I. Proynov, Y. M. Rhee, R. M. Richard, M. A. Rohrdanz, R. P. Steele, E. J. Sundstrom, H. L. Woodcock, P. M. Zimmerman, D. Zuev, B. Albrecht, E. Alguire, B. Austin, G. J. O. O. Beran, Y. A. Bernard, E. Berquist, K. Brandhorst, K. B. Bravaya, S. T. Brown, D. Casanova, C.-M. M. Chang, Y. Chen, S. H. Chien, K. D. Closser, D. L. Crittenden, M. Diedenhofen, R. A. Distasio, H. Do, A. D. Dutoi, R. G. Edgar, S. Fatehi, L. Fusti-Molnar, A. Ghysels, A. Golubeva-Zadorozhnaya, J. Gomes, M. W. D. Hanson-Heine, P. H. P. Harbach, A. W. Hauser, E. G. Hohenstein, Z. C. Holden, T.-C. C. Jagau, H. Ji, B. Kaduk, K. Khistyaev, J. J. Kim, J. J. Kim, R. A. King, P. Klunzinger, D. Kosenkov, T. Kowalczyk, C. M. Krauter, K. U. Lao, A. D. Laurent, K. V. Lawler, S. V. Levchenko, C. Y. Lin, F. Liu, E. Livshits, R. C. Lochan, A. Luenser, P. Manohar, S. F. Manzer, S.-P. P. Mao, N. Mardirossian, A. V. Marenich, S. A. Maurer, N. J. Mayhall, E. Neuscamman, C. M. Oana, R. Olivares-Amaya, D. P. Oneill, J. A. Parkhill, T. M. Perrine, R. Peverati, A. Prociuk, D. R. Rehn, E. Rosta, N. J. Russ, S. M. Sharada, S. Sharma, D. W. Small, A. Sodt, T. Stein, D. Stück, Y.-C. C. Su, A. J. W. Thom, T. Tsuchimochi, V. Vanovschi, L. Vogt, O. Vydrov, T. Wang, M. A. Watson, J. Wenzel, A. White, C. F. Williams, J. Yang, S. Yeganeh, S. R. Yost, Z.-Q. Q. You, I. Y. Zhang, X. Zhang, Y. Zhao, B. R. Brooks, G. K. L. Chan, D. M. Chipman, C. J. Cramer, W. A. Goddard, M. S. Gordon, W. J. Hehre, A. Klamt, H. F. Schaefer, M. W. Schmidt, C. D. Sherrill, D. G. Truhlar, A. Warshel, X. Xu, A. Aspuru-Guzik, R. Baer, A. T. Bell, N. A. Besley, J.-D. Da Chai, A. Dreuw, B. D. Dunietz, T. R. Furlani, S. R. Gwaltney, C.-P. P. Hsu, Y. Jung, J. Kong, D. S. Lambrecht, W. Liang, C. Ochsenfeld, V. A. Rassolov, L. V. Slipchenko, J. E. Subotnik, T. Van Voorhis, J. M. Herbert, A. I. Krylov, P. M. W. Gill and M. Head-Gordon, *Mol. Phys.*, 2015, **113**, 184–215.

(33) G. W. Robinson and R. P. Frosch, *J. Chem. Phys.*, 1963, **38**, 1187–1203.

(34) V. Lawetz, G. Orlandi and W. Siebrand, *J. Chem. Phys.*, 1972, **56**, 4058–4072.

(35) J. L. Brédas, D. Beljonne, V. Coropceanu and J. Cornil, *Chem. Rev.*, 2004, **104**, 4971–5003.

(36) K. Schmidt, S. Brovelli, V. Coropceanu, D. Beljonne, J. Cornil, C. Bazzini, T. Caronna, R. Tubino, F. Meinardi, Z. Shuai and J. L. Brédas, *J. Phys. Chem. A*, 2007, **111**, 10490–10499.

(37) D. Beljonne, Z. Shuai, G. Pourtois and J. L. Bredas, *J. Phys. Chem. A*, 2001, **105**, 3899–3907.

(38) P. K. Samanta, D. Kim, V. Coropceanu and J. L. Brédas, *J. Am. Chem. Soc.*, 2017, **139**, 4042–4051.

(39) Q. Zhang, H. Kuwabara, W. J. Potscavage, S. Huang, Y. Hatae, T. Shibata and C. Adachi, *J. Am. Chem. Soc.*, 2014, **136**, 18070–18081.

(40) P. C. Beaumont, D. G. Johnson and B. J. Parsons, *J. Chem. Soc. Faraday Trans.*, 1993, **89**, 4185–4191.

(41) S. Lamansky, P. Djurovich, D. Murphy, F. Abdel-Razzaq, R. Kwong, I. Tsyba, M. Bortz, B. Mui, R. Bau and M. E. Thompson, *Inorg. Chem.*, 2001, **40**, 1704–1711.

(42) P. H. Doan, D. R. G. Pitter, A. Kocher, J. N. Wilson and T. Goodson, *J. Am. Chem. Soc.*, 2015, **137**, 9198–9201.

(43) K. C. Tang, K. L. Liu and I. C. Chen, *Chem. Phys. Lett.*, 2004, **386**, 437–441.

(44) C. Han, Z. Zhang, D. Ding and H. Xu, *Chem*, 2018, **4**, 2154–2167.

(45) W. Li, D. Liu, F. Shen, D. Ma, Z. Wang, T. Feng, Y. Xu, B. Yang and Y. Ma, *Adv. Funct. Mater.*, 2012, **22**, 2797–2803.

(46) R. W. Chambers, T. Kajiwara and D. R. Kearns, *J. Phys. Chem.*, 1974, **78**, 380–387.

(47) C. Adachi, M. A. Baldo, S. R. Forrest, S. Lamansky, M. E. Thompson and R. C. Kwong, *Appl. Phys. Lett.*, 2001, **78**, 1622–1624.

(48) M. A. Baldo, S. Lamansky, P. E. Burrows, M. E. Thompson and S. R. Forrest, *Appl. Phys. Lett.*, 1999, **75**, 4–6.

(49) M. S. Kwon, Y. Yu, C. Coburn, A. W. Phillips, K. Chung, A. Shanker, J. Jung, G. Kim, K. Pipe, S. R. Forrest, J. H. Youk, J. Gierschner and J. Kim, *Nat. Commun.* 2015, **6**, DOI:10.1038/ncomms9947.

(50) T. J. V. Prazeres, A. Fedorov, S. P. Barbosa, J. M. G. Martinho and M. N. Berberan-Santos, *J. Phys. Chem. A*, 2008, **112**, 5034–5039.

(51) K. Kemnitz, N. Tamai, I. Yamazaki, N. Nakashima and K. Yoshihara, *J. Phys. Chem.*, 1986, **90**, 5094–5101.

(52) T. Sajoto, P. I. Djurovich, A. B. Tamayo, J. Oxgaard, W. A. Goddard and M. E. Thompson, *J. Am. Chem. Soc.*, 2009, **131**, 9813–9822.

(53) T. Hosokai, H. Matsuzaki, H. Nakanotani, K. Tokumaru, T. Tsutsui, A. Furube, K. Nasu, H. Nomura, M. Yahiro and C. Adachi, *Sci. Adv.* 2017, **5**, DOI:10.1126/sciadv.1603282.

(54) A. J. McLean, D. J. McGarvey, T. G. Truscott, C. R. Lambert and E. J. Land, *J. Chem. Soc. Faraday Trans.*, 1990, **86**, 3075.

(55) Z. Cai, R. J. Vázquez, D. Zhao, L. Li, W. Y. Lo, N. Zhang, Q. Wu, B. Keller, A. Eshun, N. Abeyasinghe, H. Banaszak-Holl, T. Goodson and L. Yu, *Chem. Mater.*, 2017, **29**, 6726–6732.

(56) T. J. Whittemore, T. A. White and C. Turro, *J. Am. Chem. Soc.*, 2018, **140**, 229–234.

(57) F. Lafolet, S. Welter, Z. Popović and L. De Cola, *J. Mater. Chem.*, 2005, 15, 2820–2828.

(58) R. Menzel and E. Thiel, *Chem. Phys. Lett.*, 1998, **291**, 237–243.

(59) L. Visscher, *Theor. Comput. Chem.*, 2002, **11**, 291–331.

(60) D. R. Lee, S.-H. Hwang, S. K. Jeon, C. W. Lee and J. Y. Lee, *Chem. Commun.*, 2015, **51**, 8105–8107.

(61) T. Hatakeyama, K. Shiren, K. Nakajima, S. Nomura, S. Nakatsuka, K. Kinoshita, J. Ni, Y. Ono and T. Ikuta, *Adv. Mater.*, 2016, **28**, 2777–2781.

(62) C. Schweitzer and R. Schmidt, *Chem. Rev.*, 2003, **103**, 1685–1758.

(63) R. Ishimatsu, S. Matsunami, K. Shizu, C. Adachi, K. Nakano and T. Imato, *J. Phys. Chem. A*, 2013, **117**, 5607–5612.

(64) H. Sun, Z. Hu, C. Zhong, X. Chen, Z. Sun and J. L. Brédas, *J. Phys. Chem. Lett.*, 2017, **8**, 2393–2398.

(65) K. E. Sapsford, L. Berti and I. L. Medintz, *Angew. Chemie - Int. Ed.*, 2006, **45**, 4562–4588.

(66) P. R. Selvin, *Nat. Struct. Mol. Biol.*, 2000, **7**, 730–734.

(67) H. Fukagawa, T. Shimizu, Y. Iwasaki and T. Yamamoto, *Sci. Rep.*, 2017, **7**, 1735.

(68) Z. Kuang, G. He, H. Song, X. Wang, Z. Hu, H. Sun, Y. Wan, Q. Guo and A. Xia, *J. Phys. Chem. C*, 2018, **122**, 3727–3737.

3.8 Supporting Information

3.8.1 Materials: All the chromophores in this study were obtained from commercial suppliers and used without further purification. BCC-TPTA was purchased from Luminescence Technology Corporation and dissolved in toluene. The $Ir(BT)_2(acac)$ was purchased from Sigma and was dissolved in THF. And, the Rhodamine B was purchased from Sigma and dissolved in ethanol.

3.8.2 Sample Preparation and Experimental Sample Handling: A stock solution (10^{-4} M) were prepared by mixing each sample in the corresponding solvent. Toluene, THF, and Ethanol were the solvent used for BCC-TPTA, $Ir(BT)_2(acac)$, and the Rhodamine B, respectively. Consequent dilutions from the stock solutions were made on each sample to run the different experiments conducted in this report. A 400 nm excitation wavelength were used in all experimental set-ups and for all the chromophores while their emissive lifetime were measured at their respective emissive λ_{MAX}. In all cases, including the temperature dependence measurements, emission quenching from purging oxygen is carried out. Specifically, the oxygen free atmosphere was created by bubbling N_2 thought the solution for at least 8 minutes. The 8 minutes criteria was based on the reproducibility of the emission spectrum and emissive lifetime characterization of the $Ir(BT)_2(acac)$ system. After 6 minutes on average, the emission intensity was at its higher counts for the $Ir(BT)_2(acac)$, meaning that oxygen was not quenching its triplet state.

3.8.3 Quantum Yield Calculation: The fluorescence quantum yields measurements were conducted by using the Williams comparative method. The optical density was measured to be ~ 0.10 or bellow to avoid reabsorption and internal filter effects. The absorption and fluorescence were measured for four samples with decreasing concentrations. The quantum yield was calculated using the following equation:

$$\phi_x = \phi_{STD} \frac{Grad_x \eta_x^2}{Grad_{STD}\, \eta_{STD}^2}$$ **Equation 3.8.3.1**

were Φ_x is the calculated quantum yield, η is the refractive index of the solvent, and $Grad$ is the slope obtained from plotting the fluorescence area in function of the optical density (OD). The quantum yields for BCC-TPTA dissolved in toluene and for $Ir(BT)_2(acac)$ dissolved in THF were measured using Coumarin 30 ($\Phi = 0.67$)[1] dissolved in acetonitrile as the standard. The same is true for the Φ_x measurements after purging out oxygen (10 minutes). Rhodamine B is a well-known standard and the Φ value can be find elsewhere. The Φ of Rhodamine B after purging out oxygen (10 minutes) were measured as well and compared to itself ($\Phi = 0.67$)[2] before purging. The emission spectra were collected on a Fluoromax-4 fluorimeter with slits set at 1 nm and an integration time of 0.100 s. Quartz cells with 10 mm path lengths were used for all the steady-state measurements. All optical measurements were carried out at STP.

3.8.4 Stern-Volmer equation handling: The emission of a chromophore can be quenched in the presence of a quencher, which is explained elsewhere.[3–5] The two main intermolecular process are responsible for this emission quenching are: quenching of the S_1 due to collisions between the chromophore and the quencher, or energy transfer from the T_1 state of the chromophore to the quencher. When the quencher is oxygen, energy transfer from the triplet of the chromophore to oxygen has been reported. The Stern-Volmer equation allow us to investigate the kinetics of these intermolecular quenching processes in function of the concentration of the quencher. For this analysis, the emissive lifetimes, before and after the quencher is added, are correlated with the ambient concentration of the oxygen in an equation expressed by:

$$\frac{t_o}{t} = 1 + K.t_o.[Q\}$$ **Equation 3.8.4.1**

In which the t_o correspond to the chromophore lifetime before the quencher is added, the t correspond to the chromophore lifetime after the quencher is added, the K correspond to the quencher rate coefficient, and the Q correspond to the quencher's concentration. It is well known that oxygen is an excellent triplet state quencher. Therefore, this equation was used in to understand the possible intermolecular quenching processes. The quencher rate constant is compared with the rate of diffusivities of the quencher to understand if the quencher can quench the chromophore via collision.

3.8.5 Steady-State and Ultrafast Spectroscopy

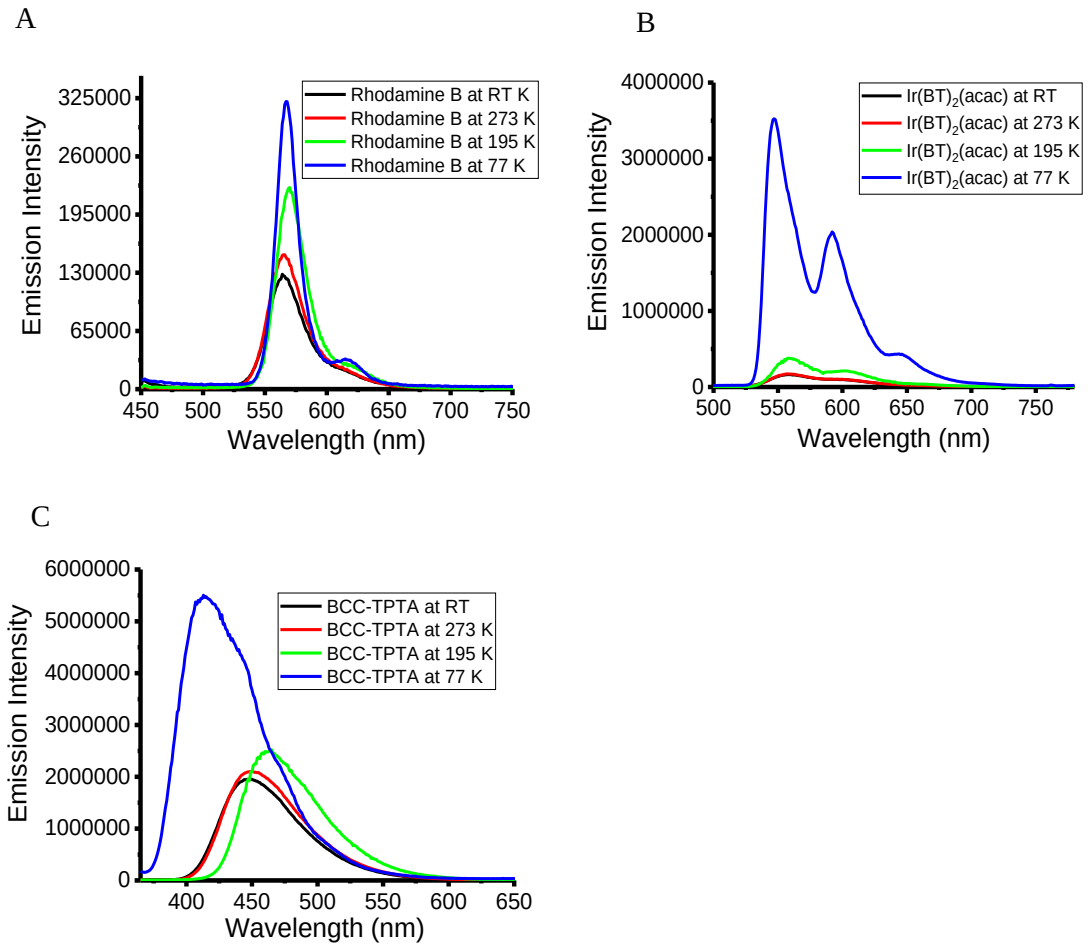

Figure 3.8.5.1. Raw emission spectrum of the investigated chromophore at RT (black), 273 K (red), 195 K (green), and at 77K (blue): Rhodamine B (A), $Ir(BT)_2acac$ (B), and BCC-TPTA in toluene (C).

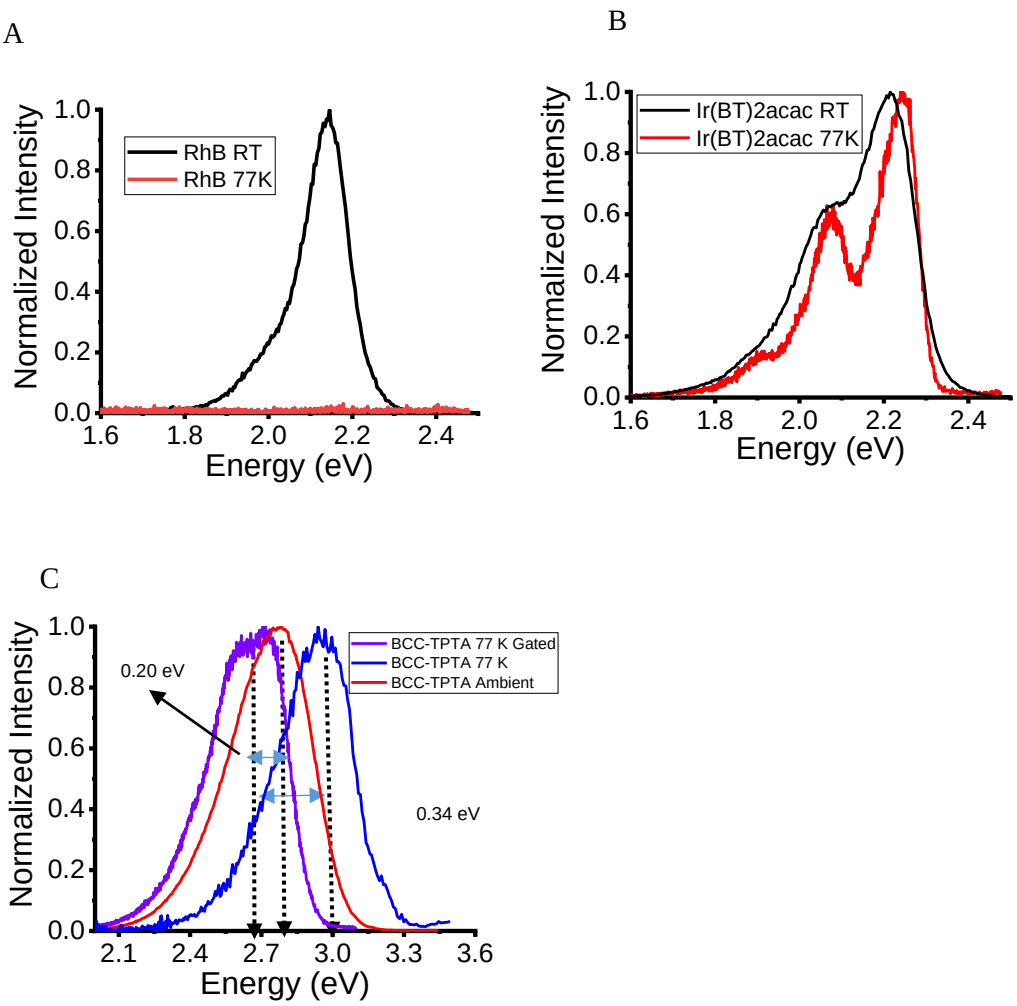

Figure 3.8.5.2. Normalized emission spectrum of the investigated chromophore at RT and at 77K: Rhodamine B (A), Ir(BT)2(acac) (B), and BCC-TPTA (C).

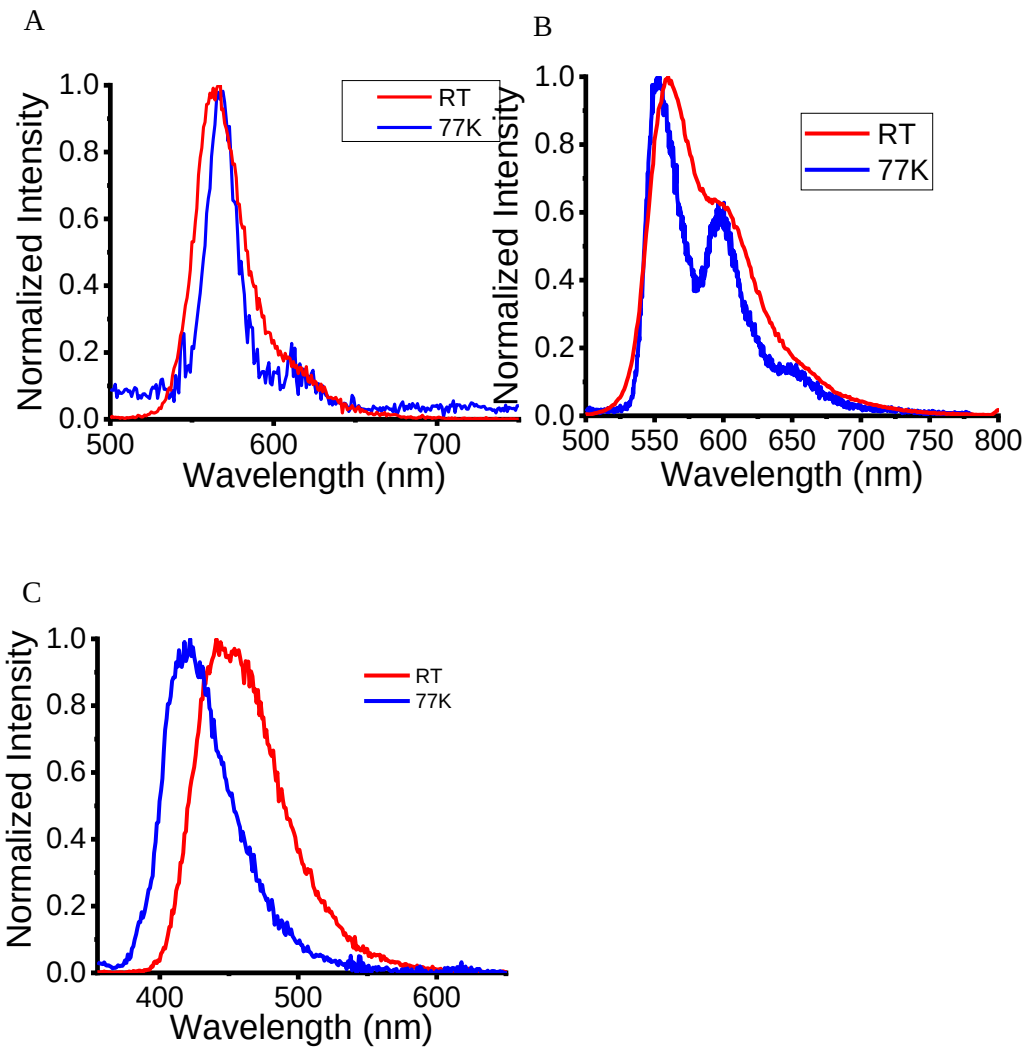

Figure 3.8.5.3. Normalized emission spectrum of the investigated chromophore at RT and at 77K: Rhodamine B (A), Ir(BT)2acac (B), and BCC-TPTA (C). No delayed between the excitation beam and the detection was done in these measurements.

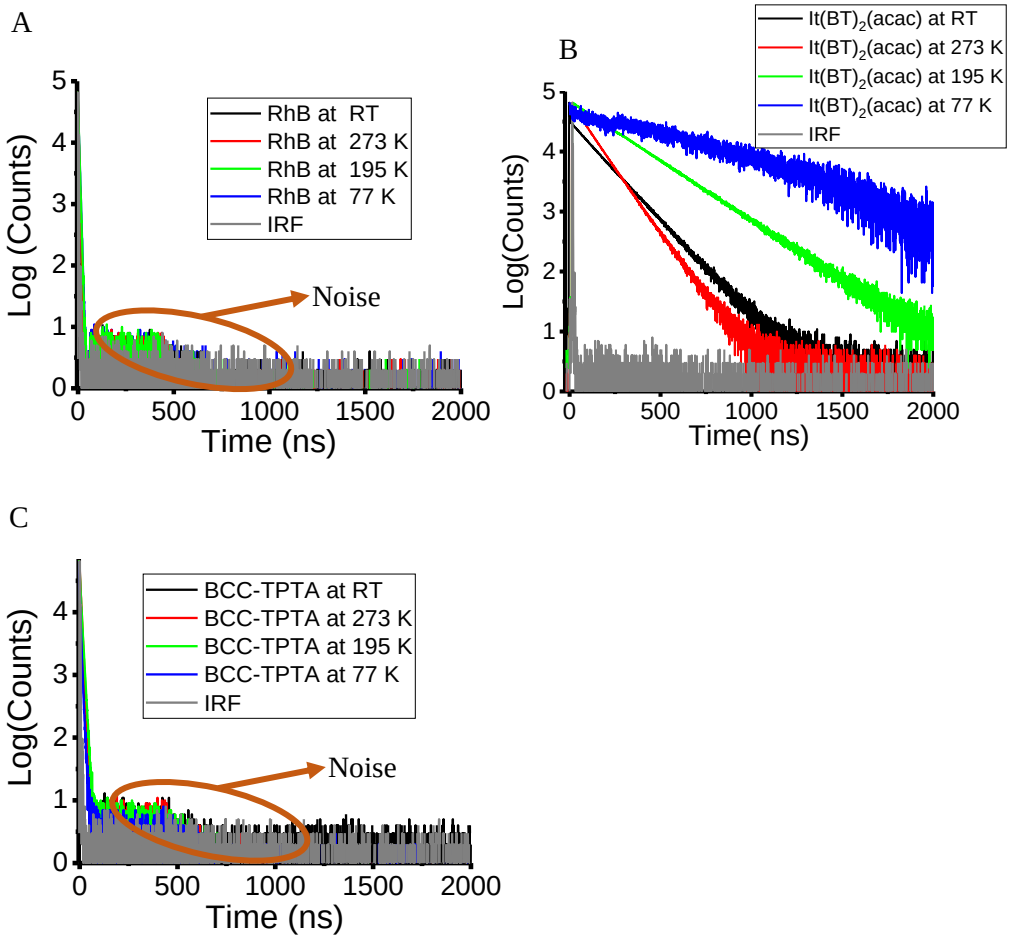

Figure 3.8.5.4. Emissive lifetime characterization at different temperature obtained with the TCSPC technique. Rhodamine B was diluted in ethanol (A), Ir(BT)2(acac) in THF (B), and BCC-TPTA in toluene (C).

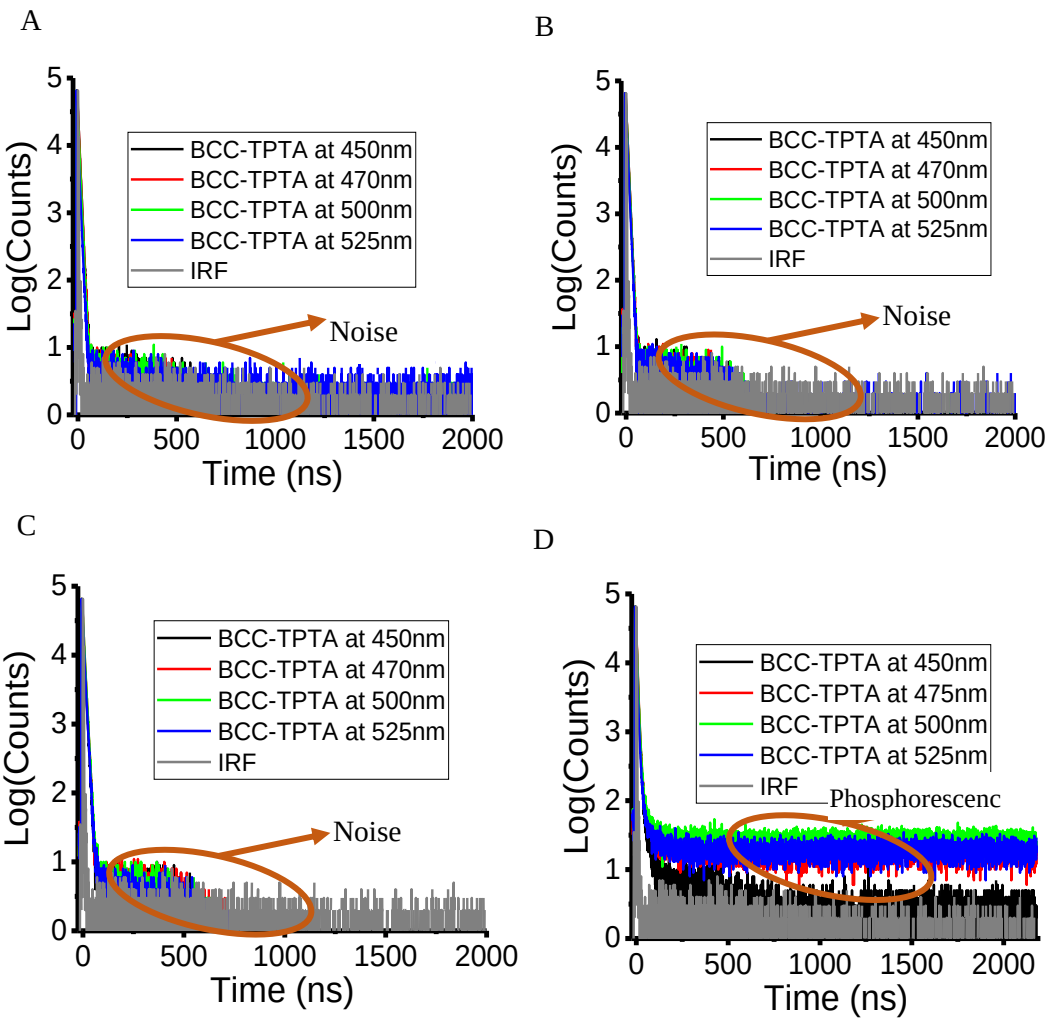

Figure 3.8.5.5. Emissive lifetime characterization at different temperature and different detection wavelengths of BCC-TPTA obtained with the TCSPC technique. Measurements were taken in toluene solutions with a 400 nm excitation wavelength. RT (A), 273 K (B), 195 K (C), and 77 K (D).

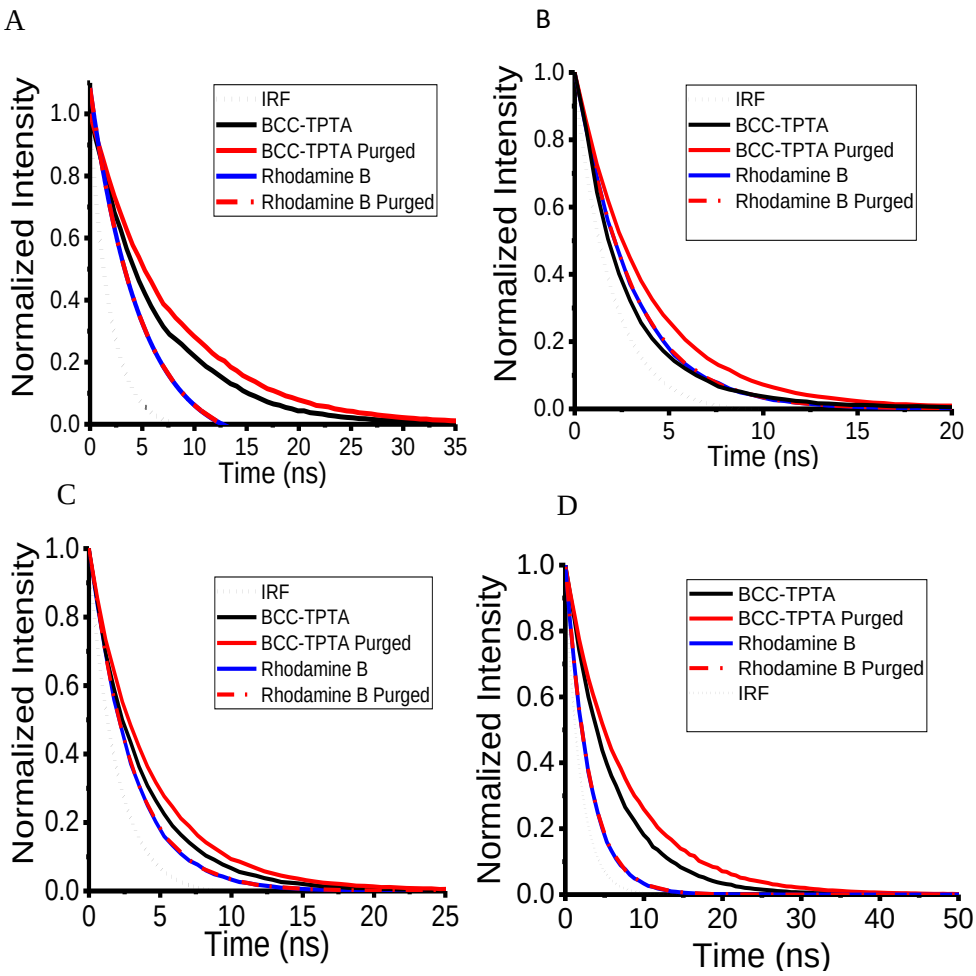

Figure 3.8.5.6. The emissive lifetime of the chromophores was investigated by using Time Correlated Single Photon Counting (TCSPC) technique: BCC-TPTA in toluene (A), BCC-TPTA in hexane (B), BCC-TPTA in cyclohexane (C), and BCC-TPTA in chloroform (D).

Table 3.8.5.1. Fluorescence lifetime of BCC-TPTA in different solvents before and after the oxygen purging process. This measurements were done with the TCSPC technique.

Sample	Emissive lifetime	Emissive lifetime (Purged)
Rhodamine B	2.97 ± 0.03 ns	2.99 ± 0.04 ns
BCC-TPTA in Hexane	2.69 ± 0.02 ns	3.9 ± 0.1 ns
BCC-TPTA in Cyclohexane	3.4 ± 0.1 ns	4.2 ± 0.1 ns
BCC-TPTA in Toluene	6.4 ns	7.8 ns
BCC-TPTA in Chloroform	10 ns	13 ns

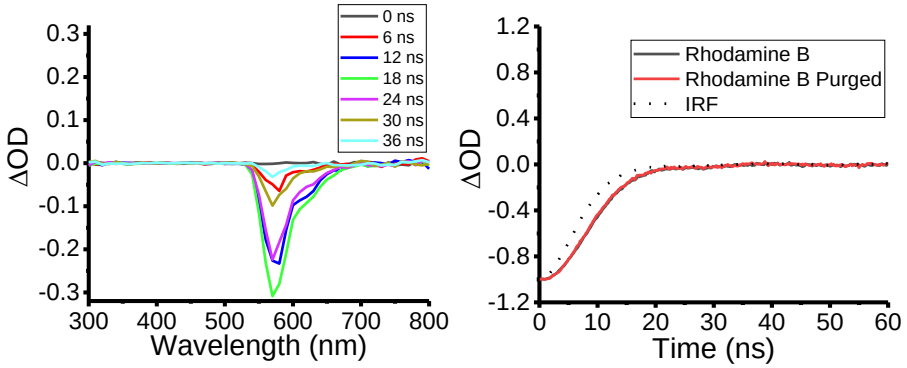

Figure 3.8.5.7. Time-resolved absorption spectra of Rhodamine B after the oxygen purging process (A) and the kinetic trace of its time-resolved absorption spectrum bands before and after the oxygen purging process (B).

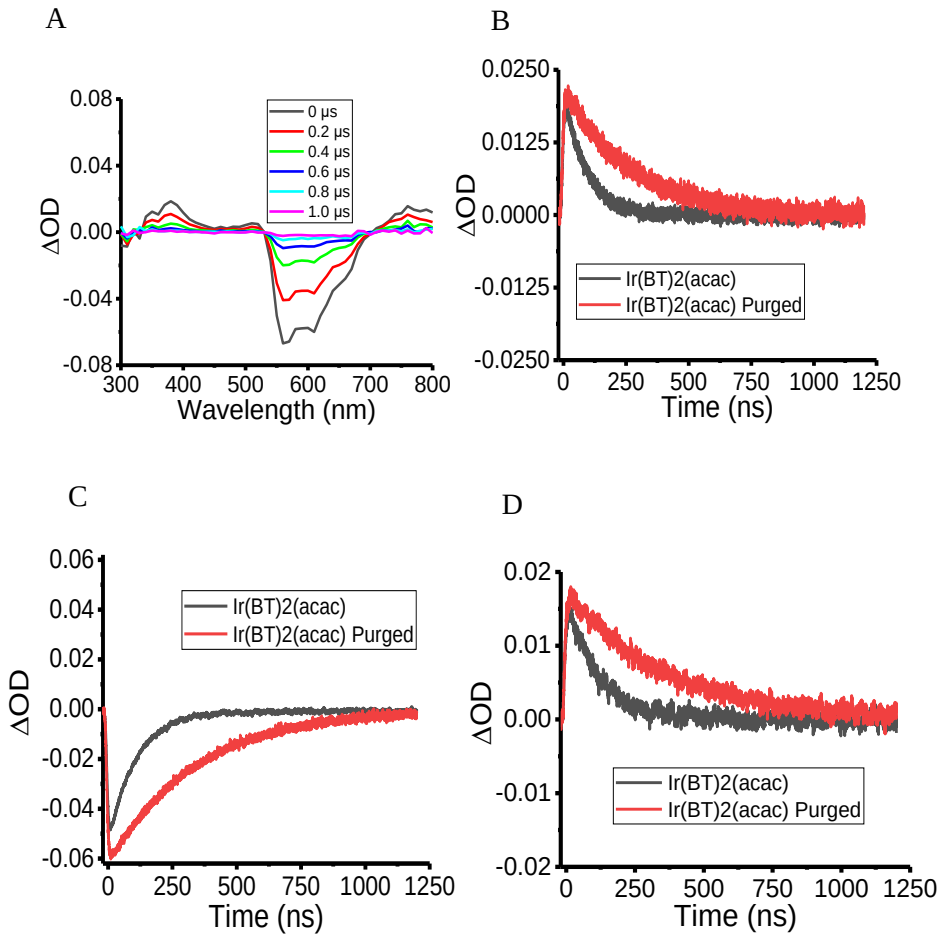

Figure 3.8.5.8. Time-resolved absorption spectrum of the Ir(BT)2acac complex after the oxygen purging process (A). The kinetic traces of the 380 ns ESA (A), 565 nm SE (B), and 780 nm ESA (C) of Ir(BT)2(acac) before and after the oxygen purging process.

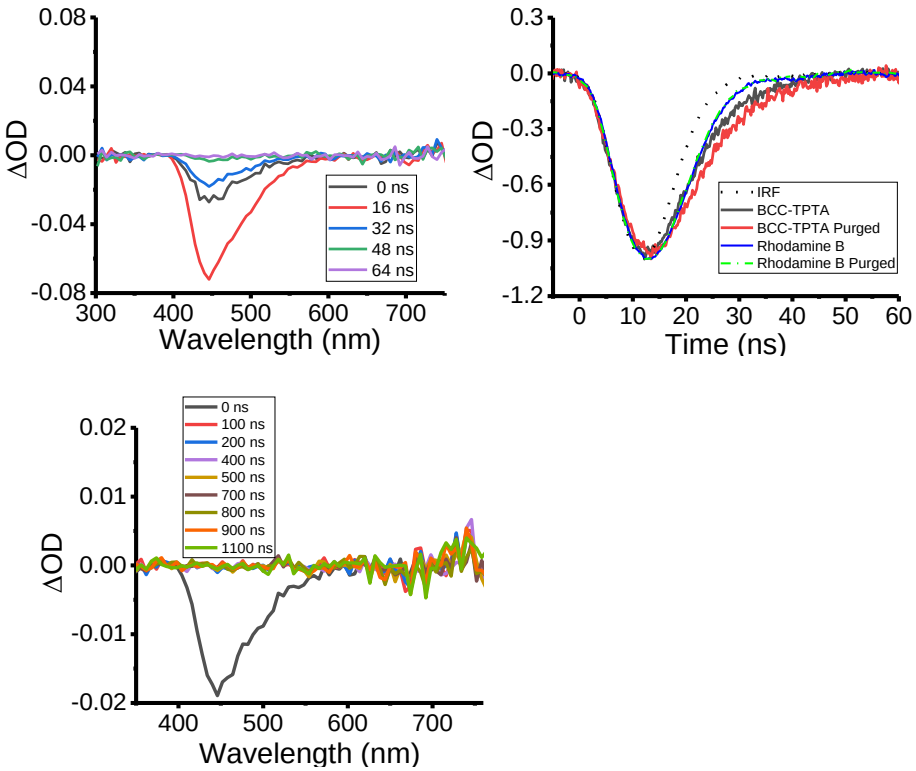

Figure 3.8.5.9. Time-resolved absorption spectra of BCC-TPTA after the oxygen purging process.

Table 3.8.5.2. Emissive lifetime and kinetic traces comparison of the investigated chromophores. The emissive lifetimes where done by the TCSPC technique while the kinetic traces were obtained from the ns TAS measurements.

Chromophore	Emissive Lifetime (TCSPC)	Emissive Lifetime Purged (TCSPC)	Negative OD Kinetic Trace (ns TAS)	Negative OD Kinetic Trace Purged (ns TAS)	ESA Kinetic Trace (ns TAS)	Purged Kinetic trace (ESA) ns TAS
Rhodamine B	2.92 ns	2.96 ns	< 8 ns	< 8 ns	n/a	n/a
$Ir(BT)_2(acac)$	97 ns	1.62 µs	103 ns	> 1 µs	93 ns (350 nm) 112 ns (760nm)	> 400 ns (350 nm) > 500 ns (760nm)
BCC-TPTA	6.4 ns	7.8 ns	10 ns	13 ns	n/a	n/a

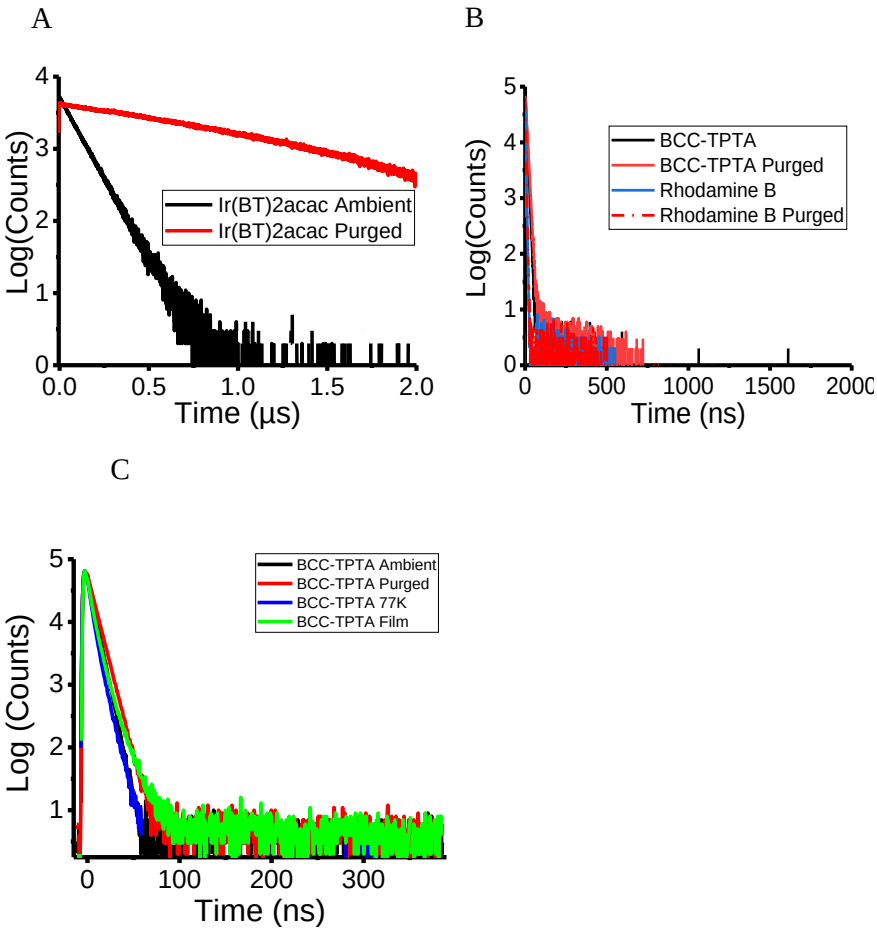

Figure 3.8.5.10. The emissive lifetime of the investigated chromophores probed with the TCSPC technique: Ir(BT)2(acac) (A), BCC-TPTA and Rhodamine B (B), BCC-TPTA in PMMA films and 77K (C).

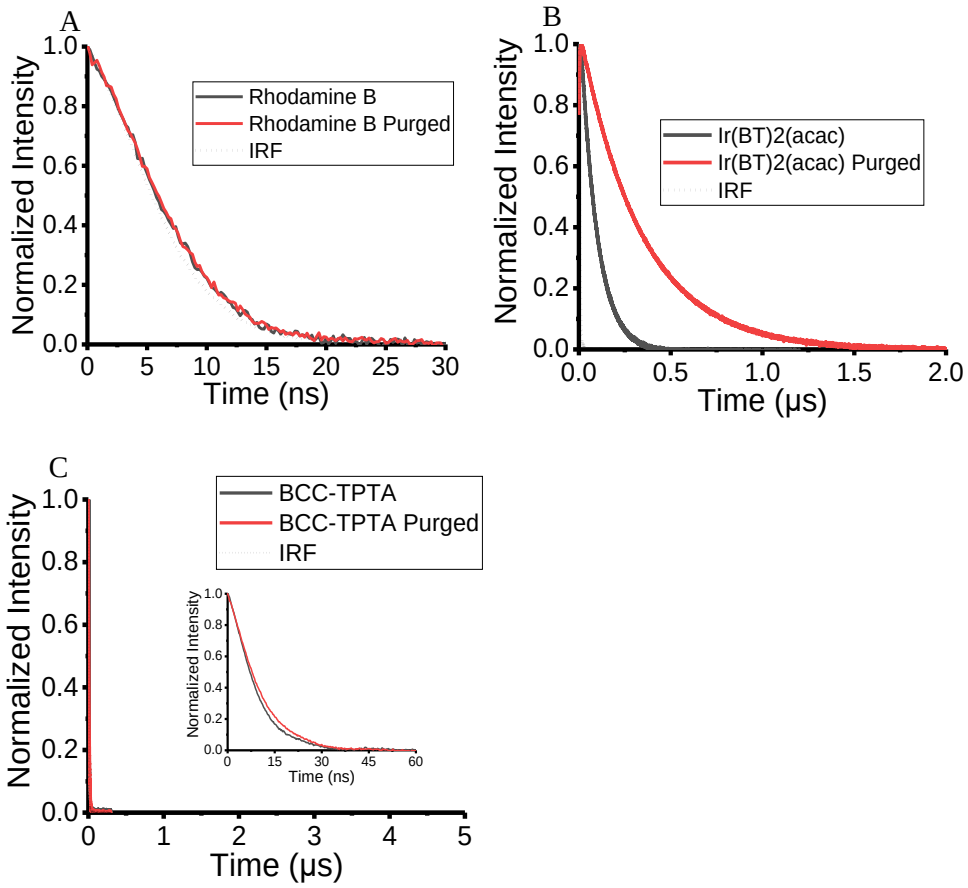

Figure 3.8.5.11. The emissive lifetime of the investigated chromophores probed with the ns TAS technique: Rhodamine B (A), Ir(BT)2(acac) (B), BCC-TPTA (C) in toluene.

Table 3.8.5.3. Emissive lifetime measurements taken with the fluorescence Up-Conversion. (a)Not measurable emission decay from this excited state.

Chromophores	Emissive Lifetime				Emissive Lifetime (Purged)			
	A_1	τ_1 (ps)	A_2	τ_2 (ps)	A_1	τ_1 (ps)	A_2	τ_2 (ps)
Rhodamine B	0.35	> 4000	~	~	0.35	> 4000	~	~
Ir(BT)$_2$(acac)	[a]	[a]	[a]	[a]	[a]	[a]	[a]	[a]
BCC-TPTA	0.14	27	0.65	1040	0.09	21	0.68	1070

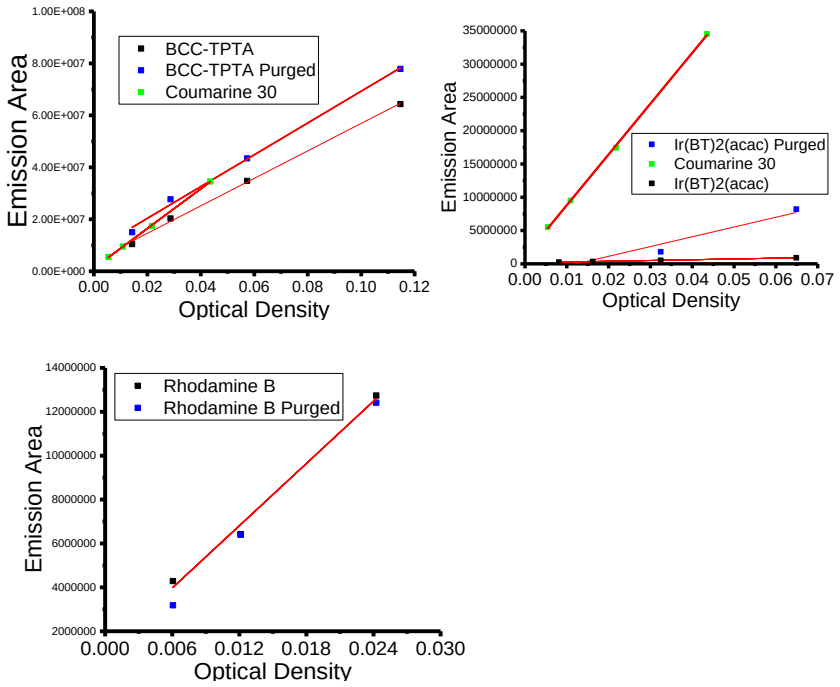

Figure 3.8.5.12. Integrated Area in function of their Optical Density. The slope/gradient of these graph were used for the Quantum Yield calculations.

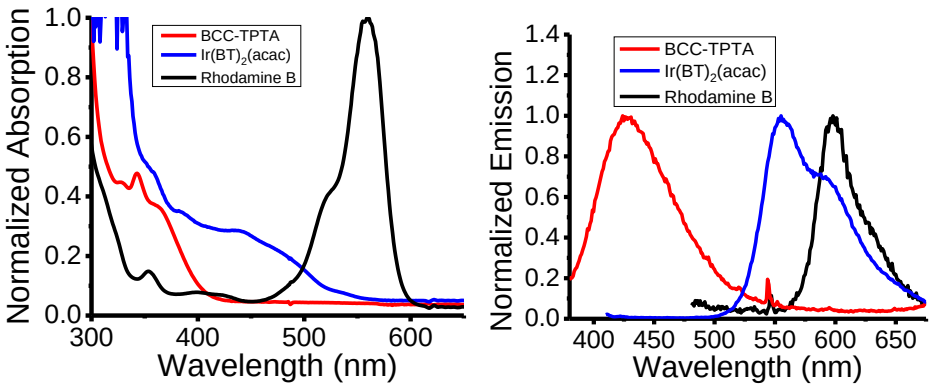

Figure 3.8.5.13. Steady state properties of the investigated chromophores measured in PMMA inert films.

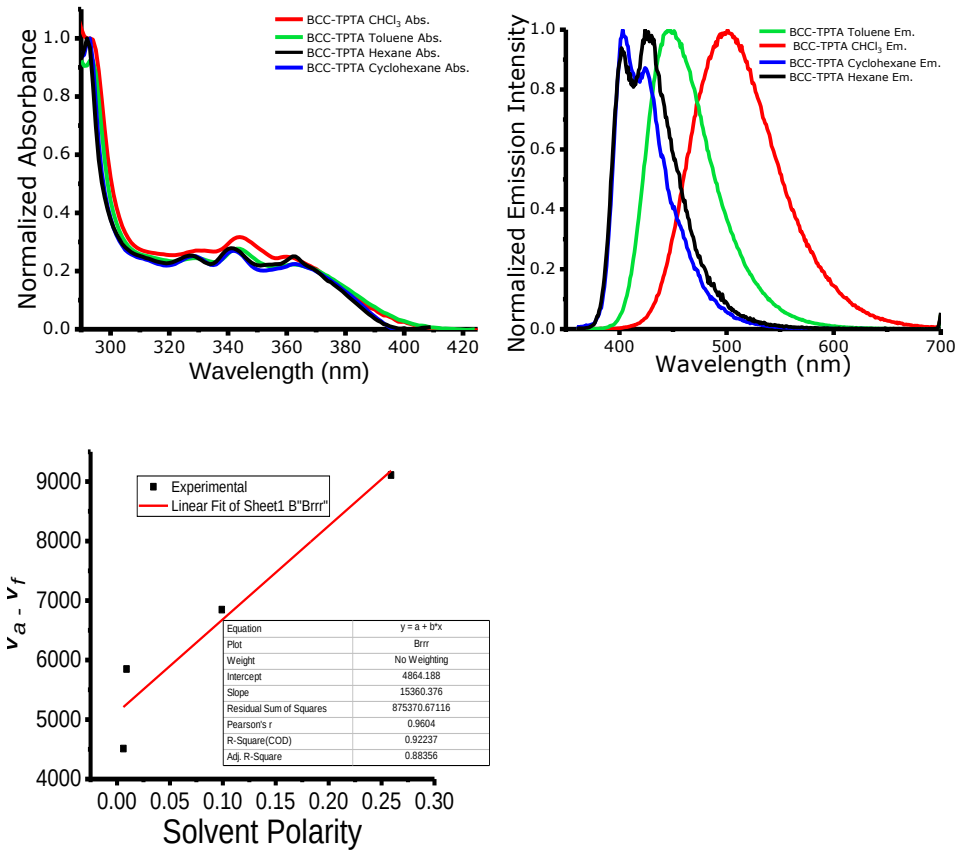

Figure 3.8.5.14. Steady state properties of the investigated chromophores measured in different solvents. From these steady state measurements was extracted the information for the Lippert-Mataga model.

Table 3.8.5.4. Spin−orbit coupling, energy gap between S1 and Tn (ΔEST), and rate constant of ISC process in Rhodamine B. (a) Results in ethylene glycol.

	$S_1 \rightarrow T_1$	$S_1 \rightarrow T_2$	$S_1 \rightarrow T_n$ Expt.[a]
Spin−orbit coupling (cm^{-1})	0.053	0.381	N/A
ΔE_{ST} (eV)	-1.369	-0.623	N/A
k_{ISC} (s^{-1})	2.3×10^{-23}	1.4×10^{4}	5.3×10^{5}

References

(1) Jones, G.; Jackson, W. R.; Choi, C. Y.; Bergmark, W. R. Solvent Effects on Emission Yield and Lifetime for Coumarin Laser Dyes. Requirements for a Rotatory Decay Mechanism. *J. Phys. Chem.* **1985**, *89*, 294–300.

(2) Beaumont, P. C.; Johnson, D. G.; Parsons, B. J. Photophysical Properties of Laser Dyes: Picosecond Laser Flash Photolysis Studies of Rhodamine 6G, Rhodamine B and Rhodamine 101. *J. Chem. Soc. Faraday Trans.* **1993**, *89*, 4185.

(3) Lakowicz, J. R.; Weber, G. Quenching of Fluorescence by Oxygen. a Probe for Structural Fluctuations in Macromolecules. *Biochemistry* **1973**, *12*, 4161–4170.

(4) Schweitzer, C.; Schmidt, R. Physical Mechanisms of Generation and Deactivation of Singlet Oxygen. *Chem. Rev.* **2003**, *103*, 1685–1758.

(5) Ware, W. R. Oxygen Quenching of Fluorescence in Solution: An Experimental Study of the Diffusion Process. *J. Phys. Chem.* **1962**, *66*, 455–458.

(6) Hirata, S.; Sakai, Y.; Masui, K.; Tanaka, H.; Lee, S. Y.; Nomura, H.; Nakamura, N.; Yasumatsu, M.; Nakanotani, H.; Zhang, Q.; et al. Highly Efficient Blue Electroluminescence Based on Thermally Activated Delayed Fluorescence. *Nat. Mater.* **2015**, *14*, 330–336.

(7) Kowalczyk, T.; Tsuchimochi, T.; Chen, P. T.; Top, L.; Van Voorhis, T. Excitation Energies and Stokes Shifts from a Restricted Open-Shell Kohn-Sham Approach. *J. Chem. Phys.* **2013**, *138*, 164101.

(8) Hait, D.; Zhu, T.; McMahon, D. P.; Van Voorhis, T. Prediction of Excited-State Energies and Singlet-Triplet Gaps of Charge-Transfer States Using a Restricted Open-Shell Kohn-Sham Approach. *J. Chem. Theory Comput.* **2016**, *12*, 3353–3359.

(9) Frank, I.; Hutter, J.; Marx, D.; Parrinello, M. Molecular Dynamics in Low-Spin Excited States. *J. Chem. Phys.* **1998**, *108*, 4060–4069.

(10) Okazaki, I.; Sato, F.; Yoshihiro, T.; Ueno, T.; Kashiwagi, H. Development of a Restricted Open Shell Kohn-Sham Program and Its Application to a Model Heme Complex. *J. Mol. Struct. THEOCHEM* **1998**, *451*, 109–119.

(11) Filatov, M.; Shaik, S. A Spin-Restricted Ensemble-Referenced Kohn–Sham Method and Its Application to Diradicaloid Situations. *Chem. Phys. Lett.* **1999**, *304*, 429–437.

(12) Shao, Y.; Gan, Z.; Epifanovsky, E.; Gilbert, A. T. B.; Wormit, M.; Kussmann, J.; Lange, A. W.; Behn, A.; Deng, J.; Feng, X.; et al. Advances in Molecular Quantum Chemistry Contained in the Q-Chem 4 Program Package. *Mol. Phys.* **2015**, *113*, 184–215.

(13) Robinson, G. W.; Frosch, R. P. Electronic Excitation Transfer and Relaxation. *J. Chem. Phys.* **1963**, *38*, 1187–1203.

(14) Lawetz, V.; Orlandi, G.; Siebrand, W. Theory of Intersystem Crossing in Aromatic Hydrocarbons. *J. Chem. Phys.* **1972**, *56*, 4058–4072.

(15) Brédas, J.-L.; Beljonne, D.; Coropceanu, V.; Cornil, J. Charge-Transfer and Energy-Transfer Processes in π-Conjugated Oligomers and Polymers: A Molecular Picture. *Chem. Rev.* **2004**, *104*, 4971–5004.

(16) Schmidt, K.; Brovelli, S.; Coropceanu, V.; Beljonne, D.; Cornil, J.; Bazzini, C.; Caronna, T.; Tubino, R.; Meinardi, F.; Shuai, Z.; et al. Intersystem Crossing Processes in Nonplanar Aromatic Heterocyclic Molecules. *J. Phys. Chem. A* **2007**, *111*, 10490–10499.

(17) Beljonne, D.; Shuai, Z.; Pourtois, G.; Bredas, J. L. Spin-Orbit Coupling and Intersystem Crossing in Conjugated Polymers: A Configuration Interaction Description. *J. Phys. Chem. A* **2001**, *105*, 3899–3907.

(18) Samanta, P. K.; Kim, D.; Coropceanu, V.; Brédas, J. L. Up-Conversion Intersystem Crossing Rates in Organic Emitters for Thermally Activated Delayed Fluorescence: Impact of the Nature of Singlet vs Triplet Excited States. *J. Am. Chem. Soc.* **2017**, *139*, 4042–4051.

(19) Zhang, Q.; Kuwabara, H.; Potscavage, W. J.; Huang, S.; Hatae, Y.; Shibata, T.; Adachi, C. Anthraquinone-Based Intramolecular Charge-Transfer Compounds: Computational Molecular Design, Thermally Activated Delayed Fluorescence, and Highly Efficient Red Electroluminescence. *J. Am. Chem. Soc.* **2014**, *136*, 18070–18081.

Chapter 4

New Direct Approach for Determining the Reverse Intersystem Crossing Rate in Organic TADF Emitters

4.1 Abstract

We developed a new optical method to determine the rate of reverse intersystem crossing (k_{rISC}) in thermally activated delayed fluorescence (TADF) organic chromophores using transient absorption spectroscopy. The k_{rISC} rates determined by our method are in agreement with those estimates from quantum chemical calculations. We correlated the k_{rISC} of the TADF-chromophores with their device performance, with an emphasis in evaluating their efficiency roll-off. It is believed that obtaining a high k_{rISC} is critical for reducing the triplet-triplet annihilation (TTA) mechanism that deteriorates their external quantum efficiency (η_{EQE}) at high brightness levels, an effect known as efficiency roll-off. We found that those chromophores with a high k_{rISC} have reduced efficiency roll-off. This is beneficial for superior device performance. In addition, we found that if the chromophore has a k_{rISC} of $\leq 10^3 s^{-1}$ its device η_{EQE} will be $\leq 5\%$. This suggests that if a chromophore have $k_{rISC} \leq 10^3 s^{-1}$ it becomes TADF-inactive. These observations between TADF active and inactive chromophores based on their k_{rISC} are not possible by using the traditional Masui method. The Masui method revealed k_{rISC} that suggested efficient triplet harvesting despite of device $\eta_{EQE} \leq 5\%$. Our method brings a higher level of accuracy for

determining the k_{rISC} and predicting the device performance of organic chromophores with TADF characteristics that were not achieved before by traditional methods.

4.2 Introduction

Organic light emitting diodes (OLEDs) based on chromophores with thermally activated delayed fluorescence (TADF) characteristics have captivated the attention of the scientific community as a potential replacement to the organometallic-based phosphorescence light emitting diodes (PHOSPHO-LED).[1–6] This is due to improvements including the devices' processability and fabrication, synthetic flexibility for optical tuning, and cost-efficiency.[1,7,8] In addition, these TADF-based OLEDs are able to emulate the high internal quantum efficiencies (η_{IQE}) offered by their PHOSPHO-LED counterparts (~ 100 %).[1,4,9] However, the key challenge hampering their commercialization is their poor device efficiency at high brightness levels, an effect known as efficiency roll-off.[10,11]

The very high η_{IQE} has been ascribed to the conversion of non-emissive triplets into emissive singlets ($T_1 \rightarrow S_1$) in a reverse intersystem crossing process (rISC), which is prompted by the combination of thermal energy with the small energy gap between the singlet-triplet manifolds (ΔE_{ST}).[2,12] The field has primarily used steady-state measurements and microsecond spectroscopy to illustrate and calculate their rate of rISC (k_{rISC}), under the premise that the k_{rISC} may help to predict their device performance.[1,7,13,14] Specifically, it is believed that obtaining a high k_{rISC} is critical for reducing the triplet-triplet annihilation (TTA) mechanism that cause η_{EQE} roll-off.[3,13,15] However, these indirect methods require a combination of selected tools and do not exclude the parallel coexistence of phosphorescence in the chromophore nor the influence of the host material if the measurements are conducted in solid state.[3,16–20] As a result, inaccurate calculations of the k_{rISC} have led to inaccurate predictions of their device performances.[11,13,19,21]

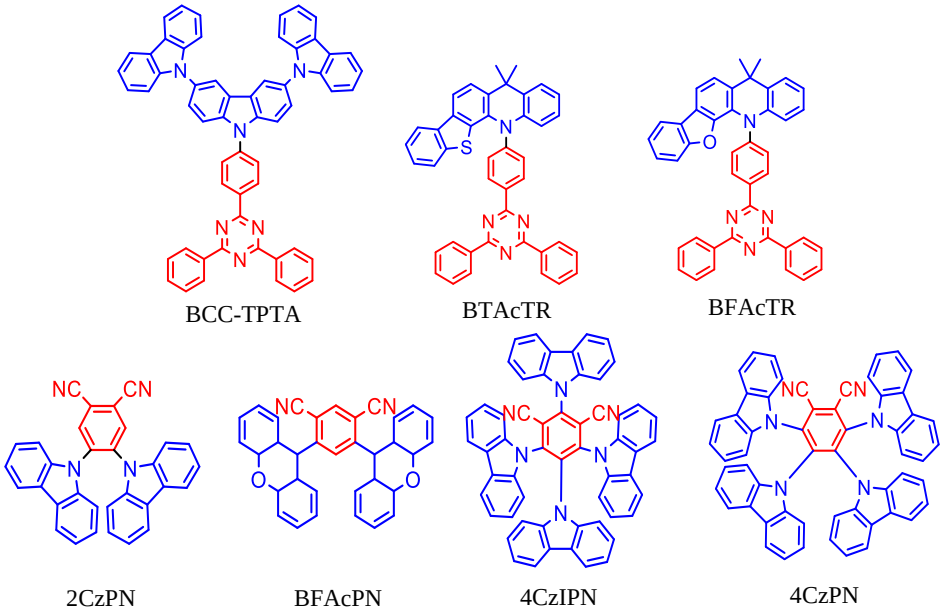

Figure 4.2.1. Molecular structure of the investigated system.

New methodologies, such as nanosecond transient absorption spectroscopy (ns TAS), can provide a powerful tool to examine the photophysical properties of organic chromophores with TADF characteristics. It is interesting to note that while there have been reports of studies investigating the quenching effect of oxygen (O_2) in the emissive properties of highly efficient and well-known TADF structures, there have not been any detailed ns TAS O_2 quenching studies of these promising materials. O_2 has been used for decades as a fundamental molecule for triplet state sensitization, as singlet oxygen is generated by energy transfer from the long-lived triplet state of the excited chromophore to the ground state of O_2.[22–24] The ns TAS is a time-resolved spectroscopic technique that can detect and resolve the dynamics of non-emissive intermediate contributing to the excited state of these chromophores.[25–27] These non-emissive conformers (singlets or triplets) are detected as positive Δ absorption bands, namely excited state absorption (ESA).[28–33] By coupling O_2 with the ns TAS technique, we aim to identify and characterize the ESA bands with a higher O_2 sensitivity, which should be observed in a significant ESA decay

lifetime lengthening (triplets). In this publication, we present the first results of ns TAS spectroscopy to determine the k_{rISC} in organic chromophores with TADF characteristics. A series of chromophores with diverse molecular structures were investigated to demonstrate our methodology (**Figure 4.2.1**). The well-known Masui method for calculating the k_{rISC} was included for comparison.

4.3 Results and Dicsussion

To demonstrate our methodology, the well-known CzPN and BCC-TPTA were used as standards. These chromophores are believed to represent the basic motif of impressive TADF systems and their efficiency set a level of quality for what other materials seek to attain.[1,2,17] Two ESA bands were detected for the CzPN system, which have been previously reported and attributed to triplet state (**Figure 4.3.1A**).[21,27] Similar bands were detected when the measurements were conducted in chloroform (**Figure 4.5.2.7**). As we previously reported, we did not detected ESA bands consistent with triplet state conformers for BCC-TPTA in toluene.[31] This is also true when the measurement was conducted in chloroform (**Figure 4.5.2.7**). This may indicate poor density of triplets. Contrarily, similar ESA bands like the ones obtained for the CzPN system were found for the rest of the investigated systems. Therefore, oxygen sensitization experiments were further carried out to characterize the relaxation pathways of these ESA bands.

As it can be observed for CzPN in **Figure 4.3.1B**, a lengthening in its ESA relaxation dynamics was obtained when the measurements were conducted in O_2-free atmospheres. A very similar mono-exponential decay constant of ~ 1.7 μs (rate = 5.8 x 10^5 s^{-1}) were obtained for both ESA bands, suggesting that they are the same species. Similar behavior was obtained when the measurements were conducted in chloroform. It is important to note that the lengthening in these ESA bands correlates well with CzPN Φ_{TADF} enhancement and its long-lived emissive lifetime

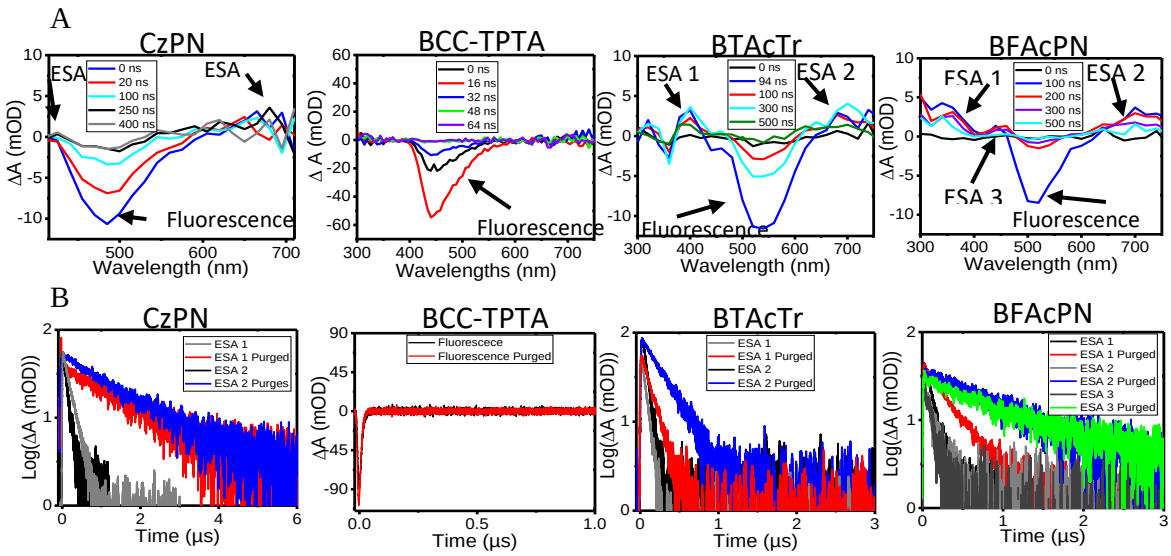

Figure 4.3.1. (A) O_2-free time-resolved absorption spectra of the investigated systems in toluene (PhMe): (B) Relaxation dynamics of the investigated systems before/after the oxygen sensitization experiments.

lengthening carried out under similar conditions (**Figure 4.3.2**). These observations suggest that these ESA bands are critical for the delayed fluorescence process in CzPN.

In the case of BTAcTr, the ESA 2 band showed a higher sensitivity to the presence of O_2 than the ESA 1 band have, and it was observed as a larger lengthening in its relaxation lifetime. This may indicative of the triplet state character for the ESA 2.[24,34] Specifically, a mono-exponential decay with time constant of 310 ns (rate = 3.2 x 10^6 s^{-1}) was obtained for the ESA 2 conformer in toluene (**Figure 4.3.1B**) and 183 ns (rate = 5.6 x 10^6 s^{-1}) in chloroform (**Figure 4.5.2.8**) at O_2-free atmosphere (**Table 4.3.1**). The lengthening in these ESA bands of BTAcTr correlates well with its Φ_{TADF} enhancement and its long-lived emissive lifetime lengthening carried out under similar conditions (**Figure 4.3.2**). These observations highlight the importance of these

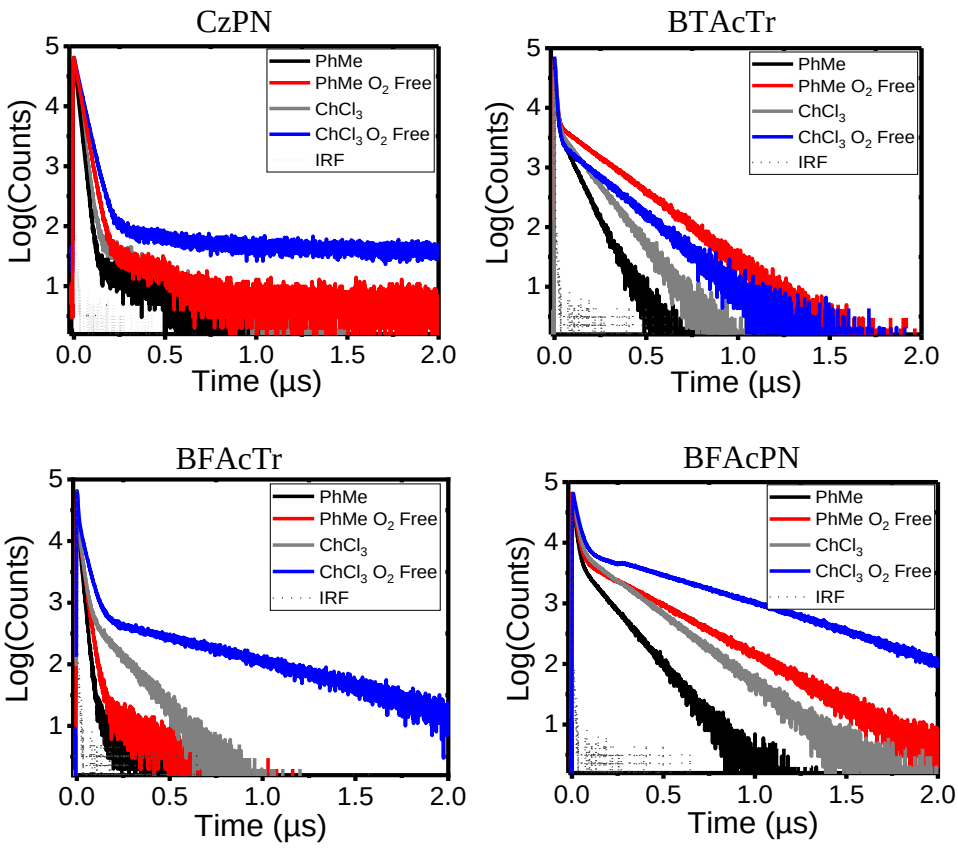

Figure 4.3.2. (A) Emissive lifetime characterization of the investigated system at RT in PhMe and $ChCl_3$.

ESA bands on the emissive properties of BTAcTr, and its O_2 sensitivity suggest that this intermediates belongs to a conformer with triplet state nature.[24] Similar behavior was obtained for the BFAcTr system in chloroform (**Figure 4.5.2.7 and Figure 4.5.2.8**). A mono-exponential decay with time constant of 244 ns (rate = 4.2 x 10^6 s^{-1}) was obtained for the ESA 2 band at O_2-free atmospheres. As with the CzPN and BTAcTr systems, the ESA bands relaxation lengthening of BFAcTr in O2-free atmospheres correlates well with its Φ_{TADF} enhancements and with its long-lived emissive lifetime lengthening carried out under similar conditions (**Figure 4.3.2**). Under these circumstances, we can attribute the ESA 2 band to triplet state conformers. This assignment became more evident when a lack of ESA bands is observed for BFAcTr in toluene solution

(**Figure 4.5.2.7**). This lack of ESA bands correlates well with its very small long-lived emissive component carried out under similar conditions and correlates well with our findings in the pristine BCC-TPTA.

In the case of BFAcPN (**Figure 4.3.1**), three ESA bands were detected with ESA 2 and ESA 3 showing similar sensitivity to the presence of oxygen. Interestingly, a very similar time constant of ~ 1.1 μs (rate = 9.1 x 10^5 s^{-1}) was obtained for them in chloroform and with a very similar time constant of ~ 1.07 μs (rate = 9.3 x 10^5 s^{-1}) was obtained for them in toluene. This observation may indicate that these ESA bands (ESA 2 and ESA 3) corresponds to the same excited state conformer. As with the CzPN, BTAcTr, and BFAcTr systems, the ESA bands relaxation lengthening of BFAcPN in O_2-free atmospheres correlates well with its Φ_{TADF} enhancements and with its long-lived emissive lifetime lengthening carried out under similar conditions (**Figure 4.3.2**). These results further highlight how critical are these ESA bands to the delay fluorescence process in these systems.

The overwhelming evidence of (1) ESA bands relaxation lengthening of the investigated systems in O_2-free atmospheres correlating well with (2) their Φ_{TADF} enhancements, and with (3) their long-lived emissive lifetime lengthening carried out under similar conditions suggest that part of the non-emissive triplet state density is converted into emissive singlets, namely via a rISC mechanism. To quantify its rate conversion (k_{rISC}) we use the deactivation rates of these O_2 sensitive ESA bands at O_2-free atmospheres and multiply them by its emissive factor, the Φ_{TADF} ($k_{rISC} = \Phi_{TADF} * k_{ESA}$). A rate of $1.0x10^4 s^{-1}$, $7.2x10^5 s^{-1}$, $4.6x10^5 s^{-1}$, and $9.8x10^4 s^{-1}$ were obtained in chloroform solutions for 2CzPN, BTAcTr, BFAcTr, and BFAcPN systems, respectively. These rates and their trends are in good agreement with those obtained by quantum chemical simulations

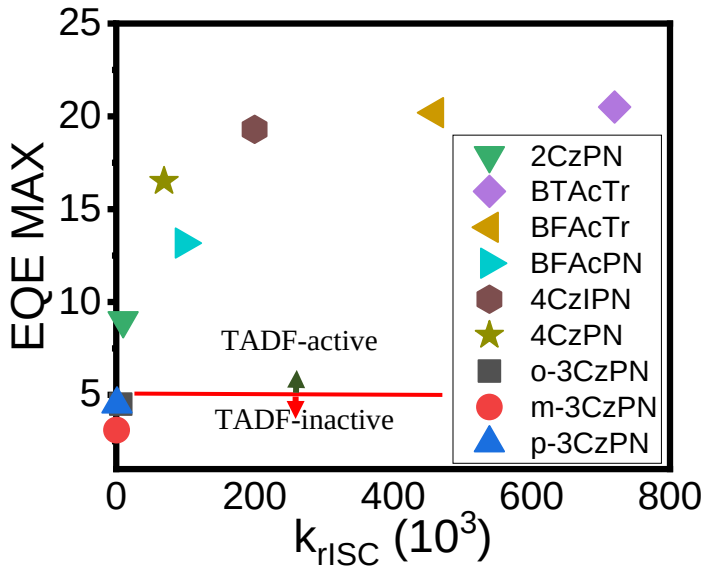

Figure 4.3.3. Correlating the Device EQE with the k_{rISC}

(QCS) in this study and those published by Brédas (**Table 4.3.1**).[5] We used the k_{rISC} determined by our methodology and correlated them with their device performances under the same device architectures. We were not surprised to see a proportional relationship between the k_{rISC} and η_{EQE} (**Figure 4.3.3**), and those TADF chromophores with the larger k_{rISC} showed the higher η_{EQE}. Specifically, η_{EQE} of 9%, 21.8%, 20.4%, and 13.2% for 2CzPN, BTAcTr, BFAcTr, and BFAcPN systems were reported, respectively. We further use our methodology to determine the k_{rISC} of TADF chromophores from the limited TAS data available in the literature to further validate our methodology. A proportional relationship between the k_{rISC} and the η_{EQE} were obtained for 4CzIPN and 4CzPN, and a k_{rISC} of $2.2\text{x}10^5 s^{-1}$ and $6.9\text{x}10^4 s^{-1}$ correlating well with η_{EQE} of 19.3% and 16.5 were observed, respectively.[2,35] It is interesting to note that if the chromophore (o-CzBN, m-CzBN, p-CzBN) possess a $k_{rISC} \leq 10^3 s^{-1}$, an $\eta_{EQE} \leq 5\%$ is obtained (**Table 4.5.2.1**). This indicates the minimum k_{rISC} that a TADF chromophore must possess to be able to harvest triplet-excitons via a rISC process and be a TADF-active emitter.

Table 4.3.1. Photophysical properties and device performances summary of the TADF-active systems. The rate of rISC was calculated following the equation: $k_{rISC} = \Phi_{TADF} * k_{ESA}$. [a]$EQE_{MAX}$ = maximum EQE value, EQE_{1000} = EQE measured at 1000 $cd.m^{-2}$.

Chromophore	k_{rISC} 10^5 s^{-1} (OS-TAS) (PhMe/ChCl3)	k_{rISC} 10^5 s^{-1} (QCS)	k_{rISC} 10^5 s^{-1} (Masui) (PhMe/ChCl3)	EQE_{MAX}/EQE_{1000} ($cd.cm^{-2}$)
2CzPN	0.11/0.22	0.12[5]	0.87[36],0.06[21]/ 6.0	9/4.0 (55%)
BCC-TPTA	Poor	69 [31]	n/a	16.8/5[1,11] (76%)
BTAcTr	7.3/7.2	11.6	297/765	21/20[37] (5%)
BFAcTr	Poor/4.6	8.32	4100/103	20.4/17[37] (15%)
BFAcPN	0.80/98	1.87	232/145	13.17/12.9 (2.1%)
4CzIPN	2.0	49.2[5]	27[21]/140[38]	19.3/18 [35] (6.7%)
4CzPN	0.69	n/a	4.65	16.5/16 [35] (10%)

It is believed that TADF emitters with a large k_{rISC} may reduce the TTA mechanism that induce the η_{EQE} roll-off in OLEDs.[1,3,15,25] In the case of the chromophroes with triazine as the acceptor, a reduced η_{EQE} roll-off was observed for BTAcTr (5%) while the higher η_{EQE} roll-off was observed for BCC-TPTA (76%), which its lack of ESA bands suggest minimal triplet exciton conversion to singlet excitons (**Figure 4.5.2.2**).[31] In the case of the TADF chromophores with benzonitrile functionalities as the acceptor, reduced η_{EQE} roll-offs were found for BFAcPN (2.1%), 4CzIPN (6%), and 4CzPN (10%) in comparison with that of 2CzPN (55).[2,35] These observations are also consistent with obtaining a large k_{rISC} and reducing the η_{EQE} roll-offs (**Figure 4.5.2.2**).

The Masui methodology of calculating the k_{rISC} was included for comparison purposes.[17] Rates of $6.0x10^5s^{-1}$, $7.7\ x10^7s^{-1}$, $1.0x10^7s^{-1}$, and $1.5x10^7s^{-1}$ were obtained in chloroform solutions for 2CzPN, BTAcTr, BFAcTr, and BFAcPN, respectively. This trend correlates well with those obtained by our method and follows the trend in device efficiencies. However, this method fails to

explain the device prtormances when the k_{rISC} are obtained in toluene solutions. In addition, the k_{rISC} obtained by the Masui method could be at least two order of magnitudes larger than those obtained by our methodology and by QCS, which suggest that it can overestimate the k_{rISC}. This overestimation becomes more evident when we evaluate the literature evidence (**Table 4.5.2.1**). It is interesting to note that $\eta_{EQE} \leq 5$ %, which implies TADF-inactive emitters,[21] could be obtained for some chromophores (o-CzBN and p-CzBN) whose k_{rISC} determined by the Masui method were within the same order of magnitude ($10^4 s^{-1}$) as with TADF-active emitters including 2CzPN and BFAcPN. In contrast, our methodology showed consistency in obtaining large k_{rISC} with high η_{EQE}, large k_{rISC} with reduced η_{EQE} roll-offs, and in obtaining $k_{rISC} \leq 10^3 s^{-1}$ with $\eta_{EQE} \leq 5\%$. These observations suggest superior accuracy for the rISC illustration and direct k_{rISC} determination by our methodology over the well-known Masui methodology.

4.3 Conclusions

In summary, we developed a new optical strategy for the direct determination of the k_{rISC} in organic chromophores with TADF characteristics. Our methodology allowed us to: 1) directly characterize the triplet state dynamics for determining the k_{rISC} in organic TADF chromophores, 2) highlight the importance of achieving a large k_{rISC} for obtaining a high η_{EQE} and for reducing the efficiency roll-off of TADF-OLEDs, and 3) highlight the importance of having $k_{rISC} > 10^3 s^{-1}$ for obtaining TADF-active molecules with $\eta_{EQE} > 5\%$. These demarcations were not possible by the well-known Masui methodology. This work may facilitate the excited state characterization of organic chromophores with TADF characteristics and will help to demarcate the potential top TADF candidates for superior device performances before time-consuming device fabrication techniques are employed.

References

(1) Hirata, S.; Sakai, Y.; Masui, K.; Tanaka, H.; Lee, S. Y.; Nomura, H.; Nakamura, N.; Yasumatsu, M.; Nakanotani, H.; Zhang, Q.; Shizu, K; Miyazaki, H.; Adachi, C. *Nat. Mater.* **2015**, *14*, 330-336.

(2) Uoyama, H.; Goushi, K.; Shizu, K.; Nomura, H.; Adachi, C. *Nature*, **2012**, *492*, 234-238.

(3) Dias, F. B.; Bourdakos, K. N.; Jankus, V.; Moss, K. C.; Kamtekar, K. T.; Bhalla, V.; Santos, J.; Bryce, M. R.; Monkman, A. P. *Adv. Mater.* **2013**, *25*, 3707-3714.

(4) Liu, Y.; Li, C.; Ren, Z.; Yan, S.; Bryce, M. R. *Nat. Rev. Mater.* **2018**, *3*, 18020.

(5) Samanta, P. K.; Kim, D.; Coropceanu, V.; Brédas, J. L. *J. Am. Chem. Soc.* **2017**, *139*, 4042-4051.

(6) Tao, Y.; Yuan, K.; Chen, T.; Xu, P.; Li, H.; Chen, R.; Zheng, C.; Zhang, L.; Huang, W. *Adv. Mater.* **2014**, *26*, 7931-7958.

(7) Kaji, H.; Suzuki, H.; Fukushima, T.; Shizu, K.; Suzuki, K.; Kubo, S.; Komino, T.; Oiwa, H.; Suzuki, F.; Wakamiya, A.; Murata, Y.; Adachi, C. *Nat. Commun.* **2015**, *6*, 8476.

(8) Chan, C. Y.; Tanaka, M.; Nakanotani, H.; Adachi, C. *Nat. Commun.* **2018**, *9*, 5036.

(9) Cui, L.-S.; Deng, Y.-L.; Tsang, D. P.-K.; Jiang, Z.-Q.; Zhang, Q.; Liao, L.-S.; Adachi, C. *Adv. Mater.* **2016**, *28*, 7807-7807.

(10) Cui, L. S.; Ruan, S. Bin; Bencheikh, F.; Nagata, R.; Zhang, L.; Inada, K.; Nakanotani, H.; Liao, L. S.; Adachi, C. *Nat. Commun.* **2017**, *8*, 2250.

(11) Jeon, S. K.; Lee, H. L.; Yook, K. S.; Lee, J. Y. *Adv. Mater.* **2019**, 1803524.

(12) Youn Lee, S.; Yasuda, T.; Nomura, H.; Adachi, C. *Appl. Phys. Lett.* **2012**, *10*, 093306.

(13) Noda, H.; Nakanotani, H.; Adachi, C. *Sci. Adv.* **2018**, *4*, eaao6910.

(14) Nakanotani, H.; Masui, K.; Nishide, J.; Shibata, T.; Adachi, C. *Sci. Rep.* **2013**, *3*, 2127.

(15) Inoue, M.; Serevičius, T.; Nakanotani, H.; Yoshida, K.; Matsushima, T.; Juršenas, S.; Adachi, C. *Chem. Phys. Lett.* **2016**, *644*, 62–67.

(16) Jankus, V.; Data, P.; Graves, D.; McGuinness, C.; Santos, J.; Bryce, M. R.; Dias, F. B.; Monkman, A. P. *Adv. Funct. Mater.* **2014**, *24*, 6178-6186.

(17) Masui, K.; Nakanotani, H.; Adachi, C. *Org. Electron.* **2013**, *14*, 2721-2726.

(18) S Serevičius, T.; Bučiūnas, T.; Bucevičius, J.; Dodonova, J.; Tumkevičius, S.; Kazlauskas, K.; Juršėnas, S. *J. Mater. Chem. C.* **2018**, *6*, 11128–11136.

(19) Yang, Z.; Mao, Z.; Xie, Z.; Zhang, Y.; Liu, S.; Zhao, J.; Xu, J.; Chi, Z.; Aldred, M. P. ***Chem. Soc. Rev.*** **2017**, ***46***, 915-1016.

(20) Chen, X. K.; Tsuchiya, Y.; Ishikawa, Y.; Zhong, C.; Adachi, C.; Brédas, J. L. *Adv. Mater.* **2017**, *29*, 1702767.

(21) Hosokai, T.; Matsuzaki, H.; Nakanotani, H.; Tokumaru, K.; Tsutsui, T.; Furube, A.; Nasu, K.; Nomura, H.; Yahiro, M.; Adachi, C. *Sci. Adv.* **2017**, *3*, e1603282.

(22) Grewer, C.; Brauer, H. D. *J. Phys. Chem.* **1994**, *98*, 4230-4235.

(23) Schweitzer, C.; Schmidt, R. *Chem. Rev.* **2007**, *103*, 1685-1758.

(24) Scurlock, R. D.; Wang, B.; Ogilby, P. R.; Sheats, J. R.; Clough, R. L. *J. Am. Chem. Soc.* **1995**, *117*, 10194-10202.

(25) Kuang, Z.; He, G.; Song, H.; Wang, X.; Hu, Z.; Sun, H.; Wan, Y.; Guo, Q.; Xia, A. *J. Phys. Chem. C.* **2018**, *122*, 3727-3737.

(26) Whittemore, T. J.; White, T. A.; Turro, C. *J. Am. Chem. Soc.* **2018**, *140*, 229-234.

(27) Peng, J.; Guo, X.; Jiang, X.; Zhao, D.; Ma, Y. *Chem. Sci.* **2016**, *7*, 1233-1237.

(28) Tang, K. C.; Liu, K. L.; Chen, I. C. *Chem. Phys. Lett.* **2004**, *386*, 437-441.

(29) Ramakrishna, G.; Goodson, T.; Joy, E. R. H.; Cooper, T. M.; McLean, D. G.; Urbas, A. *J. Phys. Chem. C* **2009**, *113*, 1060-1066.

(30) Kim, H.; Keller, B.; Ho-Wu, R.; Abeyasinghe, N.; Vázquez, R. J.; Goodson, T.; Zimmerman, P. M. *J. Am. Chem. Soc.* **2018**, *140*, 7760-7763.

(31) Vázquez, R. J.; Kim, H.; Zimmerman, P. M.; Goodson, T. *J. Mater. Chem. C.* **2019**, *7*, 4210-4221.

(32) Bergmann, L.; Hedley, G. J.; Baumann, T.; Bräse, S.; Samuel, I. D. W. *Sci. Adv.* **2016**, *2*, e1500889.

(33) Keller, B.; Cai, Z.; Muthike, A. K.; Sahu, P. K.; Kim, H.; Eshun, A.; Zimmerman, P. M.; Zhang, D.; Goodson, T. *J. Phys. Chem. C* **2018**, *122*, 27713-27733.

(34) McLean, A. J.; McGarvey, D. J.; Truscott, T. G.; Lambert, C. R.; Land, E. J. *J. Chem. Soc. Faraday Trans.* **1990**, *86*, 3075.

(35) Adachi, C. *Jpn. J. Appl. Phys.* **2014**, *53*, 060101.

(36) Wong, M. Y.; Krotkus, S.; Copley, G.; Li, W.; Murawski, C.; Hall, D.; Hedley, G. J.; Jaricot,

M.; Cordes, D. B.; Slawin, A. M. Z.; Oliver, Y.; Beljonne, D.; Muccioli, D.; Moral, M.; Sancho-García, J. C.; Gather, M. C.; Samuel, I. D. W.; Zysman-Colman, E. *ACS Appl. Mater. Interfaces* **2018**, *10*, 33360-33372.

(37) Kang, Y. J.; Yun, J. H.; Han, S. H.; Lee, J. Y. *J. Mater. Chem. C*, **2019**, *7*, 4573-4580.

(38) Ishimatsu, R.; Matsunami, S.; Shizu, K.; Adachi, C.; Nakano, K.; Imato, T. *J. Phys. Chem. A* **2013**, *117*, 5607-5612.

4.5 Supporting Information

4.5.1 Materials and Experimental Techniques

The BCC-TPTA chromophore was purchased from Luminescence Technology Corporation. The BFAcTr, BTAcTr, and BFAcPN systems were synthesized according to the literature.[36]

Sample Preparation and Experimental Sample Handling: A stock solution (10^{-4} M) were prepared by mixing each sample in the corresponding solvent. Toluene, THF, and Ethanol were the solvent used for BCC-TPTA, $Ir(BT)_2(acac)$, and the Rhodamine B, respectively. Consequent dilutions from the stock solutions were made on each sample to run the different experiments conducted in this report. A 400 nm excitation wavelength was used in all experimental set-ups and for all the chromophores while their emissive lifetime were measured at their respective emissive λ_{MAX}. In all cases, including the temperature dependence measurements, emission quenching from purging out oxygen is carried out. Specifically, the oxygen free atmosphere was created by bubbling N_2 thought the solution for at least 12 minutes. The 12 minutes criteria was based on the reproducibility of the emission spectrum intensity, quantum yield, and emissive lifetime characterization of the investigated systems.

Steady State Measurements: The absorption spectra were measured on an Agilent 8341 spectrophotometer while the emission spectra were collected on a Fluoromax-4 fluorimeter with slits set at 2.5 nm and an integration time of 0.100 s. Quartz cells with 10 mm path length were used for all the steady-state measurements, including the quantum yield calculations. All steady state optical measurements were carried out at ambient conditions unless otherwise stated in the figure caption. The low temperature emission (phosphorescence) spectrum were obtained by using a Photon Technologies International (PTI), QuantaMaster 400 scanning spectrofluorometer. The emission spectrum of the samples at low temperature (77K) were obtained after a delay > 300 μs between the excitation beam and detection.

Fluorescence Quantum Yield Calculation: The Williams comparative method was used to calculate the fluorescence quantum yields of the systems as described elsewhere.[31,38,39] The optical density was maintained around 0.10 or below to avoid reabsorption and internal filter effects in the measurements. The absorption and fluorescence were measured for at least four samples with systematic decreasing concentrations. The quantum yield was calculated using the following equation:

$$\phi_x = \phi_{STD} \frac{Grad_x \eta_x^2}{Grad_{STD}\, \eta_{STD}^2}$$ **Equation 4.5.1.1**

were Φ_x is the calculated quantum yield, η is the refractive index of the solvent, and $Grad$ is the slope obtained from plotting the fluorescence area vs the optical density (OD). The quantum yields for BFAcTr, BTAcTr, and BFAcPN were measured in toluene and chloroform solutions using BCC-TPTA (57 %)[1,31] dissolved in toluene as the standard. The same is true for the Φ_x measurements at oxygen free atmospheres. N_2 bubbling was the method to remove oxygen from the solution (12 minutes). The emission spectra were collected on a Fluoromax-4 fluorimeter with slits set at 1.5 nm and an integration time of 0.100 s. Quartz cells with 10 mm path lengths were used for all the steady-state measurements. All optical measurements were carried out at STP.

Masui method for the indirect k_{rISC} calculation: The rate of reverse intersystem crossing (k_{rISC}) was calculated followed by the equation:

$$k_{rISC} = \frac{k_p k_d \phi_{TADF}}{k_{ISC} \phi_F}$$ **Equation 4.5.1.2**

were ϕ_F is the quantum yield at oxygen rich atmospheres, ϕ_{TADF} is the delayed fluorescence quantum yield ($\phi_{OxygenFree} - \phi_F$), k_p is the rate of fluorescence (1/fluorescence lifetime), k_d the rate of delayed fluorescence (1/DF lifetime), and k_{ISC} is the rate of intersystem crossing ($(1- \phi_F)*k_p$).[17]

Time-Resolved Fluorescence and Phosphorescence Measurements: The time-correlated single photon counting (TCSPC) technique was used to measure the time-resolved fluorescence and phosphorescence of the investigated systems. The laser used for the TCSPC measurement was a Kapteyn Murnane (KM) mode-locked Ti-sapphire laser with a beam at 800 nm wavelength, with a pulse duration of ~30 fs. The output beam was frequency-doubled using a nonlinear barium borate (BBO) crystal to obtain a 400 nm beam as the excitation beam and a polarizer was used to vary the power of the excitation beam. The excitation light was focused on the sample cell using a lens of focal length 11.5 cm. Collection of fluorescence was done in a perpendicular direction of the excitation source. The incident fluorescence beam is focused into a monochromator, and the output from the monochromator was coupled to a photomultiplier tube, which convert the photons into counts.

Nanosecond Transient Absorption Spectroscopy Measurements: The absorption and lifetime of the emissive and non-emissive transient species can be fully characterizied by using this transient absorption spectroscopy technique, which has been previously described.[31,33] These measurements were done in dilute solutions and in the same solvent in which the other photophysical characterizations were carried out, unless otherwise described in the caption. A LP980 (Edinburgh) system, which contains the PMT(PMT-LP), was coupled with a Spectra-Physics QuantaRay Nd:YAG nanosecond pulsed laser and a GWU Optical Parameter Oscillator (OPO) tunable from 250 nm to 2600 nm for the excitation source. For this investigation, a 350nm and 415 nm excitation was used to pump the molecules to the excited state and a pulsed xenon lamp (300-800 nm) white light continuum source was used for probing the excited state.

Quantum Chemical Simulation: The rate of reverse intersystem crossing (k_{rISC}) can be calculated via Fermi's Golden rule,[8,9]

$$k_{\mathrm{rISC}} = \frac{2\pi}{\hbar}\rho_{FC}|\langle S|H_{\mathrm{SO}}|T\rangle|^2 \qquad \textbf{Equation 4.5.1.3}$$

where $\langle S|H_{SO}|T\rangle$ is the spin−orbit coupling element between singlet (S) and triplet (T), ρ_{FC} denotes the Franck−Condon−weighted density of states, and $\hbar$ is the reduced Planck constant of 6.582×10^{-16} eVs. The Franck−Condon−weighted density of states is evaluated with Marcus−Levich−Jortner theory,[10,11]

$$\rho_{\mathrm{FC}} = \frac{1}{\sqrt{4\pi\lambda_{\mathrm{M}}k_BT}}\sum_{n=0}^{\infty}\exp(-S)\frac{S^n}{n!}\exp\left[-\frac{(\Delta E_{\mathrm{ST}}+n\hbar\omega_{\mathrm{eff}}+\lambda_{\mathrm{M}})^2}{4\pi\lambda_{\mathrm{M}}k_BT}\right] \qquad \textbf{Equation 4.5.1.4}$$

where λ_{M} is the Marcus reorganization energy associated with the intermolecular and intramolecular low−frequency vibrations, k_{B} is for Boltzmann constant of 8.6173×10^{-5} eV/K, T is the temperature (in this study, room temperature of 298.15 K), $\hbar\omega_{\mathrm{eff}}$ represents the effective energy of a mode representing the nonclassical high−frequency intramolecular vibrations. Huang−Rhys factor associated with these modes are given as S. ΔE_{ST} indicates singlet-triplet energy gap which can be calculated as $E[T]$-$E[S]$ for rISC processes. One recent computational study on TADF mechanism discussed the rate of rISC within the same framework used in this work.[12] They computed the contribution of nonclassical intramolecular vibrations, and estimated the Marcus reorganization energy due to low−frequency intramolecular vibrations and the medium−induced

relaxation effects to be in the range of ~0.1—0.2 eV.[11,13] The approximation setting λ_M to 0.1 or 0.2 eV reproduced available experimental k_{rISC} values on the same order of magnitude. The close examination revealed that use λ_M value of 0.2 eV gave better quantitative agreement with the available experimental k_{rISC} data. Therefore, λ_M value was set to 0.2 eV in this study. In addition, they assumed the Huang−Rhys factors can be neglected without significant changes to the results for large molecules. With these conditions, the k_{rISC} values could be estimated with quantum chemically computed ΔE_{ST} and H_{SO}.

Quantum chemical simulations were performed to understand the k_{rISC} of three chromophores. The ground state geometries were determined using density functional theory (DFT). The range-separated functional, ωB97X-D, was employed with 6-31G* basis sets. The first singlet excited state (S_1) geometries were located with time-dependent DFT (TDDFT). The same functional and the basis sets employed in the ground state geometry optimization were used. The computational benchmark study reported by H. Sun, C. Zhong, and J.-L. Brédas showed that vertical singlet-triplet energy gaps obtained from nonempirically tuned range-separated functionals are highly reliable.[14] The range-split parameter ω is tuned to minimize the square sum of the difference between HOMO energy (ϵ_{HOMO}) and ionization potential (IP), and LUMO energy (ϵ_{LUMO}) and electron affinity (EA), $(\epsilon_{HOMO}+IP)^2+(\epsilon_{LUMO}+EA)^2$. It is reported that the ω value is significantly affected by the environment such as the inclusion of solvent dielectric field effect.[15] The optimal values of ω are given as 0.008, 0.008, and 0.010 for BTAcTr, BFAcTr, and BFAcPN, respectively, when solvent (chloroform, dielectric constant of 4.31) is included using a polarizable continuum model. The nonempirically tuned ωB97X-D, ω^*B97X-D, was employed to predict vertical excitation energies and spin-orbit coupling element between singlets and triplets at the S_1 geometries. For spin-orbit coupling element calculations, the one-electron Breit-Pauli Hamiltonian was used. All quantum chemical simulations were performed with Q-Chem 5.0.

4.5.2 Experimental and Theoretical Techniques

Table 4.5.2.1. Rate of rISC comparison for the TADF-inactive chromophores.

Chromophore	Φ_{TADF} (PhMe/ChCl3)	k_{rISC} 10^5 s^{-1} (OS-TAS) (PhMe/ChCl3)	k_{rISC} 10^5 s^{-1} (QCS)	k_{rISC} 10^5 s^{-1} (Masui) (PhMe/ChCl3)	EQE_{MAX}
O-3CzBN	10[16]/21[17]	0.066	n/a	0 [16,17] /0.30 [17]	4.5 [16]
M-3CzBN	2[16]/18[17]	0.00512	n/a	0 [16,17]/0.064 [17]	3.1[16]
P-3CzBN	4[16]/25[17]	0.0114	n/a	0.120[16,17]/ 0.20 [17]	4.5 [16]

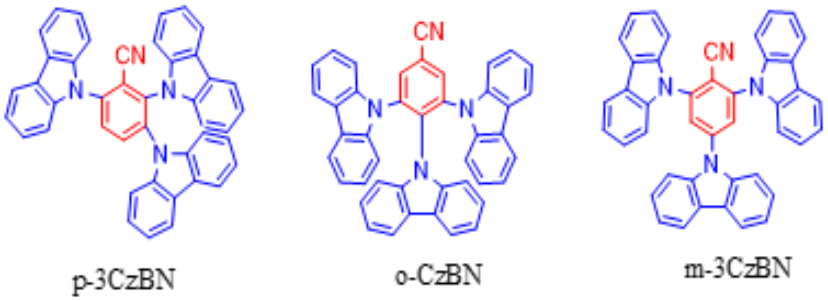

Figure 4.5.2.1. Molecular structure of the TADF-inactive chromophores.

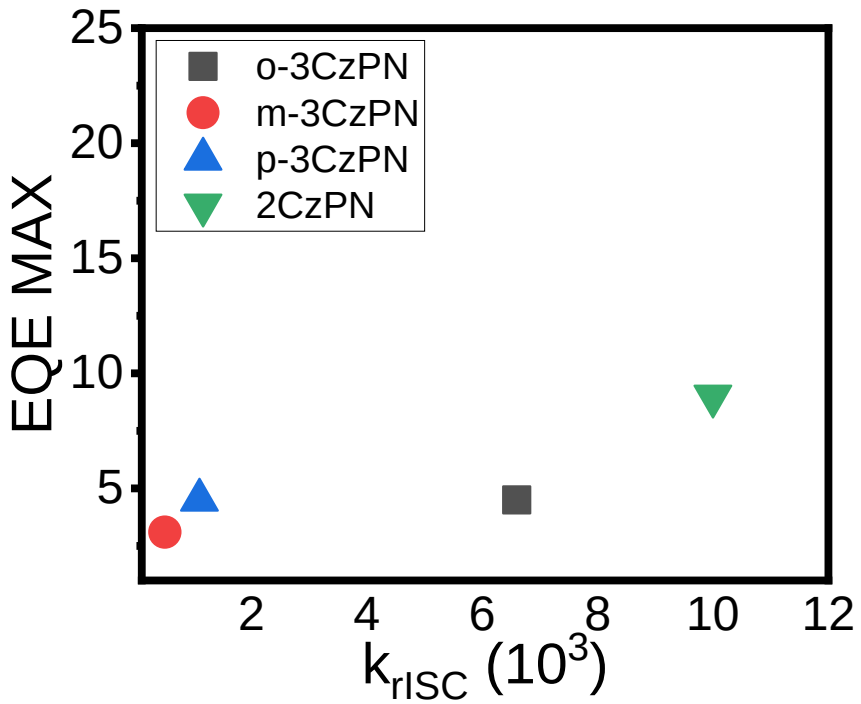

Figure 4.5.2.2. Close up of the TADF-inactive correlation of the device EQE with the k_{rISC} determined by our methodology.

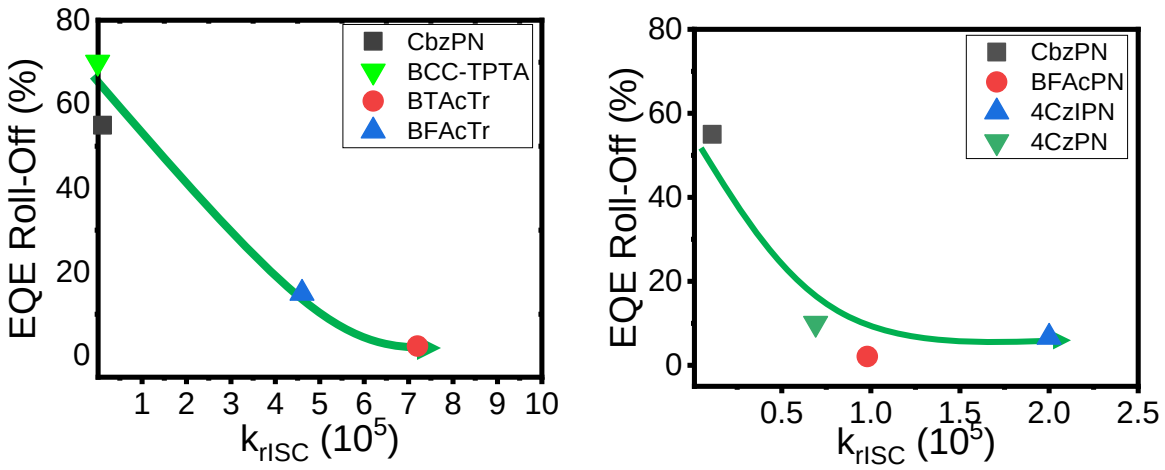

Figure 4.5.2.3. External quantum efficiency roll-off correlation with the k_{rISC} determined by our methodology for the TADF-active chromophores.

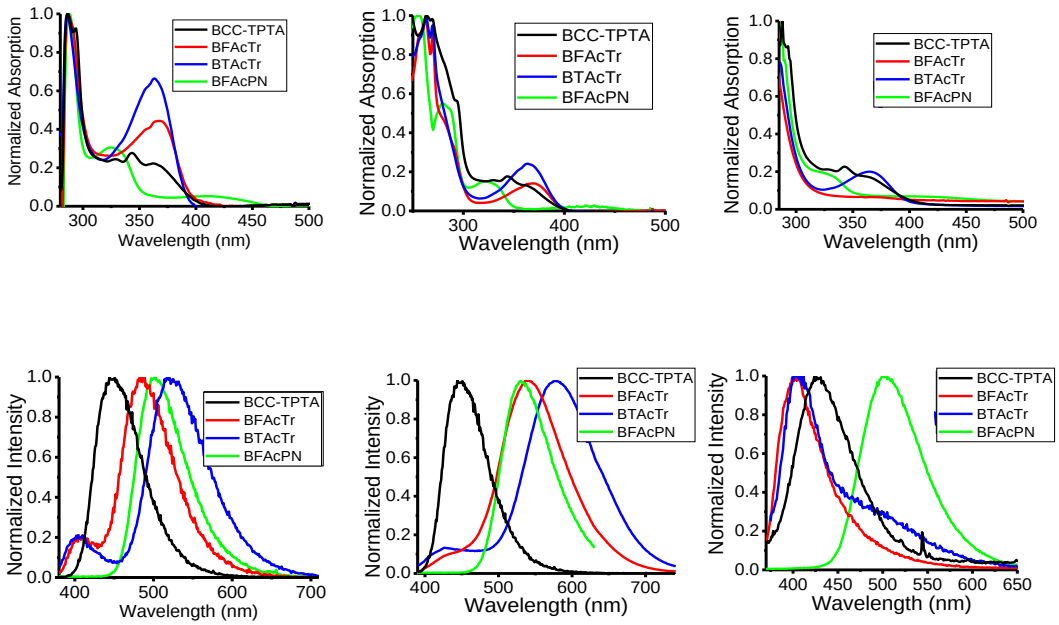

Figure 4.5.2.4. Steady State absorption and emission of the investigated system in Toluene (Column 1), Chloroform (Column 2), and PMMA (Column 3). Measurements were taken at ambient conditions.

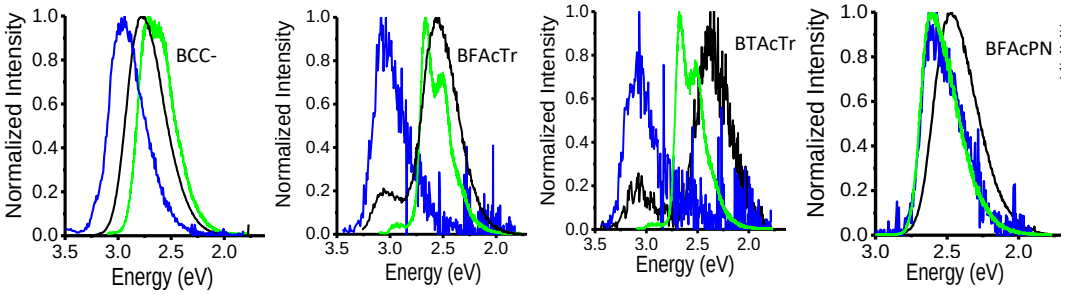

Figure 4.5.2.5. Fluorescence at RT (**Black**), fluorescence at 77K (**Blue**), and phosphorescence at 77K (**Green**) of the investigated chromophores in toluene solutions. The phosphorescence spectra waere measured with the help of an electrical shutter with a 300 µs delayed between the excitation beam and the emission detection to avoid the fluorescence (S_1) detection.

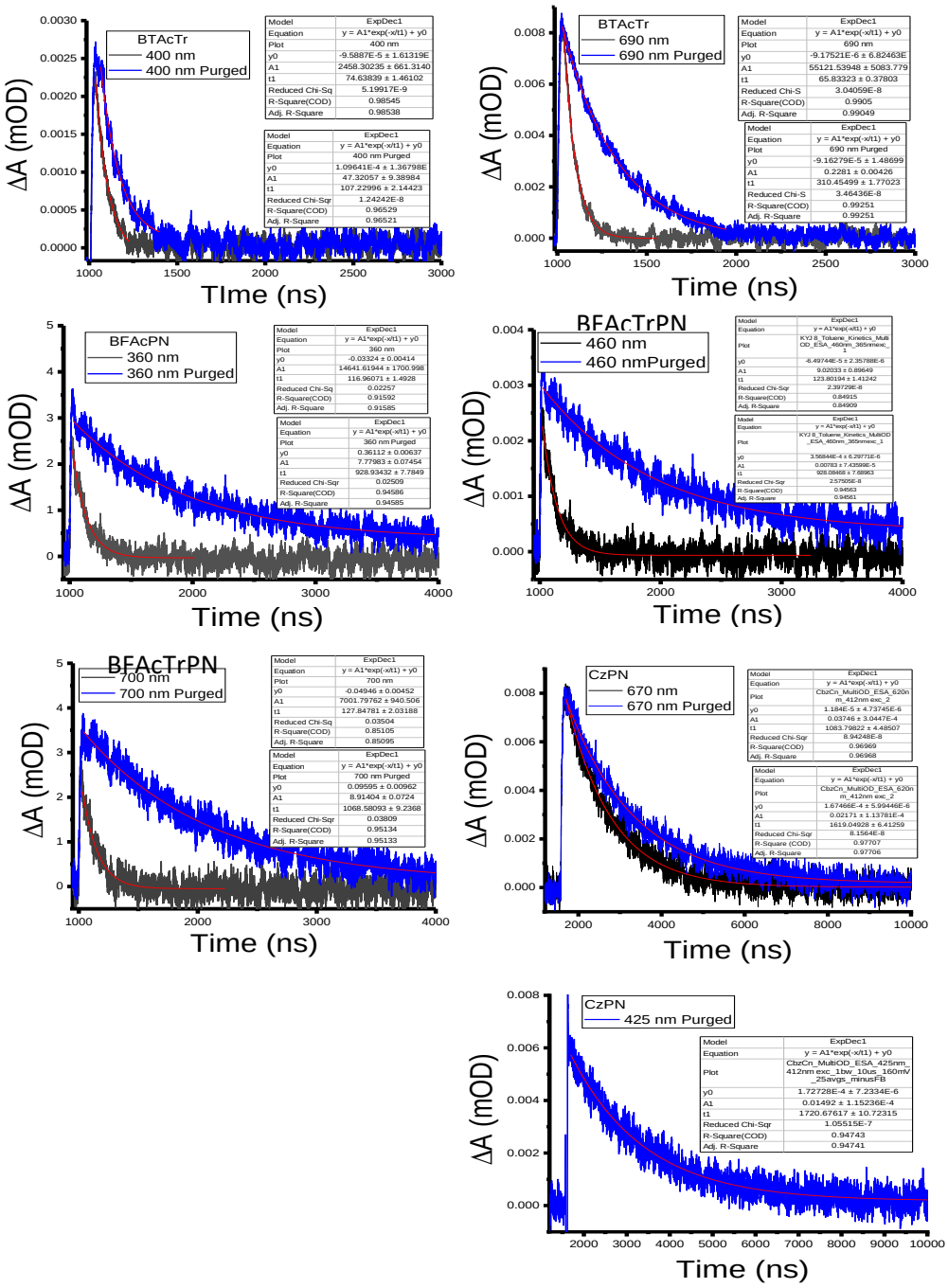

Figure 4.5.2.6. Fitting of the ESA decay of the investigated systems in diluted toluene solutions.

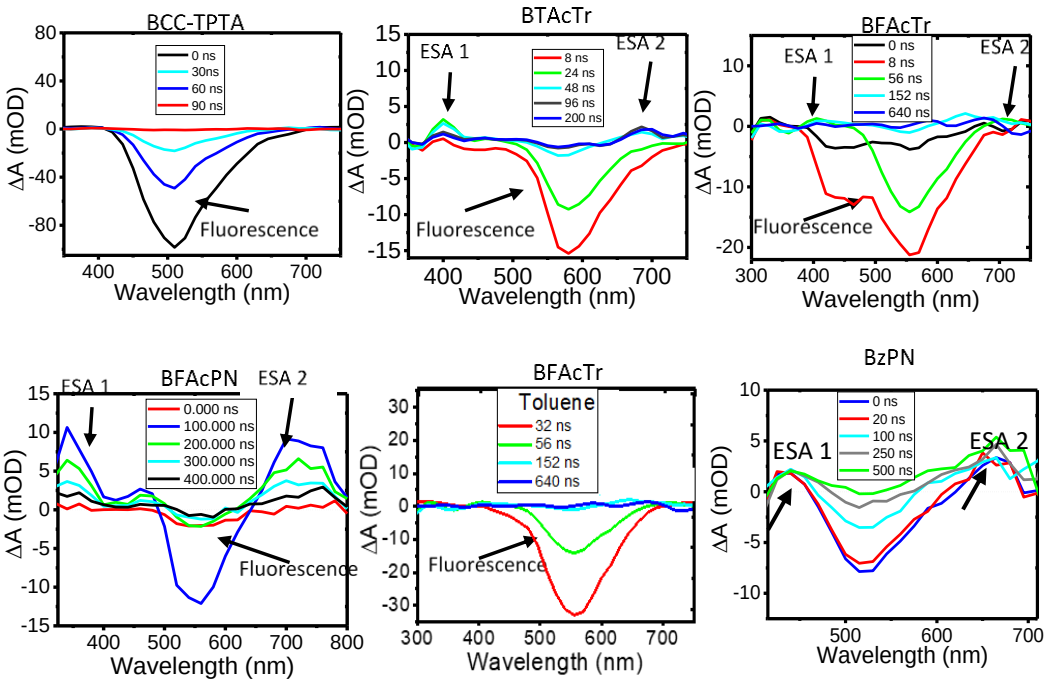

Figure 4.5.2.7. Time-resolved absorption spectra of the investigated system in chloroform solution unless indicated otherwise in the image.

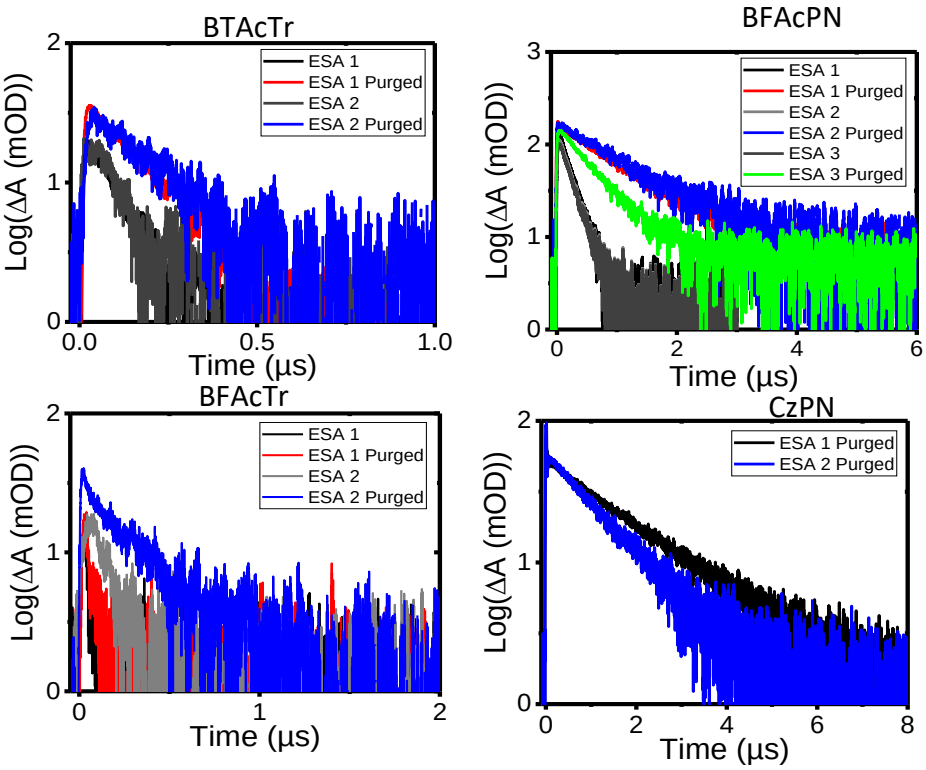

Figure 4.5.2.8. ESA decay dynamics of the investigated chromophores in diluted chloroform solutions.

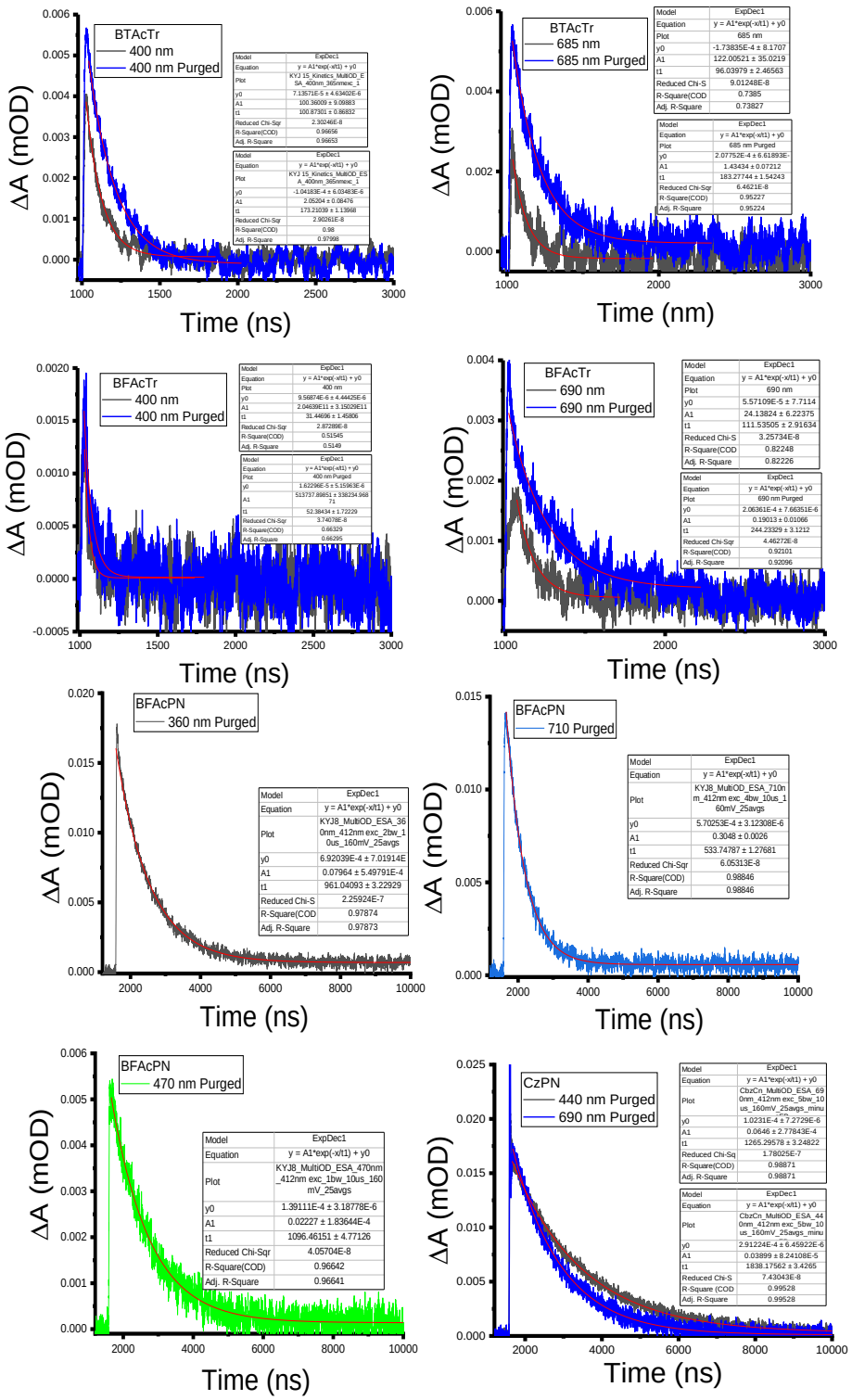

Figure 4.5.2.9. Fitting of the ESA decay of the investigated systems in diluted chloroform solutions.

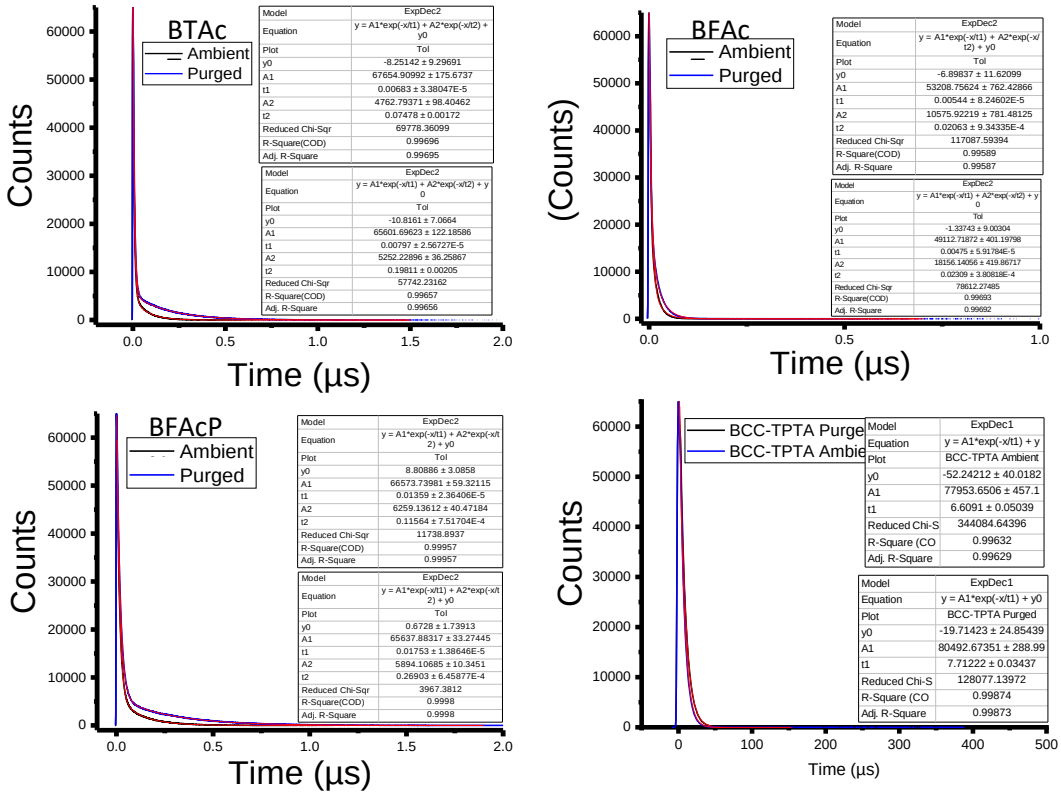

Figure 4.5.2.10. Emissive lifetime fitting of the investigated chromophores in diluted **toluene** solutions by using the TCSPC. These measurements were done before and after the oxygen purging process.

Table 4.5.2.2. Emissive lifetime of the investigated chromophores measured by the time correlated single photon counting (TCSPC) technique. The ambient, purged and 77K measurements were taken in toluene as the solvent. The rate constants were obtained by the method published by Matsui et al.[17]

Material In Toluene	Emissive lifetime (Ambient/Purged)		Emissive lifetime (iPMMA)		Phospho Lifetime	Φ (Rich/Free) (%)	Rate Constants (10^7 s^{-1})				
	S_1 (ns)	T_1 (ns)	S_1 (ns)	T_1 (ns)	T_1 (μs)		K_P	K_R	k_{ISC}	k_{rISC}	K_{DF}
BCC-TPTA	6.4/7.8	n/a	6.1	n/a	0	57/69	15	8.2	6.6	0	0
BTAcTr	6/7	13/198	11	711	0.76	1.2/24	14	0.54	14	2.97	0.54
BFAcTr	5/5	20/23	21	723	0.33	1.3/14	20	0.26	19	41	4.1
BFAcPN	13/17	115/269	45	850	0.97	1.4/10	7.4	0.10	7.0	2.32	0.37

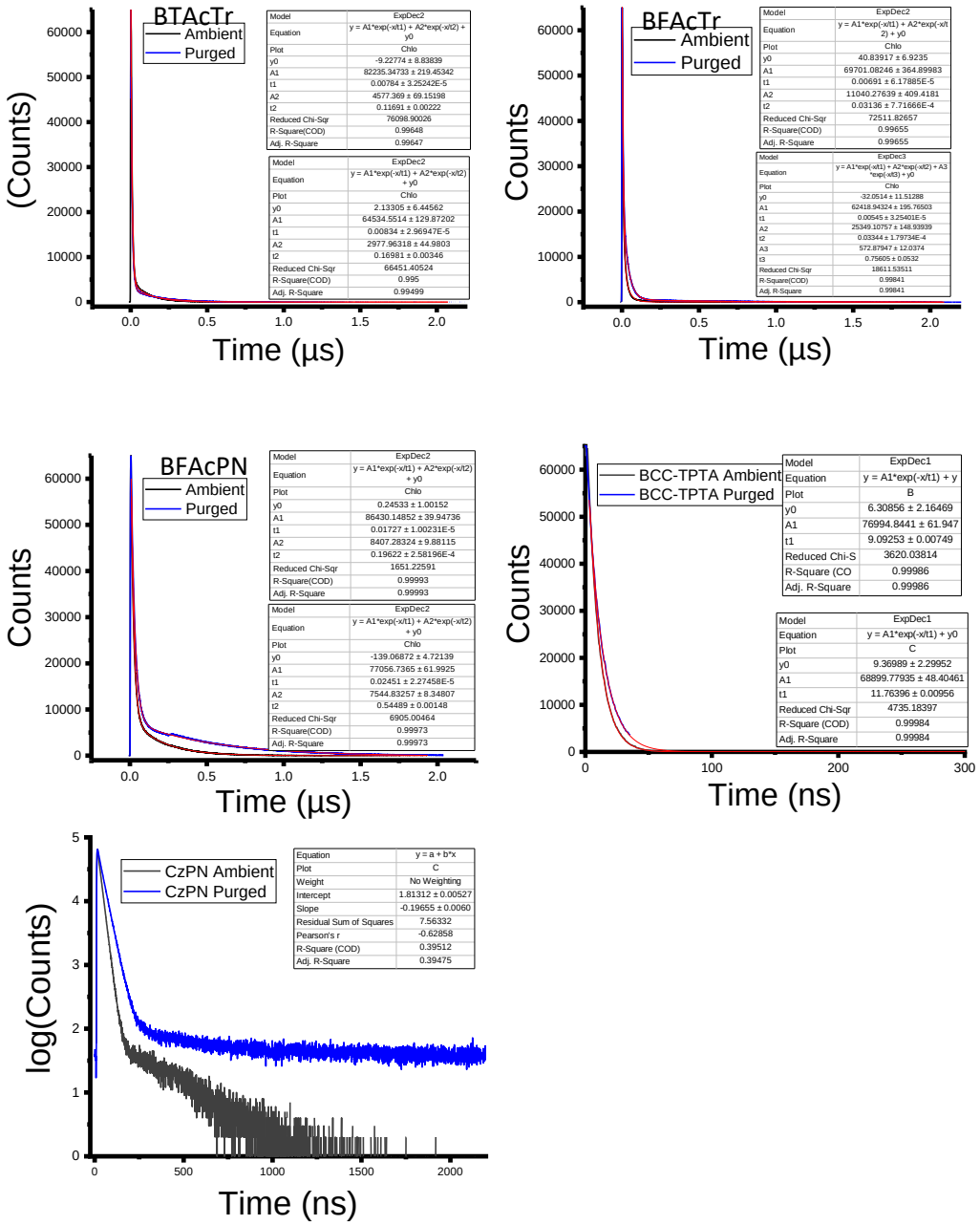

Figure 4.5.2.11. Emissive lifetime fitting of the investigated chromophores in diluted chloroform solutions by using the TCSPC. These measurements were done before and after the oxygen purging process.

Table 4.5.2.3. Emissive lifetime of the investigated chromophores measured by the time correlated single photon counting (TCSPC) technique. The ambient, purged and 77K measurements were taken in chloroform as the solvent. The rate constants were obtained by the method published by Matsui et al.[17]

Material In Chloroform	Emissive lifetime (Ambient/Purged)		Emissive lifetime (iPMMA)		Φ (Rich/Free) (%)	Rate Constants (10^7 s^{-1})				
	S_1 (ns)	T_1 (ns)	S_1	T_1		K_P	K_R	k_{ISC}	k_{rISC}	K_{DF}
BCC-TPTA	10.1/13	n/a	6.13	n/a	25/37	10	2.5	7.5	0	0
BTAcTR	7/8	116/169	11	711	1/14	8.3	0.08	8.6	7.65	0.52
BFAcTR	7/7	31/758	21	723	1.5/11.5	41	0.62	41	1.03	0.13
BFAcPN	17/24	198/544	45	850	1.6/12.4	3.3	0.05	3.2	1.45	0.18
CzPN	21/34	100/1910	n/a	n/a	6/12	4.17	0.25	3.92	0.06	0.05

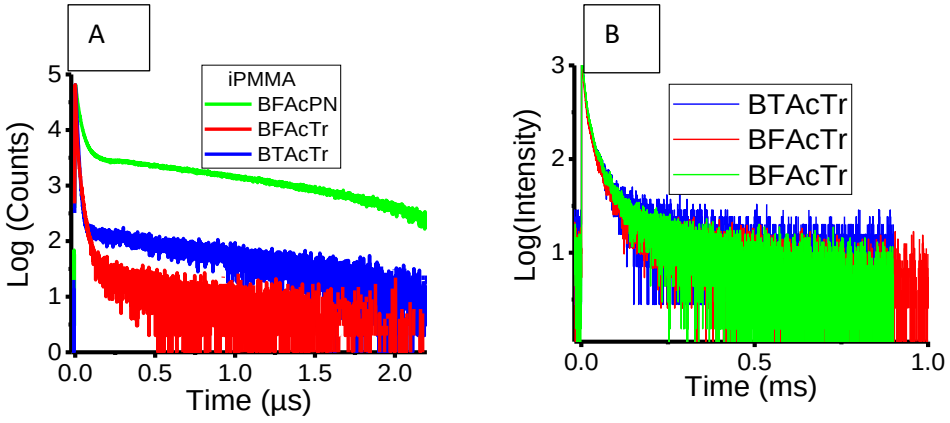

Figure 4.5.2.12. Emissive lifetime characteristics of the investigated chromophores in iPMMA carried out with the time correlated single photon counting (TCSPC) technique (A). Phosphorescence lifetime of the investigated systems obtained with the ns TAS technique (B).

Table 4.5.2.4.Spin−orbit coupling element, energy gap between S_1 and T_n (ΔE_{ST}), and rate constant of rISC process ΔE_{ST} was estimated between adjacent singlets and triplets. T_2 (T_1) state energy was used for BTAcTr and BFAcTr (BFAcPN), respectively.

	BTAcTr	BFAcTr	BFAcPN
H_{SO} (cm^{-1})	0.544	0.568	0.058
ΔE_{ST} (eV)	0.120	0.134	0.019
k_{rISC} 10^5 (s^{-1})	11.6	8.32	1.87

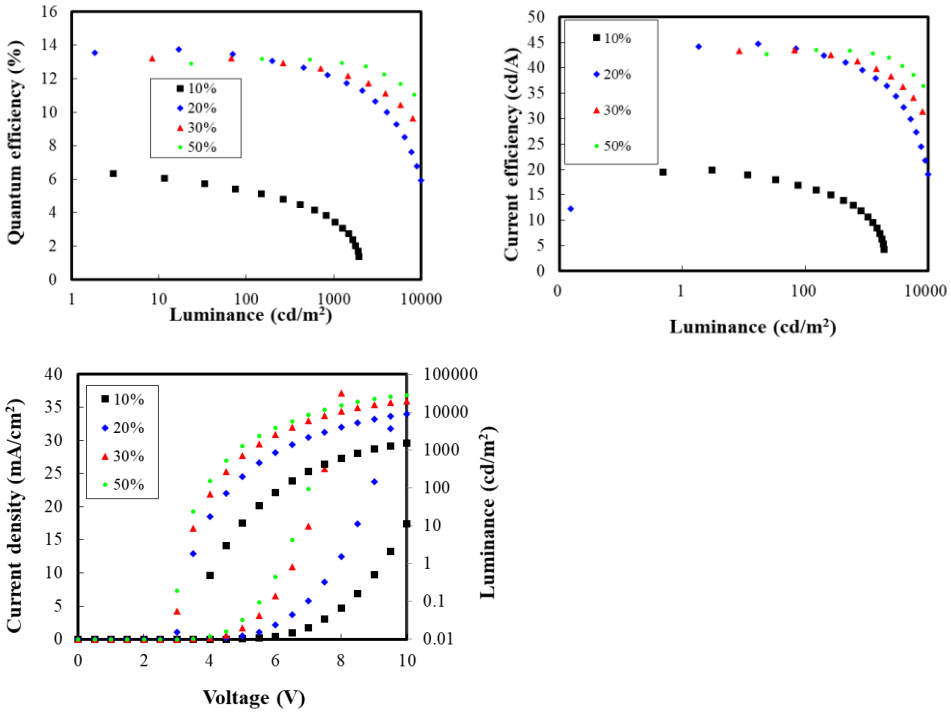

Figure 4.5.2.13. Device performances of the BFAcPN TADF emitter at different wt %.

Reference:

(1) Kang, Y. J.; Yun, J. H.; Han, S. H.; Lee, J. Y. Benzofuroacridine and Benzothienoacridine as New Donor Moieties for Emission Color Management of Thermally Activated Delayed Fluorescent Emitters. *J. Mater. Chem. C* **2019**, *7* (15), 4573–4580. https://doi.org/10.1039/c9tc00523d.

(2) Doan, P. H.; Pitter, D. R. G.; Kocher, A.; Wilson, J. N.; Goodson, T. Two-Photon Spectroscopy as a New Sensitive Method for Determining the DNA Binding Mode of Fluorescent Nuclear Dyes. *J. Am. Chem. Soc.* **2015**, *137* (29), 9198–9201. https://doi.org/10.1021/jacs.5b02674.

(3) Vázquez, R. J.; Kim, H.; Zimmerman, P. M.; Goodson, T. Using Ultra-Fast Spectroscopy to Probe the Excited State Dynamics of a Reported Highly Efficient Thermally Activated Delayed Fluorescence Chromophore. *J. Mater. Chem. C* **2019**, *7* (14), 4210–4221. https://doi.org/10.1039/c8tc05957h.

(4) Vázquez, R. J.; Kim, H.; Kobilka, B. M.; Hale, B. J.; Jeffries-El, M.; Zimmerman, P.; Goodson, T. Evaluating the Effect of Heteroatoms on the Photophysical Properties of Donor-Acceptor Conjugated Polymers Based on 2,6-Di(Thiophen-2-Yl)Benzo[1,2-b:4,5-B′]Difuran: Two-Photon Cross-Section and Ultrafast Time-Resolved Spectroscopy. *J. Phys. Chem. C* **2017**, *121* (27), 14382–14392. https://doi.org/10.1021/acs.jpcc.7b01767.

(5) Hirata, S.; Sakai, Y.; Masui, K.; Tanaka, H.; Lee, S. Y.; Nomura, H.; Nakamura, N.; Yasumatsu, M.; Nakanotani, H.; Zhang, Q.; et al. Highly Efficient Blue Electroluminescence Based on Thermally Activated Delayed Fluorescence. *Nat. Mater.* **2015**, *14* (3), 330–336. https://doi.org/10.1038/nmat4154.

(6) Masui, K.; Nakanotani, H.; Adachi, C. Analysis of Exciton Annihilation in High-Efficiency Sky-Blue Organic Light-Emitting Diodes with Thermally Activated Delayed Fluorescence. *Org. Electron. physics, Mater. Appl.* **2013**, *14* (11), 2721–2726. https://doi.org/10.1016/j.orgel.2013.07.010.

(7) Keller, B.; Cai, Z.; Muthike, A. K.; Sahu, P. K.; Kim, H.; Eshun, A.; Zimmerman, P. M.; Zhang, D.; Goodson, T. Investigating the Optical Properties of Thiophene Additions to S-Indacene Donors with Diketopyrrolopyrrole, Isoindigo, and Thienothiophene Acceptors. *J. Phys. Chem. C* **2018**, *122* (48), 27713–27733. https://doi.org/10.1021/acs.jpcc.8b08567.

(8) Lawetz, V.; Orlandi, G.; Siebrand, W. Theory of Intersystem Crossing in Aromatic Hydrocarbons. *J. Chem. Phys.* **1972**, *56* (8), 4058–4072. https://doi.org/10.1063/1.1677816.

(9) Robinson, G. W.; Frosch, R. P. Electronic Excitation Transfer and Relaxation. *J. Chem. Phys.* **1963**, *38* (5), 1187–1203. https://doi.org/10.1063/1.1733823.

(10) Brédas, J. L.; Beljonne, D.; Coropceanu, V.; Cornil, J. Charge-Transfer and Energy-Transfer Processes in π-Conjugated Oligomers and Polymers: A Molecular Picture. *Chem. Rev.* **2004**, *104* (11), 4971–5003. https://doi.org/10.1021/cr040084k.

(11) Beljonne, D.; Shuai, Z.; Pourtois, G.; Bredas, J. L. Spin-Orbit Coupling and Intersystem Crossing in Conjugated Polymers: A Configuration Interaction Description. *J. Phys. Chem. A* **2001**, *105* (15), 3899–3907. https://doi.org/10.1021/jp010187w.

(12) Samanta, P. K.; Kim, D.; Coropceanu, V.; Brédas, J. L. Up-Conversion Intersystem Crossing Rates in Organic Emitters for Thermally Activated Delayed Fluorescence: Impact of the Nature of Singlet vs Triplet Excited States. *J. Am. Chem. Soc.* **2017**, *139* (11), 4042–4051. https://doi.org/10.1021/jacs.6b12124.

(13) Schmidt, K.; Brovelli, S.; Coropceanu, V.; Beljonne, D.; Cornil, J.; Bazzini, C.; Caronna, T.; Tubino, R.; Meinardi, F.; Shuai, Z.; et al. Intersystem Crossing Processes in Nonplanar Aromatic Heterocyclic Molecules. *J. Phys. Chem. A* **2007**, *111* (42), 10490–10499. https://doi.org/10.1021/jp075248q.

(14) Sun, H.; Zhong, C.; Brédas, J. L. Reliable Prediction with Tuned Range-Separated Functionals of the Singlet-Triplet Gap in Organic Emitters for Thermally Activated Delayed Fluorescence. *J. Chem. Theory Comput.* **2015**, *11* (8), 3851–3858. https://doi.org/10.1021/acs.jctc.5b00431.

(15) Zheng, Z.; Brédas, J. L.; Coropceanu, V. Description of the Charge Transfer States at the Pentacene/C60 Interface: Combining Range-Separated Hybrid Functionals with the Polarizable Continuum Model. *J. Phys. Chem. Lett.* **2016**, *7* (13), 2616–2621. https://doi.org/10.1021/acs.jpclett.6b00911.

(16) Jeon, S. K.; Lee, H. L.; Yook, K. S.; Lee, J. Y. Recent Progress of the Lifetime of Organic Light-Emitting Diodes Based on Thermally Activated Delayed Fluorescent Material. *Adv. Mater.* **2019**, 1803524. https://doi.org/10.1002/adma.201803524.

(17) Wong, M. Y.; Krotkus, S.; Copley, G.; Li, W.; Murawski, C.; Hall, D.; Hedley, G. J.; Jaricot, M.; Cordes, D. B.; Slawin, A. M. Z.; et al. Deep-Blue Oxadiazole-Containing Thermally Activated Delayed Fluorescence Emitters for Organic Light-Emitting Diodes. *ACS Appl. Mater. Interfaces* **2018**, *10* (39), 33360–33372. https://doi.org/10.1021/acsami.8b11136.

(18) Hosokai, T.; Matsuzaki, H.; Nakanotani, H.; Tokumaru, K.; Tsutsui, T.; Furube, A.; Nasu, K.; Nomura, H.; Yahiro, M.; Adachi, C. Evidence and Mechanism of Efficient Thermally Activated Delayed Fluorescence Promoted by Delocalized Excited States. *Sci. Adv.* **2017**, *3* (5), e1603282. https://doi.org/10.1126/sciadv.1603282.

(19) Gan, S.; Hu, S.; Li, X. L.; Zeng, J.; Zhang, D.; Huang, T.; Luo, W.; Zhao, Z.; Duan, L.; Su, S. J.; et al. Heavy Atom Effect of Bromine Significantly Enhances Exciton Utilization of Delayed Fluorescence Luminogens. *ACS Appl. Mater. Interfaces* **2018**, *10* (20), 17327–17334. https://doi.org/10.1021/acsami.8b05389.

(20) Uoyama, H.; Goushi, K.; Shizu, K.; Nomura, H.; Adachi, C. Highly Efficient Organic Light-Emitting Diodes from Delayed Fluorescence. *Nature* **2012**, *492* (7428), 234–238. https://doi.org/10.1038/nature11687.

(21) Ishimatsu, R.; Matsunami, S.; Shizu, K.; Adachi, C.; Nakano, K.; Imato, T. Solvent Effect

on Thermally Activated Delayed Fluorescence by 1,2,3,5-Tetrakis(Carbazol-9-Yl)-4,6-Dicyanobenzene. *J. Phys. Chem. A* **2013**, *117* (27), 5607–5612. https://doi.org/10.1021/jp404120s.

(22) Adachi, C. Third-Generation Organic Electroluminescence Materials. *Jpn. J. Appl. Phys.* **2014**, *53* (6). https://doi.org/10.7567/JJAP.53.060101.

(23) Peng, J.; Guo, X.; Jiang, X.; Zhao, D.; Ma, Y. Developing Efficient Heavy-Atom-Free Photosensitizers Applicable to TTA Upconversion in Polymer Films. *Chem. Sci.* **2016**, *7* (2), 1233–1237. https://doi.org/10.1039/c5sc03245h.

(24) Hosokai, T.; Noda, H.; Nakanotani, H.; Nawata, T.; Nakayama, Y.; Matsuzaki, H.; Adachi, C. Solvent-Dependent Investigation of Carbazole Benzonitrile Derivatives: Does the LE3−CT1 Energy Gap Facilitate Thermally Activated Delayed Fluorescence? *J. Photonics Energy* **2018**, *8* (03), 1. https://doi.org/10.1117/1.JPE.8.032102.

(25) Yokoyama, M.; Inada, K.; Tsuchiya, Y.; Nakanotani, H.; Adachi, C. Trifluoromethane Modification of Thermally Activated Delayed Fluorescence Molecules for High-Efficiency Blue Organic Light-Emitting Diodes. *Chem. Commun.* **2018**, *54* (59), 8261–8264. https://doi.org/10.1039/c8cc03425g.

Chapter 5

Evaluating the Effect of Heteroatoms on the Photophysical Properties of Donor−Acceptor Conjugated Polymers Based on 2,6- Di(thiophen-2-yl)benzo[1,2-b:4,5-b′]difuran: Two-Photon Cross Section and Ultrafast Time-Resolved Spectroscopy

5.1 Original Publication Information

The work in this chapter was accepted by *Journal of Physical Chemistry C (JPC C)* with the title:

"Evaluating the Effect of Heteroatoms on the Photophysical Properties of Donor−Acceptor Conjugated Polymers Based on 2,6- Di(thiophen-2-yl)benzo[1,2-b:4,5-b′]difuran: Two-Photon CrossSection and Ultrafast Time-Resolved Spectroscopy" Ricardo J. Vázquez, Hyungjun Kim, Brandon M. Kobilka, Benjamin J. Hale, Malika Jeffries-EL, Paul Zimmerman, and Theodore Goodson. *J. Phys. Chem. C*, **2017**, *121*, 14382-14392.

Modifications were conducted to the manuscript to adapt it to the style of the content of this dissertation. References and supporting information of the manuscript are included in this chapter.

5.2 Abstract

We investigate the influence of the heteroatom on the electronic and photophysical properties of four conjugated polymers based on 3,7-didodecyl-2,6-di(thiophen2-yl)benzo[1,2-b:4,5-b′]difuran (BDF) as the donor and 3,6- di(thiophen-2-yl)-1,4-diketopyrrolo[3,4-c]pyrrole (TDPP) or 3,6-di(2-furanyl)-1,4-diketopyrrolo[3,4-c]pyrrole (FDPP) as the acceptor. The polymers with a furan as the linker showed higher extinction coefficients than their thiophene counterparts. Ultrafast fluorescence decay showed that the exciton relaxation process is affected by the type of linker in these conjugated polymers. Theoretical calculations showed that the polymers with a furan as the linker are more planar than their thiophene analogues. Also, theoretical calculation showed that the polymers with a thiophene as the linker have larger transition dipole moments. The two-photon absorption cross sections (TPACS) of the polymers with a furan as the linker were larger than their thiophene polymer analogues. These results suggest that the polymers with a furan as the linker have higher charge transfer character than their thiophene polymers analogues. The photovoltaics performance for these polymers are correlated with their optical properties. These results suggest that furan-derivatives are good candidates for synthetic exploration for long-range energy transport materials in photovoltaic applications.

5.3 Introduction

The development and use of organic materials is of great interest in the scientific and industrial community due to their potential optoelectronic applications. There has been a great deal of success for the polymers used in solar and light emitting devices.[1,2] Organic polymeric systems such as PTB7 have reached power-conversion efficiencies (PCE) above 10%.[3] Even greater accomplishments in light emitting diode devices has been reported when organic polymers are incorporated as the active material.[4] However, the PCE of photovoltaic devices based on organic

polymers have not been able to achieve such a high efficiency as silicon-based photovoltaic devices.[5] The use of conjugated polymers may offer further opportunities in order to enhance the solar cell efficiencies if one can understand the fundamental structure-function relationship which gives rise to the dynamics of the exciton in these systems.[6–16]

There has been reports trying to unravel the electronic and exciton interactions of useful conjugated polymers for solar applications.[17,18] For example, the processes of exciton diffusion (ED), charge transfer (CT), and excitation energy transport (EET) has been thoroughly investigated by a variety of optical and electronic techniques.[19] In the case of ED, the absorption of a photon promotes an entangled interaction between the excited electron and the associated hole in a bound excited state.[20] The interaction between the excited electron and the associated hole (exciton) needs to be broken in order to produce charge carriers that will result in electrical current. Therefore, the ability of the excitons to diffuse in order to arrive the respective interface for exciton splitting is fundamental in the photovoltaic process. This process is known as the exciton diffusion,[21] and it can be studied by using ultra-fast spectroscopy (UFS) and time-resolved fluorescence (TRF) techniques.[9,12,22–24] In electron donor−acceptor polymers, the electrons and holes are weakly localized between the donor-acceptor (D-A) interface, therefore, they are considered as CT excitons.[25,26] The charge transfer character of a system can be evaluate by using nonlinear optics (NLO) such as two-photon absorption (TPA) techniques, which is proportional to the square of the dipole moment.[27–30] Recently, studies have suggested that organic materials with a high dipole moment can prevent the exciton recombination process.[31] It is also important to have insight into the exciton mechanism of delocalization away from the original absorbing point. The mechanism of delocalization depends on how strong the excitons are coupled within the

molecule.[32-34] If the electronic interaction is strong a coherent mechanism dominates, while if the electronic interaction is weak an incoherent hopping-type mechanism dominates.[34–36]

Thiophene derivatives have been widely used as active materials for optoelectronic applications.[37] Recently, efforts to incorporate furan derivatives into main-chains where thiophene derivatives are normally used have emerged.[37,38] In addition to the common isoelectric properties that furan has with thiophene, studies have shown that the incorporation of furan derivatives has an immediate impact in the polymer solubility. From a synthetic point of view, this could mean the possibility of synthesizing polymers with significantly higher molecular weights without the need to have a large or branched alkyl side chain.[39]

In solar cell devices, studies have shown a slightly higher PCE (reaching 5%) for polymers that replace thiophene with furan derivatives in their main-chain.[40] Specifically, for the polymers under investigation a 0.18% to 1.31% PCE increase for furan polymers over the thiophene polymer analogues was reported.[39] The furan molecule contains a smaller size atom with a higher electronegativity. It also has been suggested that the less aromaticity of furan in comparison with thiophene could facilitate the formation of quinoidal structures, which could result in the stabilization of the HOMO levels and enhancing the planarity of the polymer.[41] However, a deeper photophysical insight of the exciton behavior in these polymers should be established. By understanding these differences in the exciton dynamics one can explain the higher PCE % reported when a furan is incorporated into the mainchain. In this report we elucidate the photophysical processes occurring in a selected group of conjugated polymers based on 2,6-di(thiophen-2-yl)benzo[1,2-b:4,5-b′]difurans (BDF) as the donor and diketopyrrolopyrrole (DPP) as the acceptor. The resulting conjugate donor−acceptor polymers are shown in **Figure 5.3.1.** We are most interested in the electronic intermolecular and intramolecular interactions between the

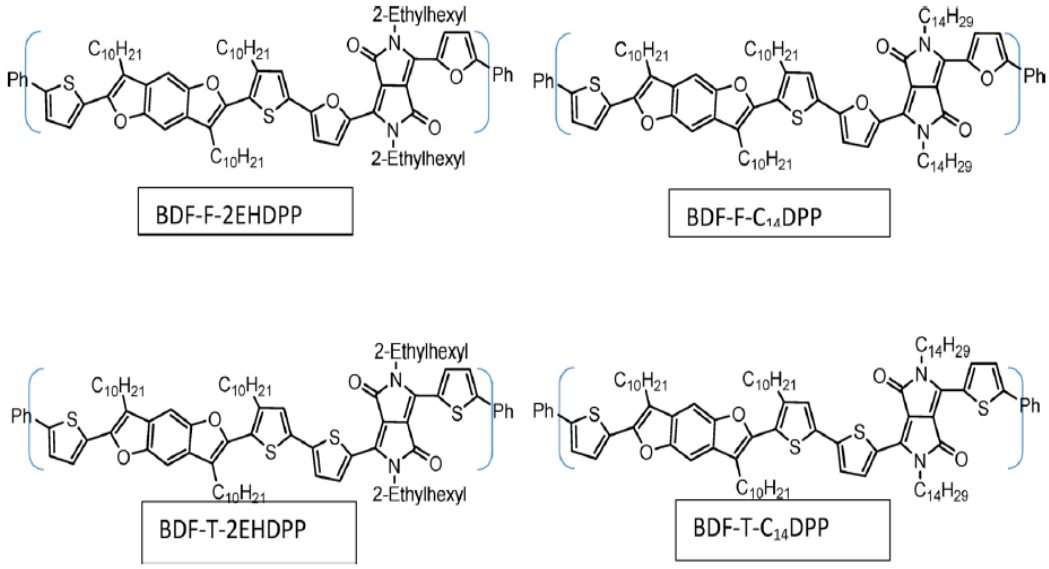

Figure 5.3.1. Repeating unit of the investigated polymers. All of the polymers are constituted from a Benzodifuran (BDF) unit as the donor, a thiophene or a furan as the linker, and a diketopyrolopyrrolle (DPP) as the acceptor unit. 2-ethylhexyl or tetradecyl as a side chain groups were varied for solubility purposes.

donor-acceptor moieties. We investigated the steady state, time-resolved fluorescence, and non-linear optical properties of these conjugated polymers. We also present electronic structure calculations regarding the electronic states and transition dipole moments in these polymers.

5.4 Experimental Techniques

5.4.1 Materials

The polymers investigated in this paper were synthesized via a Stille polycondensation reaction of (5,5′- (3,7-didecylbenzo[1,2-b:4,5-b′]difuran-2,6-diyl)bis(4-decylthiophene-5,2-diyl))bis(trimethylstannane)[42] and 3,6-bis(5-bromofuran-2-yl)-2,5-bis(2-ethylhexyl)pyrrolo[3,4-c]pyrrole-1,4- (2H,5H)-dione, 3,6-bis(5-bromofuran-2-yl)-2,5-bis(tetradecyl)- pyrrolo[3,4-c]pyrrole-1,4(2H,5H)-dione, 3,6-di(5-bromo-2- thienyl)-2,5-bis(2-ethylhexyl)pyrrolo[3,4-c]pyrrole-1,4- (2H,5H)-dione or bis(5-bromothiophen-2-yl)-2,5-bis- (tetradecyl)pyrrolo[3,4-

c]pyrrole-1,4(2H,5H)-dione, respectively.[39] The molecular weights of the polymers were determined using gel permeation chromatography (GPC) at 50 °C using THF as the eluent with a flow rate of 1.0 mL/min. Calibration was based on polystyrene standards.

5.4.2 Steady-State Measurements

All of the measurements were performed at room temperature. Concentrations ranging from 1.0×10^{-3} to 3.0×10^{-6} M were used for the measurements. The samples were placed in 4 mm quartz cuvettes. Steady-state absorption spectra were measured using an Agilent 8432 UV−visible absorption spectrophotometer. The emission spectrum measurements were performed with a Fluoromax-2 spectrophotometer. Absorption spectra measurements were taken before and after each measurement to ensure that there was no appreciable photodegradation during the fluorescence lifetime or two-photon absorption measurements. The fluorescence quantum yields (Q.Y.) of the samples were calculated using a known procedure,[43,44] and zinc phthalocyanine in toluene ($\phi = 0.3$) was used as the standard.[45] The excitation wavelength for the Q.Y. calculation was 650 nm.

5.4.3 Density Functional Theory Calculation

Theoretical investigation has been performed in order to analyze the experimental results of the two photon absorption cross-section. It is impossible to calculate the electronic structure of the full polymer; therefore, the polymer repeating units have been taken to approximate the polymer's chemical property. The long alkyl chains are replaced by the short chains such as decyl groups (C10H21) to methyl groups and phenyl end groups to methyl groups. Also two side chain groups, 2-ethlhexyl and tetradecyl groups (C14H29), are simplified to 2-ethylpropyl and butyl groups, respectively, to save computational time without significant effect on the electronic properties. The ground state geometry of each monomer was obtained by computations using

density functional theory (DFT). The ωB97X-D functional basis sets are employed.[46,47] The ground state calculations were conducted using Q-Chem 4.0.[48] Excited state simulations using time-dependent DFT (TDDFT) were performed to analyze the trend of lifetime. The same functional used in the ground state calculations and smaller basis sets, 3-21G*, were employed for the geometry optimization of the first singlet excited state (S1) in the gas phase. Single-point energy calculations to evaluate the electronic property (Fluorescence emission energy and corresponding transition dipole moment) were performed using 6-31G* basis sets, and the medium effect is included using polarizable continuum. The dielectric constant of dichloromethane is 8.91. All excited state calculations were conducted using Q-Chem 4.0.[48]

5.4.4 Time-Resolved Fluorescence Measurements.

The time-resolved fluorescence experiments were performed using an ultrafast fluorescence up-conversion setup that had previously been described.[49] A mode-locked Ti-sapphire femtosecond laser (Spectra Physics Tsunami) was used to generate 80 fs pulses at 800 nm wavelength with a repetition rate of 82 MHz. This mode-locked laser was pumped by a 532 nm continuous light output from another laser (Spectra Physics Millennia), which has a gain medium of neodymium-doped yttrium vanadate (Nd:YVO4). A 400 nm excitation pulse was generated by a second harmonic β- barium borate crystal, and the residual 800 nm beam was made to pass through a computer-controlled motorized optical delay line. The polarization of the excitation beam was controlled by a berek compensator. The power of the excitation beam varied between 33 to 36 mW. The fluorescence emitted by the sample was upconverted by a nonlinear crystal of β-barium borate by using the residual 800 nm beam, which had been delayed by the optical delay line with a gate step of 6.25 fs. By this procedure, the measurement of the fluorescence is enabled and can be measured temporally. The monochromator is used to select the wavelength of the up-

converted beam of interest, and the selected beam is detected by a photomultiplier tube (R152P, Hamamatsu, Hamamatsu City, Japan). The photomultiplier tube converts the detected beam into photon counts, which can be read from a computer. Coumarin 30, Coumarin 153, and Cresyl Violet dyes were used for calibrating the laser at different collection wavelengths. The instrument response function (IRF) has been determined from the Raman signal of water to have a width of 110 fs.[30] Lifetimes of fluorescence decay were obtained by fitting the fluorescence decay profile to the most accurate fit. Mono and multi-exponential decay functions convoluted with IRF in MATLAB and Origin 8 were necessary for the data analysis. The time-correlated single photon counting (TCSPC) technique, which has been described previously, was used to study the long component of the investigated polymers.[50] The laser used for the TCSPC measurement was a Kapteyn Murnane (KM) mode-locked Ti-sapphire laser. The output beam from the KM laser was at 800 nm wavelength, with pulse duration of ∼30 fs. The output beam was frequency-doubled using a nonlinear barium borate crystal to obtain a 400 nm beam. A polarizer was used to vary the power of the 400 nm beam that excites the sample. Focus on the sample cell (quartz cuvette, 0.4 cm path length) was ensured using a lens of focal length 11.5 cm. Collection of fluorescence was done in a direction perpendicular to the incident beam into a monochromator, and the output from the monochromator was coupled to a photomultiplier tube, which converted the photons into counts.

5.4.5 Two-Photon Excited Fluorescence Measurements

Two-photon spectroscopy was performed using a mode-locked Ti:sapphire laser which is tunable from 700 to 900 nm delivering 110 fs output pulses at a repetition rate of 80 MHz. Emission scans were performed at 830 nm excitation while scanning 690−700 nm emission, but the exact emission detection wavelength during the power dependence scan was selected by the

emission wavelength that produced the highest number of counts at 415 nm excitation (by absorbing simultaneously two photons of half of the energy; 830 nm). Rhodamine B was used as the standard. Input power from the laser was varied using a variable neutral density filter. Two-photon power-dependent fluorescence intensity was utilized to determine the two-photon absorption cross section through the two-photon emission fluorescence (TPEF) method.[51]

5.5 Results

5.5.1 Synthesis and Molecular Weight Determination

All of the four polymers used in this investigation are based on the electron-donating moiety 3,7-didodecyl-2,6-di(thiophen-2- yl)benzo[1,2-b:4,5-b′]difuran and the electron-accepting moieties 3,6-di(thiophen-2-yl)-1,4-diketopyrrolo[3,4-c]pyrrole or 3,6-di(2-furanyl)-1,4-diketopyrrolo[3,4-c]pyrrole. The composition of the conjugated monomers was varied to evaluate the impact of heteroatom substitution on the photophysical properties of the resulting polymers. The length of the side chain on each of the comonomers was also varied to improve the solubility and processabillity of the polymers.

5.5.2 Steady-State Absorption and Fluorescence Emission

Figure 5.5.2.1 shows the normalized steady-state absorption of the investigated polymers. The measurements were recorded from chloroform solutions, and their relevant data are summarized in **Table 5.5.2.1**. All of the four polymers exhibited two distinct absorption bands as is typical for such electron donor−acceptor polymers.[39,52,53] The absorption maximum of the polymers (near 650 nm) can be attributed to the intermolecular charge transfer between the electron-donating and electron-accepting units, while the small peak (near 400 nm) can be attributed to the localized π−π* transition between the BDF and DPP units.[54] A similar behavior has been documented in π-conjugated polymers having similar donor−acceptor interactions.[55]

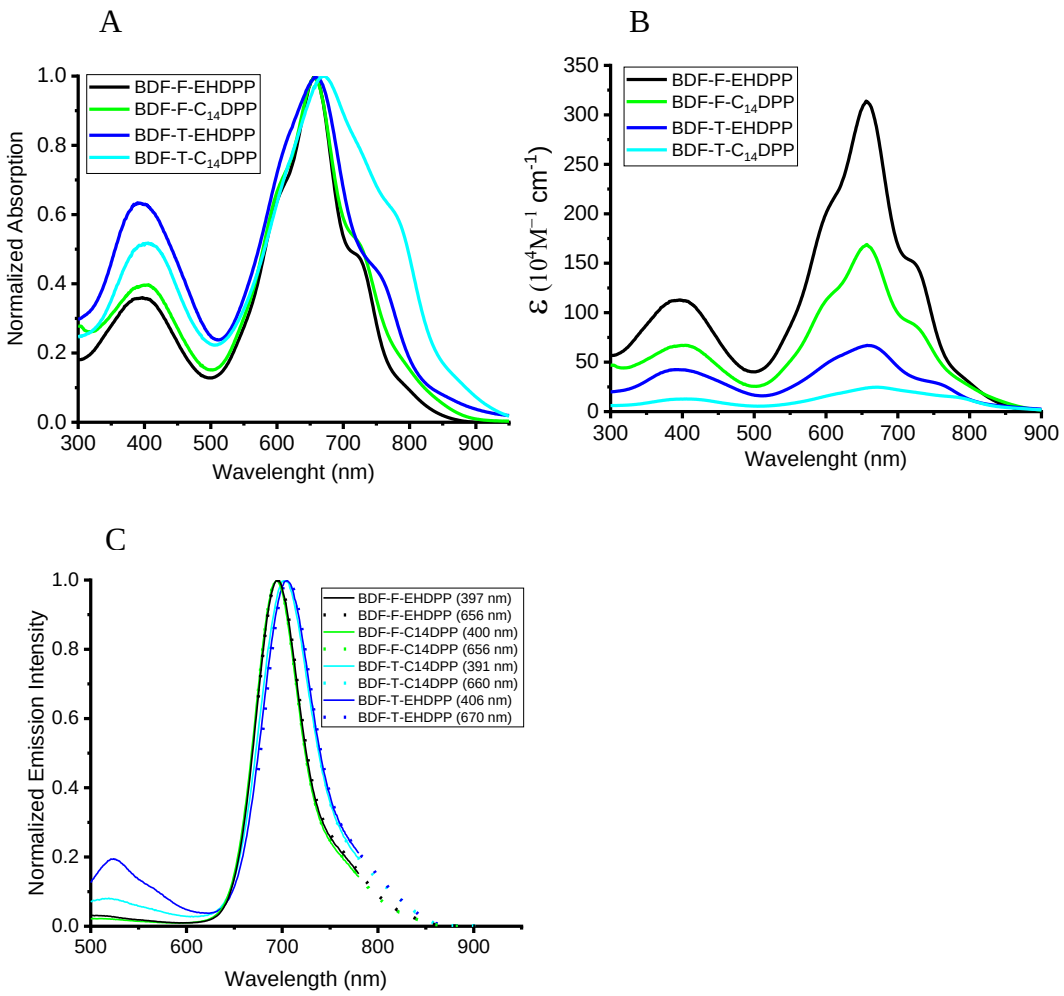

Figure 5.5.2.1. Steady-state spectra of the investigated polymers in chloroform: normalized absorption spectra (A), molar extinction coefficient spectra (B), and normalized emission spectra at different excitation wavelengths (C). Panel C shows the emission spectra when both absorption bands are excited. Interestingly, the polymers show the same emission spectrum regardless of the absorption band that was excited (400 or 650 nm region). The specific excitation wavelength used is shown in the legend.

Theoretical calculations of the first and second singlet excitation were conducted, and we were able to corroborate that the high energy transition (S_2) correspond to a π-π^* transition in the polymer backbone while the low energy transition (S_1) correspond to the charge transfer state between the BDF and PDI units. The core of the absorption for all of the

Table 5.5.2.1. Summary of the Steady-State and Solar Cell Performance of the Investigated Polymers

Sample	Molecular Weight (kDa)	PCE (%)[39]	Absorbance λ_{Max} (nm)	ε 10^4 ($M^{-1}cm^{-1}$)	ε/repeating unit 10^4 ($M^{-1}cm^{1}$)	Emission λ_{Max} (nm)	Φ (%)	HOMO/ LUMO (eV)[40]
BDF-F-2EHDPP	55.6	2.28	397, 656	113 at 397 nm 313 at 656 nm	2.75 at 397 nm 7.6 at 656 nm	692	6.7	-5.5/-3.7
BDF-F-C_{14}DPP	44.2	2.77	400, 656	67 at 400 nm 168 at 656 nm	2.31 at 400 nm 5.79 at 656 nm	692	3.6	-5.5/-3.8
BDF-T-2EHDPP	24.0	2.10	391, 660	43 at 391 nm 67 at 660 nm	2.52 at 391 nm 3.94 at 660 nm	525, 703	3.5	-5.6/-3.8
BDF-T-C_{14}DPP	8	0.97	406, 670	13 at 406 nm 24 at 670 nm	2.60 at 406 nm 4.8 at 670 nm	560, 695	1.9	-5.6/-3.7

polymers extends in the visible region toward the NIR region, near the peak of the solar flux, making them suitable for photovoltaic applications.[56] The molar extinction coefficient (**Figure 5.5.2.1B**) is higher for those polymers containing a furan. This could contribute to the reported higher PCE for these polymers.[39]

The steady-state emission spectra at different excitation wavelengths for the investigated polymers are shown in **Figure 5.5.2.1C**. The measurements were recorded from chloroform solution, and their relevant data were summarized in **Table 5.5.2.1**. All of the polymers have a major emissive peak near 700 nm, but the thiophene-containing polymers showed another significant emissive peak near the 550 nm region. As it can be observed in **Figure 5.5.2.1C**, the emissive band near 700 nm can be accessed by exciting both the near 400 nm and the near 650 nm bands. To address the possibility of self-absorption, we conducted an easy experiment in which we evaluated the emission intensity as a function of wavelength at different concentrations for all of the investigated polymers (**Figure 5.8.1**). The reabsorption phenomena has been documented as a distortion in the emissive band when the emissive band overlap with the absorption band.[57]

As can be observed in **Figure 5.8.1**, there is no distortion of the emissive band (near 650 nm) upon increasing the optical density/concentration at the range of optical density/concentration in which the experiments were carried out. This experiment shows no evidence of reabsorption in the investigated materials at the range of optical density/concentration in which the experiments were carried out. In order to have a deeper insight into the absorption bands that contributes to these emissive states the excitation spectra were recorded. As expected, the excitation spectrum at near 550 nm of the thiophene-containing polymers shows higher intensity than their furan analogues. The quantum yields (Φ) of the investigated polymers are shown in **Table 5.5.2.1**. The polymers that contain furan showed a relatively higher Φ than their thiophene analogues. It has been suggested that higher Φ values are detrimental to the photovoltaic efficiency due to enhanced radiative decay pathways of the exciton.[36] On the other hand, low quantum yield has been correlated with enhanced non-radiative process. In these polymers, the systems with higher PCE also had higher Φ values. Therefore, other parameters such as exciton relaxation and TPA capabilities must be taken into considerations for the larger PCE obtained.

5.5.3 Two-Photon Absorption

The two-photon excited fluorescence method was conducted in order to measure the TPA cross-section of the polymers. The results indicate that the polymers with a furan in the main-chain have one order of magnitude higher TPA cross-section than their thiophene analogs (**Table 5.5.3.1**). The TPA cross sections have been strongly associated with the charge transfer character of the material.[63] Also, studies have been suggested that the morphology of the materials (planarity) could be an important feature for the TPA nature.[14,64,74] Under these circumstances a higher transition dipole moment suggests a better coupling/interaction between the donor-acceptor junctions. This subsequently will lead to a better energy transfer between the two moieties. These

Table 5.5.3.1. Two-photon absorption cross-section

Polymer	TPA Cross-Section (GM)	TPA Cross-Section per monomer (GM)
BDF-F-2EHDPP	2790.4	69.76
BDF-F-C14DPP	2183.4	75.2
BDF-T-2EHDPP	205.6	12
BDF-T-C14DPP	109.9	24.00

connections were also made with the electronic structure calculations (see below). The DFT calculations showed that the polymers with a furan as the linker have lower dihedral angles between the donor-linker and linker-acceptor junction, thus making them more planar than the thiophene analogues. Our results agree with previous studies, and the TPA cross-section values have a linear relationship with the lower dihedral angles between the donor-linker-acceptor of the polymers. This indicates that the FDPP-containing polymers are more planar, have much better charge separation properties, and have a higher charge transfer character than their corresponding thiophene polymer analogues.[13,27] The values of the TPA cross-section are reported by polymer and by repeating units.

5.5.4 Time-Resolved Fluorescence Decay

Up-conversion measurements were carried out in order to investigate the fluorescence lifetime of the polymers. In order to study the fluorescence lifetime component of the donor part (BDT) the instrument was tuned up to detect the 525−560 nm emission wavelength. To study the fluorescence lifetime component of the acceptor part the instrument was tuned up to detect the 693−700 nm emission wavelength. Time correlated single photon counting (TCSPC) experiments were also conducted in order to elucidate the long component of the fluorescence lifetime.[58] A multi-exponential decay function was used to fit the fluorescence lifetime dynamics of the BDT

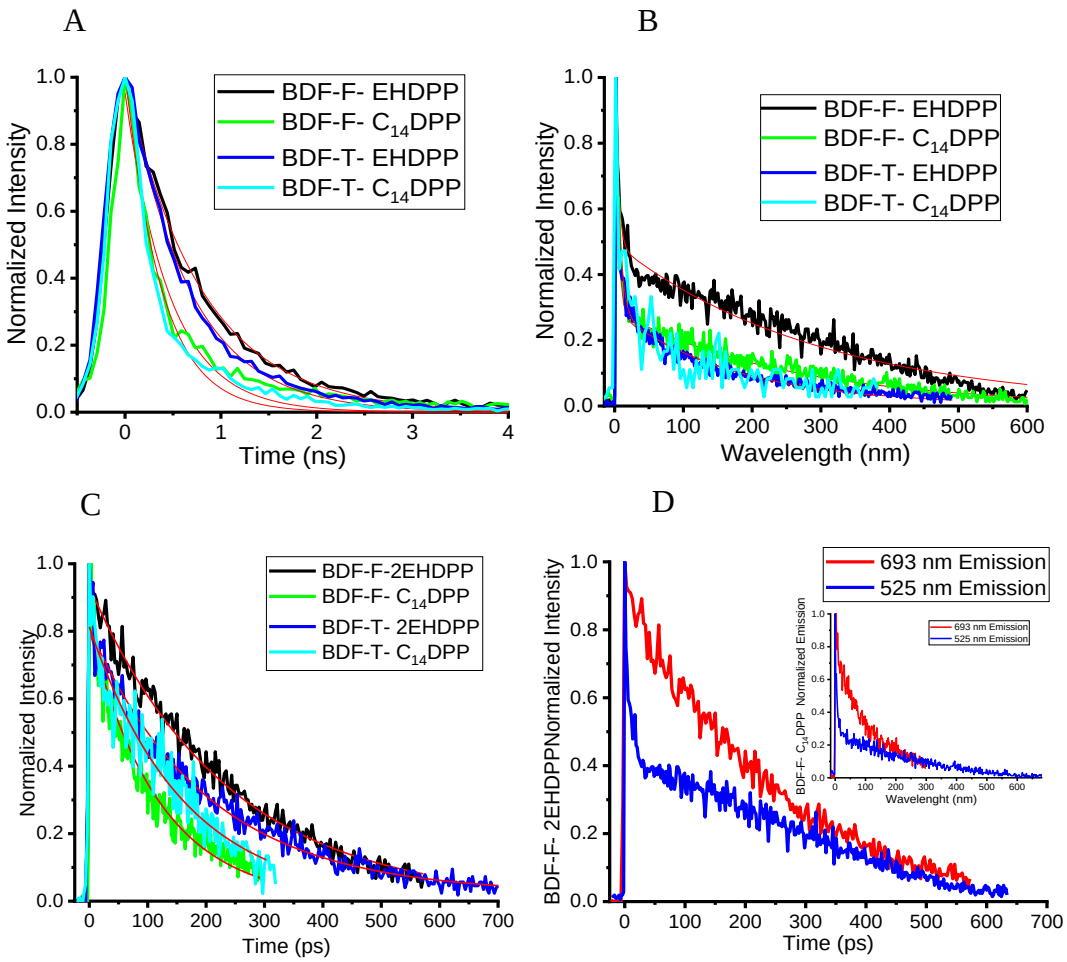

Figure 5.5.4.1. Fluorescence life-time dynamics of the investigated polymers. TCSPC setup were used to investigate the long component dynamics of the acceptor at 690-700nm region (A) and the Fluorescence Up-Conversion set-up were used to investigate the short components of both, the donor at 525-560nm (B) and the acceptor 690-700nm (C) emission region. Using the BDF-F-2EHDPP and the BDF-F-C_{14}DPP polymers as an example of the difference between the excited state fluorescence lifetime decay profile between the donor and the acceptor (D). For the donors, the Fluorescence Up-Conversion data were collected at 525 nm for all of the investigated polymers but 560 nm emission were used for the BDF-T-C14DPP polymer instead.

unit while a mono-exponential decay function was used to fit the DPP exciton lifetime dynamics, and the relevant data are summarized in **Table 5.5.4.1**. The measured fluorescence lifetime of the polymers in this study are similar to previously reported fluorescence lifetime dynamics of conjugated polymers based on thiophene derivatives as the donor and DPP as the acceptor.[36,58]

Table 5.5.4.1. Emissive lifetime characterization of the light harvesting polymers.

	Fluorescence Up-Conversion							TCSPC
	525-560 nm region				600-700 nm region			
Compound	A_1	T_1 (ps)	A_2	T_2 (ps)	A_1	T_1 (ps)	Rise Time (fs)	T_1 (ps)
BDF-F-EHDPP	0.73	4.33	0.49	296	0.95	233	500(Rise Time)	757
BDF-F-C_{14}DPP	0.97	4.87	0.29	250	0.82	119	n/a (IRF)	406
BDF-T-EHDPP	1.0	4.35	0.29	178	0.80	220	250(Rise Time)	628
BDF-T-C_{14}DPP	0.84	6.36	0.29	174	0.83	160	n/a (IRF)	354

Our measurements showed a slower fluorescence lifetime dynamics for the polymers with furan as the linker. If we evaluate the effect of the side chain in the acceptor's fluorescence lifetime, the polymers with the 2-ethylhexyl as the side chains have almost two times slower decay dynamics than their analogs with the 14 carbons as a side chain. Specifically, the up-conversion data showed that the fast first decay relaxation process for the near 550 nm emissive band (coming from the donor) of the polymers was unaffected by the type of linker nor by the side chain type. Whereas, the polymers with furan as the linker showed a slower second components fluorescence decay lifetime than their thiophene analogs. The same trend was observed for the up-conversion measurements of the near 650 nm emission band (acceptor part). The polymers with a furan molecule as the linker showed a longer fluorescence lifetime. Theoretical calculations (see below) show that the polymers with a thiophene in their main-chain have a larger transition dipole moment.

The rate of radiative decay (Γ) for an isolated molecule is proportional to the cube of emission energy (ΔE) and the square of the corresponding transition dipole moment.[61,62] Giving that they have almost identical band gap energies (emission energy), we attributed these shorter lifetime

dynamics by the polymers with a thiophene in their main-chain due to their larger transition dipole moment. Interestingly, only the polymers with the 2-ethylhexyl as a side chain exhibited a measurable rise time in the up-conversion profile. This is evidence of an energy transfer process from the donor moiety to the acceptor moiety. The lack of a rise time in the polymers with a linear side chain could be due to a faster energy transfer that overlaps with the IRF of the instrument. This result indicates that the donor is able to delocalize energy along the linkers which enhance energy transfer between the donor moiety and the acceptor moiety.[59,70−73] The same trend was observed with the TCSPC data. A slower long-decay component for the polymers with furan as the linker was observed. The faster lifetime decay dynamics reported for the polymers with thiophene as the linker are in agreement with a higher transition dipole moment.[60,61] The fluorescence lifetime of the investigated polymers were measured by using the fluorescence up-conversion technique and the time correlated single photon counting (TCSPC) technique. Fluorescence lifetime in the 525−560 nm (donor) exhibits a two component decay while the fluorescence lifetime dynamics in the 600−700 nm region (acceptor) exhibits a single component lifetime decay. The UPC and the TCSPC lifetime measurements of the 600−700 nm emissive band do not match in value but they match in the tendency of the lifetime. This is because the UPC resolution is in the short picoseconds range while the TCSPC goes to the microsecond range. Thus, the long component measurements by the TCSPC are more accurate.

5.5.5 Density Functional Theory Calculations of the Investigated Polymers

The optimized structures of the four repeating units and corresponding xyz coordinates are listed in the Supporting Information. The previous work of Pond et al.[58] shows that the molecular planarity is very important to determine the TPA cross section.[62] In this study, three dihedral angles are measured to quantify the planarity of optimized monomer structures: two dihedral angles

involving nitrogen atoms bonded to side chains in DPP (red and blue one in **Figure 5.5.5.1**) and one dihedral angle of donor/acceptor interface (green one in **Figure 5.5.5.1**). There is a noticeable difference in the dihedral angles depending on the type of linker on the polymer. For the polymer with the thiophene as a linker, the sulfur atom has a much larger atomic radius than the oxygen atom in the furan linker, and this causes severe steric hindrance with adjacent carbonyl groups in DPP. This results in relatively large distortion at the donor/acceptor interface for the thiophene linker, 28.3° and 23.6° for BDF-T2EHDPP and BDF-T-C14DPP, respectively. In contrast to that, polymers with furan as linkers remain almost planar with dihedral angle values of 3.5° and 4.7° for BDF-F-2EHDPP and BDF-F-C14DPP, respectively. The size effects are obviously observed in the other two dihedral angles, too. (see the Supporting Information)

The type of linker as well as the type of alkyl side chains affects dihedral angles within the DPP group, especially for the thiophene linker. Compared to the linear chain tetradecyl groups, the branched alkyl groups, 2-ethylhexyl, induce high geometric restrain. The geometric effects of the 2-ethyl branch are measured to increase the dihedral angles by 13.2° and 7.4° than the chain groups for the dihedral angle in red and blue color, respectively. The effect of alkyl side chain on the planarity is negligible for the furan linker. The dependence of alkyl side chain effect on the type of linker group can be explained as follows. The breaking of planarity due to the large size of the sulfur atom causes repulsion between side chain and linker groups, and this repulsion enhances

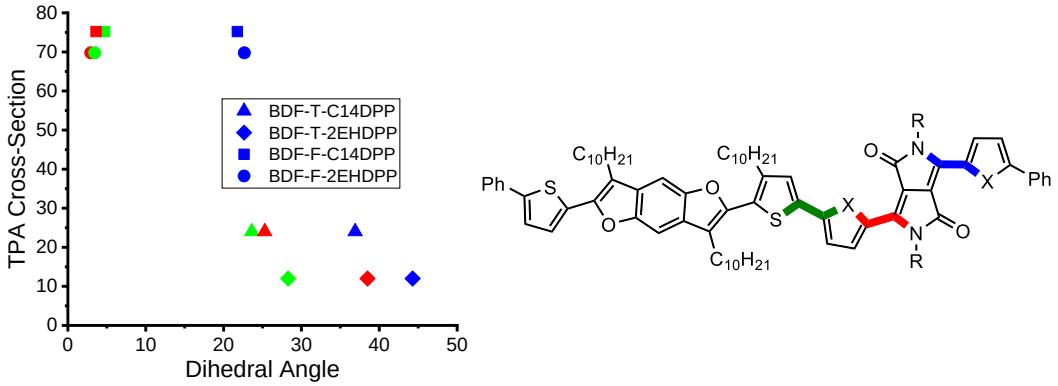

Figure 5.5.5.1. (A) Linear correlation between the TPA cross section and individual dihedral angles (square: BDF-F-C14DPP, circle: BDF-F-2EHDPP, triangle: BDF-T-C14DPP, diamond: BDF-T-2EHDPP, color code of each dihedral angle value is corresponding to the ones in panel B). (B) Selected three dihedral angles to measure the planarity of monomers.

the distortion more. The furan linker does not affect the planarity, and repulsion between side chain and linker groups is avoidable. We have found a linear correlation between the planarity of the polymers and the two photon absorption cross-section: the more planar (the smaller dihedral angle), the higher the cross section (**Figure 5.5.5.1A**).

The rate of radiative decay (Γ) for an isolated molecule is proportional to the cube of emission energy (ΔE) and the square of corresponding transition dipole moment (μ_{tr}). The predicted emission energy of the four monomers is almost the same.[61,62] This outcome is in line with the result of the electrochemical study which gives almost invariant HOMO/LUMO level depending on the type of monomer. The transition dipole moment of the thiophene linker, however, is larger than the one of the furan linker by more than 1 D. The analogy with a classical dipole moment model gives that the larger transition dipole moment of the thiophene linkers comes from the longer monomer length due to the widening at the donor/acceptor interface. The

Table 5.5.5.1. The predicted emission energy (eV), transition dipole moment (D), rate of radiative decay (arbitrary unit), and lifetime (ps) of four monomers of interest.

	ΔE	μ_{tr}	Γ	Lifetime
BDF-F-2EHDPP	2.23	4.98	273.15	757
BDF-F-C_{14}DPP	2.15	4.74	222.03	406
BDF-T-2EHDPP	2.19	6.05	386.0	628
BDF-T-C_{14}DPP	2.18	6.12	390.2	354

approximated rates based on these predictions are listed in **Table 5.5.5.1**. The four data points are severely scattered, and no linear correlation is found. A closer examination, however, reveals that TDDFT simulations can explain the faster radiative decaying of the thiophene linker than the furan linker within the same alkyl side chain, with a similar driving force and a larger transition dipole moment. The reason why the simulations fail to give linear correlation might be due to the omission of non-radiative decay pathways. The comparison of quantum yield between side chains for the same linker group shows that the quantum yield of the tetradecyl side chain is almost half of the 2-ethylhexyl group's one. This implies that the contribution of non-radiative decay is larger for the tetradecyl side chain. The consideration of a non-radiative decay pathway might be necessary to give a linear correlation.

5.6 Discussion

The aim of this study was to probe and correlate the photophysical properties of four new conjugated polymers with their respective photovoltaic performance. The polymers, but those that have a furan as the linker between the donor and the acceptor moieties, showed higher molar extinction coefficients. Organic materials with high extinction coefficients are important for both

(1) the device fabrication and (2) creation of charge carriers.[63] Organic materials with a higher extinction coefficient will promote the development of lightweight and more flexible devices.[63] Furthermore, harvesting more photons is proportional to the generation of free carrier concentrations which could result in higher PCE.[36]

It has been reported that BDF derivatives in either solution or in the solid state emit in the 400−500 nm spectral region.[64] Interestingly, our measured emission spectrum showed a more intense emission band near 550 nm for those polymers containing thiophene as the linkers. This increase in the emission intensity is likely due to a weaker electronic interaction between the BDF and the DPP than their furan analogues.58 On the other hand, the lower emission intensity near 550 nm by the polymers with a furan as the linker suggests that a more efficient energy transfer process could be happening. The TPA cross-section was measured and the data shows a larger TPA cross-section by the polymer with a furan molecule in their main-chain. This data indicates a better communication between the donor and acceptor units for those polymers that have a furan as a linker in their main-chain. With the power of a pulsed laser, we can easily excite the materials and detect the near 550 nm emission band for all of the investigated polymer via the up-conversion fluorescence technique. As can be observed in **Table 5.5.4.1**, longer lifetime dynamics was measured for those polymers that have furan as a linker by detecting both near 550 nm and near 650 nm wavelengths. The same trend was observed for the long component lifetimes measured by the time correlated single photon counting. This agreement in the fluorescence lifetime in both emissive band and by using two different instruments suggest that the emissive bands of the near 550 nm are not artificial. The fluorescence quantum yields were measured and the furan-containing polymers have relatively higher quantum yields than the thiophene-containing polymers analogs. Studies have shown higher quantum yield values for monomers/molecules with a thiophene in

their backbone over their furan analogs. These monomers have shown triplet character and results have been explained by the possible heavy atom effect by the thiophene containing materials over the furan analogues.[65] In this study, the polymer with a furan molecule in the main-chain showed higher quantum yield. We attributed these slightly higher quantum yields from the polymers with a furan molecule in their mainchain due to a better energy transfer from the donor to the acceptor over their thiophene analogs. Further studies in order to evaluate the charge transfer character of the materials were conducted and are discussed below.

Previous studies have tried to elucidate the exciton lifetime for thiophene and furan derivatives. A multi-exponential excitonic lifetime behavior has been documented for materials based on furan or thiophene derivatives.[66] In the case of electron donor−acceptor systems, distyrylfurans have shown slower excitonic lifetimes than their distyrylthiophenes analogues.[67] We found longer fluorescence lifetime for the polymers with a furan molecule as the linker than their thiophene analogues. The rate of radiative decay (Γ) for an isolated molecule is proportional to the cube of emission energy (ΔE) and the square of corresponding transition dipole moment.[61,62] Our theoretical calculations showed that the polymers with a thiophene molecule in their main-chain have a larger transition dipole moment than the furan analogues. As aforementioned, given that our polymers have almost identical ΔE, this data suggest that the fluorescence lifetime of the investigated polymers can be explained by the transition dipole moment. The polymers with a furan molecule in their main-chain have a longer fluorescence lifetime than their thiophene analogues due to their shorter transition dipole moment. This discrepancy in the exciton lifetime may play a role in the reported enhanced PCE by the polymers with a furan in their main-chain. In solar cell devices, the fluorescence lifetime is proportional to the exciton diffusion length.[68] Longer fluorescence decay suggests more time for the exciton to reach the respective interface for

subsequent exciton splitting, resulting in the generation of more charge carriers for photovoltaic conversion.

The TPEF techniques allow us to determine the two-photon absorption cross sections of the polymers. The polymers with a furan molecule as the linker showed larger two-photon absorption cross sections compared to their thiophene polymer analogues. This indicates a better charge separation between the donor and the acceptor leading to a potential higher charge carrier generation.[75,36] It has been documented that the morphology of a material may play an important role in the two photon cross-section value.[11] The DFT calculations showed that the polymers with a furan as the linker have lower dihedral angles between the donor-linker and linker-acceptor junction, thus making them more planar than the thiophene polymer analogues. As mentioned above, under these circumstances a larger TPA cross section suggests a better coupling/communication between the donor−acceptor junctions. This subsequently will lead to a better energy transfer between the two moieties. Previous reports have demonstrated that an enhanced two photon absorption cross-section may play a role in preventing the exciton recombination process.[69] We believe that the dipole moment of the molecule can interact with the entanglement of the exciton and decrease the Coulombic interactions. This will result in easier exciton splitting for subsequent charge carrier generation.

5.7 Conclusions

We have investigated the photophysical properties of four conjugated polymers based on benzodifuran (BDF) as the donor and diketopyrrolopyrrole (DPP) as the acceptor by modifying the proximity of a furan or a thiophene as linkers to the DPP acceptor unit. All of the polymers absorb in the visible spectral region. The polymers with a furan molecule incorporated to the main-chain showed a higher extinction coefficient than their thiophene polymer analogs. Ultrafast

spectroscopy showed that the polymers with a furan molecule in their main-chain have longer fluorescence lifetimes. The two photon excited fluorescence measurements showed that the polymers with a furan molecule in their main-chain have a larger TPA cross-section than their thiophene analogs. Theoretical calculation showed that the polymers with a thiophene molecule in their main-chain have a larger transition dipole moment than their furan analogues. The TD-DFT calculations were also correlated with the TPA cross-section, and there is a linear relationship between the TPA cross-section and the dihedral angles between the donor-linker-acceptor junctions of the investigated polymers, indicating that the planarity of the polymer plays an important role in the ability of a material to absorb subsequently two-photons and, consequently, in the charge transfer character of the polymer.

For the investigated polymers, our results further demonstrated that the incorporation of a furan molecule into polymers backbones that are typically dominated by thiophenes could have an impact in the photophysical properties of the polymers. The bigger extinction coefficient by the polymers with a furan as the linker could result in the creation of more charge carriers due to a higher excited state population. The longer fluorescence lifetime by the polymers with a furan as the linker can be beneficial for achieving a longer exciton diffusion length, which can result in more excitons arriving the interface for exciton splitting. The TD-DFT shows that the polymers with a furan as the linker have lower dihedral angles between the donor-linker acceptor junctions. These results agree with previous studies, and the polymers with a more planarity showed the bigger TPA cross section than their polymer analogues. The combination of the TD-DFT calculations and the TPA cross-section values demonstrate the importance of the morphology for the charge transfer character and the subsequence photovoltaic performance of a material. All of the aforementioned electronic processes could be contributing and can explain the slightly larger

PCE reported for those polymers with a furan as the linker, thus suggesting that furan derivatives could be advantageous for synthetic exploration in order to develop materials with long-range energy transport for photovoltaic applications.

5.8 Supporting Information

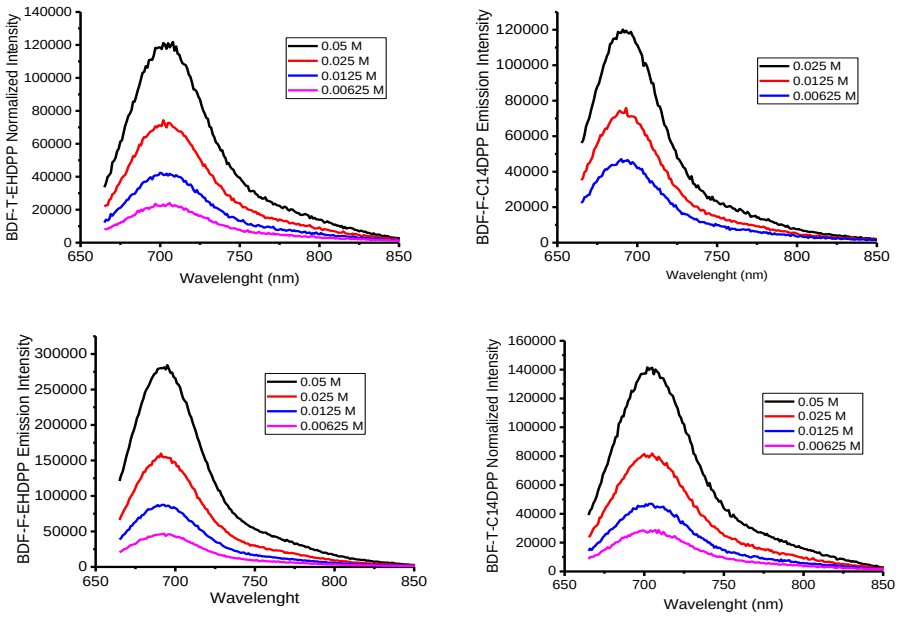

Figure 5.8.1. Emission spectrum at different concentration for the investigated polymers.

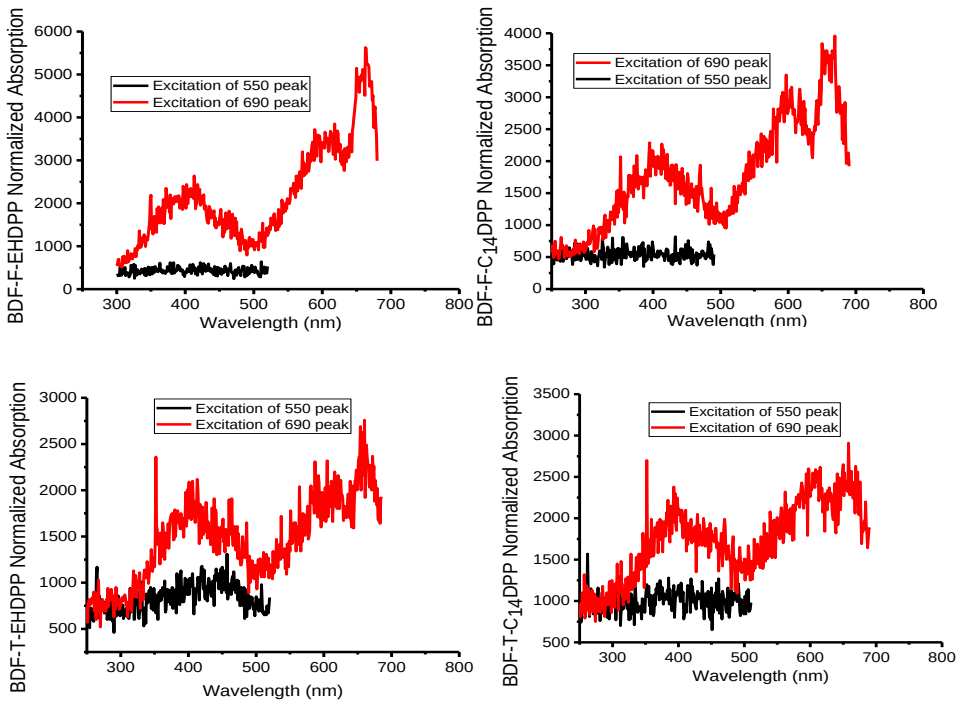

Figure 5.8.2. Excitation spectrums of the investigated polymers.

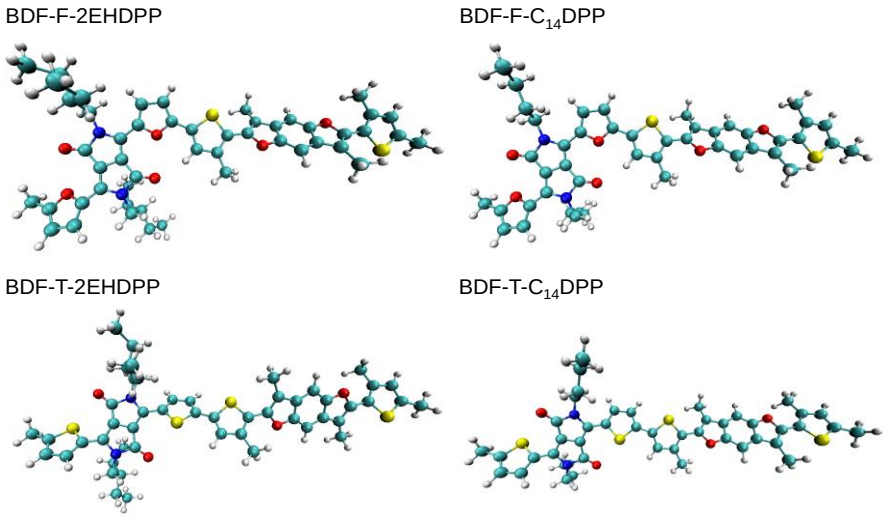

Figure 5.8.3. The optimized structure of four investigated monomers. Color scheme: carbon atom, cyan; hydrogen atom, white; oxygen atom, red; nitrogen atom, blue; sulfur atom, yellow.

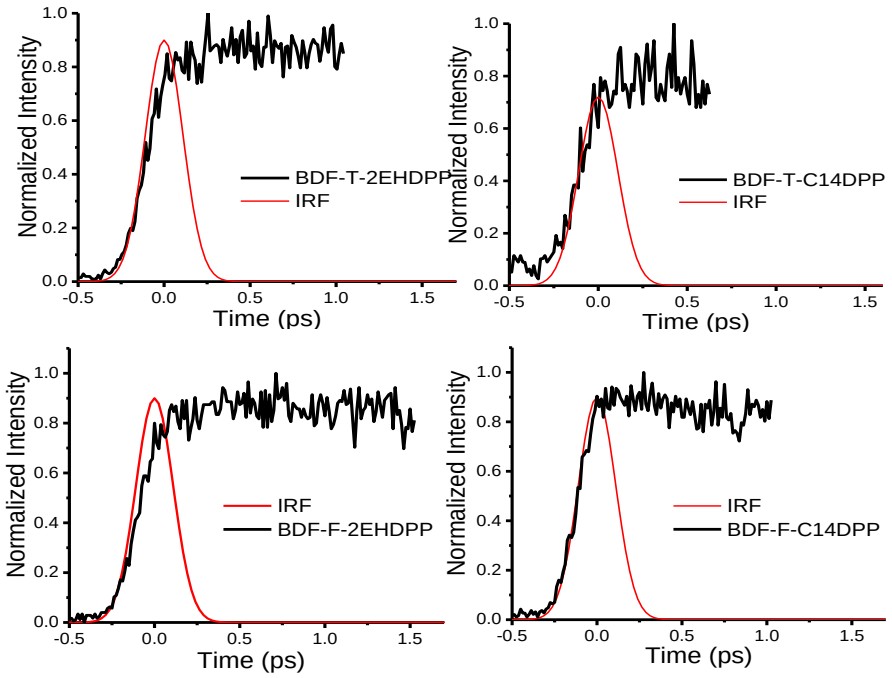

Figure 5.8.4. Rise time of the investigated polymers at 693nm emission.

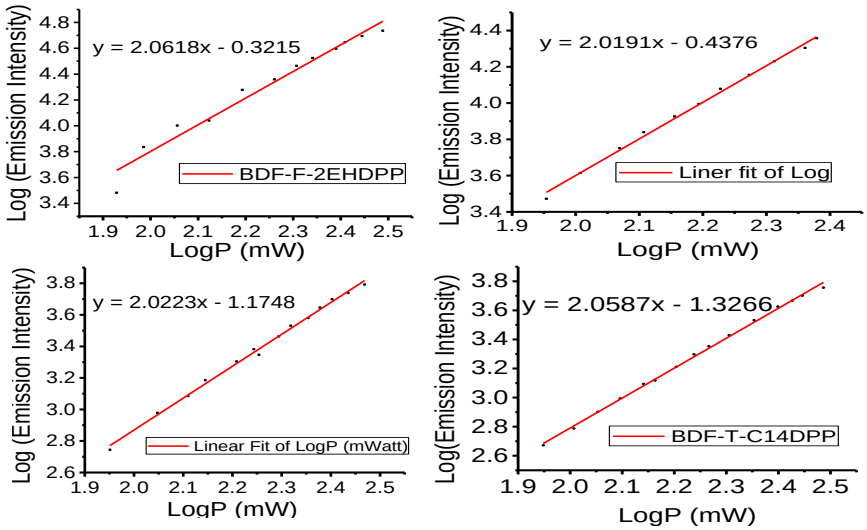

Figure 5.8.5. Two Photon Absorption (**TPA**) at an 860 nm incident wavelength. Logarithm of the emission intensity in function of the logarithm of the power of the investigated polymer. Using a comparison method, the intercept, quantum yield, refraction index and concentration of the sample and the standard (Rhodamine B) were used to calculate the TPA cross-section of the sample.

Table 5.8.1. Dihedral angles between the donor-linker (Green), linker-acceptor (Red), and acceptor-linker (Blue) junctions.

Monomer	Color in Figure 3	Dihedral angle	TPA Cross-section (Expt.)
BDF-F-2EHDPP (Square)	Red	3.0	69.76
	Green	3.5	
	Blue	22.7	
BDF-F-C14DPP (Diamond)	Red	3.6	75.2
	Green	4.7	
	Blue	21.8	
BDF-T-2EHDPP (Circle)	Red	38.5	12
	Green	28.3	
	Blue	44.3	
BDF-T-C14DPP (Triangle)	Red	25.3	24
	Green	23.6	
	Blue	36.9	

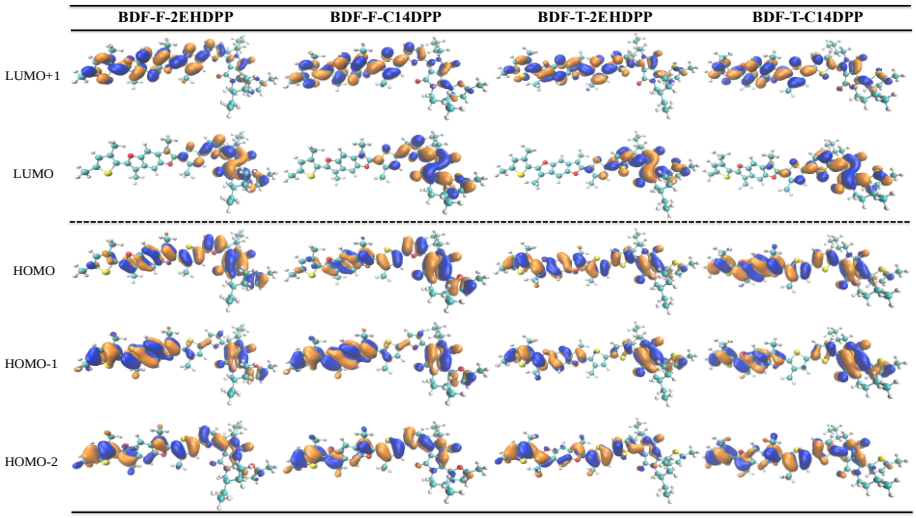

Figure 5.8.6. Molecular orbitals of the investigated polymers involved in the first and second singlet excitation. (See the main text for the detailed level of theory. (Isodensity=0.02)

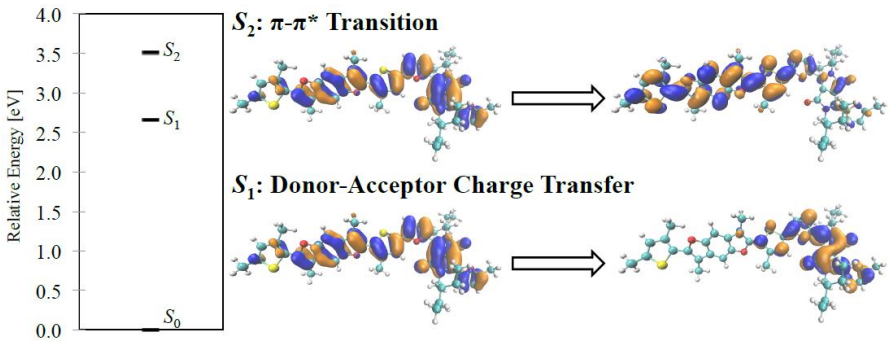

Figure 5.8.7. Graphical description of the main transition for the first and second singlet excitation (S_1 and S_2), respectively, and corresponding energy diagram from TDDFT calculations. BDF-F-2EHDPP is selected as an example.

Table 5.8.2. Excitation energy and character of main transitions from TDDFT calculation. HOMO and LUMO are represented as H and L, respectively.

	Excitation Energy [eV]	Character	Transition Probability [%]
BDF-F-2EHDPP			
S_0 → S_1	2.66	H → L	72.3
		H-1 → L	19.0
S_0 → S_2	3.51	H → L+1	29.3
		H-1 → L	27.1
		H-2 → L	21.9
BDF-F-C14DPP			
S_0 → S_1	2.66	H → L	73.4
		H-1 → L	17.9
S_0 → S_2	3.53	H → L+1	29.5
		H-1 → L	26.2
		H-2 → L	21.2
BDF-T-2EHDPP			
S_0 → S_1	2.87	H → L	56.1
		H-1 → L	34.2
S_0 → S_2	3.59	H → L+1	38.8
		H-2 → L	21.2
		H-1 → L	11.7
BDF-T-C14DPP			
S_0 → S_1	2.74	H → L	50.8
		H-1 → L	38.5
S_0 → S_2	3.44	H → L+1	39.6
		H-2 → L	18.8
		H-1 → L	16.5

Table 5.8.3. Cartesian coordinates of the optimized structures

BDF-F-2EHDPP

S 7.0016695176 -2.8033631993 -1.5616335329
C 8.3652211585 -2.7117559045 -2.6249142392
C 8.3003475165 -1.5786661782 -3.3803136625
C 7.1636413016 -0.7547318709 -3.1222751686
C 6.3619210765 -1.2886634753 -2.1412703405
C 5.1154533375 -0.7575191221 -1.6192642252
O 4.3590539898 -0.0470726656 -2.5240265695
C 3.2526308391 0.3812871925 -1.8607299327
C 3.2887118501 -0.0715412967 -0.5259363437
C 4.5243794766 -0.8053551017 -0.3914544645
C 9.4243999870 -3.7708719421 -2.6328866336
C 2.2573504077 0.2533522609 0.3578969665
C 1.2489913550 1.0299406765 -0.1819430524
C 1.2159906989 1.4864712249 -1.5154092904
C 2.2446332864 1.1564405597 -2.4011159778
C 5.0256567918 -1.4307009978 0.8707804869
O 0.1509783014 1.4721968080 0.4866581633
C -0.5888516410 2.2073075683 -0.4118168689
C -0.0040617147 2.2469979898 -1.6419376201
C -0.4994469517 2.8958220609 -2.8942635235
C -1.8079811659 2.7901780797 0.1195197784
S -2.2740045473 4.4071591754 -0.3278148183
C -3.6724217874 4.3280682013 0.6869897326
C -3.7561341967 3.1243426416 1.3375952653
C -2.6911228800 2.2376318995 1.0205649048
C -2.5769153689 0.8575690125 1.6055311110
H 9.0593927528 -1.3189715188 -4.1119178804
C 6.9144758358 0.5353938973 -3.8540868501
H 9.9037874341 -3.8727755998 -1.6531782432
H 10.1970024034 -3.5079299187 -3.3608274278
H 9.0189756224 -4.7503179953 -2.9095466402
H 2.2421158910 -0.0740383154 1.3914510110
H 2.2621485876 1.4884389584 -3.4331906885
H 4.8191219776 -0.7768752565 1.7253383482
H 6.1041800122 -1.6051278524 0.8338335304
H 4.5356426494 -2.3918306504 1.0669659161
H -1.5632454506 3.1387397025 -2.8284839155
H -0.3572803669 2.2268237187 -3.7502390652
H 0.0456988594 3.8227984706 -3.1084985219
H -4.5734152523 2.8887309233 2.0135824572
H -3.5538623911 0.5155143912 1.9577143417
H -1.8855025044 0.8469272474

2.4545169057
H -2.1996117555 0.1408932928 0.8710891476
H 7.8405832018 0.8994293013 -4.3088731345
H 6.1740251397 0.4030710416 -4.6497227182
H 6.5324639399 1.3100577665 -3.1843279427
C -4.6139718559 5.4152298488 0.7882311545
O -5.6872866194 5.1755095913 1.5617661642
C -6.4640892771 6.2899402678 1.5829004670
C -5.8739005632 7.2564635699 0.8016368842
C -4.6812530572 6.6908765523 0.2870835191
C -7.6386968341 6.1325816508 2.3953657855
C -7.9663357892 5.0236965813 3.1481292194
C -9.1997337411 5.2854588395 3.8186293618
C -9.6488629580 6.6190308487 3.4579165699
O -10.6138764378 7.2961181955 3.7579198238
N -8.6397561426 7.0768403106 2.5579149516
C -7.4974785667 3.7112290357 3.5646623946
O -6.5370350489 3.0156122975 3.2797082292
N -8.4943919644 3.2744482738 4.4878253457
C -9.4993878218 4.2197183823 4.6281885599
C -10.6347483885 4.0909957096 5.5070524355
O -11.7098219033 4.8480820813 5.1605781305
C -12.6486348935 4.7063326872 6.1185972701
C -12.1954096539 3.8601113144 7.0881225544
C -10.8881441893 3.4580109015 6.6945308123
C -13.9137828674 5.4582110429 5.9158714470
H -6.2247090082 8.2595455091 0.6190163047
H -3.9601462098 7.1682952030 -0.3603423906
C -8.7451336542 8.4109030343 1.9995411407
C -8.5001547230 1.8818176392 4.9061194536
H -12.7288951930 3.5671054756 7.9806771709
H -10.2141068050 2.8244023594 7.2511027490
H -13.7063766445 6.5213125324 5.7592953766
H -14.5587468122 5.3456447068 6.7901791792
H -14.4519444711 5.0899314680 5.0357220354
C -8.9775089519 0.8986826484 3.8240789905
C -10.3883333655 1.2404324812 3.2985204129
C -10.4097912038 2.1255040354 2.0515949757
C -8.9137265826 -0.5277138153 4.3939415006
C -8.9238810692 -1.6092392007 3.3133842698
C -8.3326056233 9.5347833466 2.9678069320
C -8.4692425747 10.8886149781 2.2362530294
C -9.1218372136 11.9885485715 3.0739930485
C -6.9392360334 9.3057728094

3.5664061255
C -6.5259256088 10.3400101713 4.6123205349
H -9.7974573609 8.5528654267 1.7350330528
H -8.1714283111 8.4520229326 1.0718674979
H -9.1290256206 1.7816818796 5.7918362229
H -7.4740790031 1.6369114616 5.1938312568
H -8.2615957080 0.9629899587 2.9938970363
H -10.9700675343 1.7099085854 4.1027837090
H -10.9167285172 0.3088632431 3.0622589415
H -9.9137595498 3.0869235255 2.2121758462
H -11.4383189148 2.3353585179 1.7398178471
H -9.9003500002 1.6272138817 1.2188877163
H -9.7586043274 -0.6774687221 5.0811344055
H -8.0016723965 -0.6430383194 4.9946906582
H -9.8160845177 -1.5426142810 2.6812990574
H -8.9046939206 -2.6109162745 3.7547162430
H -8.0479440775 -1.5092756073 2.6630045846
H -9.0615384222 9.5082741665 3.7888388965
H -9.0695670126 10.7540560346 1.3259670605
H -7.4787869072 11.2182398811 1.8928003490
H -10.1322152095 11.6906374958 3.3749388565
H -9.2010151527 12.9228214063 2.5082374786
H -8.5535664443 12.1936983346 3.9864770845
H -6.1918653458 9.2937774183 2.7613715939
H -6.9098424255 8.3103266197 4.0255777349
H -6.4244473921 11.3396362224 4.1763824887
H -5.5621781283 10.0745126029 5.0581098918
H -7.2662847038 10.3977064710 5.4184337959

BDF-F-C14DPP

S 7.1586103549 -2.6927800278 -1.8916443419
C 8.5050086012 -2.6154590348 -2.9776045598
C 8.4452367094 -1.4762517974 -3.7241254776
C 7.3268650747 -0.6357555719 -3.4408728234
C 6.5337294005 -1.1636589460 -2.4494115676
C 5.3059698847 -0.6170633330 -1.9001170316
O 4.5501414869 0.1231802641 -2.7810614903
C 3.4589766932 0.5555907527 -2.0956922334
C 3.5040594231 0.0764705866 -0.7703052846
C 4.7298042643 -0.6783814961 -0.6656076335
C 9.5505839460 -3.6876144505 -3.0059190730
C 2.4864895045 0.3971072704 0.1308723922
C 1.4822734593 1.1966668845 -0.3824011892
C 1.4414908320 1.6815860387 -1.7057016987

C	2.4567773176	1.3564854994	-2.6086272188
C	5.2379445919	-1.3381535744	0.5763134886
O	0.3933665328	1.6315148805	0.3051116774
C	-0.3499668728	2.3891845939	-0.5713605835
C	0.2257345738	2.4533355906	-1.8046188731
C	-0.2792931871	3.1325053625	-3.0368265333
C	-1.5694010151	2.9543447187	-0.0210467910
S	-2.0344919433	4.5885066571	-0.4011401875
C	-3.4412524518	4.4622285330	0.5986940836
C	-3.5266842068	3.2301261621	1.1935018527
C	-2.4578888928	2.3600203705	0.8472913481
C	-2.3464636241	0.9561470242	1.3729403386
H	9.1963793006	-1.2231362838	-4.4661579943
C	7.0867144347	0.6629782786	-4.1603121515
H	9.1269734661	-4.6628088149	-3.2700015698
H	10.0506690312	-3.7925408107	-2.0369311786
H	10.3097507434	-3.4365610061	-3.7519836587
H	2.4770341226	0.0485523422	1.1575592856
H	2.4672589163	1.7075118946	-3.6344955783
H	5.0355098633	-0.7086121881	1.4497725224
H	6.3165429781	-1.5099997839	0.5289006695
H	4.7505587213	-2.3052008733	0.7488138061
H	-1.3417117172	3.3767403358	-2.9548732926
H	-0.1472072181	2.4834950203	-3.9096420479
H	0.2664311107	4.0627180719	-3.2349544600
H	-4.3487913524	2.9626509132	1.8515426914
H	-3.3230053996	0.6038234610	1.7157174275
H	-1.6504049556	0.9074499213	2.2167003034
H	-1.9762429071	0.2686794809	0.6074049933
H	8.0125757835	1.0179197114	-4.6227819247
H	6.3359083887	0.5464804603	-4.9487583257
H	6.7222454990	1.4375608040	-3.4809103332
C	-4.3903553284	5.5373459563	0.7501182162
O	-5.4758353365	5.2342485088	1.4850774136
C	-6.2619753004	6.3375066958	1.5689924227
C	-5.6692468131	7.3630125056	0.8697770095
C	-4.4607211492	6.8449460277	0.3395599017
C	-7.4513024276	6.1247095631	2.3444815354
C	-7.8008439063	4.9752264984	3.0191419212
C	-9.0549561324	5.1977492544	3.6650327474
C	-9.4898537691	6.5554956380	3.3777195132
O	-10.4513671865	7.2220439255	3.7079260076
N	-8.4558241130	7.0590617090	2.5286841627

C -7.3347006876 3.6473780909 3.3803046106
O -6.3595587865 2.9748250164 3.0884703822
N -8.3504790058 3.1610465961 4.2558783548
C -9.3737311888 4.0866314196 4.4053468716
C -10.5525936298 3.8893172828 5.2116224313
O -11.6085964795 4.6753779746 4.8675954119
C -12.6099555238 4.4384941445 5.7393186855
C -12.2166257583 3.5036332407 6.6517724669
C -10.8825652471 3.1444250349 6.3120455762
C -13.8638086933 5.2064986734 5.5277289390
H -6.0347961708 8.3720417126 0.7562104025
H -3.7313083834 7.3736300979 -0.2567119683
C -8.4769940787 8.4381617424 2.0861117783
C -8.3160286299 1.7633220814 4.6560487350
H -12.8079558642 3.1212309754 7.4710426184
H -10.2481152316 2.4568745422 6.8498350481
H -13.6680913845 6.2826788827 5.5709062661
H -14.5948346929 4.9469623545 6.2967122528
H -14.2959042600 4.9862017912 4.5458904330
C -8.8491863880 0.8122371326 3.5822533124
C -10.3288689119 1.0034717306 3.2477375898
C -10.8158498620 0.0065661594 2.1975424878
C -7.6130891471 9.3484854376 2.9600779131
C -7.5886465230 10.7897278560 2.4534671924
C -6.7234547515 11.6974641949 3.3260076183
H -9.5230017300 8.7508111015 2.1420372461
H -8.1755202766 8.4819274654 1.0338970086
H -8.8695896338 1.6413860239 5.5869278568
H -7.2670045391 1.5345393456 4.8590007009
H -8.2407372456 0.9359897607 2.6783923399
H -10.4953223679 2.0247436570 2.8828383113
H -10.9276063760 0.9027393936 4.1623939739
H -10.2500842381 0.1142675101 1.2651001652
H -11.8751424934 0.1586667808 1.9669146800
H -10.6924029944 -1.0256694978 2.5451869637
H -8.0084383157 9.3165570855 3.9826399042
H -8.6141679254 11.1794605710 2.4161214073
H -7.2144568977 10.8089018217 1.4198499148
H -7.0935165682 11.7154071735 4.3571269429
H -6.7197591215 12.7261183503 2.9518598544
H -5.6863439784 11.3439857789 3.3509461132
H -8.6822215692 -0.2144267514 3.9353141466
H -6.5895722533 8.9545200898 3.0062564362

BDF-T-2EHDPP

S 8.2300554407 -1.5458991425 -2.8320364034
C 9.3478822017 -1.1345914176 -4.0880995051
C 8.8686931015 -0.0941021445 -4.8272171227
C 7.5918147779 0.3914361547 -4.4123152911
C 7.1062348781 -0.3106125645 -3.3346976576
C 5.8616350182 -0.0934509160 -2.6187397297
O 5.4380806442 1.2158965983 -2.5752413747
C 4.2588786693 1.2252213604 -1.9001282518
C 3.9298795522 -0.0832158361 -1.4903507626
C 4.9923292894 -0.9282437846 -1.9811774281
C 10.6301702548 -1.8866706730 -4.2731079018
C 2.7507030069 -0.3251394058 -0.7821701655
C 1.9729851167 0.7935085629 -0.5459931830
C 2.2999739741 2.1006162063 -0.9606697987
C 3.4831700347 2.3437723975 -1.6627945799
C 5.0564307239 -2.4144761153 -1.8304159678
O 0.7815153663 0.7976715072 0.1085399734
C 0.3411459705 2.1020752681 0.1160283304
C 1.2159503444 2.9393269365 -0.5067203717
C 1.1240257162 4.4211265356 -0.6807250610
C -0.9434177901 2.3175320862 0.7606936417
S -2.1420330410 3.3370981994 0.0239097170
C -3.2849111899 2.9967584736 1.2804488234
C -2.7470727038 2.1443591118 2.2091209971
C -1.4103588548 1.7480026970 1.9230329381
C -0.6141643469 0.8180527758 2.7953212891
H 9.4099204716 0.3225947590 -5.6710498265
C 6.8990830899 1.5364860351 -5.0987239076
H 10.4524813189 -2.9494940361 -4.4699330717
H 11.2740913863 -1.8139573342 -3.3897425080
H 11.1769978178 -1.4712530159 -5.1240991825
H 2.4549113737 -1.3132190619 -0.4478324814
H 3.7752147964 3.3308217441 -2.0034956445
H 4.0634833831 -2.8534194007 -1.9786765667
H 5.3976290198 -2.7053960399 -0.8298243787
H 5.7349856470 -2.8643177801 -2.5600116855
H 0.3627998331 4.8549001417 -0.0267505965
H 0.8740602888 4.6893124218 -1.7139251229
H 2.0836694133 4.8932820708 -0.4422949900
H -3.2983295031 1.7905833460 3.0745332767
H -1.0083918757 0.8170725139 3.8156070259
H 0.4379867890 1.1128304173 2.8321779121
H -0.6510674740 -0.2080718444

2.4153347933
H 7.2858706754 1.6590371664 -6.1148619418
H 5.8192062654 1.3797984530 -5.1567630914
H 7.0607729653 2.4750847369 -4.5582582014
C -4.6077869793 3.5985651890 1.2506882000
S -5.4846622122 3.9048104286 2.7110603411
C -6.8153411410 4.5885270780 1.8370949871
C -6.5760242063 4.5688405150 0.4832516731
C -5.3237238200 4.0047754657 0.1496805699
C -7.9993997734 5.0508940158 2.5372124425
C -8.6461849323 4.4737988062 3.5969736975
C -9.7985926051 5.2555229109 3.9144886159
C -9.8375973298 6.3952663534 3.0126095611
O -10.5892062239 7.3453109302 2.8987134522
N -8.6988801076 6.1984122999 2.1754164286
C -8.6191686384 3.3214276210 4.4822663224
O -7.8631495501 2.3745290813 4.5958806379
N -9.7751173001 3.5004365712 5.2980006990
C -10.4672734826 4.6560192962 4.9487581660
C -11.6766419726 5.0955960609 5.6224242484
S -12.9941427779 5.7760030499 4.7205602539
C -13.9244550320 6.0386752163 6.1532926836
C -13.2346003703 5.6373733155 7.2646461661
C -11.9560206835 5.0996983195 6.9663162028
C -15.2975111962 6.6348164309 6.0903904960
H -7.2991503958 4.9025751922 -0.2511732042
H -4.9711707082 3.8744890667 -0.8670854959
C -8.2549397220 7.2860135806 1.3188859215
C -10.2215331307 2.4007733157 6.1378196882
H -13.6323011575 5.7265755225 8.2694021483
H -11.2518867150 4.7648724284 7.7188799796
H -15.2780475066 7.6501974925 5.6804470951
H -15.7230846083 6.6834753404 7.0963836392
H -15.9689169009 6.0353111146 5.4664983016
C -10.8506035691 1.2256947253 5.3697033301
C -12.0221537085 1.6623277903 4.4655924672
C -11.6325182155 2.0310400388 3.0328105525
C -11.2916027087 0.1678775975 6.3961198098
C -11.4907366057 -1.2202474132 5.7899525188
C -7.5985082149 8.4539742487 2.0760842204
C -7.1421652031 9.5076226218 1.0437812191
C -7.3601962932 10.9544575445 1.4888857005
C -6.4595776412 7.9525123758 2.9777386872
C -5.7218144295 9.0480857705

3.7458322487
H -9.1375101653 7.6501278568 0.7856729470
H -7.5509522676 6.8930951295 0.5838966533
H -10.9423233598 2.7832072295 6.8621536809
H -9.3434686983 2.0470401533 6.6855487124
H -10.0626857381 0.7861805693 4.7436973953
H -12.5500459417 2.5017942194 4.9388197660
H -12.7543622982 0.8471020443 4.4153109760
H -10.9514115948 2.8853051420 2.9853309071
H -12.5204586641 2.2868713657 2.4449880357
H -11.1363177627 1.1865359213 2.5411308011
H -12.2203017285 0.5052602651 6.8777615826
H -10.5384693558 0.0984736869 7.1923338696
H -12.2369763014 -1.2113166656 4.9879708049
H -11.8279462026 -1.9369184695 6.5457949079
H -10.5522478799 -1.5940745458 5.3659282241
H -8.3726346873 8.9009576233 2.7137239248
H -7.6907369779 9.3568521570 0.1038745645
H -6.0836048922 9.3429272732 0.8005019691
H -8.4248471978 11.1447234332 1.6635532133
H -7.0134010526 11.6589614298 0.7254785775
H -6.8278031057 11.1776463687 2.4178863892
H -5.7405739784 7.3910344935 2.3633925650
H -6.8675409569 7.2371984140 3.7025272973
H -5.1710459902 9.7151190760 3.0745245874
H -4.9968786045 8.6099171485 4.4392669601
H -6.4192686656 9.6577632071 4.3314810508

BDF-T-C14DPP

S 8.6721894696 -1.0004358655 -2.1854025296
C 9.7216413196 -0.9146479437 -3.5566828420
C 9.0871919351 -0.3100496577 -4.6004849076
C 7.7465960969 0.0998489873 -4.3308263323
C 7.3702455709 -0.2117965268 -3.0414869506
C 6.1018159804 0.0310538628 -2.3861491628
O 5.1762942315 0.7061327940 -3.1456416114
C 4.0594632246 0.8433501103 -2.3840463604
C 4.2668451807 0.2484422709 -1.1226970717
C 5.6118421207 -0.2731200245 -1.1472533693
C 11.1210406682 -1.4460547959 -3.5038974928
C 3.2489128672 0.2615860600 -0.1648982951
C 2.0809184716 0.8863166230 -0.5614603483
C 1.8796332642 1.4829890322 -1.8220446922
C 2.8941312489 1.4686319010 -2.7814006596
C 6.2904841251 -0.9858551350

-0.0183838588
O 0.9587118961 1.0226479482 0.1964378514
C 0.0378359357 1.6948781658 -0.5761167420
C 0.5318279295 1.9951531420 -1.8101282878
C -0.1396242837 2.6706013141 -2.9625856130
C -1.2450929724 1.9396484758 0.0562214656
S -2.1102977370 3.4163956825 -0.2537660944
C -3.4181368372 2.9348719462 0.7747122458
C -3.1596021041 1.7156682977 1.3458036843
C -1.9236178811 1.1363996544 0.9461131207
C -1.4558955304 -0.2102111882 1.4243181154
H 9.5651320631 -0.1530558556 -5.5624302124
C 6.9006734360 0.7800632738 -5.3733080308
H 11.1486147624 -2.4854526199 -3.1597741893
H 11.7525757611 -0.8550176753 -2.8309810787
H 11.5656200563 -1.4094843640 -4.5023080751
H 3.3548826736 -0.1817979040 0.8189624105
H 2.7854628582 1.9149480716 -3.7635386982
H 5.6101893608 -1.0857406418 0.8319791206
H 7.1774995222 -0.4454245263 0.3312594805
H 6.6103686527 -1.9939413693 -0.3054171901
H -1.2269518363 2.6790179397 -2.8511523990
H 0.0984743797 2.1484734864 -3.8959542624
H 0.1961410365 3.7087235919 -3.0710552969
H -3.8575968194 1.2157798651 2.0099032782
H -2.2962777527 -0.7866299399 1.8214227210
H -0.7074464264 -0.1098903414 2.2169327993
H -0.9941235701 -0.7820977913 0.6152006333
H 7.4656129493 0.8840099519 -6.3041048606
H 5.9901249195 0.2123590536 -5.5848879913
H 6.5873385956 1.7764824705 -5.0496253312
C -4.5909259625 3.7786598305 0.9232347687
S -5.5907894889 3.6649680920 2.3263869896
C -6.6626020877 4.9036331869 1.7366846458
C -6.2391515676 5.3597842142 0.5074531385
C -5.0686577585 4.7233628868 0.0442186453
C -7.8211666122 5.2879843579 2.5172873026
C -8.5159921441 4.5426410926 3.4373965656
C -9.5851529140 5.3284647868 3.9593134750
C -9.5316951522 6.6404652380 3.3410067022
O -10.1955335203 7.6505921032 3.4779805023
N -8.4332040050 6.5394259627 2.4319394859
C -8.5559623522 3.2424001658 4.0850600232
O -7.8873182481 2.2304528970

3.9661197999
N -9.6476836334 3.3494629939 4.9942654463
C -10.2564738201 4.5999117255 4.9044573908
C -11.3797848555 4.9962899629 5.7340052800
S -12.6517965588 5.9844429643 5.0849733979
C -13.4859161598 6.0182344753 6.5967134232
C -12.7995674936 5.3175635468 7.5509730602
C -11.6015873128 4.7353248636 7.0635559709
C -14.7717567664 6.7699378791 6.7596164534
H -6.7689464800 6.1036592485 -0.0710795684
H -4.6074449180 4.9303184543 -0.9145991602
C -7.9450555952 7.7440802413 1.7820910889
C -10.1807731147 2.1393720391 5.6055457677
H -13.1400483297 5.2321715365 8.5768038273
H -10.9087733581 4.1790848755 7.6836941500
H -15.5359645537 6.4232038168 6.0558953175
H -14.6312686486 7.8438448920 6.5960710475
H -15.1554734056 6.6292594537 7.7736729503
C -10.9942201185 1.2859322181 4.6295262815
C -12.1931703572 2.0116805305 4.0180741213
C -13.0333716516 1.1000673745 3.1259280599
C -6.6597891039 8.2879950283 2.4035452967
C -6.1353954686 9.5147514635 1.6583097085
C -4.8876074667 10.1068300434 2.3102052619
H -8.7536005742 8.4702236000 1.9013131797
H -7.8264261386 7.5771041689 0.7084472843
H -10.7977996997 2.4213054096 6.4582933492
H -9.3240810258 1.5710641449 5.9757620973
H -10.3274199254 0.9286811868 3.8357755536
H -11.8407867982 2.8677574540 3.4289499733
H -12.8198056119 2.4274141021 4.8187238700
H -12.4290325122 0.6859030020 2.3107501607
H -13.8722256374 1.6429053255 2.6788727855
H -13.4430744509 0.2581924714 3.6959936766
H -6.8642646295 8.5428157622 3.4510747431
H -6.9228920030 10.2787950244 1.6128830317
H -5.9110237177 9.2383815584 0.6189288224
H -5.0964653503 10.4203515140 3.3390493124
H -4.5255776962 10.9800316692 1.7583348851
H -4.0777742286 9.3692893227 2.3437721184
H -11.3390559052 0.3972653342 5.1750450594
H -5.8884419246 7.5080347008 2.4101073910

References

(1) Guo, X.; Baumgarten, M.; Müllen, K. Designing π-Conjugated Polymers for Organic Electronics. *Prog. Polym. Sci.* **2013***, 38*, 1832-1908.

(2) Bildirir, H.; Gregoriou, V.; Avgeropoulos, A.; Scherf, U.; Chochos, C. L. Porous Organic Polymers as Emerging New Materials for Organic Photovoltaic Applications: Current Status and Future Challenges. *Mater. Horiz.* **2017**, DOI: 10.1039/C6MH00570E.

(3) Chen, J. D.; Cui, C.; Li, Y. Q.; Zhou, L.; Ou, Q. D.; Li, C.; Tang, J. X. Single-Junction Polymer Solar Cells Exceeding 10% Power Conversion Efficiency. *Adv. Mater.* **2015**, *27*, 1035-1041.

(4) Coe-Sullivan, S. Optoelectronics: Quantum Dot Developments. *Nat. Photonics.* **2009**, *3*, 315-316.

(5) Green, M. A.; Emery, K.; Hishikawa, Y.; Warta, W.; Dunlop, E. D. Solar Cell Efficiency Tables (Version 45). *Prog. Photovoltaics.* **2015**, *23*, 1-9.

(6) Furgal, J. C.; Jung, J. H.; Goodson, T.; Laine, R. M. Analyzing Structure-Photophysical Property Relationships for Isolated T8, T10, and T12 Stilbenevinylsilsesquioxanes. *J. Am. Chem. Soc.* **2013**, *135*, 12259-12269.

(7) Donehue, J. E.; Varnavski, O. P.; Cemborski, R.; Iyoda, M.; Goodson, T. Probing Coherence in Synthetic Cyclic Light-Harvesting Pigments. *J. Am. Chem. Soc.* **2011**, *133*, 4819-4828.

(8) Bhaskar, A.; Ramakrishna, G.; Lu, Z.; Twieg, R.; Hales, J. M.; Hagan, D. J.; Goodson, T. Investigation of Two-Photon Absorption Properties in Branched Alkene and Alkyne Chromophores. *J. Am. Chem. Soc.* **2006**, *128*, 11840-11849.

(9) Guo, M.; Varnavski, O.; Narayanan, A.; Mongin, O.; Majoral, J. P.; Blanchard-Desce, M.; Goodson, T. Investigations of Energy Migration in an Organic Dendrimer Macromolecule for Sensory Signal Amplification. *J. Phys. Chem. A.* **2009**, *113*, 4763-4771.

(10) Varnavski, O. P.; Ostrowski, J. C.; Sukhomlinova, L.; Twieg, R. J.; Bazan, G. C.; Goodson, T. Coherent Effects in Energy Transport in Model Dendritic Structures Investigated by Ultrafast Fluorescence Anisotropy Spectroscopy. *J. Am. Chem. Soc.* **2002**, *124*, 1736-1743.

(11) Raymond, J. E.; Bhaskar, A.; Goodson, T.; Makiuchi, N.; Ogawa, K.; Kobuke, Y. Synthesis and Two-Photon Absorption Enhancement of Porphyrin Macrocycles. *J. Am. Chem. Soc.* **2008**, *130*, 17212-17213.

(12) Goodson, T. Optical Excitations in Organic Dendrimers Investigated by Time-Resolved and Nonlinear Optical Spectroscopy. *Acc. Chem. Res.* **2005**, *38*, 99-107.

(13) Ramakrishna, G.; Goodson, T.; Rogers-Haley, J. E.; Cooper, T. M.; McLean, D. G.; Urbas, A. Ultrafast Intersystem Crossing: Excited State Dynamics of Platinum Acetylide

Complexes. *J. Phys. Chem. C.* **2008**, *113*, 1060-1066.

(14) Bhaskar, A.; Guda, R.; Haley, M. M.; Goodson, T. Building Symmetric Two-Dimensional Two-Photon Materials. *J. Am. Chem. Soc.* **2006**, *128*, 13972-13973.

(15) Goodson, T. Time-Resolved Spectroscopy of Organic Dendrimers and Branched Chromophores. *Annu. Rev. Phys. Chem*. **2005**, *56*, 581-603.

(16) Ispasoiu, R. G.; Balogh, L.; Varnavski, O. P.; Tomalia, D. A.; Goodson, T. Large Optical Limiting and Ultrafast Luminescence Dynamics from Novel Metal-Dendrimer Nanocomposite Materials. *J. Am. Chem. Soc*, **2000**, *122*, 11005-11006.

(17) Dou, L.; Liu, Y.; Hong, Z.; Li, G.; Yang, Y. Low-Bandgap Near-IR Conjugated Polymers/Molecules for Organic Electronics. *Chem. Rev.* **2015**, *115*, 12633-12665.

(18) Gélinas, S.; Rao, A.; Kumar, A.; Smith, S. L.; Chin, A. W.; Clark, J.; Friend, R. H. Ultrafast Long-Range Charge Separation in Organic Semiconductor Photovoltaic Diodes. *Science*, **2014**, *343*, 512-516.

(19) Cho, H. S.; Rhee, H.; Song, J. K.; Min, C. K.; Takase, M.; Aratani, N.; Kim, D. Excitation Energy Transport Processes of Porphyrin Monomer, Dimer, Cyclic Trimer, and Hexamer Probed by Ultrafast Fluorescence Anisotropy Decay. *J. Am. Chem. Soc.* **2003**, *125*, 5849-5860.

(20) Luhman, W. A.; Holmes, R. J. Enhanced Exciton Diffusion in an Organic Photovoltaic Cell by Energy Transfer Using a Phosphorescent Sensitizer. *App. Phys. Lett.* **2009**, *94*, 110.

(21) Pivrikas, A.; Sariciftci, N. S.; Juška, G.; Österbacka, R. A Review of Charge Transport and Recombination in Polymer/Fullerene Organic Solar Cells. *Prog. Photovoltaics.* **2007**, *15*, 677-696.

(22) Varnavski, O.; Ispasoiu, R. G.; Balogh, L.; Tomalia, D.; Goodson, T. Ultrafast Time-Resolved Photoluminescence From Novel Metal-Dendrimer Nanocomposites. *J. Chem. Phys.*, **2001**, *114*, 1962-1965.

(23) Keller, J. M.; Glusac, K. D.; Danilov, E. O.; McIlroy, S.; Sreearuothai, P.; R. Cook, A.; Schanze, K. S. Negative Polaron and Triplet Exciton Diffusion in Organometallic "Molecular Wires". *J. Am. Chem. Soc.* **2011**, *133*, 11289-11298.

(24) Kazaoui, S.; Minami, N.; Tanabe, Y.; Byrne, H. J.; Eilmes, A.; Petelenz, P. Comprehensive Analysis of Intermolecular Charge-Transfer Excited States in C_{60} and C_{70} films. *Phys. Rev. B.* **1998**, *58*, 7689.

(25) Veldman, D.; Meskers, S. C.; Janssen, R. A. The Energy of Charge-Transfer States in Electron Donor-Acceptor Blends: Insight into the Energy Losses in Organic Solar Cells. *Adv. Funct. Mat.* **2009**, *19*, 1939-1948.

(26) Wong, W. Y.; Wang, X. Z.; He, Z.; Djurišić, A. B.; Yip, C. T.; Cheung, K. Y., Chan, W. K.

Metallated Conjugated Polymers as a New Avenue Towards High-Efficiency Polymer Solar Cells. *Nat. Mater.* **2007**, *6*, 521-527.

(27) Ramakrishna, G.; Varnavski, O.; Kim, J.; Lee, D.; Goodson, T. Quantum-Sized Gold Clusters as Efficient Two-Photon Absorbers. *J. Am. Chem. Soc.* **2008**, *130*, 5032-5033.

(28) Devadas, M. S.; Kim, J.; Sinn, E.; Lee, D.; Goodson, T.; Ramakrishna, G. Unique Ultrafast Visible Luminescence in Monolayer-Protected Au_{25} clusters. *J. Phys. Chem. C.* **2010**, *114*, 22417-22423.

(29) Lahankar, S. A.; West, R.; Varnavski, O.; Xie, X.; Goodson, T.; Sukhomlinova, L.; Twieg, R. Electronic Interactions in a Branched Chromophore Investigated by Nonlinear Optical and Time-Resolved Spectroscopy. *J. Chem. Phys.* **2004**, *120*, 337-344.

(30) Flynn, D. C.; Ramakrishna, G.; Yang, H. B.; Northrop, B. H.; Stang, P. J.; Goodson, T. Ultrafast Optical Excitations in Supramolecular Metallacycles with Charge Transfer Properties. *J. Am. Chem. Soc.* **2010**, *132*, 1348-1358..

(31) Carsten, B.; Szarko, J. M.; Son, H. J.; Wang, W.; Lu, L.; He, F.; Rolczynski, B. S.; Lou, S. J.; Chen, L. X.; Yu, L. Examining the Effect of the Dipole Moment on Charge Separation in Donor-Acceptor Polymers for Organic Photovoltaic Applications. *J. Am. Chem. Soc.* **2011**, *133*, 20468–20475.

(32) Wang, Y.; Ranasinghe, M. I.; Goodson, T. Ultrafast Fluorescence Investigation of Excitation Energy Transfer in Different Dendritic Core Branched Structures. *J. Am. Chem. Soc.* **2003**, *125*, 9562-9563.

(33) Varnavski, O.; Samuel, I. D.W.; Pålsson, L. O.; Beavington, R.; Burn, P. L.; Goodson, T. Investigations of Excitation Energy Transfer and Intramolecular Interactions in a Nitrogen Corded Distrylbenzene Dendrimer System. *J. Chem. Phys.* **2002**, *116*, 8893-8903.

(34) Ranasinghe, M. I.; Varnavski, O. P.; Pawlas, J.; Hauck, S. I.; Louie, J.; Hartwig, J. F.; Goodson, T. Femtosecond Excitation Energy Transport in Triarylamine Dendrimers. *J. Am. Chem. Soc.* **2002**, *124*, 6520-6521.

(35) Varnavski, O. P.; Goodson, T.; Mohamed, M. B.; El-Sayed, M. A. Femtosecond excitation dynamics in gold nanospheres and nanorods. *Phy. Rev.* **2005**, 72(23), 235405.

(36) Keller, B.; McLean, A.; Kim, B. G.; Chung, K.; Kim, J.; Goodson, T. Ultrafast Spectroscopic Study of Donor-Acceptor Benzodithiophene Light Harvesting Organic Conjugated Polymers. *J. Phys. Chem. C.* **2016**, *120*, 9088-9096.

(37) Saadeh, H.; Goodson, T.; Yu, L. Synthesis of a Polyphenylene-co-Furan and Polyphenylene-co-Thiophene and Comparison of their Electroluminescent Properties. *Macromolecules*, **1997**, *30*, 4608-4612.

(38) Yamamoto, T.; Zhou, Z.; Kanbara, T.; Shimura, M.; Kizu, K.; Maruyama, T.; Nakamura, Y.; Fukuda, T.; Lee, B.-L.; Ooba, N.; Tomaru, S.; Kurihara, T.; Kaino, T.; Kubota, K.;

Sasaki, S. π-Conjugated Donor-Acceptor Copolymers Constituted of π-Excessive and π-Deficient Arylene Units. Optical and Electrochemical Properties in Relation to CT Structure of the Polymer. *J. Am. Chem. Soc.* **1996**, *118*, 10389-10399.

(39) Kobilka, B. M.; Hale, B. J.; Ewan, M. D.; Dubrovskiy, A. V.; Nelson, T. L.; Duzhko, V.; Jeffries-EL, M. Influence of Heteroatoms on Photovoltaic Performance of Donor-Acceptor Copolymers Based on 2, 6-di(Thiophen-2-yl)Benzo [1, 2-b: 4, 5-b′] Difurans and Diketopyrrolopyrrole. *Polym. Chem.* **2013**, *4*, 5329.

(40) Woo, C. H.; Beaujuge, P. M.; Holcombe, T. W.; Lee, O. P.; Fréchet, J. M. Incorporation of Furan into Low Band-Gap Polymers for Efficient Solar Cells. *J. Am. Chem. Soc.* **2010**, *132*, 15547-15549.

(41) Huo, L.; Huang, Y.; Fan, B.; Guo, X.; Jing, Y.; Zhang, M.; Li, Y.; Hou, J. Synthesis of a 4,8-Dialkoxy-Benzo[1,2-b:4,5-b']diFuran unit and its Application in Photovoltaic Polymer. *Chem. Commun.* **2012**, *48*, 3318–3320.

(42) Kobilka, B. M.; Dubrovskiy, A. V.; Ewan, M. D.; Tomlinson, A. L.; Larock, R. C.; Chaudhary, S.; Jeffries-EL, M. Synthesis of 3, 7-diiodo-2, 6-di(Thiophen-2-yl)Benzo [1, 2-b: 4, 5-b′] diFurans: Functional Building Blocks for the Design of New Conjugated Polymers. *Chem. Comm.* **2012**, *48*, 8919-8921.

(43) Furgal, J. C.; Jung, J. H.; Goodson, T.; Laine, R. M. Analyzing Structure-Photophysical Property Relationships for Isolated T8, T10, and T12 Stilbenevinylsilsesquioxanes. *J. Am. Chem. Soc.***2013**, *135*, 12259-12269.

(44) Maciejewski, A.; Steer, R. P. Spectral and Photophysical Properties of 9, 10-Diphenylanthracene in Perfluoro-n-Hexane: the Influence of Solute-Solvent Interactions. *J. Photochem.* **1986**, *35*, 59-69.

(45) Adegoke, O. O.; Ince, M.; Mishra, A.; Green, A.; Varnavski, O.; Martínez-Díaz, M. V.; Goodson, T. Synthesis and Ultrafast Time Resolved Spectroscopy of Peripherally Functionalized Zinc Phthalocyanine Bearing Oligothienylene-ethynylene Subunits. *J. Phys. Chem. C.* **2013**, *117*, 20912-20918.

(46) Chai, J. D., Head-Gordon, M. Long-Range Corrected Hybrid Density Functionals with Damped Atom-Atom Dispersion Corrections. *Phys. Chem. Chem. Phys*. **2008**, *10*, 6615-6620.

(47) Chai, J. D.; Head-Gordon, M. Systematic Optimization of Long-Range Corrected Hybrid Density Functionals. *J. Chem. Phys.* **2008,** *128*, 084106.

(48) Shao, Y.; Gan, Z.; Epifanovsky, E.; Gilbert, A. T.; Wormit, M.; Kussmann, J.; Ghosh, D. Advances in Molecular Quantum Chemistry Contained in the Q-Chem 4 Program Package. *Mol. Phys.* **2015**, *113*, 184-215.

(49) Varnavski, O.; Samuel, I. D. W.; Pålsson, L. O.; Beavington, R.; Burn, P. L.; Goodson, T. Investigations of Excitation Energy Transfer and Intramolecular Interactions in a Nitrogen

Corded Distrylbenzene Dendrimer System. *J. Chem. Phys.* **2002**, *116*, 8893-8903.

(50) Ramakrishna, G.; Bhaskar, A.; Goodson, T. Ultrafast Excited State Relaxation Dynamics of Branched Donor-π-Acceptor Chromophore: Evidence of a Charge-Delocalized State. J. *Phys. Chem. B.* ***2006***, *110*, 20872-20878.

(51) Chi, C. Y.; Chen, M. C.; Liaw, D. J.; Wu, H. Y.; Huang, Y. C.; Tai, Y. A Bifunctional Copolymer Additive to Utilize Photoenergy Transfer and to Improve Hole Mobility for Organic Ternary Bulk-Heterojunction Solar Cell. *ACS Appl. Mater. Interfaces*, **2014**, *6*, 12119-12125.

(52) Li, W.; Roelofs, W. S.; Turbiez, M.; Wienk, M. M.; Janssen, R. A. Polymer Solar Cells with Diketopyrrolopyrrole Conjugated Polymers as the Electron Donor and Electron Acceptor. *Adv. Mate*. **2014**, *26*, 3304-3309.

(53) Lin, H. W.; Lee, W. Y.; Chen, W. C. Selenophene-DPP Donor-Acceptor Conjugated Polymer for High Performance Ambipolar Field Effect Transistor and Nonvolatile Memory Applications. *J. Mater. Chem.* **2012**, *22*, 2120-2128.

(54) Huang, P.; Du, J.; Gunathilake, S. S.; Rainbolt, E. A.; Murphy, J. W.; Black, K. T.; Biewer, M. C. Benzodifuran and Benzodithiophene Donor-Acceptor Polymers for Bulk Heterojunction Solar Cells. *J. Mater. Chem.* **2015**, *3*, 6980-6989.

(55) Beaujuge, P. M.; Amb, C. M.; Reynolds, J. R. Spectral Engineering in π-Conjugated Polymers with Intramolecular Donor-Acceptor Interactions. *Acc. Chem. Res.* **2010**, *43*, 1396-1407.

(56) Liang, Y.; Xu, Z.; Xia, J.; Tsai, S. T.; Wu, Y.; Li, G.; Yu, L. For the Bright Future-Bulk Heterojunction Polymer Solar Cells with Power Conversion Efficiency of 7.4%. *Adv. Mater.* **2012**, *22*, 138-138.

(57) Davis, N.J.; Francisco, J.; Tabachnyk, M.,; Richter, J.M.; Lamboll, R.D.; Booker, E.P.; Rivarola, F.W.R.; Griffiths, J.T.; Ducati, C.; Menke, S.M; Deschler, F. Photon Reabsorption in Mixed CsPbCl3: CsPbI3 Perovskite Nanocrystal Films for Light-Emitting Diodes. *J. Phys. Chem.* C, **201**7, *121*, p.3790.

(58) Adegoke, O. O.; Jung, I. H.; Orr, M.; Yu, L.; Goodson, T. Effect of Acceptor Strength on Optical and Electronic Properties in Conjugated Polymers for Solar Applications. *J. Am. Chem. Soc.* **2015**, *137*, 5759-5769.

(59) Brédas, J. L.; Beljonne, D.; Coropceanu, V.; Cornil, J. Charge-Transfer and Energy-Transfer Processes in π-Conjugated Oligomers and Polymers: a Molecular Picture. *Chem. Rev.* **2004**, *104*, 4971-5004.

(60) Luo, Y.; Xu, Y.; Zhang, W.; Li, W.; Li, M.; He, R.; Shen, W. Theoretical Insights into the Phosphorescence Quantum Yields of Cyclometalated (C∧C*) Platinum (II) NHC Complexes: π-Conjugation Controls the Radiative and Nonradiative Decay Processes. *J. Phys. Chem. C.* **2016**, *120*, 3462-3471.

(61) Caricato, M.; Andreussi, O.; Corni, S. Semiempirical (ZINDO-PCM) Approach to Predict the Radiative and Nonradiative Decay Rates of a Molecule Close to Metal Particles. *J. Phys. Chem. B.* **2006**, *110*, 16652-16659.

(62) Pond, S.J.;Rumi, M.; Levin, M.D.; Parker, T.C.; Beljonne, D.; Day, M.W.; Brédas, J.L.; Marder, S.R; Perry, J.W. One-and Two-Photon Spectroscopy of Donor-Acceptor-Donor Distyrylbenzene Derivatives: Effect of Cyano Substitution and Distortion from Planarity. *J. Phys. Chem. A.* **2002**, *106*, 11470-11480.

(63) Wang, Q.; Zhang, S.; Xu, B.; Ye, L.; Yao, H.; Cui, Y.; Hou, J. Effectively Improving Extinction Coefficient of Benzodithiophene and Benzodithiophenedione-Based Photovoltaic Polymer by Grafting Alkylthio Functional Groups. *Chem. - Asian J.* **2016,** *11*, 2650-2655.

(64) Mitsui, C.; Tsuji, H.; Sato, Y.; Nakamura, E. Carbazolyl Benzo [1, 2-b: 4, 5-b′] Difuran: An Ambipolar Host Material for Full-Color Organic Light-Emitting Diodes. *Chem. - asian J.* **2012**, *7*, 1443-1450.

(65) Ohulchanskyy, T. Y.; Donnelly, D. J.; Detty, M. R.; Prasad, P. N. Heteroatom Substitution Induced Changes in Excited-State Photophysics and Singlet Oxygen Generation in Chalcogenoxanthylium Dyes: Effect of Sulfur and Selenium Substitutions. *J. Phys. Chem. B.* **2004**, *108*, 8668-8672.

(66) Kamada, K.; Ueda, M.; Ohta, K.; Wang, Y.; Ushida, K.; Tominaga, Y. Molecular dynamics of Thiophene Homologues Investigated by Femtosecond Optical Kerr Effect and Low Frequency Raman Scattering Spectroscopies. *J. Chem. Phys.* **1998**, *109*, 10948-10957.

(67) Carlotti, B.; Kikaš, I.; Škorić, I.; Spalletti, A.; Elisei, F. Photophysics of Push–Pull Distyrylfurans, Thiophenes and Pyridines by Fast and Ultrafast Techniques. *ChemPhysChem*, **2013**, *14*, 970-981.

(68) Günes, S.; Neugebauer, H.; Sariciftci, N. S. Conjugated Polymer-Based Organic Solar Cells. *Chem. Rev.* **2007**, *107*, 1324-1338.

(69) Carsten, B.; Szarko, J. M.; Son, H. J.; Wang, W.; Lu, L.; He, F.; Yu, L. Examining the Effect of the Dipole Moment on Charge Separation in Donor-Acceptor Polymers for Organic Photovoltaic Applications. *J. Am. Chem. Soc.* **2011**, *133*, 20468-20475.

(70) Laine, R.M.; Sulaiman, S.; Brick, C.; Roll, M.; Tamaki, R.; Asuncion, M.Z.; Neurock, M.; Filhol, J.S.; Lee, C.Y.; Zhang, J; Goodson, T. Synthesis and Photophysical Properties of Stilbeneoctasilsesquioxanes. Emission Behavior Coupled with Theoretical Modeling Studies Suggest a 3-D Excited State Involving the Silica Core. *J. Am. Chem. Soc.* **2010**, *132*, 3708-3722.

(71) Yau, S.H.; Varnavski, O.; Gilbertson, J.D.; Chandler, B.; Ramakrishna, G.; Goodson, T. Ultrafast Optical Study of Small Gold Monolayer Protected Clusters: a Closer Look at Emission. *J. Phys. Chem. C*, **2010**, *114*, 15979-15985.

(72) Yan, X.; Goodson, T.; Imaoka, T.; Yamamoto, K. Up-Converted Emission in a Series of Phenylazomethine Dendrimers with a Porphyrin Core. *J. Phys. Chem. B.* **2005**, *109*, 9321-9329.

(73) Wang, X.; Mader, M.M.; Toth, J.E.; Yu, X.; Jin, N.; Campbell, R.M.; Smallwood, J.K.; Christe, M.E.; Chatterjee, A.; Goodson, T.; Vlahos, C.J. Complete Inhibition of Anisomycin and UV Radiation But Not Cytokine Induced JNK and p38 Activation by an Aryl-Substituted Dihydropyrrolopyrazole Quinoline and Mixed Lineage Kinase 7 Small Interfering RNA. *J. Biol. Chem.* **2005**, *280*, 9298-19305.

(74) Bhaskar, A.; Ramakrishna, G.; Twieg, R.J.; Goodson, T. Zinc Sensing Via Enhancement of Two-Photon Excited Fluorescence. *J. Phys. Chem. C.* **2007**, *111*, 14607-14611.

(75) Guo, M.; Varnavski, O.; Narayanan, A.; Mongin, O.; Majoral, J.P.; Blanchard-Desce, M.; Goodson, T. Investigations of Energy Migration in an Organic Dendrimer Macromolecule for Sensory Signal Amplification. *J. Phys. Chem. C.* **2007**, *113*, 4763-4771.

Chapter 6

Two Photon Absorption Study of Low-Bandgap, Fully Conjugated Perylene Diimide-Thienoacene-Perylene Diimide Ladder-Type Molecules

6.1 Original Publication Information

The work in this chapter was accepted by the *Chemistry of Materials* (*Chem. Mater*.) with the title:

"*Two Photon Absorption Study of Low-Bandgap, Fully Conjugated Perylene Diimide-Thienoacene-Perylene Diimide Ladder-Type Molecules*" Zhengxu Cai, Ricardo J. Vazquez, Donglin Zhao, Lianwei Li, Wai-yip Lo, Na Zhang, Qinghe Wu, Bradley Keller, Audrey Eshun, Neranga Abeyasinghe, Halley Banaszak-Holl, Theodore Goodson, III, and Luping Yu. *Chem. Mater.* **2017**, *29* (16), 6726–6732.

Modifications were conducted to the manuscript to adapt it to the style of the content of this dissertation. References and supporting information of the manuscript are included in this chapter.

6.2 Abstract

A new series of donor−acceptor ladder-type molecules were synthesized via Scholl reaction. These molecules contain up to 25- fused rings but still show good air stability and good solubility. The ring-fusing reaction is found to be sensitive to the nature of the side-chain in donor units. The molecular conformations were investigated by 2D NMR and DFT calculations. The photophysical properties were investigated and an intense intramolecular charge-transfer was observed. All of the molecules exhibit two-photon absorption (TPA) activity, and their TPA cross-section shows a linear relationship with increasing conjugation length of the thienoacene-PDI derivatives.

6.3 Introduction

The nature of excited states in organic molecules is what determines their numerous optical properties such as energy transfer, electron transfer, light emission, photovoltaic effect, two-photon absorption (TPA), singlet fission, and so on.[1−6] However, rational design of organic materials to achieve an excited state with tailored optical properties is still a significant challenge.[7,8] The control in the degree of electron delocalization on π-orbitals is an effective approach to the modification of physical and optical properties of organic conjugated molecules.[9,10]

In the past few decades, ladder-type materials have been continuously investigated for their potential applications in organic electronics.[11−13] Different types of structures have been developed, ranging from all hydrocarbon polyacenes to systems containing heterocyclic aromatic rings.[14,15] In the past years, different polyacenes have been reported, but their stability, solubility, and processability are major issues that prevent them from extensive exploration for applications.[16,17] Recently, we reported a novel method to synthesize conjugated heteroacenes with

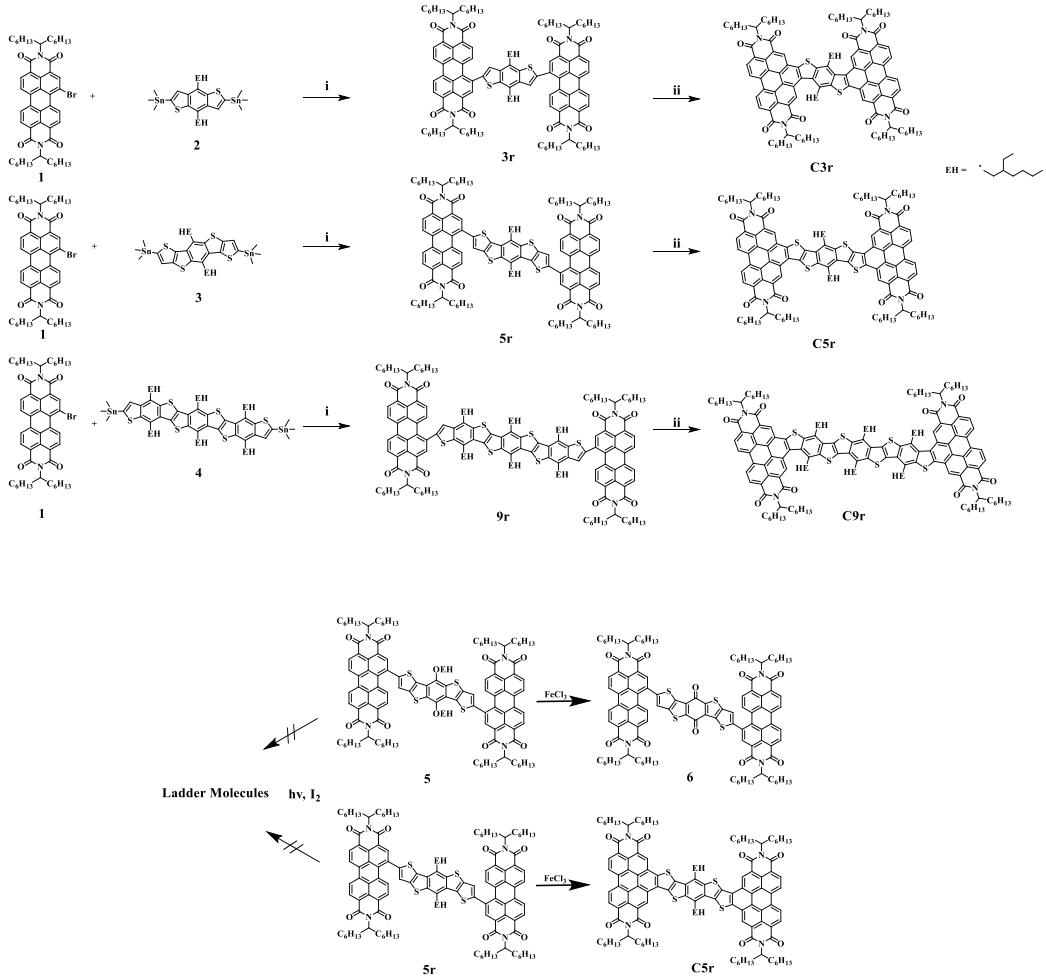

Scheme 6.3.1. Synthetic route of fused ring molecules. (i) $Pd_2(dba)_3$, P(*o*-MePh)$_3$; (ii) $FeCl_3$. (A). Synthetic strategies of conjugated molecules (B).

excellent solubility in organic solvents due to the sidechain modification. These molecules were investigated via nonlinear optical techniques and were shown to exhibit a sizable TPA cross-section.[18–20] However, these materials are rather electron-rich and can be slowly oxidized due to high HOMO energy level caused by fused thienyl units.[12] The TPA cross-section was only moderate because of their rather uniform structures that lack functionality necessary for enhanced optical nonlinearity.[21] In order to address these issues, we designed new molecules that

incorporated an electron withdrawing unit to the heteroacene cores. Recent studies also suggest that the intra- and intermolecular interactions of the donor and acceptor moieties can modulate the excited state properties.[22–25] The D−A ladder-type structures lock the π systems into a planar conformation that minimizes the bond twisting observed in linear conjugated structures, which can offer an effective way to improve properties.[26–32]

In this paper, we report the synthesis, characterization, electrochemical, and photophysical properties of these new ladder-type oligomers. The compounds consisted of thienoacene derivatives (Dn) as the donor and perylene-diimide (PDI) as the acceptor (**Scheme 6.3.1)**. The PDI motif was introduced in order to further extend the conjugation, stabilize the molecular structures due to its strong electron withdrawing property, and modulate the optical and electronic properties. 2D NMR measurements and density functional theory (DFT) calculation were used to investigate molecular structure and conformation and the relationship between the structure and optical/ electrical properties.

6.4 Experimental Techniques

6.4.1 Materials Synthesis and Characterization Techniques.

All of the chemicals were purchased from Aldrich. All reagents purchased commercially were used without further purification except for toluene and tetrahydrofuran (THF), which were dried over sodium/ benzophenone. 1 H NMR and 13C NMR spectra were recorded on a Bruker DRX-500 spectrometer with tetramethylsilane as an internal reference. High Resolution MALDI-TOF spectra were recorded on Bruker Solarix 9.4T. Compounds 2-4 were synthesized according to the procedures developed in our lab.[18–20,48]

Synthesis of Compound 3: to a round-bottom flask equipped with a condenser was added 1 (530 mg, 0.64 mmol), 2 (215 mg, 0.29 mmol), Pd2(dba)3 (26 mg, 0.03 mmol), and P(o-MePh)3

(43 mg, 0.12 mmol). The system was evacuated and refilled with N2 three times, then charged with toluene (50 mL). The reaction mixture was refluxed under N2 for 16 h. After cooling to room temperature, the reaction mixture was concentrated under reduced pressure. The residue was purified by column chromatography with hexane and CH2Cl2 (1:1, v/ v) as the eluent. Compound 3r was obtained as a red solid (422 mg, 76% yield). 1 H NMR (CD2Cl4 353 K ppm): δ 8.86 (s, 2H), 8.77−8.67 (m, 8H), 8.42 (d, J = 10, 2H), 8.25 (d, J = 10, 2H), 7.72 (s, 2H), 5.24−5.15 (m, 4H), 3.22−3.09 (m 4H), 2.30−2.22 (m, 8H), 2.01− 1.92 (m, 10H), 1.40−1.28 (m, 80H), 0.92−0.86 (m, 30H), 0.77 (t, J = 7.5, 6H). 13C NMR (CDCl3, ppm): δ 164.7, 164.3, 163.7, 163.5, 144.4, 139.5, 139.01, 139.4, 137.9, 137.8, 136.9, 136.1, 135.0, 134.2, 131.8, 131.5, 131.1, 130.8, 130.1, 130.0, 129.2, 129.1, 128.1, 127.5, 124.1, 123.7, 123.4, 123.0, 122.7, 122.2, 122.0, 54.9, 54.7, 40.3, 38.4, 32.4, 31.8, 31.8, 29.3, 29.2, 28.8, 27.0, 26.9, 23.0, 22.6, 22.6, 14.1, 14.1, 14.0, 11.1. High Resolution MALDI-TOF: calcd. for [C126H158N4O8S2] −, 1919.15266, found, 1919.15098. Elemental analysis: calcd. for C126H158N4O8S2: C, 78.79; H, 8.29, N, 2.92, S, 3.34; found: C, 78.66; H, 8.38, N, 2.97, S, 3.14.

Synthesis of Compound 5r.: to a round-bottom flask equipped with a condenser was added 1 (462 mg, 0.55 mmol), 3 (215 mg, 0.25 mmol), Pd2(dba)3 (26 mg, 0.03 mmol), and P(o-MePh)3 (43 mg, 0.12 mmol). The system was evacuated and refilled with N2 three times, then charged with toluene (40 mL). The reaction mixture was refluxed under N2 for 16 h. After cooling to room temperature, the reaction mixture was concentrated under reduced pressure. The residue was purified by column chromatography with hexane and CH2Cl2 (1:1, v/ v) as the eluent. Compound 5r was obtained as a red solid (403 mg, 78% yield). 1 H NMR (CD2Cl4 353 K ppm): δ 8.82 (s, 2H), 8.76−8.66 (m, 8H), 843 (d, J = 8.5, 2H), 8.27 (d, J = 8.5, 2H), 7.67 (s, 2H), 5.22 (m, 2H), 5.15 (m, 2H), 3.30 (m, 4H), 2.31−2.22 (m, 10H), 1.97−0.90 (m, 8H), 1.50−1.20 (m, 80H), 0.92−0.87

(m, 30H), 0.76 (t, J = 11, 6H). 13C NMR (CDCl3, ppm): δ 164.7, 164.5, 163.6, 163.3, 147.0, 141.8, 139.0, 137.1, 136.3, 135.1, 135.0, 134.1, 133.8, 133.1, 131.8, 131.5, 130.8, 130.1, 129.9, 129.1, 129.0, 128.7, 127.5, 124.1, 123.7, 123.4, 122.9, 122.7, 122.3, 119.9, 54.9, 54.7, 39.1, 39.0, 32.8, 32.4, 31.8, 31.8, 29.7, 29.2, 28.7, 27.0, 23.0 22.6, 22.6, 14.1, 14.0, 13.9, 11.2. High Resolution MALDI-TOF: calcd for [C130H158N4O8S4] −, 2031.09680, found, 2031.09616. Elemental analysis: calcd. for C130H158N4O8S4: C, 76.81, H, 7.83, N, 2.76, S, 6.31; found: C, 77.00; H, 7.90, N, 2.80, S, 6.13.

Synthesis of Compound 9r: to a round-bottom flask equipped with a condenser was added 1 (240 mg, 0.29 mmol), 4 (198 mg, 0.13 mmol), Pd2(dba)3 (12 mg, 0.01 mmol) and P(o-MePh)3 (14 mg, 0.04 mmol). The system was evacuated and refilled with N2 three times, then charged with toluene (40 mL). The reaction mixture was refluxed under N2 for 16 h. After cooling to room temperature, the reaction mixture was concentrated under reduced pressure. The residue was purified by column chromatography with hexane and CH2Cl2 (1:1, v/ v) as the eluent. Compound 9r was obtained as a solid (323 mg, 92% yield). 1 H NMR (CDCl3 ppm): δ 8.87 (s, 2H), 8.72 (m, 8H), 8.39 (s, 2H), 8.20 (d, J = 7.5, 2H), 7.76 (s, 2H), 5.23 (s, 2H), 5.15 (s, 2H), 3.60−3.27 (m, 12H), 2.47 (s, 2H), 2.38 (s, 2H), 2.30 (s, 4H), 2.24 (s, 4H), 2.13 (s, 2H), 1.98 (s, 4H), 1.90 (s, 4H), 1.73−1.33 (m, 108H), 1.08−0.89 (m, 64H). 13C NMR (CDCl3, ppm): δ 164.7, 163.7, 144.0, 142.1, 141.5, 140.1, 137.6, 136.8, 136.1, 135.0, 134.0, 133.8, 132.3, 131.8, 130.6, 130.3, 129.9, 129.1, 128.8, 128.5, 128.1, 127.3, 123.7, 123.4, 122.9, 122.0, 54.9, 54.7, 40.1, 39.8, 39.4, 38.8, 37.9, 31.8, 29.2, 27.0, 23.2, 22.6, 22.6, 14.1, 14.1, 11.2, 11.0. High Resolution MALDITOF: calcd. for [C174H226N4O8S6]+ , 2691.57195, found, 2691.57202. Elemental analysis: calcd. for C174H226N4O8S6: C, 77.57; H, 8.46, N, 2.08, S, 7.14; found: C, 77.72; H, 8.51, N, 2.09, S, 6.95.

Synthesis of Compound C3r: a solution of FeCl3 (676 mg, 4.17 mmol) in 2 mL nitromethane was added dropwise to a stirred solution of compound 3r (400 mg, 0.21 mmol) in 10 mL CH2Cl2. The reaction was stirred with argon. After stirring for 10 h at room temperature, 1 mL methanol was added to the solution. The solvent was evaporated under reduced pressure, and the crude product was filtered with silica gel with a large amount of CHCl3 to yield the solid product (367 mg, 92%).1 H NMR (C2D2Cl4, ppm, 353 K): δ 10.01 (s, 2H), 9.84 (s, 2H), 9.42 (s, 4H), 9.13 (s, 4H), 5.50 (s, 4H), 4.11 (s, 4H), 2.38 (s, 8H), 2.01 (br, 10H), 1.45−1.14 (m, 78H), 0.93−0.72 (m, 38H). 13C NMR (CDCl3, ppm): δ 165.4, 164.1, 141.6, 140.1, 134.9, 133.7, 133.3, 131.9, 131.4, 129.4, 128.7, 127.7, 126.6, 125.7, 124.6, 124.4, 123.5, 122.9, 122.3, 122.0, 55.1, 39.6, 39.1, 32.6, 32.2, 31.8, 29.7, 29.3, 27.1, 22.6, 14.1, 10.8. High Resolution MALDI-TOF: calcd. for [C126H154N4O8S2]+ , 1915.12026, found, 1915.12064. Elemental analysis: calcd. for C126H154N4O8S2: C, 78.95; H, 8.10, N, 2.92, S, 3.35; found: C, 78.65; H, 8.11, N, 2.95, S, 3.51.

Synthesis of Compound C5r: a solution of FeCl3 (319 mg, 1.97 mmol) in 2 mL nitromethane was added dropwise to a stirred solution of compound 5r (200 mg, 0.10 mmol) in 8 mL CH2Cl2. The reaction was stirred with argon. After stirring for 10 h at room temperature, 1 mL methanol was added to the solution. The solvent was evaporated under reduced pressure, and the crude product was filtered with silica gel with a large amount of CHCl3 to yield the solid product (180 mg, 90%).1 H NMR (C2D2Cl4 ppm, 353 K): δ 9.88 (s, 2H), 8.82−8,70 (br, 10H), 5.51 (s 2H), 5.32 (s 2H), 3.76 (s, 4H), 2.61−2.21 (m, 18H), 1.55−1.42 (m, 82H), 1.09−0.86 (m, 34H). 13C NMR (CDCl3, ppm): δ 164.6, 163.6, 142.6, 141.6, 134.2, 134.0, 131.7, 129.7, 129.1, 128.8, 128.7, 128.5, 128.0, 126.7, 125.8, 124.8, 124.4, 123.7, 123.2, 122.7, 122.2, 121.1, 55.7, 33.4, 32.4, 32.3, 32.2, 31.9, 30.3, 30.1, 29.7, 29.3, 29.1, 27.7, 27.2, 23.1, 23.0, 22.6, 14.4, 14.1. High Resolution MALDITOF: calcd. for [C130H154N4O8S4] + , 2027.06440, found,

2027.06477. Elemental analysis: calcd. for C130H154N4O8S4: C, 76.96, H, 7.65, N, 2.76, S, 6.32; found: C, 77.12; H, 7.73, N, 2.80, S, 6.46.

Synthesis of Compound C9r: a solution of FeCl3 (240 mg, 1.48 mmol) in 2 mL nitromethane was added dropwise to a stirred solution of compound 9r (200 mg, 0.07 mmol) in 8 mL CH2Cl2. The reaction was stirred with argon. After stirring for 10 h at room temperature, 1 mL methanol was added to the solution. The solvent was evaporated under reduced pressure, and the crude product was filtered with silica gel with a large amount of CHCl3 to yield the solid product (187 mg, 94%). 1 H NMR (C2D4Cl4, 353 K, ppm): δ 10.22 (br, 2H), 9.83 (s, 2H), 9.42 (s, 4H), 9.16 (s, 4H), 5.46 (s, 4H), 3.99 (br, 12H), 2.10 (br, 12H), 1.84 (br, 10H), 1.48−0.92 (m, 172H). 13C NMR (CDCl3, ppm): δ 165.5, 164.4, 131.9, 131.5, 129.2, 128.0, 127.6, 126.7, 124.6, 123.5, 122.5, 121.9, 55.0, 39.6, 39.4, 32.6, 32.2, 32.0, 31.9, 29.7, 29.3, 27.4, 27.1, 22.8, 22.7, 14.2, 14.1. High Resolution MALDI-TOF: calcd. for [C174H222N4O8S6] + , 2687.54684, found, 2687.54150. Elemental analysis: calcd. for C174H222N4O8S6: C, 77.69, H, 8.32, N, 2.08, S, 7.15; found: C, 77.81, H, 8.57, N, 2.07, S, 7.00.

6.4.2 Ultrafast and Steady-State Spectroscopic Techniques

Steady-state absorbance spectra were measured using an Agilent 8432 UV−visible absorption spectrophotometer in chloroform solutions. The emission spectrum measurements were performed with a Fluoromax-2 spectrophotometer. Absorption spectra measurements were 308 taken before and after each measurement to ensure that there was no appreciable photo-degradation during the fluorescence lifetime measurements or two-photon absorption. The fluorescence quantum yields of the samples were calculated using a known procedure, and Zinc Phthalocyanine in toluene ($\phi = 0.074$) were used as the standard.

The time-resolved fluorescence experiments were performed using a ultrafast fluorescence Up-Conversion setup that had previously been described.4 Mode-locked Ti-sapphire femtosecond laser (Spectra Physics Tsunami) was used to generate 80 fs pulses at 800 nm wavelength with a repetition rate of 82 MHz. This mode-locked laser was pumped by a 532 nm continuous light output from another laser (Spectra Physics Millennia), which has a gain medium of neodymium-doped yttrium vanadate (Nd:YVO4). An excitation pulse of 400 nm was generated by a second harmonic β- barium borate crystal, and the residual 800 nm beam was made to pass through a computer-controlled motorized optical delay line. The polarization of the excitation beam was controlled by a berek compensator. The power of the excitation beam varied between 17 and 20 mW. The fluorescence emitted by the sample was up-converted by a nonlinear crystal of β-barium borate by using the residual 800 nm beam, which had been delayed by the optical delay line with a gate step of 6.25 fs. This procedure enabled the fluorescence to be measured temporally. The monochromator is used to select the wavelength of the up-converted beam of interest, and the selected beam is detected by a photomultiplier tube (R152P, Hamamatsu, Hamamatsu City, Japan). The photomultiplier tube converts the detected beam into photon counts, which can be read from a computer. Coumarin 30 and Cresyl violet dyes were used for calibrating the laser. The instrument response function (IRF) has been determined from the Raman signal of water to have a width of 110 fs. Lifetimes of fluorescence decay were obtained by fitting the fluorescence decay profile with multi-exponential decay functions convoluted with IRF in MATLAB and Origin 8.

Two-photon spectroscopy was performed using a mode-locked Ti : Sapphire laser which is tunable from 700 to 900 nm delivering 110 fs output pulses at a repetition rate of 80 MHz which pumps an OPAL optical parametric oscillator (OPO) lithium borate (LBO) crystal which allows for 1.3 and 1.5 μm output excitations with output power of 200 mW. Emission scans were

performed at 800 nm excitation while scanning 415-760 nm emission, but the exact emission detection wavelength during the power dependence scan was selected by the emission wavelength that produced the highest number of counts at ~450 nm and ~715 nm. Coumarin 307 was used as the standard. Input power from the laser was varied using a variable neutral density filter. Two-photon power-dependent fluorescence intensity was utilized to determine the two-photon absorption cross section through the two-photon emission fluorescence (TPEF) method.

6.5 Results and Discussion

6.5.1 Synthesis and Characterization of the Ladder-Type Molecules.

A strategy was developed to synthesize the compounds (**Scheme 6.3.1A**). First, the Stille coupling reaction was used to connect the heteroacenes derivative with the PDI units. Photochemical reaction was attempted to form the cyclized product and failed (**Scheme 6.3.1B**). It was found that Scholl reaction using ferric chloride can efficiently cyclize the heteroacenes derivatives with the PDI unit. The desired annulated compounds were obtained in high yields (>90%), if the side chain was an alkyl group. Quinoidal structure was formed with the same ring fusing method for the compounds with alkoxy substituent.[33] It was noted that the electron rich substituent favors oxidative cyclodehydrogenation.[34,35] Thus, the successful cyclo-dehydrogenation of these fused-ring compounds with electron deficient PDI to the desired product is an attractive outcome.

NMR spectroscopic techniques were used to elucidate the molecular conformations of the resulting compounds. Both 1D and 2D NMR experiments were carried out for the nonfused systems for the sake of comparison and elucidation of the fully conjugated materials. It was found

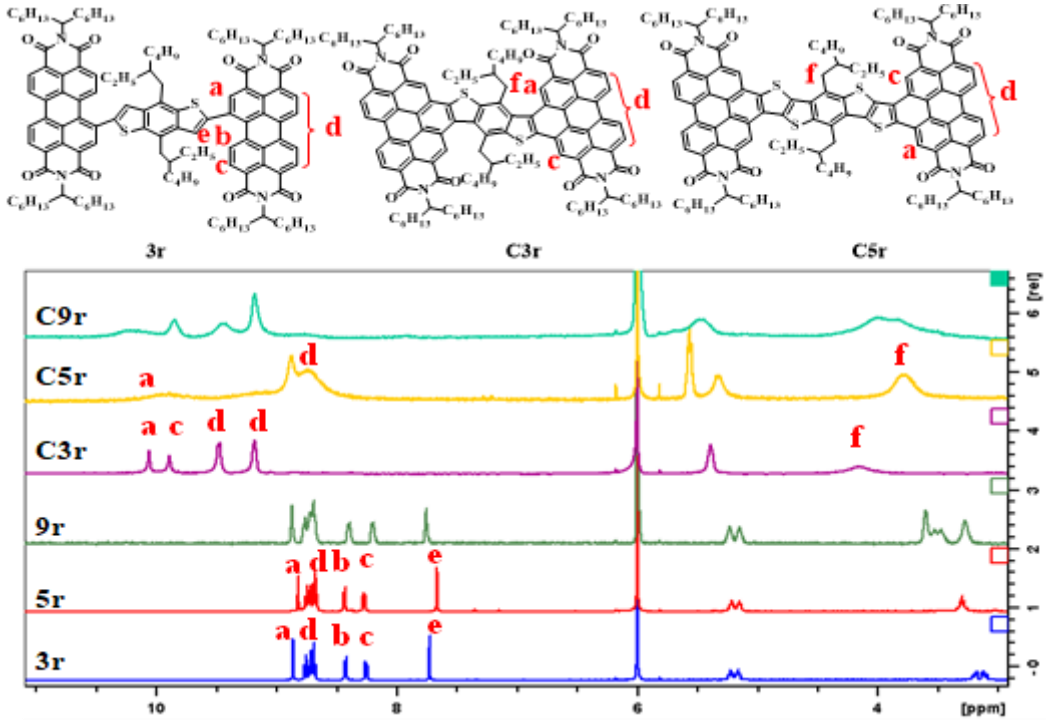

Figure 6.5.1. NMR spectra of fused and non-fused compounds.

that the non-fused ring compounds showed similar chemical shifts in the aryl region (**Figure 6.5.1**). The proton signal in benzodithiophene unit (e in **Figure 6.4.1**) and aryl gulf-facing protons (b) disappeared for the fused ring compounds, while the other four gulf-facing protons (a and c) in PDI were downshifted to ~10 ppm.[26–28] All aryl protons in C3r and C9r experience a diatropic shift to low field after cyclization. The chemical shifts of proton peaks d in C5r showed only a minor change compared with the uncyclized version. NOESY spectra of C3r and C5r were obtained to explain these differences (C9r showed strong tendency to form aggregation and a very weak 2D NMR signal). We found that the NOESY spectra of C3r showed the Nuclear Overhauser Effect (NOE) between the CH2 in 2-ethylhexyl group (proton f) and proton a in the PDIcore (see of the Supporting Information, SI), indicating that two proton nuclei are spatially close. A strong

Table 6.5.1. Optical and electrical properties of **C3r**, **C5r**, and **C9r.** Energy levels were calculated based on the respective onset oxidation and reduction potentials of the ladder molecules with the following equations: LUMO = − ($E_{onset\ red}$ − $E_{onset\ Fc}$ + 4.8) eV, HOMO = − ($E_{onset\ ox}$ − $E_{onset\ Fc}$ + 4.8) eV, Ferrocene (Fc) was used as inner reference which the HOMO energy level was considered as -4.8 eV. [b] Based on the absorption spectra data; [c] Based on DFT calculations; [d]Dihedral angles between the PDI plane and adjacent thienoacene parts based on DFT calculations; [e] **C3r** shows mono-exponential decay behavior with an energy rising time of 120 fs.

	HOMO[a] (eV)	LUMO[a] (eV)	Bandgap[b] (opt[b]/cv[a]/cal[c])	Dihedral[d]	QY. (%)	τ_1 (ps)	τ_2 (ps)	TPA (GM)
C3r	-5.90	-3.84	2.03/2.06/2.48	23.9°	13.5	18.5	n/a[e]	1.2
C5r	-5.69	-3.82	1.86/1.87/2.22	2.0°	5.0	3.3	121.8	29.8
C9r	-5.51	-3.78	1.77/1.73/2.02	28.6°	0.2	0.9	9.5	124.6

steric hindrance between the alkyl chains in benzodithiophene (BDT) and the PDI cores causes twisted conformation for the C3r molecule and the PDI moiety. The lateral hydrogen (proton d) in PDI thus shifted to low field, as observed in other twisted structures.[26,28,35] The C5r molecule showed only the cross peaks in that region in NOESY spectrum (**Figure 6.7.4**), indicating the lack of sterically hindered interaction in the molecule. As shown by DFT calculation, molecule C5r is highly planar, and the lateral hydrogen (proton d) in PDI exhibited minimum change after cyclization, with a dihedral angle of only 2.0° (**Table 6.5.1**).

DFT calculations offer further confirmation that the fused ring compounds C3r and C9r are twisted because of the strong steric hindrance between the alkyl chain in heteroacenes and the PDI core. These results are consistent with those from NMR measurements. A pictorial presentation of molecular structures and the LUMO and HOMO are shown in **Figures 6.7.5** and **Figures 6.7.6**, respectively. The resulting energy levels are summarized in **Table 6.5.1**. It was found that the HOMO orbitals are mainly localized on thienoacene parts, while the LUMO orbitals are localized on the PDI units (**Figure 6.7.6**). Both the HOMO and LUMO orbitals, to some degree, extend to the whole molecules in the fused ring system due to ring-fusing effect.

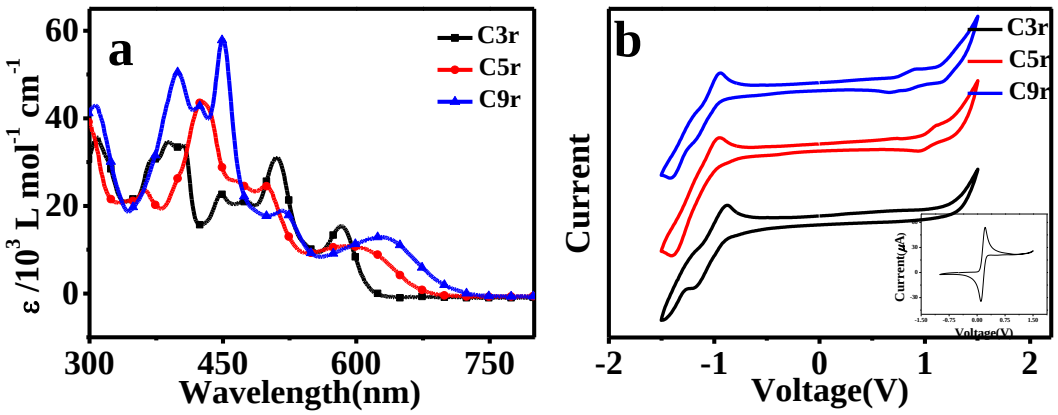

Figure 6.5.2.1 (a) Absorption spectra of ladder molecules; (b) CV of ladder molecules in $CHCl_3$.

6.5.2 Optical and Electrical Properties of the Ladder-Type Molecules.

The absorption spectra of all molecules were shown in **Figure 6.5.1a**. As expected, the molar extinction coefficient increased as the conjugation of the BDT derivative units increased in the region of 300−450 nm. The peaks around 525 nm attributed to the PDI unit gradually became weaker as the conjugation length increased. The absorption peak at 600−650 nm range was attributed to the charge transfer state between thienoacenes and PDI units. The spectra of the fused ring series in this region exhibit higher intensity than the non-fused system, suggesting a stronger intramolecular charge transfer in fused-ring compounds (**Figure 6.7.8**).[35,36] Both the HOMO and LUMO energy levels were determined by cyclic voltammetry (vs Fc/Fc+) (**Figure 6.5.1b**), and the HOMO energy levels show an increase and LUMO a slight increase as the donor length increase because the large conjugation enhances the electron donating abilities, resulting in narrowed bandgaps. In addition, Compared to non-fused compounds, fused PDI derivatives exhibit larger bandgap, which can be attributed to the delocalization of frontier orbitals weakening the intramolecular charge transfer between donor units and PDI moieties. All these trends are in agreement with those obtained from theoretical calculation and optical measurements.

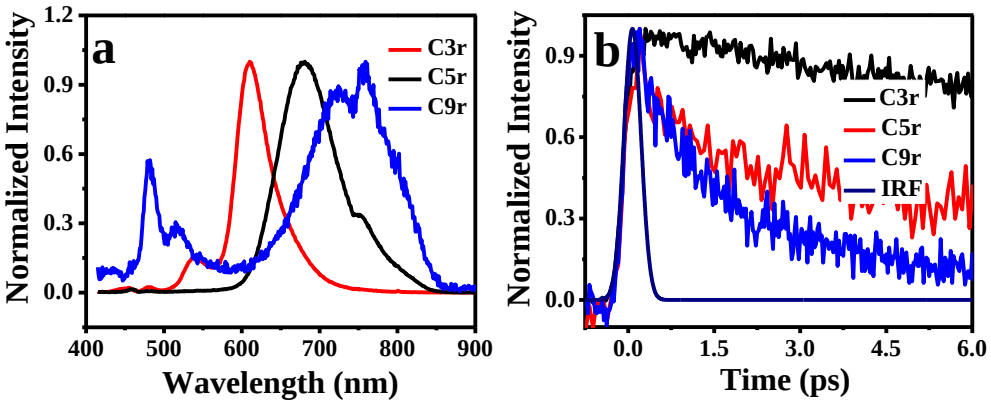

Figure 6.5.2.2. (a) Absorption spectra of ladder molecules; (b) CV of ladder molecules in $CHCl_3$.

The emission spectra of three ladder molecules are shown in **Figures 6.5.2.2**, in which some of the emission peaks observed in thienoacenes and PDI were retained (**Figure 6.7.8**). A marked difference is that both the C3r and C9r showed emission peaks between 450 to 550 nm, while C5r showed no emission in that region. These emissions can be attributed to the twisted structures of the C3r and C9r. The C3r and C9r molecules retain the localized emission peaks observed in PDI. The main emission peaks are red-shifted when the length of the thienoacene cores is extended. The emission peaks at 600− 700 nm are new and not observed in the emission spectra of thienoacenes alone nor in the emission spectra of the PDI monomer (**Figure 6.7.8**). Thus, the fluorescence decay dynamics at 600 nm can be attributed to the electronically coupled PDI and thienoacene charge transfer states.

In order to investigate this effect of extending the conjugation length of the thienoacene core on the fluorescence decay dynamics, studies in time-resolved fluorescence upconversion were carried out.[37–39] The dynamics of the C3r exhibited a rising time (**Figure 6.7.9**) of 120 fs before a slower relaxation of the fluorescence at 18.5 ps, suggesting energy transfer from the BDT core to the charge transfer state.[40] Interestingly, the C3r molecule demonstrates the longest-lived mono-

exponential emission (τ1) while the lifetimes are gradually decreased (**Table 6.5.1**) with increasing of the conjugation length. The C5r shows a very long lifetime, τ2 (**Table 6.5.1**). This can be attributed to the increased conjugation length and planar structure in the C5r system, which will make the excited state more delocalized, thus increasing the τ2 lifetime.[41] From C3r to C9r, the increase in the length of molecules, extended the conjugation. This opens up many possible non-radiative relaxation channels causing the quantum yield to gradually drop as the conjugation length is increased. The charge transfer from the thienoacene core to the PDI core may quench the fluorescence of the molecule as the electron donating abilities increase.[42] The trend in the lifetimes is consistent with the observed trend in the quantum yield values for the three fused ring systems with the quantum yield of the C3r being 13.5% and that of C9r approaching he trend in the lifetimes is consistent with the observed trend in the quantum yield values for the three fused ring systems with the quantum yield of the C3r being 13.5% and that of C9r approaching.

Efficient charge delocalization and charge transfer due to increase in conjugation have been previously documented and can be investigated by using the TPA technique.[43] Specifically, a proportional relationship between the TPA cross-section and the increase in the effective conjugation length (π-orbitals) of the thienoacenes core has been reported.[18] Furthermore, enhancement in the TPA cross-section has been reported in materials with quadrupolar (A-D-A) configuration.[44] As expected, the compounds showed an enhancement in the TPA cross-section proportional to the length of the thienoacene-PDI cores (**Table 6.5.1**). C9r shows the highest TPA cross-section value of 125 GM. It has been also documented that a TPA cross-section enhancement can be achieved by the incorporation of an electron withdrawing groups.[45,46] In order to understand the direct effect of incorporating the electron withdrawing unit, the two photon absorption of thienoacenes (**Table 6.7.2**) and non-fused ring compounds were also carried out (see section **6.7**)

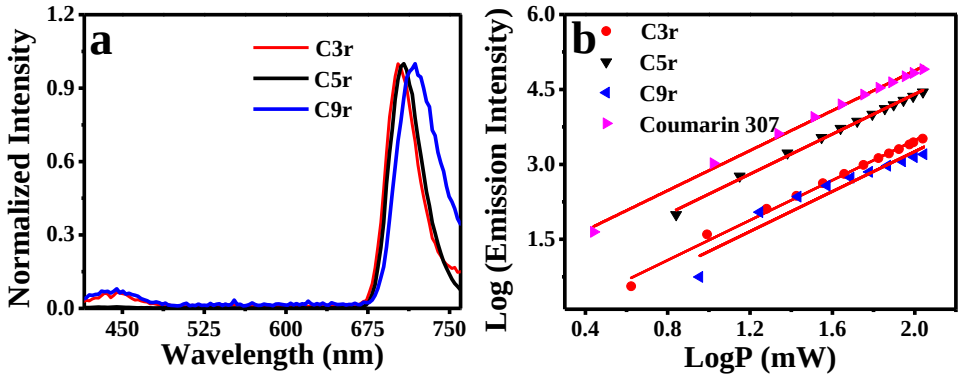

Figure 6.5.2.3. Two photon emission spectra of ladder molecules; (b) Power dependence of the two-photon-excited emission of ladder molecules at ~ 720 nm.

Information). The results suggest that both enhancing the length of donor unit and adding an electron withdrawing unit will have an impact in the nonlinear optical properties of the oligomers but enhancing the delocalization length will have a higher impact on this property. The TPA cross-section is strongly associated with the charge transfer character of the material.[18] Lately, it has been suggested that the dipole moment of the molecule could interact with the entanglement of the exciton resulting in a decrease in the Coulombic interactions between the electron and the associated hole.[47]

6.6 Conclusions

A series of A-D-A conjugated molecules based on heteroacenes were designed, synthesized, and characterized. To avoid dealkylation/oxidation reaction, the Scholl reaction using ferric chloride as oxidant was used to the synthesis of annulated compounds. Optical and electrochemical characterization of these ladder-type molecules indicated intramolecular charge transfer states between the donor and the acceptor units, which was corroborated with the ultrafast optical measurements. All of the materials exhibited good TPA activity. The results indicate that the ladder-type A-D-A structures can enhance the TPA cross-section of the heteroacene

derivatives. These molecules are of interest for further exploration in electrical and optical properties, such as their applications in photovoltaic devices due to their internal charge transfer properties.

6.7 Supporting Information

Their DFT calculation were performed at the level of B3LYP /6-31G** by using Gaussian 09 in vacuum model. To facilitate the calculation, the heptylhexyl chains in PDI were replaced with a methyl group, while the ethylhexyl groups in heteroacenes were replaced by isobutyl to avoid missing the steric hindrance effect. Isovalue for printing the frontier molecular orbitals was 0.02. Thermogravimetric analysis (TGA) (SDT Q600 TGA/DSC) measurements were performed under a nitrogen atmosphere at a heating rate of 10 °C/min.

Cyclic voltammetry was used to study the electrochemical properties of these compounds. They were measured as 10^{-3} M solutions in anhydrous $CHCl_3$ containing 0.1 M Bu_4NPF_6 as the electrolyte with Pt as the working electrode, Ag/Ag^+ as the reference electrode, and a Pt wire as the contrast electrode at a scan rate of 50 mV/s. For calibration, the redox potential of ferrocene/ ferrocenium (Fc/Fc^+) was measured under the same conditions and it was located at 0.15 V vs Ag/Ag^+. It was assumed that the redox potential of Fc/Fc^+ has an absolute energy level of -4.80 eV relative to vacuum. Energy levels were calculated based on the respective onset oxidation and reduction potentials of A-D-A molecules and their fused-ring compounds with the following equations: LUMO = - ($E_{onset\ red}$ - $E_{onset\ Fc}$ + 4.8) eV, HOMO = - ($E_{onset\ ox}$ - $E_{onset\ Fc}$ + 4.8) eV.

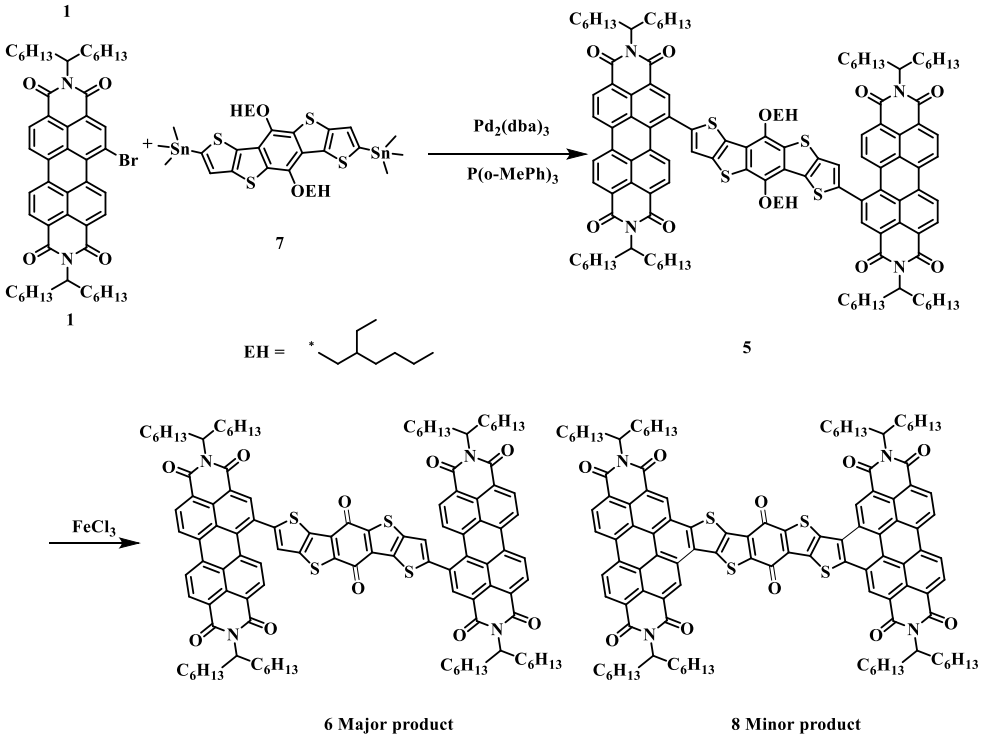

Scheme 6.7.1 Synthetic routes of quinoidal structure.

Synthesis of Compound **5**: To a round-bottom flask equipped with a condenser was added **1** (177 mg, 0.21 mmol), **7** (75 mg, 0.09 mmol), $Pd_2(dba)_3$ (13 mg, 0.02 mmol) and P(*o*-MePh)$_3$ (16 mg, 0.05 mmol). The system was evacuated and refilled with N_2 three times, then charged with toluene (40 ml). The reaction mixture was refluxed under N_2 for 16 hours. After cooling to room temperature, the reaction mixture was concentrated under reduced pressure. The residue was purified by column chromatography with hexane and CH_2Cl_2 (1:1, v/v) as the eluent. Compound **5** was obtained as a red solid (152 mg, 86.9% yield). ^{1}H NMR ($CDCl_3$ ppm): δ 8.83-8.66 (m, 10H), 8.40 (d, *J* = 8 Hz, 2H), 8.27 (br, 2H), 7.56 (s, 2H), 5.25-5.17 (br, 4H), 4.30 (s, 4H), 2.28-2.22 (br, 8H), 1.89-1.86 (br, 10H), 1.35-1.22 (m, 80H), 0.89-0.83 (m, 30H), 0.77 (t, J = 7 Hz, 6H). ^{13}C NMR ($CDCl_3$, ppm): δ 164.8, 164.3, 163.7, 163.2, 147.9, 144.1, 138.4, 134.2, 133.5, 133.4, 131.3, 129.8,

129.2, 129.1, 128.1, 127.5, 125.8, 123.8, 122.9, 119.7, 129.0, 128.7, 127.5, 124.1, 123.7, 123.4, 122.9, 122.7, 122.3, 119.9, 76.1, 54.9, 54.7, 40.6, 32.4, 31.8, 31.8, 30.2, 29.2, 29.0, 26.9, 23.5, 23.0, 22.6, 14.1, 14.1, 14.0, 11.2. MALDI-TOF: calcd for [$C_{130}H_{158}N_4O_{10}S_4$], 2063.1, found, 2063.7. Elemental analysis: calcd. for $C_{130}H_{158}N_4O_{10}S_4$: C, 75.61, H, 7.71, N, 2.71, S, 6.21; found: C, 75.87, H, 7.77, N, 2.77, S, 6.35.

Synthesis of Compound **6** and **8**: A solution of $FeCl_3$ (75 mg, 0.46 mmol) in 2 ml nitromethane was added dropwise to a stirred solution of compound **5** (98 mg, 0.05 mmol) in 8 ml CH_2Cl_2. The reaction was stirred with N_2. After stirring for 2 h at room temperature, 1 ml methanol was added to the solution. The solvent was evaporated under reduced pressure, and the residue was purified by column chromatography with hexane and CH_2Cl_2 (1:3, v/v) as the eluent to obtain **6** (58 mg, 67%), then further with CH_2Cl_2 and MeOH (20:1, v/v) to obtain **8 (**6 mg, 7%**)**. Compound **8**: MALDI-TOF: calcd for [$C_{114}H_{120}N_4O_{10}S_4$], 1832.8, found, 1833.0. ^{1}H NMR was also measured in CD_2Cl_4 in 353 K, very weak signal was shown in aromatic region due to the poor solubility. Compound **6**: ^{1}H NMR ($CDCl_3$ ppm): δ 8.70-8.69 (m, 10H), 8.27 (d, *J* = 8.5 Hz, 4H), 7.66 (s 2H), 5.24-5.15 (br 4H), 2.29-2.22 (br, 8H), 1.89-1.85 (br, 8H), 1.36-1.24 (m, 64H), 0.86 (m, 24H). ^{13}C NMR ($CDCl_3$, ppm): δ 173.7, 164.6, 164.3, 163.5, 163.2, 154.1, 145.1, 144.5, 138.3, 135.8, 135.0, 134.0, 133.9, 133.5, 132.0, 131.7, 131.4, 130.9, 130.0, 129.3, 129.1, 128.0, 127.3, 124.2, 123.9, 123.7, 123.4, 123.2, 54.9, 54.8, 31.8, 31.7, 29.2, 29.2, 26.9, 22.6, 14.1, 14.1. MALDI-TOF: calcd for [$C_{114}H_{124}N_4O_{10}S_4$], 1836.8, found, 1837.1. Elemental analysis: calcd. for $C_{114}H_{124}N_4O_{10}S_4$: C, 74.48; H, 6.80; N, 3.05; found: C, 74.17, H, 7.05, N, 2.95.

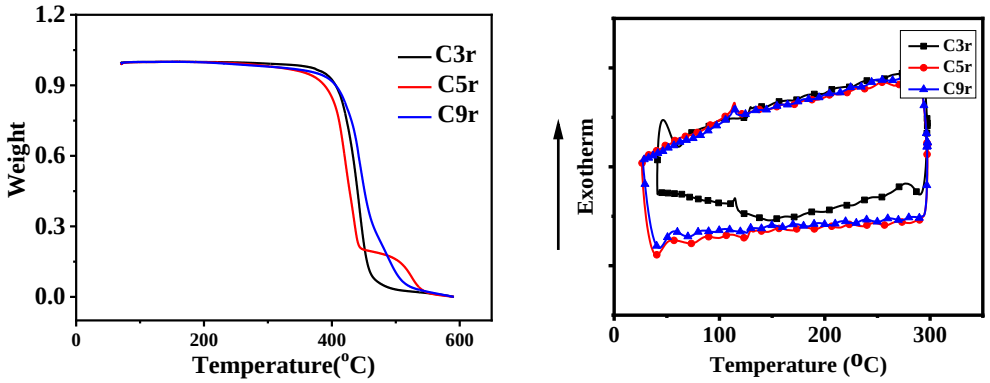

Figure 6.7.1. TGA curves (*left*) of all compounds: heating rate: 10 °C /min. from 70 °C to 550 °C under nitrogen atmosphere. Thermogravimetric analysis (TGA) reveals that both non-fused ring and fused ring molecules are thermally stable up to 400 °C. DSC measurements (*right*) were also performed on a DSC 2920 instrument. Samples (~5 mg) were annealed by heating to 300 °C at 20 °C/min, cooled to 0 °C at 20 °C/min, and then analyzed while being heated to 300 °C at 20 °C/min. No obvious melting peak was shown in the temperature window.

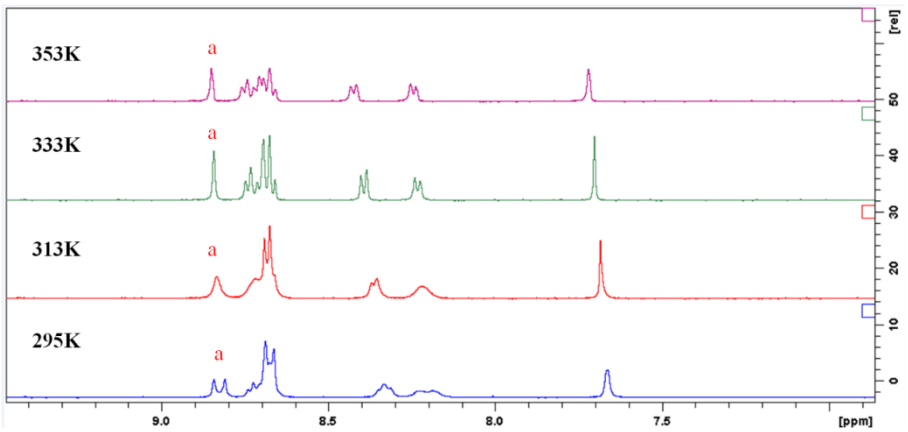

Figure 6.7.2. Variable temperature ^{1}H NMR spectra of 3r showing the split of proton *a* result from hindered rotation of the asymmetry ethylhexyl groups.

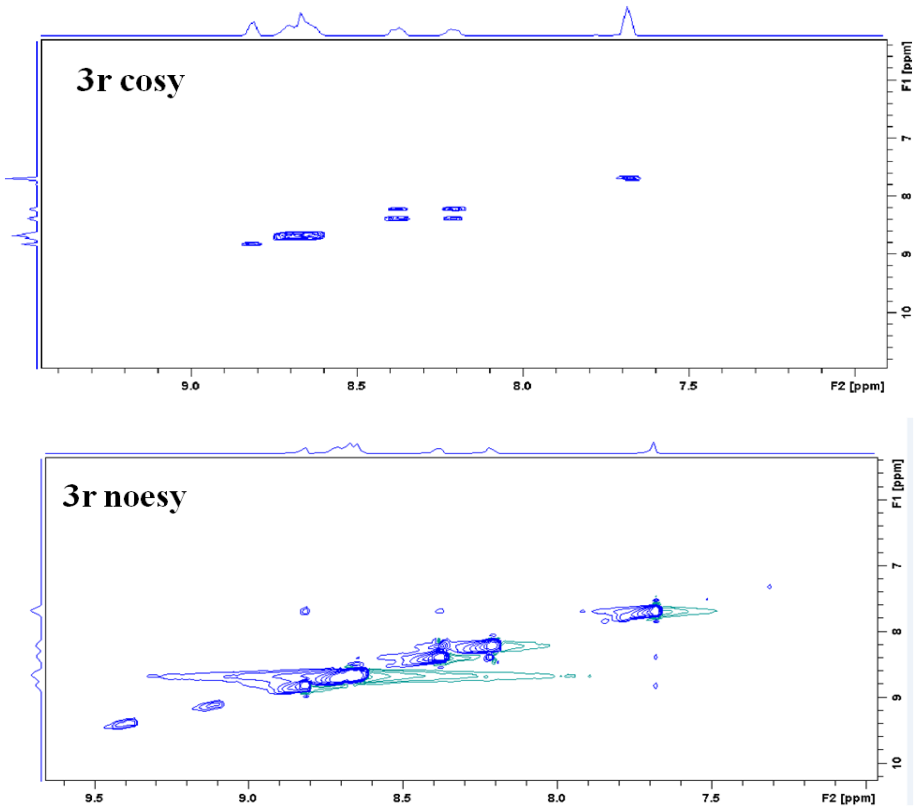

Figure 6.7.3. COSY (up) and NOESY (down) spectra of 3r in 353 K in $C_2D_2Cl_4$

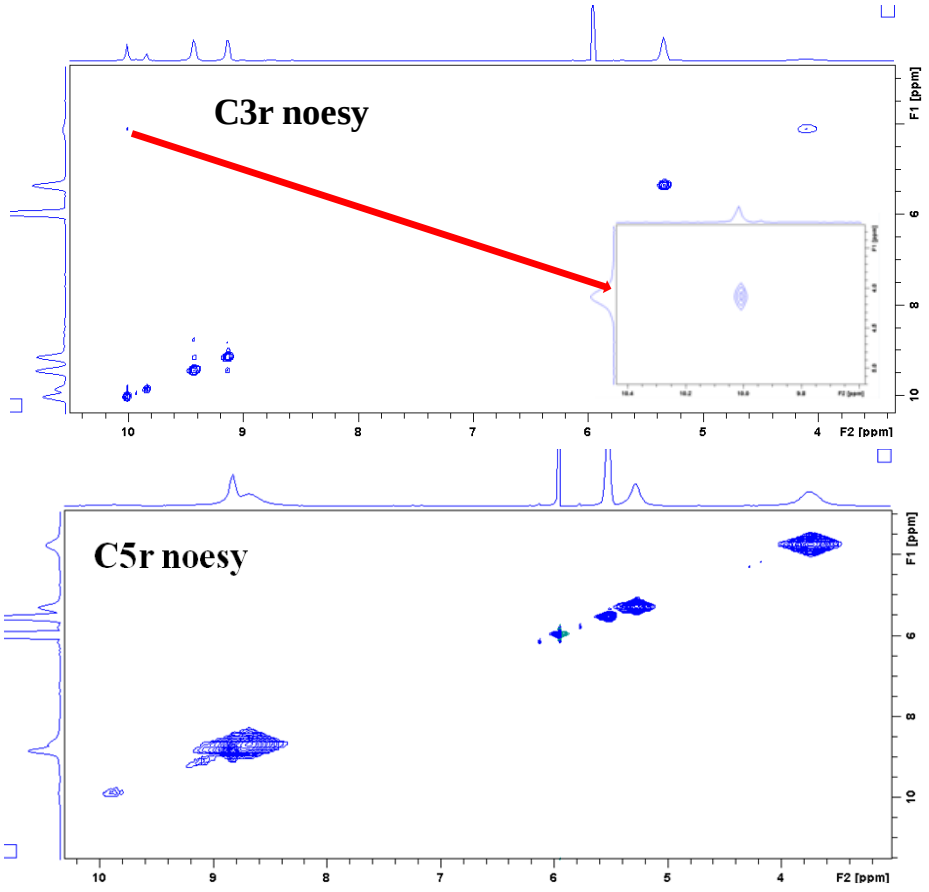

Figure 6.7.4. NOESY spectra of C3r (up) and C5r (down) in 353 K in $C_2D_2Cl_4$

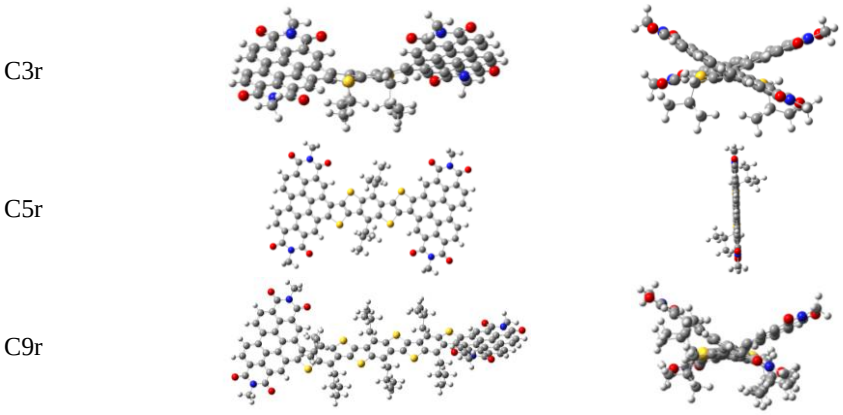

Figure 6.7.5. Optimized geometry of ladder type molecules. To facilitate the calculation, the heptylhexyl chains in PDI were replaced with a methyl group, while the ethylhexyl groups in heteroacenes were replaced by isobutyl to avoid missing the steric hindrance effect.

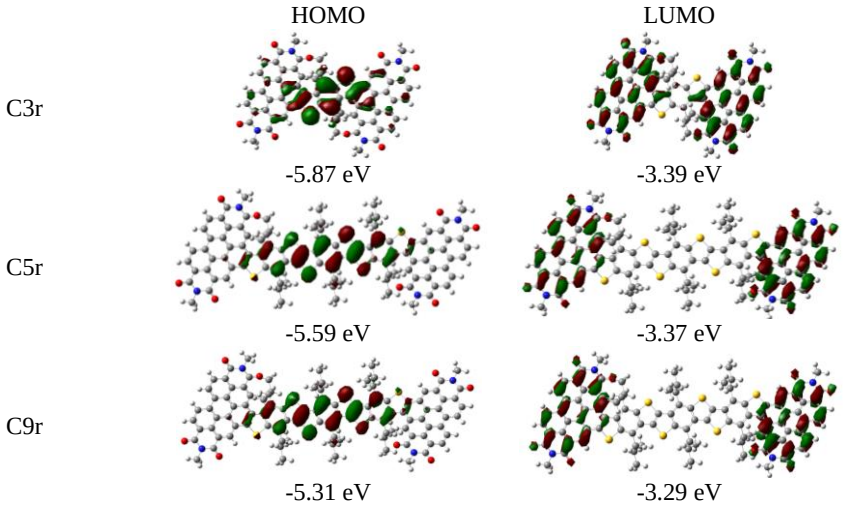

Figure 6.7.6. HOMO and LUMO molecular orbital distribution and the energy levels of ladder type molecules. Isovalue was 0.02 for printing both HOMO and LUMO orbitals.

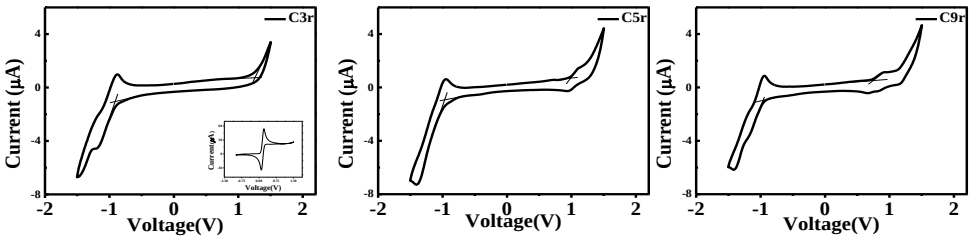

Figure 6.7.7. CV of ladder type molecules in $CHCl_3$.

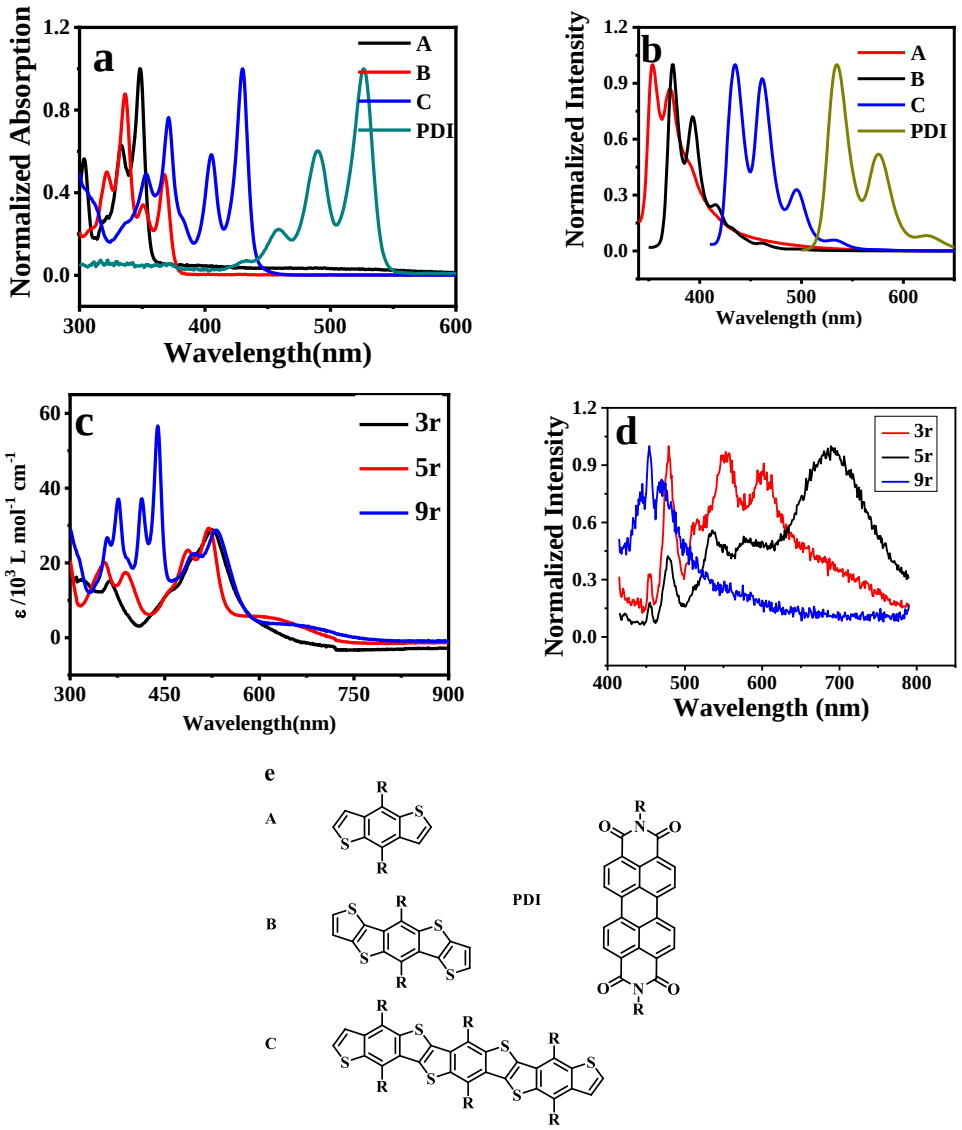

Figure 6.7.8. (a) Absorption spectra of thienoacenes and PDI unit; (b) Fluorescence spectra of thienoacenes and PDI unit; (c) Absorption spectra of non-fused ring compounds; (d) Fluorescence spectra of non-fused ring compounds; (e) Molecular structures of thienoacenes and PDI unit.

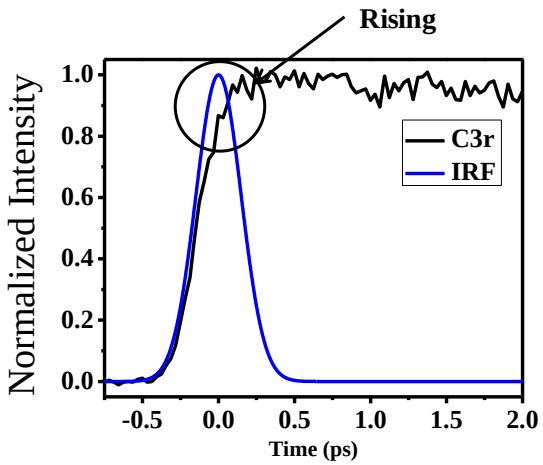

Figure 6.7.9. Energy rising component of the C3r at 600 emission wavelength.

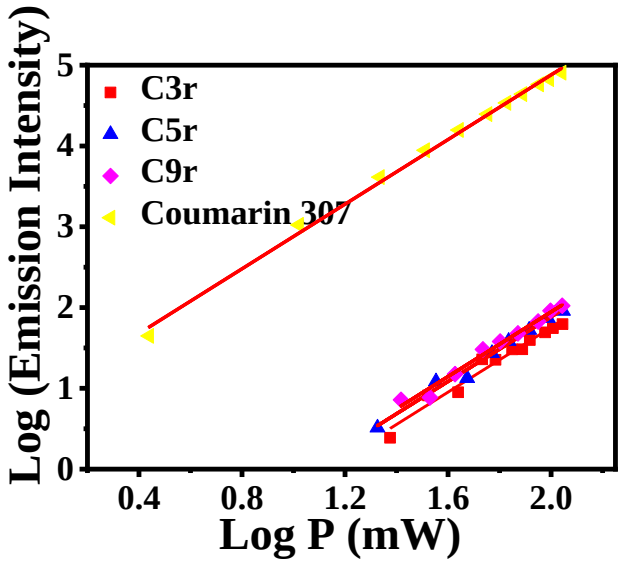

Figure 6.7.10. Power dependence of the two-photon-excited emission of all molecules at ~ 440-460 nm.

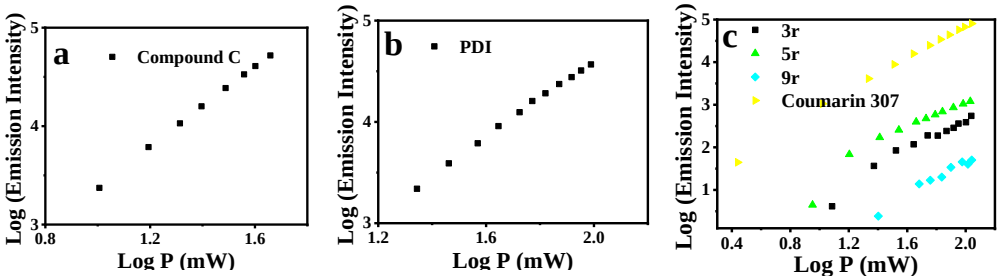

Figure 6.7.11. Power dependence of the two-photon-excited emission of Compound C (a), PDI (b) and non fused ring molecules (c).

Table 6.7.1. TPA cross-section values. [a] Due to instrument limitations, we were not able to measure the TPA cross-section

Compound	TPA (GM)
3r	5.20
5r	32.94
9r	0.66
A	[a]
B	[a]
C	24
PDI	1

Two photon absorption of D-A units (**A**, **B**, **C** and **PDI** in **Figure 6.7.8**) and non-fused ring compounds were also carried out. Efficient charge delocalization and charge transfer due to an increase in conjugation have been documented and can be measured by using TPA techniques. Also, a proportional increase of the TPA cross-section with enhancement in the conjugation length has been previously reported for thienoacene derivatives with slightly higher conjugation length (11R-21R). Our measurements shows that compound **C** have a TPA cross-section of 24 GM (**Table 6.7.11**). This value is in agreement with the tendency of previous studies in which longer thienoacene derivatives shows higher TPA-cross section. Specifically, the TPA cross-section value of compound **C** (24 GM) is slightly lower than the reported value of 11R (64 GM). The TPA cross-section of the C**9r** is enhanced drastically after cyclization. This is in agreement with previous

studies that show a strong correlation between the planarity of the material and a higher two-photon absorption cross-section. We were not able to measure the TPA cross-section of the A and B molecules. Interestingly, we observed an enhancement in the TPA cross section when the donor unit length is increased (**Table 6.7.1**). These results suggest that both enhancing the length of donor unit and adding an electron withdrawing unit will have an impact in the non-linear optical properties of the oligomers but enhancing the delocalization length will have a higher impact on this property. The TPA cross-section of the material has been linked with good charge transfer character properties on the photovoltaic process. Lately, it has been suggested that the dipole moment of the molecule could interact with the entanglement of the exciton resulting in a decrease in the Coulombic interactions between the electron and the associated hole. These oligomers represent a way to expand and probe acceptor materials for photovoltaic applications with tunable optical properties.

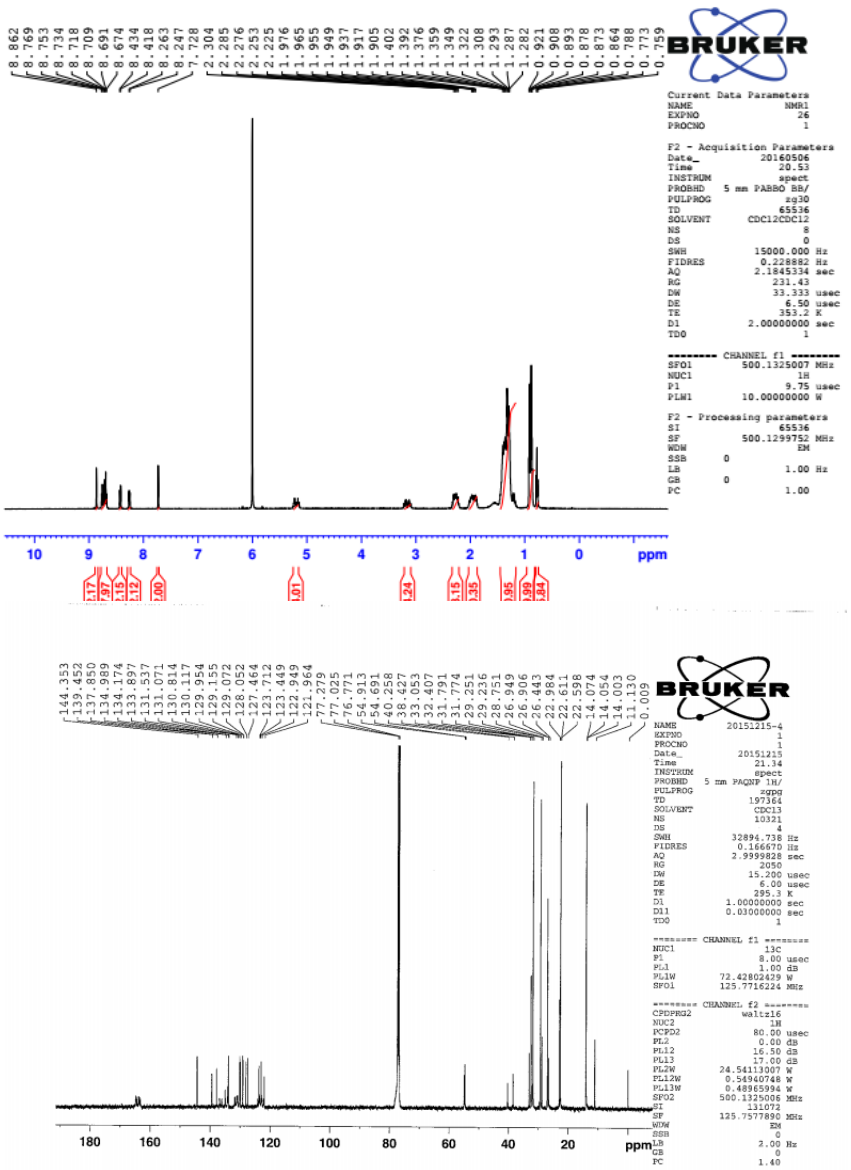

Figure 6.7.12. Compound 3r NMR spectra.

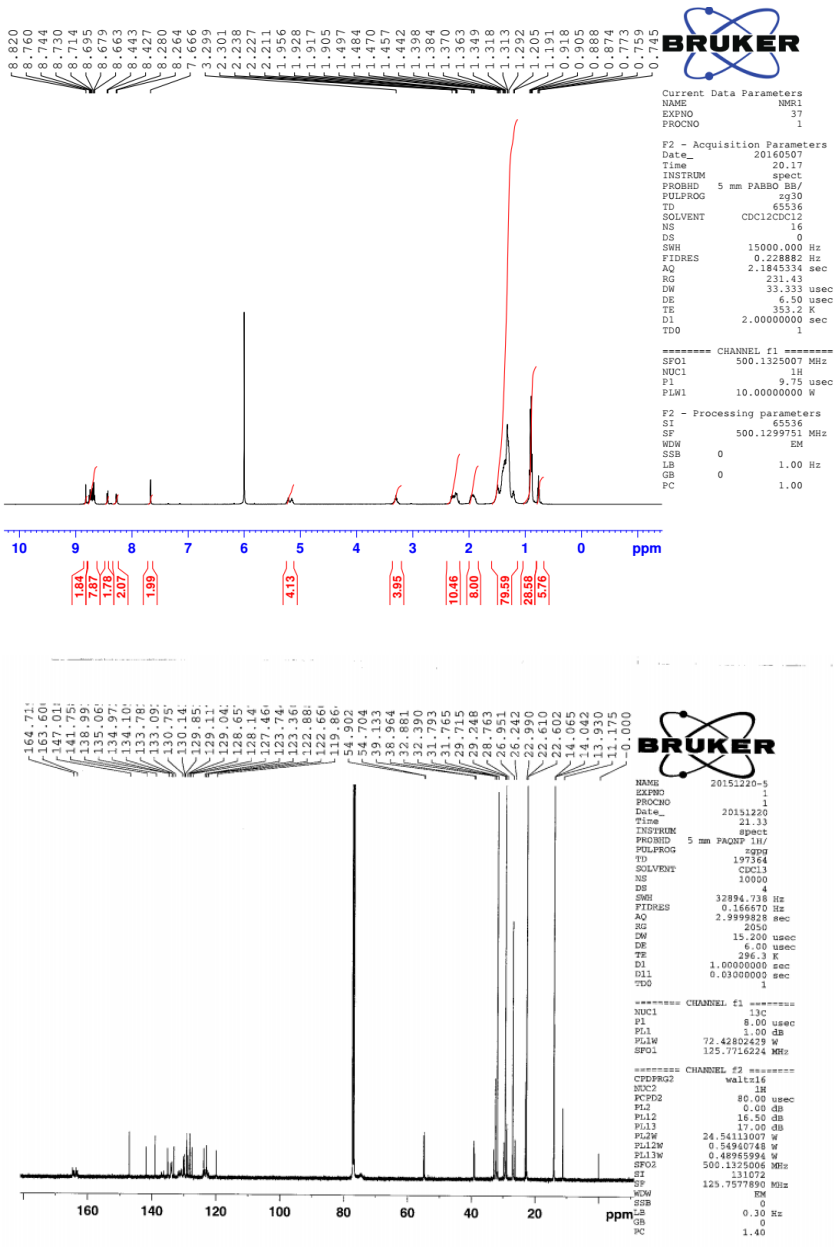

Figure 6.7.13. Compound 5r NMR spectra.

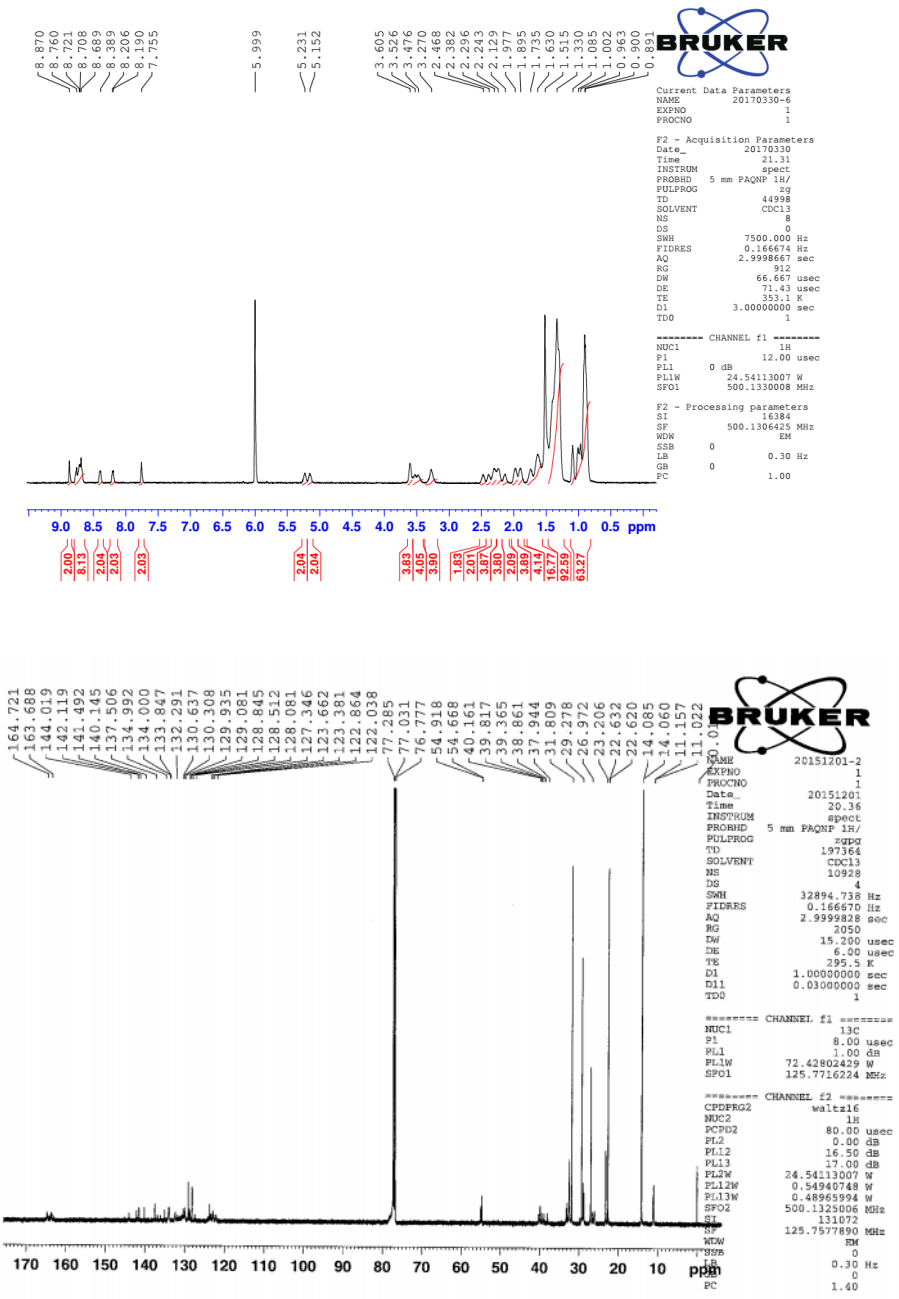

Figure 6.7.14 Compound 9r NMR spectra.

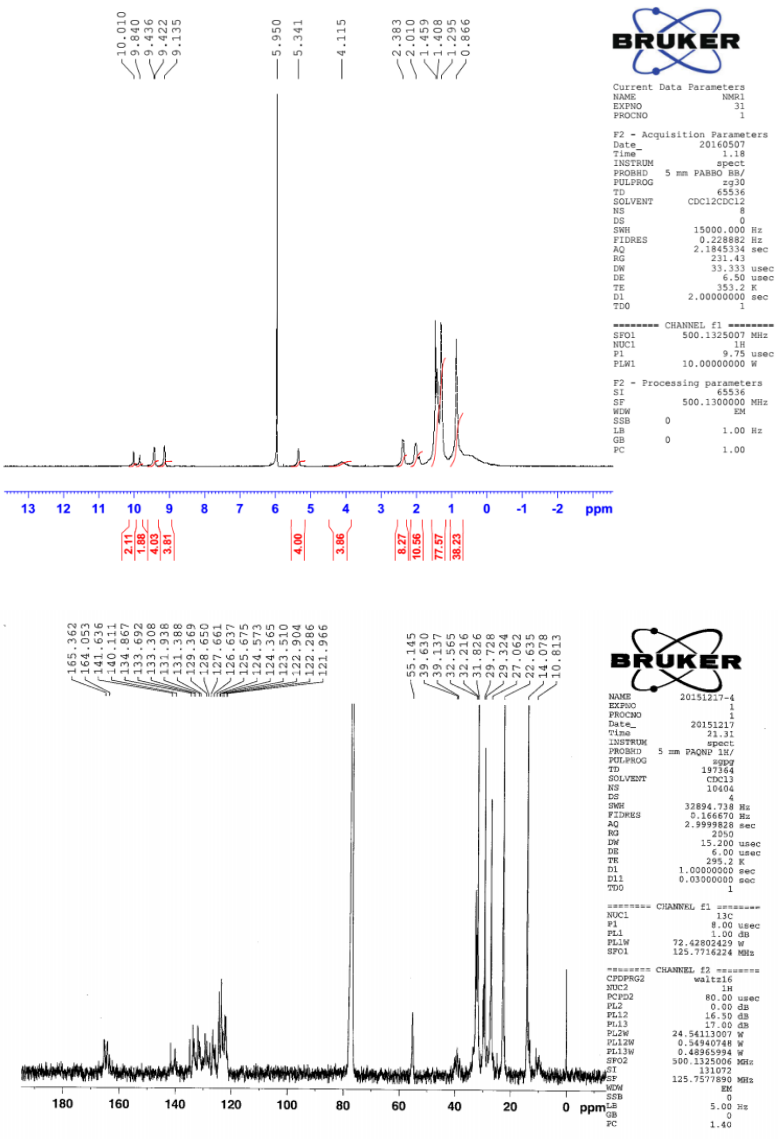

Figure 6.7.15. Compound C3r NMR spectra.

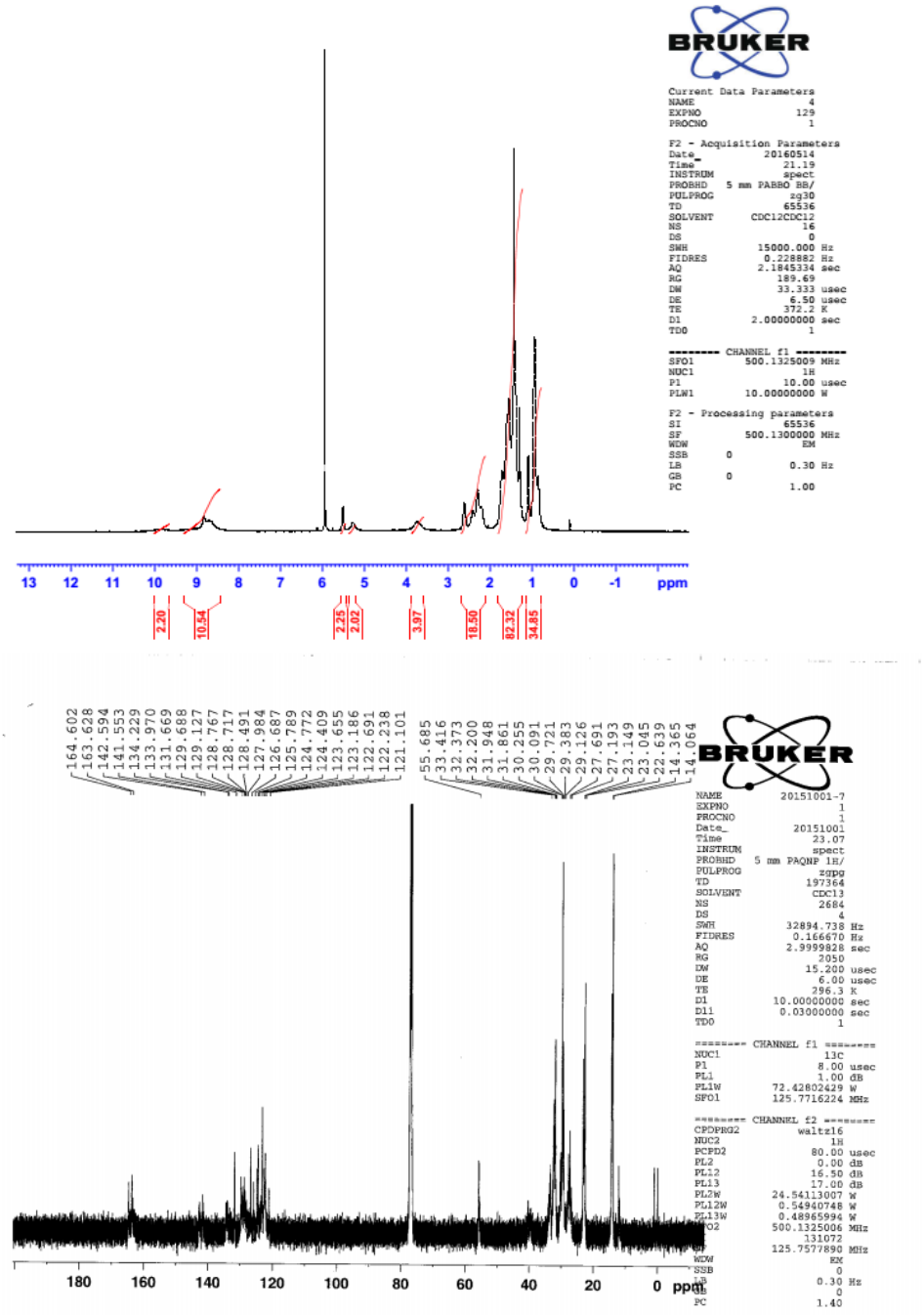

Figure 6.7.16. Compound C5r NMR spectra.

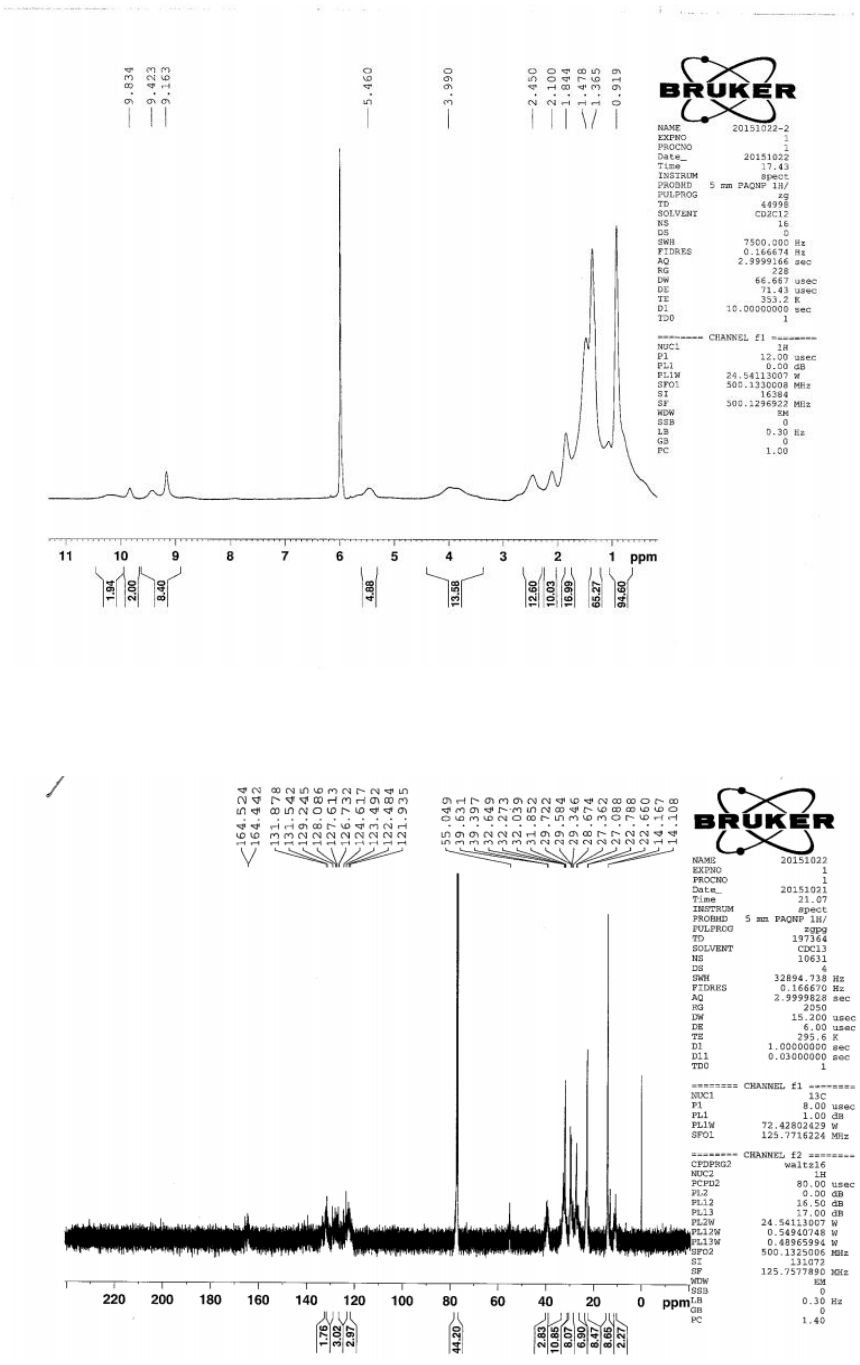

Figure 6.7.17. Compound C9r NMR and spectra.

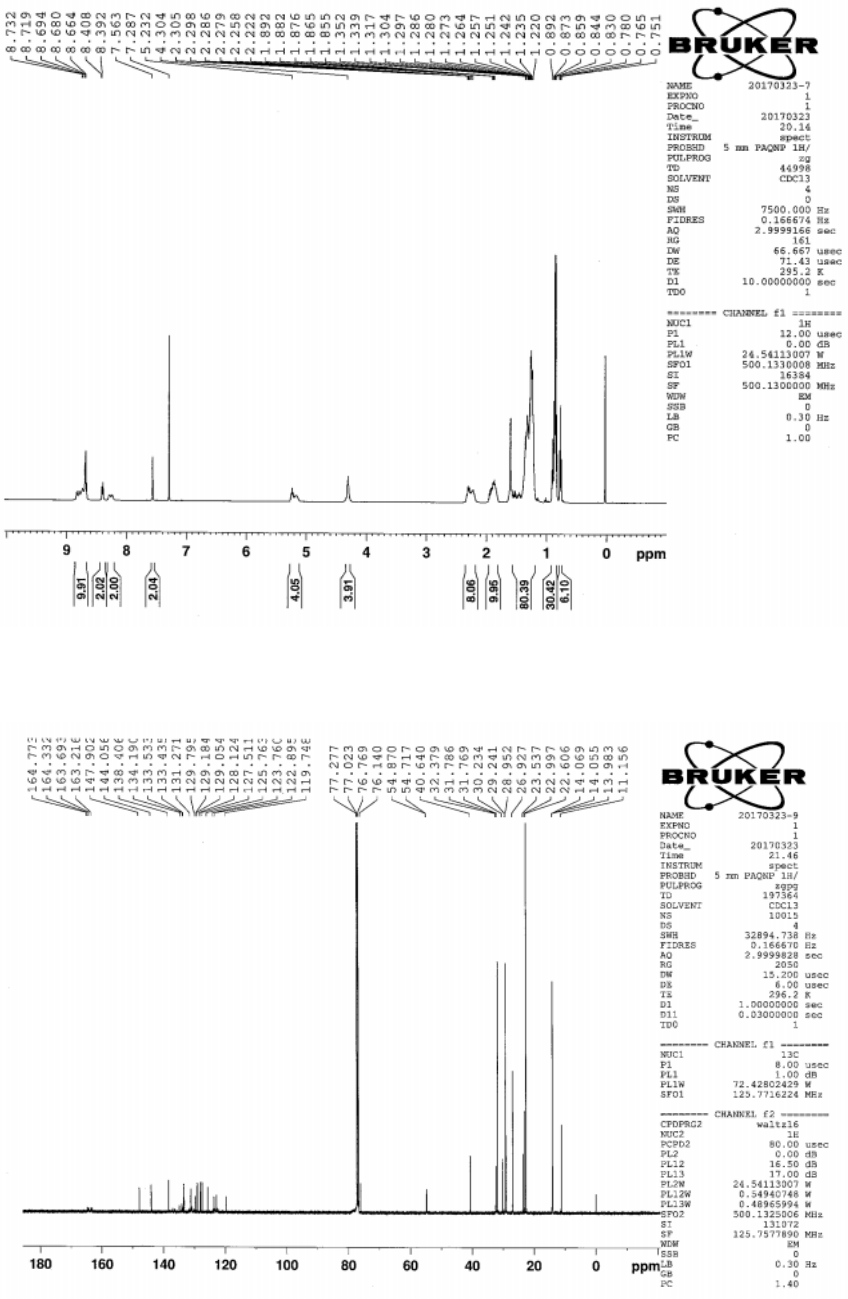

Figure 6.7.18. Intermediate 5 NMR and spectra.

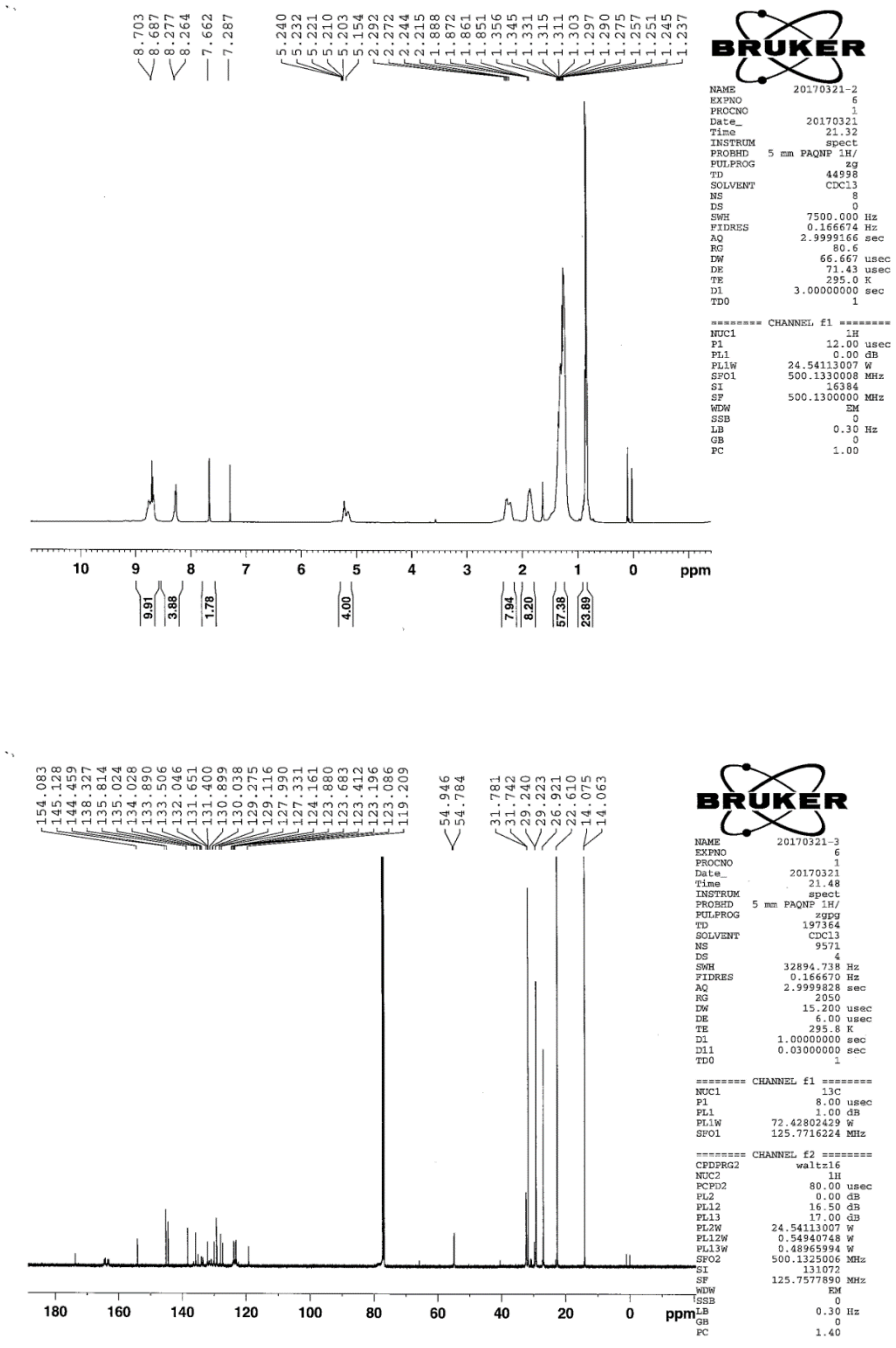

Figure 6.7.19. Intermediate 6 NMR and C NMA spectra.

References

(1) Demchenko, A. P.; Tang, K.-C.; Chou, P.-T. Excited-state proton coupled charge transfer modulated by molecular structure and media polarization. *Chem. Soc. Rev.* **2013**, *42*, 1379-1408.

(2) Ito, A.; Shimizu, A.; Kishida, N.; Kawanaka, Y.; Kosumi, D.; Hashimoto, H.; Teki, Y. Excited-state dynamics of pentacene derivatives with stable radical substituents. *Angew. Chem. Int. Ed.* **2014**, *53*, 6715-6719.

(3) Goushi, K.; Yoshida, K.; Sato K.; Adachi, C. Organic light-emitting diodes employing efficient reverse intersystem crossing for triplet-to-singlet state conversion. *Nat. Photon.* **2012**, *6*, 253-258.

(4) Zhao, D.; Wu, Q.; Cai, Z.; Zheng, T.; Chen, W.; Lu J.; Yu, L. Electron acceptors based on α-substituted perylene diimide (PDI) for organic solar cells. *Chem. Mater.* **2016**, *28*, 1139-1146.

(5) Harpham, M. R.; Süzer, Ö.; Ma, C.-Q.; Bäuerle P.; Goodson, T. Thiophene dendrimers as entangled photon sensor materials. *J. Am. Chem. Soc.* **2009**, *131*, 973-979.

(6) Sanders, S. N.; Kumarasamy, E.; Pun, A. B.; Steigerwald, M. L.; Sfeir, M. Y.; Campos, L. M. Intramolecular singlet fission in oligoacene heterodimers. *Angew. Chem. Int. Ed.* **2016**, *55*, 3373-3377.

(7) Rosenberg, M.; Dahlstrand, C.; Kilså K.; Ottosson, H. Excited state aromaticity and antiaromaticity: opportunities for photophysical and photochemical rationalizations. *Chem. Rev.* **2014**, *114*, 5379-5425.

(8) Würthner, F.; Saha-Möller, C. R.; Fimmel, B.; Ogi, S.; Leowanawat, P.; Schmidt, D. Perylene bisimide dye assemblies as archetype functional supramolecular materials. *Chem. Rev.* **2016**, *116*, 962-1052.

(9) Kang, H.; Kim, G.; Kim, J.; Kwon, S.; Kim, H.; Lee, K. Bulk-heterojunction organic solar cells: five core technologies for their commercialization. *Adv. Mater.* **2016**, *28*, 7821-7861.

(10) Wu, J.-S.; Cheng, S.-W.; Cheng, Y.-J.; Hsu, C.-S. Donor-acceptor conjugated polymers based on multifused ladder-type arenes for organic solar cells. *Chem. Soc. Rev.* **2015**, *44*, 1113-1154.

(11) Liu, J.; Narita, A.; Osella, S.; Zhang, W.; Schollmeyer, D.; Beljonne, D.; Feng, X.; Müllen, K. Unexpected scholl reaction of 6,7,13,14-tetraarylbenzo[*k*]tetraphene: selective formation of five-membered rings in polycyclic aromatic hydrocarbons. *J. Am. Chem. Soc.* **2016**, *138*, 2602-2608.

(12) Ip, H.-W.; Ng, C.-F.; Chow, H.-F.; Kuck, D. Three-fold scholl-type cycloheptatriene ring formation around a tribenzotriquinacene core: toward warped graphenes. *J. Am. Chem. Soc.* **2016**, *138*, 13778-13781.

(13) Cai, Z.; Zhang, H.; Geng, H.; Liu, Z.; Yang, S.; Luo, H.; Jiang, L.; Peng, Q.; Zhang, G.; Chen, J.; Yi, Y.; Hu, W.; Zhang, D. Thiepin-fused heteroacenes: simple synthesis, unusual structure, and semiconductors with less anisotropic behavior. *Chem. Eur. J.* **2013**, *19*, 14573-14580.

(14) Bunz, U. H. F. The larger linear N-heteroacenes. *Acc. Chem. Res.* **2015**, *48*, 1676-1686.

(15) Stępień, M.; Gońka, E.; Żyła, M.; Sprutta, N. Heterocyclic nanographenes and other polycyclic heteroaromatic compounds: synthetic routes, properties, and applications. *Chem. Rev.* **2016**, *117*, 3479-3716.

(16) Narita, A.; Wang, X.-Y.; Feng, X.; Müllen, K. New advances in nanographene chemistry. *Chem. Soc. Rev.* **2015**, *44*, 6616-6643.

(17) Hammer, B. A. G.; Müllen, K. Dimensional evolution of polyphenylenes: expanding in all directions. *Chem. Rev.* **2016**, *116*, 2103-2140.

(18) Zheng, T.; Cai, Z.; Ho-Wu, R.; Yau, S. H.; Shaparov, V.; Goodson, T.; Yu, L. Synthesis of ladder-type thienoacenes and their electronic and optical properties. *J. Am. Chem. Soc.* **2016**, *138*, 868-875.

(19) Cai, Z.; Lo, W.-Y.; Zheng, T.; Li, L.; Zhang, N.; Hu, Y.; Yu, L. Exceptional single-molecule transport properties of ladder-type heteroacene molecular wires. *J. Am. Chem. Soc.* **2016**, *138*, 10630-10635.

(20) Zheng, T.; Lu, L.; Jackson, N. E.; Lou, S. J.; Chen, L. X.; Yu, L. Roles of quinoidal character and regioregularity in determining the optoelectronic and photovoltaic properties of conjugated copolymers. *Macromolecules* **2014**, *47*, 6252-6259.

(21) Usta, H.; Risko, C.; Wang, Z.; Huang, H.; Deliomeroglu, M. K.; Zhukhovitskiy, A.; Facchetti, A.; Marks, T. J. Design, synthesis, and characterization of ladder-type molecules and polymers. air-stable, solution-processable *n*-channel and ambipolar semiconductors for thin-film transistors via experiment and theory. *J. Am. Chem. Soc.* **2009**, *131*, 5586-5608.

(22) Cai, Z.; Guo, Y.; Yang, S.; Peng, Q.; Luo, H.; Liu, Z.; Zhang, G.; Liu, Y.; Zhang, D. New donor-acceptor-donor molecules with Pechmann dye as the core moiety for solution-processed good-performance organic field-effect transistors. *Chem. Mater.* **2013**, *25*, 471-478.

(23) Cai, Z.; Luo, H.; Chen, X.; Zhang, G.; Liu, Z.; Zhang, D. Extended conjugated donor-acceptor molecules with *E*-(1,2-difluorovinyl) and diketopyrrolopyrrole (DPP) moieties toward high-performance ambipolar organic semiconductors. *Chem. Asian J.* **2014**, *9*, 1068-1075.

(24) Cai, Z.; Luo, H.; Qi, P.; Wang, J.; Zhang, G.; Liu, Z.; Zhang, D. Alternating conjugated electron donor-acceptor polymers entailing Pechmann dye framework as the electron acceptor moieties for high performance organic semiconductors with tunable characteristics. *Macromolecules* **2014**, *47*, 2899-2906.

(25) Sekita, M.; Ballesteros, B.; Diederich, F.; Guldi, D. M.; Bottari, G.; Torres, T. Intense ground-state charge-transfer interactions in low-bandgap, panchromatic phthalocyanine-tetracyanobuta-1,3-diene conjugates. *Angew. Chem. Int. Ed.* **2016**, *55*, 5560-5564.

(26) Zhong, Y.; Kumar, B.; Oh, S.; Trinh, M. T.; Wu, Y.; Elbert, K.; Li, P.; Zhu, X.; Xiao, S.; Ng, F.; Steigerwald, M. L.; Nuckolls, C. Helical ribbons for molecular electronics. *J. Am. Chem. Soc.* **2014**, *136*, 8122-8130.

(27) Chiu, C.-Y.; Kim, B.; Gorodetsky, A. A.; Sattler, W.; Wei, S.; Sattler, A.; Steigerwald, M.; Nuckolls, C. Shape-shifting in contorted dibenzotetrathienocoronenes. *Chem. Sci.* **2011**, *2*, 1480-1486.

(28) Nagarajan, K.; Mallia, A. R.; Muraleedharan, K.; Hariharan, M. Enhanced intersystem crossing in core-twisted aromatics. *Chem. Sci.* **2017**, *8*, 1776-1782.

(29) Yuan, Z.; Lee, S.-L.; Chen, L. Li, C.; Mali, K. S.; De Feyter, S.; Müllen, K. Processable rylene diimide dyes up to 4 nm in length: synthesis and STM visualization. *Chem. Eur. J.* **2013**, *19*, 11842-11846.

(30) Yuan, Z.; Xiao, Y.; Yang, Y.; Xiong, T. Soluble ladder conjugated polymer composed of perylenediimides and thieno[3,2-b]thiophene (LCPT): a highly efficient synthesis via photocyclization with the sunlight. *Macromolecules* **2011**, *44*, 1788-1791.

(31) Kass, K.-J.; Forster, M.; Scherf. U. Incorporating an alternating donor-acceptor structure into a ladder polymer backbone. *Angew.Chem. Int. Ed.* **2016**, *55*,7816-7820.

(32) Lee, J.; Kalin, A. J.; Yuan, T.; Al-Hashimi, M.; Fang, L. Fully conjugated ladder polymers. *Chem. Sci.*, **2017**, *8*, 2503-2521.

(33) Both the fused and non-fused structures were observed in the ring fusing process, the major product is non-fused ring product, details see supporting information.

(34) Hilton, C. L.; Crowfoot, J. M.; Rempala, P.; King, B. T. 18,18′-Dihexyl[9,9′]biphenanthro[9,10-*b*]triphenylene: construction and consequences of a profoundly hindered aryl-aryl single bond. *J. Am. Chem. Soc.* **2008**, *130*, 13392-13399.

(35) Zhong, H.; Wu, C.-H.; Li, C.-Z.; Carpenter, J.; Chueh, C.-C.; Chen, J.-Y.; Ade, H.; Jen, A. K.-Y. Rigidifying nonplanar perylene diimides by ring fusion toward geometry-tunable acceptors for high-performance fullerene-free solar cells. *Adv. Mater.* **2016**, *28*, 951-958.

(36) Yu, Y. W.; Li, Y. J.; Qin, Z. H.; Jiang, R. S.; Liu, H. B.; Li, Y. L. Designed synthesis and supramolecular architectures of furan-substituted perylene diimide. *J. Colloid Interface Sci.* **2013**, *399*, 13-18.

(37) Badaeva, E.; Harpham, M. R.; Guda, R.; Süzer, Ö.; Ma, C.-Q.; Bäuerle, P.; Goodson, T.; Tretiak, S. Excited-state structure of oligothiophene dendrimers: computational and experimental study. *J. Phys. Chem. B* **2010**, *114*, 15808-15817.

(38) Furgal, J. C.; Jung, J. H.; Goodson, T.; Laine, R. M. Analyzing structure–photophysical property relationships for isolated T_8, T_{10}, and T_{12} stilbenevinylsilsesquioxanes. *J. Am. Chem. Soc.* **2013**, *135*, 12259-12269.

(39) Guo, M.; Yan, X.; Goodson, T. Electron mobility in a novel hyper-branched phthalocyanine dendrimer. *Adv. Mater.* **2008**, *20*, 4167-4171.

(40) Yuan, M.; Durban, M. M.; Kazarinoff, P. D.; Zeigler, D. F.; Rice, A. H.; Segawa, Y.; Luscombe, C. K. Synthesis and characterization of fused-thiophene containing naphthalene diimide *n*-type copolymers for organic thin film transistor and all-polymer solar cell applications. *J. Polym. Sci., Part A: Polym. Chem.* **2013**, *51*, 4061-4069.

(41) Ramakrishna, G.; Bhaskar, A.; Goodson, T. Ultrafast excited state relaxation dynamics of branched donor-π-acceptor chromophore: evidence of a charge-delocalized state. *J. Phys. Chem. B* **2006**, *110*, 20872-20878.

(42) Irie, M.; Sakemura, K.; Okinaka, M.; Uchida, K. Photochromism of dithienylethenes with electron-donating substituents. *J. Org. Chem.* **1995**, *60*, 8305-8309.

(43) Bhaskar, A.; Ramakrishna, G.; Lu, Z.; Twieg, R.; Hales, J. M.; Hagan, D. J.; Van Stryland, E.; Goodson, T. Investigation of two-photon absorption properties in branched alkene and alkyne chromophores. *J. Am. Chem. Soc.* **2006**, *128*, 11840-11849.

(44) Ricci, F; Carlotti, B.; Keller, B.; Bonnaccorso, C.; Fortuna, C. G.; Goodson, T.; Elisei, F.; Spalletti, A. Enhancement of two-photon absorption parallels intramolecular charge-transfer efficiency in quadrupolar versus dipolar cationic chromophores. *J. Phys. Chem. C*, **2017**, *121*, 3987-4001.

(45) Alam, M. M.; Chattopadhyaya, M.; Chakrabarti, S.; Ruud, K. Chemical control of channel interference in two-photon absorption processes. *Acc. Chem. Res.* **2014**, *47*, 1604-1612.

(46) Guo, L.; Wong, M. S. Multiphoton excited fluorescent materials for frequency upconversion emission and fluorescent probes. *Adv. Mater.* **2014**, *26*, 5400-5428.

(47) Vázquez, R. J.; Kim, H.; Kobilka, B. M.; Hale, B. J.; Jeffries-EL, M.; Zimmerman, P.; Goodson, T. Evaluating the effect of heteroatoms on the photophysical properties of donor–acceptor conjugated polymers based on 2,6-di(thiophen-2-yl)benzo[1,2-b:4,5-b′]difuran: two-photon cross-section and ultrafast time-resolved spectroscopy *J. Phys. Chem. C* 2017, 121, 14382-14392.

Chapter 7

Enacting Two-Electron Transfer from a Double-Triplet State of Intramolecular Singlet Fission

7.1 Original Publication Information

The work in this chapter was accepted by the *Journal of the American Chemical Society* (*JACS*) with the title:

"*Enacting Two-Electron Transfer from a Double-Triplet State of Intramolecular Singlet Fission"* Hyungjun Kim, Bradley Keller, Rosina Ho-Wu, Neranga Abeyasinghe, Ricardo J. Vazquez, Theodore Goodson, III, and Paul M. Zimmerman. *J. Am. Chem. Soc.* **2018**, *140*, 25, 7760-7763

Modifications were conducted to the manuscript to adapt it to the style of the content of this dissertation. References and supporting information of the manuscript are included in this chapter.

7.2 Abstract

A simulation-led strategy enacts twoelectron transfer between an intramolecular singlet fission chromophore (tetracyanomethylene quinoidal bithiopehene with β,β′-solubilizing groups) and multielectron acceptor (anthraquinone). The thermodynamic plausibility of multielectron transfer from a double-triplet state and the absorption spectra of electron transfer (ET) products were predicted using quantum chemical simulations. These predictions are consistent with experimental observations of reduced lifetimes in time-resolved fluorescence spectroscopy, changes in transmission profile, and appearance of new absorption bands in transient absorption spectroscopy, all of which support multi-ET in the QOT2/AQ mixture. The analysis suggests 2ET is favored over 1ET by a 2.5:1 ratio.

7.3 Introduction

Generating, transferring, and storing multiple electrons from single photons could prove revolutionary for solar energy technologies. One promising process, singlet fission (SF), produces two excited electrons from a single photon.[1] The multielectron excited state in SF can be conceived as an entangled double-triplet[2–8] and thus denoted as TT. The correlation between the two triplets makes TT a unique state that is not identical in character to 2 × T1. [9–13] Separation of the TT state is a challenging task by itself, requiring special molecular organization and delicate tuning of the intra- or intermolecular coupling.[4,14] Toward the goals of achieving efficient solar energy harvesting, we propose an alternative way of extracting two excited electrons directly from a TT state in a bimolecular, 2-electron process. Tetracyanomethylene quinoidal bithiophene with β,β′-solubilizing groups (QOT2)[15] was herein tested to demonstrate this concept (**Figure 7.3.1A**). Our groups have revealed a long-lived QOT2 excited state with characteristics that closely relate to the

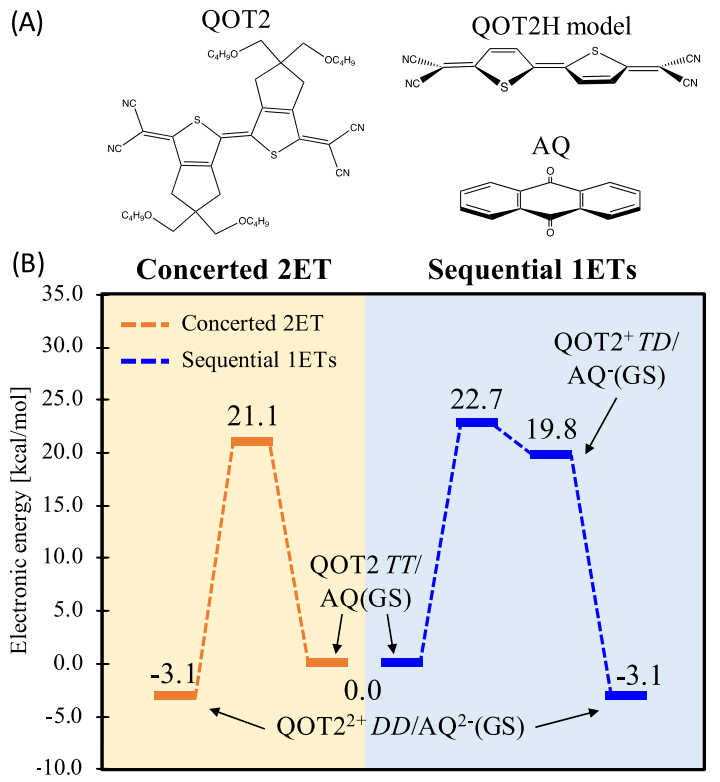

(C)

		QOT2		AQ	
		Charge	Spin	Charge	Spin
Before ET	QOT2 *TT*/AQ(GS)	0	↑↑,↓↓	0	0
After 1ET	$QOT2^{+}$ *TD*/AQ^{-}(GS)	+1	↑↑,↓	-1	↓
After 2ET	$QOT2^{2+}$ *DD*/AQ^{2-}(GS)	+2	↑,↓	-2	0

Figure 7.3.1. (A) Chemical structures of QOT2, AQ and QOT2H model. (B) Jablonski diagram for sequential 1ETs and concerted 2ET. (C) Diabatic representation of three states in (B). (Up-arrow and down-arrow represent up-spin and down-spin, respectively. (See SI)

TT state ($2^1 A_g$) of SF, generated from a bright singlet state in subps.[2,4] As a single, tightly coupled π system, QOT2 is unique among intramolecular SF (iSF) chromophores because its TT state is not spontaneously separated into two free triplets in solution.[2,4] This special property provides an opportunity to trap the double-triplet and achieve multielectron extraction. In principle, two-electron transfer (2ET) from an entangled TT state may be advantageous for efficient energy harvesting, as competing relaxation channels will be outcompeted. Such 2ET has been suggested

to occur in intermolecular SF (xSF) materials.[6,16,17] Though free triplet harvesting from iSF has been observed,[18] evidence demonstrating 2ET from a TT state of iSF chromophores is lacking. Herein, the possibility of 2ET from an iSF TT state will be realized by a detailed quantum chemical study of the photo-electrochemical properties of QOT2, and its coupling to a suitable acceptor for the two electrons. These simulations will be backed up by evidence from multiple types of spectroscopy that support 2ET. The search for a suitable acceptor molecule centered on anthraquinones, a plausible energy storage unit with 2e- redox properties.[19–21] Our prior study of a variety of these materials indicated that 9,10-anthraquinone (AQ) has a 2-electron affinity of 5.99 eV,[20] which is within the range of acceptance of electrons from the QOT2 TT state. Quantum chemical simulations employing the QOT2H model give 10.27 eV as an estimate of the QOT2 TT state double ionization potential. This analysis predicts 2ET from the QOT2 TT state is thermodynamically viable (ΔE = -0.69 eV), but unfavorable from the ground state QOT2 (ΔE = +3.39 eV, see supporting Information).

7.4 Results and Discussion

Atomistic simulations were employed to examine the mechanistic feasibility of 2ET from the QOT2 TT state. For the key ET steps, constrained density functional theory[22] (CDFT) was used to estimate the plausibility of these reactions, where ET from each T leads to a doublet (D) state. The molecular structures before ET (QOT2 TT/AQ), after 1ET ($QOT2^{+}$ TD/AQ^{-}), and after 2ET ($QOT2^{2+}$ DD/AQ^{2-}), are shown in **Figure 7.4.1.1A**. As expected, the QOT2/AQ complex forms a π−π stacking structure, which is consistent with 1:1 QOT2:AQ binding observed in UV−vis absorption intensity changes. There are two primary ways of transferring two electrons, which are illustrated in **Figure 7.3.1.1**: Concerted 2ET, and sequential 1ETs. A third, remote

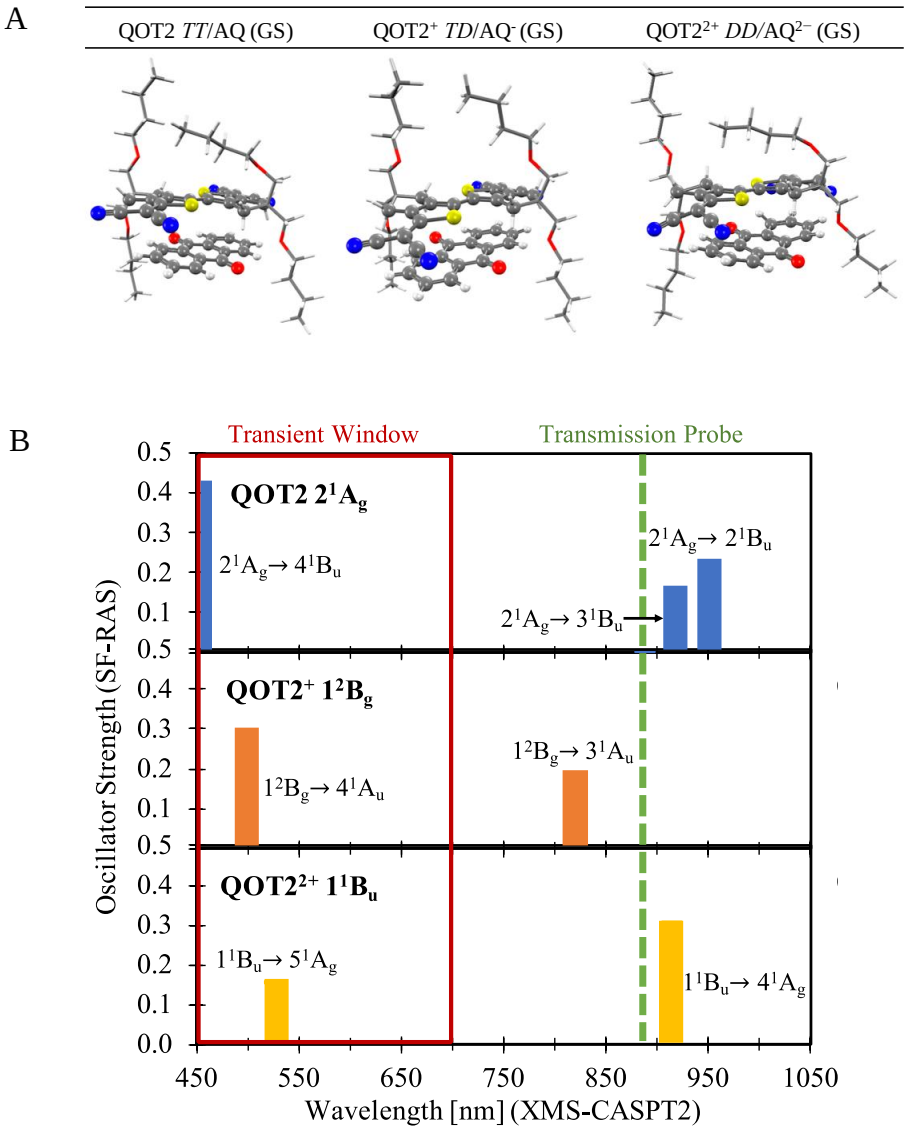

Figure 7.4.1.1. (A) Optimized structure of QOT2/AQ before ET (left panel; QOT2 *TT*/AQ(GS)), after 1ET (middle panel; $QOT2^{+}$ *TD*/AQ^{-}(GS)), and after 2ET (bottom panel; $QOT2^{2+}$ *DD*/AQ^{2-}(GS)) described by CDFT. Color scheme: hydrogen atom, white; carbon atom, black; nitrogen atom, blue; oxygen atom, red; sulfur atom, yellow. (B) Absorption spectra predicted by XMS-CASPT2 and Spin-Flip RAS for the QOT2 2^1A_g state (top), and its oxidized forms, $QOT2^{+}$ 1^2B_g and $QOT2^{2+}$ 1^1B_u states (middle and bottom).

possibility, involves ET to triplet AQ and is discussed in SI **Figure 7.6.3.5**. The two main paths have barriers of 21.1 and 22.7 kcal/mol, where the second 1ET in the sequential pathway is

barrierless, and therefore no transition state is shown. Overall, this result suggests 2ET could occur through either pathway, and that the concerted pathway may have a slight advantage over the 1ET path. Previous investigations revealed that the separation of TT into two independent triplets is not efficient in QOT2 due to the high energy of the quintet state.[2,4] **Figure 7.3.1.1**, on the other hand, shows that ET pathways from TT are plausible, and therefore are expected to be operative in the presence of AQ acceptor.

Having evidence from the simulations that 2ET from QOT2 TT to AQ is plausible, the absorption spectra of ET products were also examined. Though the spectra of reduced AQ are available from the literature,[23] the spectra of oxidized QOT2 TT are not trivial to obtain experimentally. Solubilizing groups were replaced by hydrogen atoms (QOT2H model **Figure 7.3.1.1A**) for high-level ab initio quantum chemical simulations. XMS-CASPT2 and Spin-Flip RAS methods assigned the electronic state of neutral QOT2 TT, and singly and doubly oxidized QOT2 TT to have $2^1 A_g$, $1^2 B_g$, and 11 Bu symmetries, respectively (**Table 7.6.3.3**). Starting from these states, transition wavelengths and dipole moments were computed (**Figure 7.4.1.1B**) to provide a baseline for subsequent spectroscopic analysis. Because of the wide range of wavelengths involved, multiple techniques were needed to identify the signatures of 1ET and 2ET products.

With these spectral peaks from the simulations in hand, time-resolved fluorescence decay was used to monitor the lifetime of the QOT2 excited singlet state in a QOT2/AQ mixture (**Figure 7.6.3.7**). In the mixture, the significantly decreased short (27.3 ps) and long (181.2 ps)

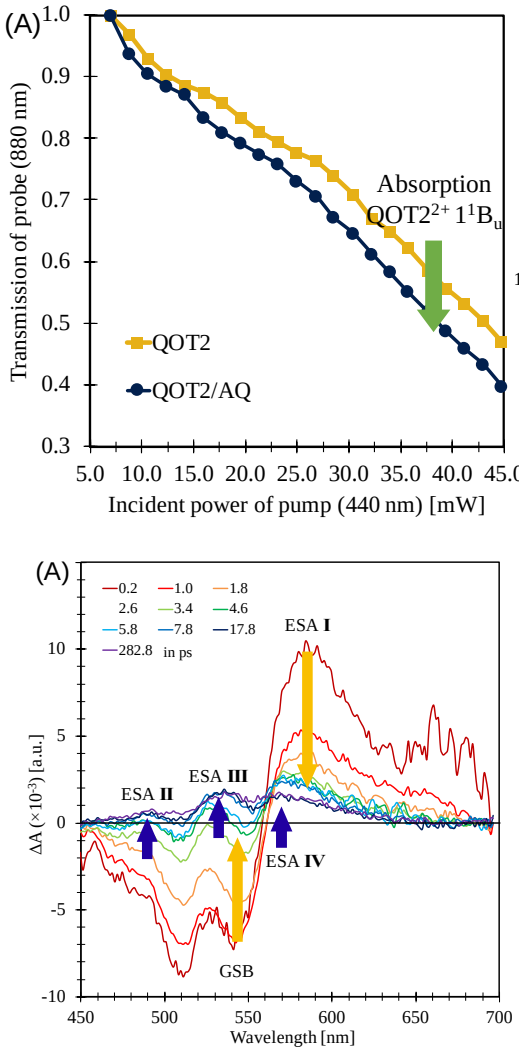

Figure 7.4.1.2. (A) Transmission profile of QOT2 and QOT2/AQ based on a probe of 880 nm after excitation at 440 nm by a pump. (B) Transient absorption spectrum of QOT2/AQ.

fluorescence time scales compared to pure QOT2 (41.5 and 785.9 ps) are measured. The faster decay of the mixture indicates the appearance of nonradiative sink that can consume exciton population, with ET being a likely cause.[24] On shorter time scales (less than 10 ps), the behavior of QOT2 and the QOT2/AQ mixture are nearly identical in transient absorption (**Table 7.6.3.5**). This is consistent with prior observations of sub ps formation of QOT2 TT state,[2] indicating that

the initial generation of TT is unperturbed by AQ. (Immediate ET from a bright singlet state results in a QOT2 ground-state cation, which is not observed; see SI **Figure 7.6.3.8**.)

To support these first indications of ET, transmission at 880 nm was measured when QOT2 was excited by a 440 nm pump (two-color pump−probe transmission). QOT2 excited at 440 nm has been reported to yield $2^1 A_g$ (TT) state which absorbs at 880 nm.[2] Because transmission at 880 nm depends on the QOT2 TT population, this signal can measure changes in the TT state population. Significantly reduced transmission (0.47 at 45 mW power) compared the transmission through solvent was observed in the QOT2 sample (**Figure 7.4.1.2A**). In the QOT2/AQ mixture, the transmission was reduced further to 0.40 (green **Figure 7.4.1.2A**). To explain this change, **Figure 7.4.1.1B** shows that $QOT2^{2+}$ $1^1 B_u$ has a larger molar absorptivity ($3.4 \times 10^4\ M^{-1}\ cm^{-1}$), double that of neutral QOT2 TT state ($1.7 \times 104\ M^{-1}\ cm^{-1}$) at 880 nm (**Figure 7.6.3.11**). In contrast, $QOT2^+$ TD ($QOT2^+$ $1^2 B_g$) was predicted to be less likely to absorb the probe light. The reduction in transmission with AQ present is therefore consistent with 2ET through the formation of the $QOT2^{2+}$ $1^1 B_u$ state.

Transient absorption spectroscopy (TAS) was performed to provide evidence of 2ET beyond the fluorescence and transmission experiments. Within its available spectral window of 450−700 nm and the pump beam of 400 nm, TAS can provide signatures of the ET products in addition to the QOT2 ground state bleach (GSB) at 450−560 nm and ESA I at 560− 700 nm (**Figure 7.6.3.11**). The AQ ESAs are short-lived, and therefore do not contribute to these spectra at time scales longer than 1 ps. In addition to the QOT2 features, three new ESA bands arise when AQ was added to the mixture: ESA II at ∼488 nm, ESA III at ∼528 nm, and ESA IV at ∼569 nm (**Figure 7.4.1.2B**).

Table 7.4.1. Characteristic Bands in the Transient Absorption Spectra Depending on One- or Two-Electron Transfer (nm)

Bands	Wavelength[a]	1ET	2ET
GSB	450 – 560	QOT2 GSB	
ESA I	560 – 700	QOT2 ESA	
ESA II	~ 488	$QOT2^{+}$ 1^2B_g (498)	AQ^{2-} (470)
ESA III	~ 528	–	$QOT2^{2+}$ 1^1B_u (529)
ESA IV	~ 569	AQ^{-} (550)	–

The assignment of new long-lived signals was made using the simulated absorption peaks (**Figure 7.4.1.2B**) for QOT2 TT and its cations ($QOT2^{+}$ TD and $QOT2^{2+}$ DD) alongside the known signals for AQ anions[23] (**Table 7.4.1**). The occurrence of ESA II can be assigned to $QOT2^{+}$ 1^2 B_g and/or doubly reduced AQ, which are close to the observed absorption peak near 488 nm. According to our simulations, $QOT2^{2+}$ 1^1 B_u absorbs at 529 nm, which overlaps with ESA III. The last feature, ESA IV, is centered at 569 nm and assigned to the single ET product, AQ−, which is known to absorb at 550 nm. These results indicate the presence of mixture of species generated from 1ET and 2ET. TAS, therefore, supports the theoretical predictions of ET from QOT2 TT to AQ, and suggests that 2ET is feasible. Spectral differences between QOT2/AQ and its components revealed that signals from ET products appear in less than 3 ps, and live longer than 280 ps (**Figure 7.6.3.12**). Bands from ion−ion interactions are not detectable in the current transient window, because these likely exist only in the IR region.[25] Based on the fluorescence, transmission, and TAS data, the exciton and ET dynamics of QOT2/AQ are summarized in **Figure 7.4.1.3A**.

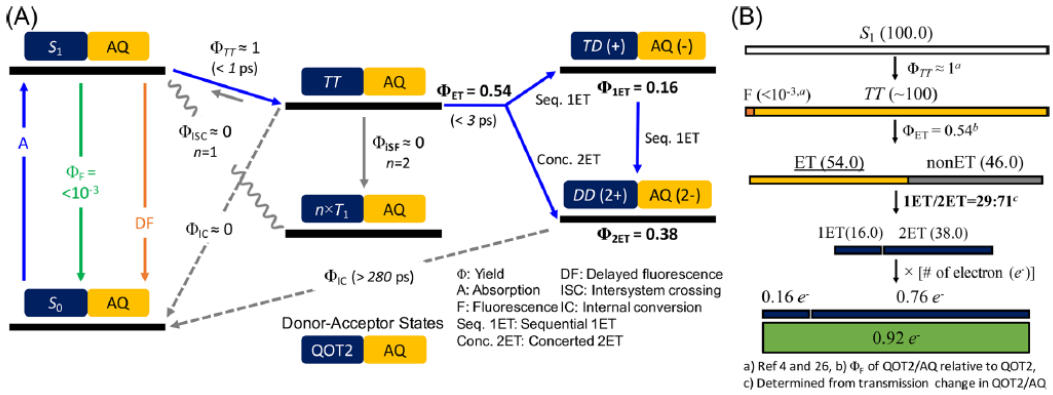

Figure 7.4.1.3. (A) Transmission profile of QOT2 and QOT2/AQ based on a probe of 880 nm after excitation at 440 nm by a pump. (B) Transient absorption spectrum of QOT2/AQ.

The relative 1ET/2ET contribution and total ET yield were estimated using the postulated mechanism in **Figure 7.4.1.3A** (see SI Section **Figure 7.6.3.10** for further discussion on plausible decay pathways). The similar early behavior of TAS decay observed in QOT2 and QOT2/AQ, small fluorescence quantum yield of QOT2 (<10^{-3})[26] and the subps QOT2 TT formation suggest the TT yield is nearly unity in QOT2/AQ.[4] The relative fluorescence yield of QOT2/AQ compared to QOT2 was measured to be 46%. Assuming S1 and TT equilibrium, this means that 54% of TT excitons proceed through a new channel, ET, opened by the AQ acceptor. The relative quantum yield of QOT2/AQ compared to QOT2 (46%), transmission change in QOT2/AQ (0.47 to 0.40) and the molar absorptivity of QOT2 TT and $QOT2^{2+}$ DD at 880 nm estimated by quantum simulations ($1.7 \times 10^4\ M^{-1}\ cm^{-1}$ and $3.4 \times 10^4\ M^{-1}\ cm^{-1}$) can be combined to estimate the ratio of 1ET:2ET product as 29:71 (full calculation in SI **Figure 7.6.3.11**). Using this ratio of 1ET:2ET product, the overall ET yield is estimated to be 0.92 (including error: 0.83−1.07) electrons per absorbed photon in QOT2/AQ (**Figure 7.4.1.3B**).

7.5 Conclusions

In summary, this study presents a theoretically designed molecular system to harvest multiple electrons from strongly correlated TT states on a single chromophore. Instrumental to this development were the characterization of QOT2's TT state[2,4] and screening of 2e- redox acceptors,[20] which paved the way for the present study. The observed ET yield of 83 to 107% is quite promising for an initial test case involving an unfunctionalized anthraquinone acceptor. Nonetheless, the majority of these ETs occur through a 2e− mechanism (71% of total ET), which is unique among iSF chromophores. Further optimization and computational screening of acceptors coupled to the QOT2 iSF donor could increase the ET yield further. Future studies will examine the mechanism of 2ET in more detail, provide additional evidence for direct charge carrier extraction from the TT state, and provide useful, robust guidelines for designing molecular species for multi-ET. In conclusion, tightly coupled TT states may be a strong design principle to overcome the Shockley-Queisser limit and create highly efficient, easily processable solar cells.[27]

References

(1) Smith, M. B.; Michl, J. Chem. Rev. 2010, 110 (11), 6891.

(2) Varnavski, O.; Abeyasinghe, N.; Arago, J.; Serrano-Pe´ rez, J. J.;´ Ortí, E.; Lopez Navarrete, J. T.; Takimiya, K.; Casanova, D.; Casado,´ J.; Goodson, T. J. Phys. Chem. Lett. 2015, 6 (8), 1375.

(3) Feng, X.; Luzanov, A. V.; Krylov, A. I. J. Phys. Chem. Lett. 2013, 4 (22), 3845.

(4) Chien, A. D.; Molina, A. R.; Abeyasinghe, N.; Varnavski, O. P.; Goodson, T.; Zimmerman, P. M. J. Phys. Chem. C 2015, 119 (51), 28258.

(5) Weiss, L. R.; Bayliss, S. L.; Kraffert, F.; Thorley, K. J.; Anthony, J. E.; Bittl, R.; Friend, R. H.; Rao, A.; Greenham, N. C.; Behrends, J. Nat. Phys. 2017, 13 (2), 176.

(6) Yong, C. K.; Musser, A. J.; Bayliss, S. L.; Lukman, S.; Tamura, H.; Bubnova, O.; Hallani, R. K.; Meneau, A.; Resel, R.; Maruyama, M.; Hotta, S.; Herz, L. M.; Beljonne, D.; Anthony, J. E.; Clark, J.; Sirringhaus, H. Nat. Commun. 2017, 8 (May), 15953.

(7) Grieco, C.; Kennehan, E. R.; Kim, H.; Pensack, R. D.; Brigeman, A. N.; Rimshaw, A.; Payne, M. M.; Anthony, J. E.; Giebink, N. C.; Scholes, G. D.; Asbury, J. B. J. Phys. Chem. C 2018, 122 (4), 2012.

(8) Burdett, J. J.; Bardeen, C. J. J. Am. Chem. Soc. 2012, 134 (20), 8597. (9)

Zimmerman, P. M.; Zhang, Z.; Musgrave, C. B. Nat. Chem. 2010, 2 (8), 648.

(10) Stern, H. L.; Musser, A. J.; Gelinas, S.; Parkinson, P.; Herz, L. M.; Bruzek, M. J.; Anthony, J.; Friend, R. H.; Walker, B. J. Proc. Natl. Acad. Sci. U. S. A. 2015, 112 (25), 7656. (11) Chien, A. D.; Zimmerman, P. M. J. Chem. Phys. 2017, 146 (1), 014103.

(12) Khan, S.; Mazumdar, S. J. Phys. Chem. Lett. 2017, 8 (23), 5943.

(13) Grieco, C.; Kennehan, E. R.; Rimshaw, A.; Payne, M. M.; Anthony, J. E.; Asbury, J. B. J. Phys. Chem. Lett. 2017, 8 (23), 5700.

(14) Kumarasamy, E.; Sanders, S. N.; Tayebjee, M. J. Y.; Asadpoordarvish, A.; Hele, T. J. H.; Fuemmeler, E. G.; Pun, A. B.; Yablon, L. M.; Low, J. Z.; Paley, D. W.; Dean, J. C.; Choi, B.; Scholes, G. D.; Steigerwald, M. L.; Ananth, N.; McCamey, D. R.; Sfeir, M. Y.; Campos, L. M. J. Am. Chem. Soc. 2017, 139 (36), 12488.

(15) Takahashi, T.; Matsuoka, K.; Takimiya, K.; Otsubo, T.; Aso, Y. J. Am. Chem. Soc. 2005, 127 (25), 8928.

(16) Chan, W.-L.; Ligges, M.; Jailaubekov, A.; Kaake, L.; Miaja-Avila, L.; Zhu, X.-Y. Science (Washington, DC, U. S.) 2011, 334 (6062), 1541.

(17) Congreve, D. N.; Lee, J.; Thompson, N. J.; Hontz, E.; Yost, S. R.; Reusswig, P. D.; Bahlke, M. E.; Reineke, S.; Van Voorhis, T.; Baldo, M. A. Science (Washington, DC, U. S.) 2013, 340 (6130), 334.

(18) Pun, A. B.; Sanders, S. N.; Kumarasamy, E.; Sfeir, M. Y.; Congreve, D. N.; Campos, L. M. Adv. Mater. 2017, 29 (41), 1701416.

(19) Huskinson, B.; Marshak, M. P.; Suh, C.; Er, S.; Gerhardt, M. R.; Galvin, C. J.; Chen, X.; Aspuru-Guzik, A.; Gordon, R. G.; Aziz, M. J. Nature 2014, 505 (7482), 195.

(20) Kim, H.; Goodson, T.; Zimmerman, P. M. J. Phys. Chem. C 2016, 120 (39), 22235.

(21) Kuss-Petermann, M.; Orazietti, M.; Neuburger, M.; Hamm, P.; Wenger, O. S. J. Am. Chem. Soc. 2017, 139 (14), 5225.

(22) Kaduk, B.; Kowalczyk, T.; Van Voorhis, T. Chem. Rev. 2012, 112 (1), 321.

(23) Babaei, A.; Connor, P. A.; McQuillan, A. J.; Umapathy, S. J. Chem. Educ. 1997, 74 (10), 1200.

(24) Lee, S.; Hwang, D.; Jung, S. Il; Kim, D. J. Phys. Chem. Lett. 2017, 8 (4), 884.

(25) Dereka, B.; Koch, M.; Vauthey, E. Acc. Chem. Res. 2017, 50 (2), 426.

(26) Wang, Z.; Kobayashi, T. New J. Phys. 2008, 10 (12), 123021.

(27) Lee, J.; Jadhav, P.; Reusswig, P. D.; Yost, S. R.; Thompson, N. J.; Congreve, D. N.; Hontz, E.; Van Voorhis, T.; Baldo, M. A. Acc. Chem. Res. 2013, 46 (6), 1300.

7.6 Supporting Information

7.6.1 QOT2 Structure

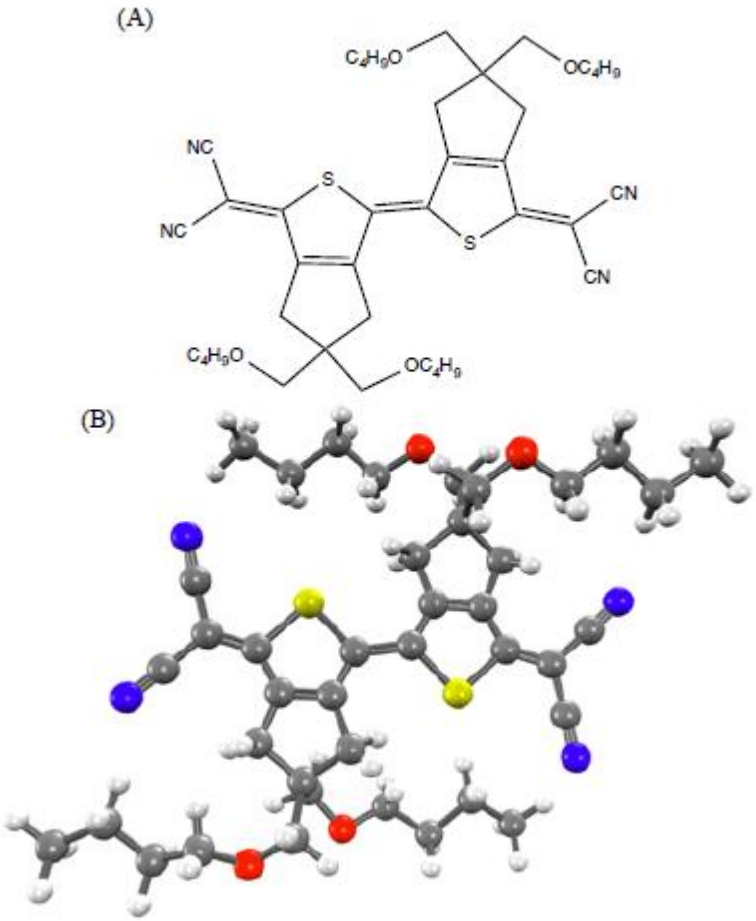

Figure 7.6.1.1. (A) Chemical structure of QOT2 chromophore (A) in the skeletal formula, and (B) in balland- stick model. Color scheme: hydrogen atom, white; carbon atom, black; nitrogen atom, blue; oxygen atom, red; sulfur atom, yellow.

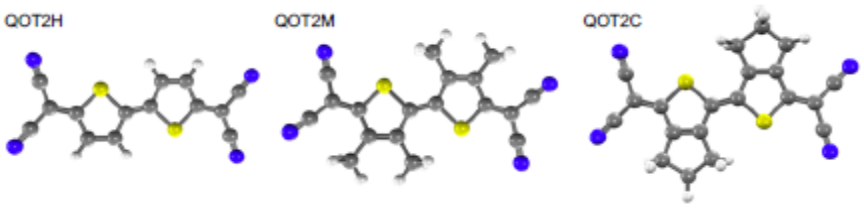

Figure 7.6.1.2. Three model structure of QOT2 chromophore, QOT2H, QOT2M, and QOT2C.

The structure of QOT2 chromophore and model structure with the substituents removed is listed in **Figure 7.6.1**.1 It is expected that removal of solubilizing groups has a minor effect on the accuracy of quantum chemical absorption energy simulation since most of low-lying excited states involve pi transitions within the backbone. In order to confirm this assumption, we tested three model structures, QOT2H, QOT2M, and QOT2C which replace all solubilizing groups of the QOT2 chromophore with hydrogen atoms, methyl groups, and 5-carbon rings, respectively, in the increasing order of increasing similarity to the QOT2 chromophore structure. All three models are predicted to remain in planar structures, and there are no noticeable geometric changes. Excitation energy calculated using !B97X-D/6- S3 QOT2H QOT2M QOT2C **Figure 7.6.1.2**: Three model structure of QOT2 chromophore, QOT2H, QOT2M, and QOT2C. 31G* is 2.73 eV, 2.73 eV, 2.72 eV for QOT2H, QOT2M, and QOT2C, respectively. In addition to two publications from our groups,[1,2] Marian et al. also employed the QOT2H model structures to simulate the absorption energy and excited state dynamics, and the results are well correlated with available experimental findings.[3] These results suggested that electronic transition of QOT2 is not affected by the solubilizing groups, and justified the use of QOT2H model, the simplest model structure replacing solubilizing groups with H atoms, in high-level ab initio calculations without the significant loss of accuracy.

7.6.2 Computational Details.

Constrained density functional theory (CDFT) is the approach which can diabatize electronic states by imposing the charge and spin constraints on specific regions of molecules.[4] B3LYP functional with empirical dispersion correction of Grimme5 (B3LYP-D) and 6-31G* is used to optimize the QOT2/AQ structures. All CDFT calculations are performed using Q-Chem version 4.0.[5].The scaling factor (s6) of 1.05 for dispersion energy calculation is used as recommended for B3LYP-D. Single point energy is refined by M06-HF-D functional6 with s6 value of 1.00. M06-HF incorporates full Hartree-Fock (HF) exchange for all interelectronic distances to give improved asymptotic Coulomb interaction, and this functional is known to perform well for charge-transfer excitation (mean absolute error less than 2.1 kcal/mol).[6,7] Cancellation of errors, however, frequently occurs in barrier height estimates, giving more credential in the CDFT energetics. Basis sets were increased to 6-311G*. The solvent (acetonitrile) medium effect was described using a polarizable continuum model with dielectric constant of 35.69.Electronic coupling (Hab) was estimated using CDFT-configuration interaction (CDFT-CI).[8] Since CDFT-CI calculations were not feasible for the full QOT2/AQ geometries, and we replaced the solubilizing groups by hydrogen atoms. The same level of theory used in the single point energy calculations was applied. The electronic coupling at the smallest energy gap was approximated as the average of electronic coupling of two local minimum structures connecting ET potential energy curve.

Table 7.6.2.1. Characterization of Diabatic States of the QOT2/AQ Complex Investigated in This Study Using Charge and Spin

Table S1: Characterization of Diabatic States of the QOT2/AQ Complex Investigated in This Study Using Charge and Spin

		QOT2 Half		QOT2 Another Half		Whole QOT2		AQ	
		Charge	Spin	Charge	Spin	Charge	Spin	Charge	Spin
Before ET	QOT2 *TT*/AQ (GS)	0	↑↑	0	↓↓	0	↑↑,↓↓	0	0
	QOT2 *TT*/AQ (T_1)	0	↑↑	0	↓↓	0	↑↑,↓↓	0	↑↑
After 1 ET	$QOT2^{+}$ *TD*/AQ^{-} (GS)	0	↑↑	+1	↓	+1	↑↑,↓/↓↓,↑	-1	↓/↑
	$QOT2^{+}$ (GS)/AQ^{-} (GS)					+1	↑	-1	↓
After 2 ET	$QOT2^{2+}$ *DD*/AQ^{2-} (GS)	+1	↑	+1	↓	+2	↑,↓	-2	0
	$QOT2^{2+}$ (GS)/AQ^{2-} (GS)					+2	0	-2	0

Absorption spectra of QOT2 TT, QOT2+ TD, and QOT22+ DD (QOT2 21Ag, QOT2+ 12Bg, and QOT22+11Bu) are predicted to analyze the experimental results. C2h symmetry is imposed on the QOT2 molecule, and active space consisting of 10 electrons in 8 π orbitals (10e,8o) is selected. Singly and doubly ionized QOT2 TT is described using the active space of (9e,8o) and (8e,8o), respectively, without any changes in the molecular orbitals. All the geometries are optimized using XMS-CASPT2 method6 and 6-31G* basis sets with level shift of 0.20. XMS-CASPT2 has been known for better description of energetics than plane CASPT2 near conical intersection.[7] Also,the XMS-CASPT2 calculation has proven its ability to predict the absorption of neutral QOT2 TT state successfully.8 Refined single point energy has been obtained using valence triple-zeta plus polarization basis sets, TZVPP. In addition to level shift, IPEA shift of 0.10 has been applied in single point energy calculations to avoid intruder states.[9] All XMS-CASPT2 calculations are carried out using MOLPRO version 2012.1.[10]

Transition dipole moments (TDM) is necessary to evaluate oscillator strength, but XMS-CASPT2 TDM is not available yet in MOLPRO version 2012.1. CASSCF TDM with relatively small active space gives inconsistent results due to the lack of dynamic correlation.[8] As an alternative approach, Spin-Flip RAS TDM which has larger amount of dynamic correlation than 222 CASSCF is implemented by Chien et al. in a development version of Q-Chem 4.0. All TDM

value are this work is calculated using Spin-Flip RAS with 6-31G* based on the XMS-CASPT2 geometries.

7.6.3 Experimental Details

Chemical Species: AQ was commercially available and used without further purification. QOT2 was epared by Juan Casado. (Department of Chemistry, University of Malaga, Spain) Acetonitrile as selected as solvent owing to high solubility of QOT2/AQ mixture. All experiments were performed in acetonitrile.

Steady-State UV-Vis Absorption: The concentration of QOT2 was fixed to 0.05 mM for both pure and mixture cases. The pure AQ absorption spectrum was easured at [AQ]=0.15 mM. The concentration dependence was examined by increasing [AQ] in QOT2/AQ mixture from 0.05 mM, 0.10mMto 0.15 mM, while [QOT2] was fixed to 0.05 mM. (The ratio of QOT2:AQ is 1:1, 1:2, and 1:3, respectively). The absorption spectra of QOT2/AQ mixture were measured at these three concentrations UV-Vis absorption spectrum were recorded with an Agilent Technologies 8453 spectrophotometer.

Steady-State Photoluminescence: The concentration of QOT2 was fixed to 0.05 mM for both pure and mixture case. For AQ, the concentration of 0.15 mM was used to obtain pure AQ and QOT2/AQ mixture photoluminescence spectra. Photoluminescence emission were measured using a Fluomax-2 fluorometer.

Time-Resolved Fluorescence Decay: Femtosecond upconversion spectroscopy is employed to resolve temporally the polarized fluorescence. The optical setup for our upconversion experiments is the same setup that was reported in the previous works. The sample solution was exposed to a frequency-doubled light from a mode-locked Ti-sapphire laser (Tsunami, Spectra Physics). This setup produces pulses of light S9 with wavelength of 400 nm. The sample was

placed in the rotating cuvette to avoid any possible degradation and accumulation effect. The horizontally polarized fluorescence emitted from the sample was upconverted in a nonlinear crystal of BBO using a pump beam at about 800 nm hat was first passed through a variable delay line. This system acts as an optical gate and enables the fluorescence to be resolved temporally with a time resolution of _ 200 fs. Spectral resolution was achieved by dispersing the upconverted light in a monochromator and detecting it by using a photo multiplier tube (Hamamatsu R1527P). The excitation average power was kept at a level below 0.5 mW. For the concentration, [QOT2]=0.025 mM and [AQ]=0.075 mM were used to obtain time-resolved fluorescence decay of each pure sample. The same concentration was used to obtain mixture's spectrum.

Transient Absorption Spectroscopy: The output of an amplified laser beam was split to generate pump and probe beam pulses with a beam splitter (85 % and 15 %). The pump beam was produced by an optical parametric amplifier (OPA-800c). The pump beam used in this study was obtained from either the second- or fourth harmonic generation of the signal beam and this was focused on the sample cuvette. The probe beam was delayed with a computer controlled motion controller and then focused on to a 2 mm sapphire plate to generate a white light continuum. The white light was then overlapped with the pump beam in a 1.5 mm quartz cuvette containing the sample and the change in absorbance for the signal was collected by a CCD detector (Ocean Optics). Data acquisition was controlled by software from Ultrafast System Inc. Typical power of probe beam was < 0.1 _J, while the pump beam ranged from 0.1 to 0.4 _J per pulse. The pulse duration was obtained by fitting the solvent response, which was determined as _ 130 fs. All chemical samples are excited by a pump beam with a wavelength of 400 nm. The sample was stirred with a rotating magnetic stirrer. For the concentration, [QOT2]=0.05 mM and [AQ]=0.15

mM was used to obtain transient absorption spectra of each pure sample. The same concentration was used to obtain mixture's spectrum.

Transmission Profile: For transmission profile, we have investigated the excited state absorption of QOT2 at 880 nm (1.41 eV) with a femtosecond pulsed at 440 nm (2.82 eV). The light with wavelength of 880 nm plays a role of probe beam, roduced by tunable Mai Tai laser system (Spectra Physics) giving 130 fs pulses with a repetition rate of 80 MHz. Second harmonic of the probe beam with wavelength of 440 nm has been produced in BBO crystal and this is a pump laser. The selected wavelength region is reasonable since there is negligible steady-state absorption. A variable neutral ensity filter is placed to cut down the excitation power. The position of focusing lens is adjusted to place focusing point on the sample. Blank AN solvent gives a reference line. A calibrated photodiode was used to measure the incident power. The transmitted power has been measured with a wide aperture power meter which is free of any thermal lensing effect. For the concentration, [QOT2]=0.025 mM and [AQ]=0.075 mM were used to obtain time-resolved fluorescence decay of each pure sample. The same concentration was used to obtain mixture's spectrum.

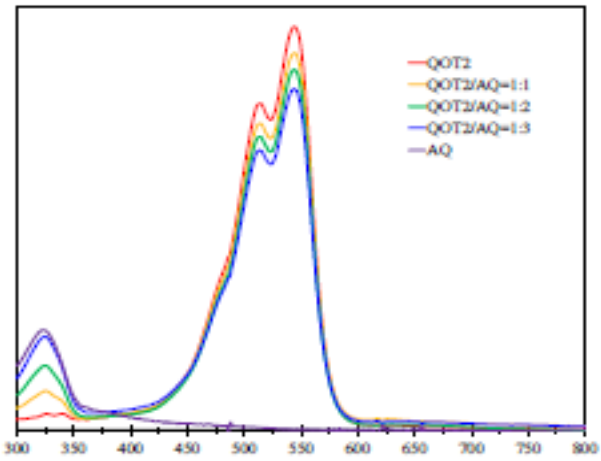

Figure 7.6.3.1. Normalized UV-Vis absorption of QOT2, AQ, and three different concentration ratio of QOT2/AQ in AN. Each spectrum was normalized with the reference to the largest absorption intensity of QOT2. (QOT2 absorption at 544 nm)

Quantum chemical simulations show that QOT2 and AQ can form a complex in the ground state. Using a dispersion-corrected density functional (M06-HF-D/6-311G*/PCM(acetonitrile) /B3LYP-D/6-31G*), the significant binding energy (52.1 kcal/mol) strongly suggests the hermodynamic plausibility of such a state, where the large quadrupole moments and -stacking permit such an interaction. In order to confirm the presence of QOT2/AQ aggregation in the ground state, the concentration dependency of absorption intensity was examined by increasing [AQ] in QOT2/AQ mixture from 0.05 mM, 0.10 mM to 0.15 mM, while the concentration of QOT2 is fixed to 0.05 mM. (The ratio of QOT2:AQ correspond to 1:1, 1:2, and 1:3,respectively). The absorption spectra of QOT2/AQ mixture were measured at these three concentration ratios. There is clear decrease in the main absorption intensity of QOT2 (510 – 540 nm) as the concentration of AQ increases. (From red curve to blue curve) This result suggests that QOT2 and AQ already form a donor-acceptor _-complex in the ground state.

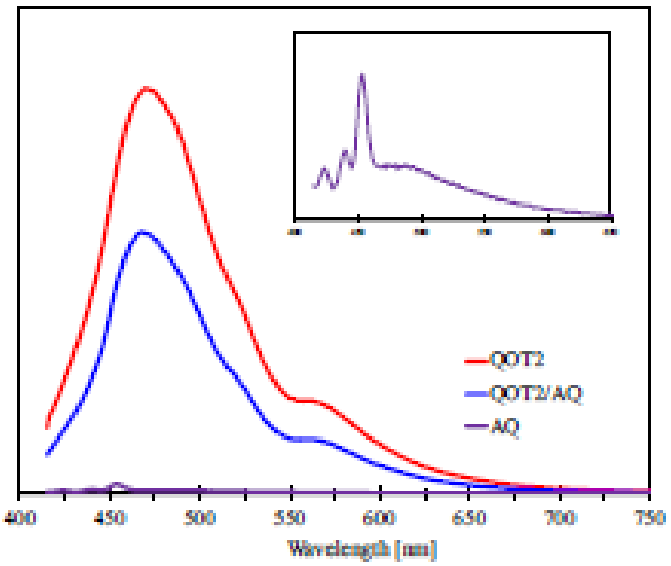

Figure 7.6.3.2. Photoluminescence emission of QOT2, AQ, and QOT2/AQ (1:3) in AN. All samples are excited at 400 nm. Inset: Photoluminescence emission of AQ.

The emission peak of AQ is assigned by comparing with the previous result. The mission at the shortest wavelength (430 nm) was attributed to thermally activated delayed fluorescence. Other two peaks were assigned to phosphorescence. The contribution of triplet AQ acceptor is discussed in bellow.

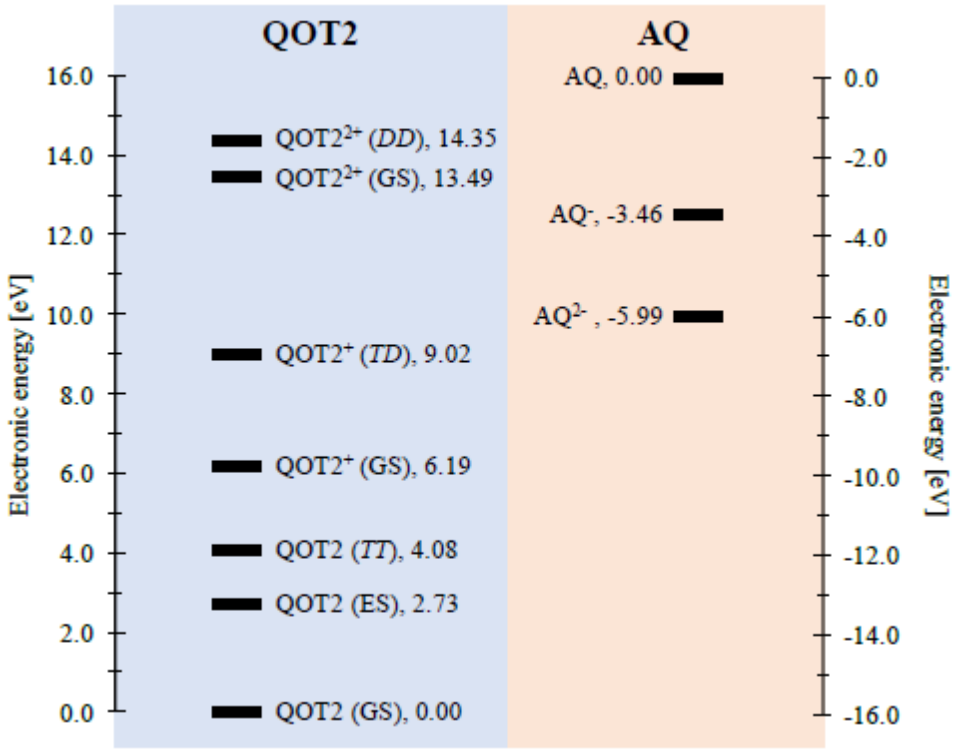

Figure 7.6.3.3. Relative energy levels of QOT2, AQ, and their relevant ET products.

Level of Theory

for GS:

!B97X-D/G3Large/PCM(AN)//!B97X-D/6-31G*

for QOT2 (TT), QOT2+ (TD) and QOT22+ (DD):

C(!B97X-D)/G3Large/PCM(AN)//C(!B97X-D)/6-31G*

C(!B97X-D): Constrained !B97X-D

for ES:

TD-(!B97X-D)/G3Large/PCM(AN)//!B97X-D/6-31G*

DIP for ground state QOT2

DIPQOT2 GS = EQOT22+ (GS) □ EQOT2 (GS) = 14.35 eV

DIPQOT2 TT = EQOT22+ (DD) □ EQOT2 (TT) = 10.27 eV

DEA for ground state AQ

DEAAQ = EAQ □ EAQ2- = □5.99 eV

Position of Localized Charge

The position of localized charge was determined as the center of mass for the subunit of each molecule.

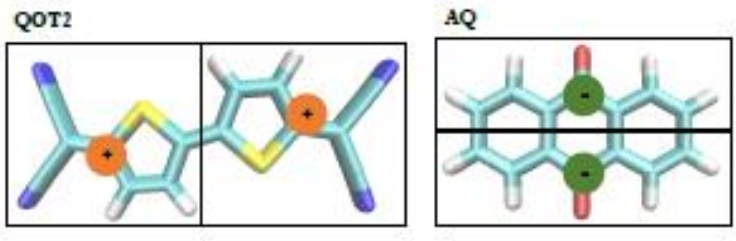

Figure 7.6.3.4. Relative energy levels of QOT2, AQ, and their relevant ET products.

Figure 7.6.3.5. Position of localized charges on the ground state QOT2/AQ complex.

Table 7.6.3.1. Coulomb Interaction between Four Point Charges in QOT2/AQ Complex

Index[a]	Distance (Å)	Coulomb energy (eV)
A-B	6.70	+2.15
A-C	4.20	-3.43
A-D	4.54	-3.17
B-C	5.76	-2.50
B-D	4.74	-3.04
C-D	2.87	+5.02
Sum		-4.97

Thermodynamic Driving Force of 2ET

ΔE =$\mathrm{DIP_{QOT2}}$ + $\mathrm{DEA_{AQ}}$ + Coulomb Interaction

for QOT2 GS: $\Delta E = 14.35 - 5.99 - 4.97 = \mathbf{3.39}$ eV

for QOT2 *TT*: $\Delta E = 10.27 - 5.99 - 4.97 = \mathbf{-0.69}$ eV

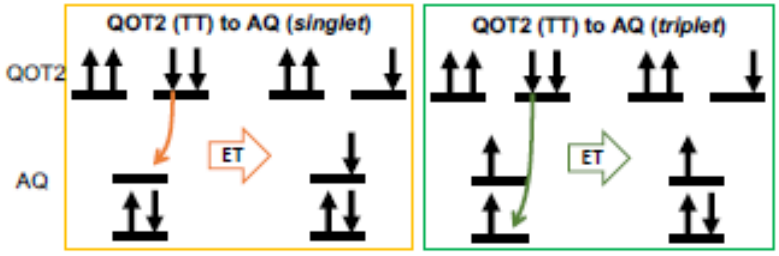

Figure 7.6.3.6. Schematic representation of electron transfer from QOT2 TT to AQ (singlet) and AQ

The observation of triplet AQ formation led us to think the contribution of triplet AQ acceptor. The AQ acceptor in singlet excited state is not considered since their population is negligible compared to T1 state. (The excited state population ratio of S1 over T1 is 10^{-4}.)

The triplet AQ acceptor can provide the larger driving force, since there is vacancy in the energetically lower molecular orbital compared to AQ neutral. The CDFT energetics indicates that

there is no barrier for the sequential 1ETs to triplet AQ. The contribution of this pathway depends on the number of AQ in the T1 state, which is determined by the absorption wavelength. (<5 % and <3 % of AQ S0 would be in T1 by the pump laser with the wavelength of 400 nm and 440 nm, respectively) Even though triplet AQ population is not significant, the thermodynamically unfavorable sequential 1ET pathway from QOT2 TT and AQ singlet ground state (_E(1ET)=19.8 kcal/mol) becomes thermodynamically favorable state due to the formation of AQ triplet (_E(1ET)=-44.3 kcal/mol).

However, triplet AQ state does not interfere the analysis of our spectroscopic experiments. AQ Triplet absorption in acetonitrile was measured at 380 and 660 nm, which are not placed in the transient window nor near the transmission probe. As expected, triplet AQ state does not exhibit any absorption near 880 nm after excited at 440 nm in the transmission experiment. Therefore, the transmission results still can be analyzed based on QOT2 TT and its oxidized forms. (TD and DD states) For the transient absorption spectroscopy, the pure AQ solution excited at 400 nm exhibited excited state absorption near 450 – 560 nm at 0.2 ps, but they disappear very quickly.

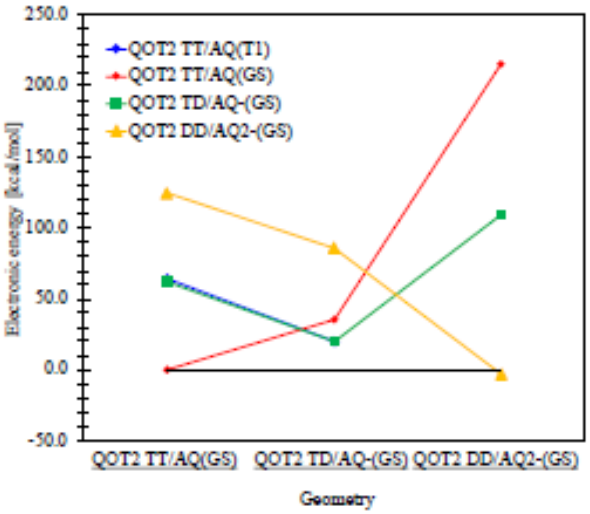

Figure 7.6.3.7. Electronic energies of three states at three local minimum structures.

Table 7.6.3.2. Electronic Coupling (Hab), Reorganization Energy, and ET Barrier (Ey) Estimated from CDFT and CDFT-CI simulations[a].

	H_{ab}	λ	$\Delta E^{\dagger b}$	$\Delta E^{\dagger c}$
Concerted 2ET	9.3	127.5	30.3	21.1
The first ET in the sequential 1ETs	5.0	41.9	22.7	17.7
The second ET in the sequential 1ETs	15.2	89.0	12.3	0 (-2.9)

a) All energies value are reported in kcal/mol.
b) ET barrier estimated with $\Delta E^{\dagger} = (\lambda + \Delta E^{\circ})^2/4\lambda$
c) ET barrier estimated with $\Delta E^{\dagger} = (\lambda + \Delta E^{\circ})^2/4\lambda - |H_{ab}|$

The predicted ET barrier is 17.7 kcal/mol for the first ET in the sequential 1ETs, and 21.1 kcal/mol for the concerted 2ET. There would be no barrier for the second ET in the sequential 1ETs, which means once the 1st 1ET in the sequential 1ETs pathway occurs, the 2nd 1ET follows spontaneously to form thermodynamically stable 2ET product. One thing to notice is the predicted ET barriers for the first ET in the sequential 1ETs (17.7 kcal/mol) is lower than the product energy, which might be the result of over correction by neglecting the solvent effect.

Table 7.6.3.3. Population of QOT2 TT, and Ionized QOT2 TT.

Table S4: Population of QOT2 *TT*, and Ionized QOT2 *TT*.

	QOT2 *TT*[a]	$QOT2^{+}$ *TD*[b]	$QOT2^{2+}$ *DD*[b]
Symmetry	2^1A_g	1^2B_g	1^1B_u
$8a_u$	0.33	0.10	0.15
$7b_g$	1.16	0.64	0.24
$7a_u$	0.97	0.89	0.96
$6b_g$	1.60	1.49	1.11

a) The geometry is optimized using XMS-CASPT2/6-31G* with the active space of (10e,8o).
b) The same level of theory used for QOT2 *TT* is applied with different active spaces, (9e,8o) and (8e,8o) for $QOT2^{+}$ *TD* and $QOT2^{2+}$ *DD* , respectively.

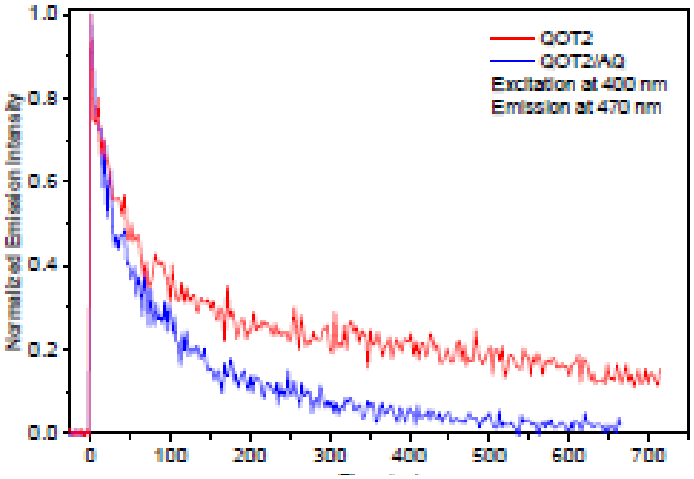

Figure 7.6.3.8. Time-resolved fluorescence decay measurement of QOT2 and QOT2/AQ (triplet).

Table 7.6.3.4. Lifetime of Excited Singlet State of QOT2 and QOT2/AQ Using Time-Resolved Fluorescence Decay.[a]

	τ_1[b]	τ_2[b]
QOT2/AQ	27.3	181.2
QOT2	41.5	785.9
τ_n ratio[c]	0.66	0.23

a) Normalized fluorescence intensity is fitted to $y = A_1e^{-t/\tau_1} + A_2e^{-t/\tau_2}$

b) τ_1 and τ_2 are the lifetime of short and long component, respectively.

c) τ_n ratio $= \dfrac{\tau_n \text{ of QOT2/AQ}}{\tau_n \text{ of QOT2}}$ ($n = 1$ or 2)

Table 7.6.3.5. Lifetime of QOT2 and QOT2/AQ from Transient Absorption Spectroscopy.[a,b]

	QOT2		QOT2/AQ	
Wavelength	τ_1	τ_2	τ_1	τ_2
488	2.04	4.66	2.03	42.01
529	2.04	4.66	1.87	> 2000
569	2.10	4.92	1.98	150.00

a) Transient absorption intensity is fitted to $y = A_1e^{-t/\tau_1} + A_2e^{-t/\tau_2}$

b) τ_1 and τ_2 are the lifetime of short and long component, respectively.

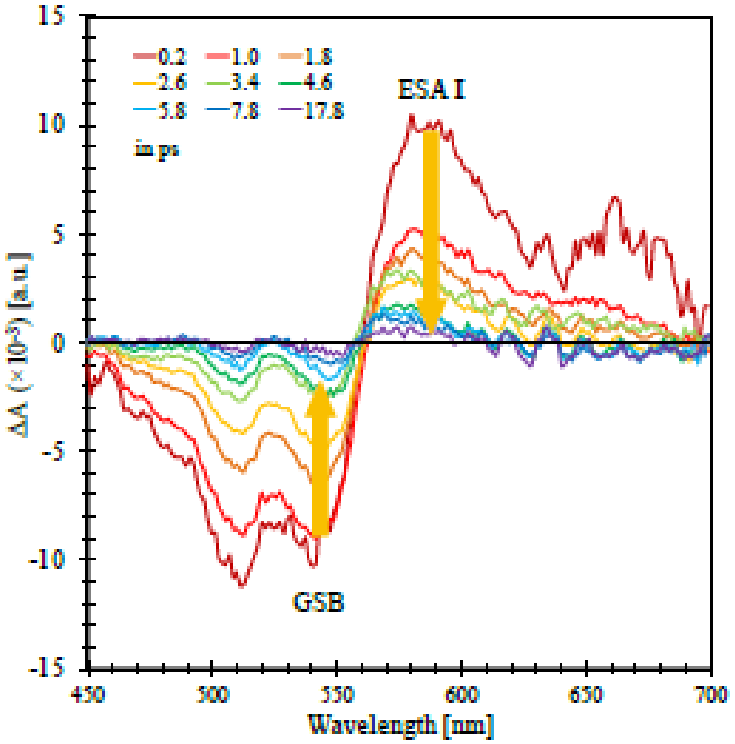

Figure 7.6.3.9. Transient absorption spectrum of QOT2 at selected decaying time as the function of probe wavelength. The characteristic bands of QOT2 (GSB and ESA I) are marked with yellow arrows. The same experimental setup and condition to obtain the spectrum of QOT2/AQ mixture is used.

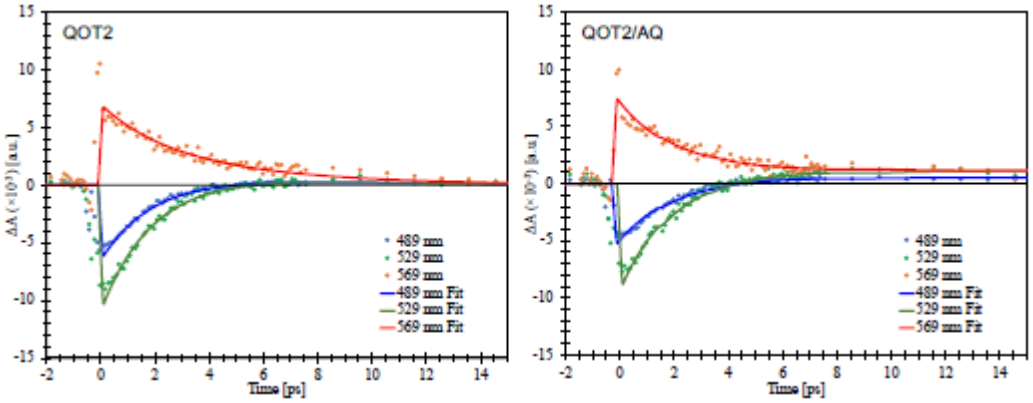

Figure 7.6.3.10. Evolution of transient absorption intensities of QOT2 (left) and QOT2/AQ (right) at three wavelength (489, 529, and 569 nm). Solid line represents the biexponential fits.

The kinetics of transient absorption spectra were established to analyze the lifetime of QOT2 and QOT2/AQ decay. The transient absorption spectra of both samples were well described with a biexponential fit. The short lifetimes, which govern the very initial stage of singlet fission on QOT2 molecule were evaluated at three wavelengths, 488 nm, 529 nm, and 569 nm, and compared between QOT2 and QOT2/AQ. For pure QOT2, the short lifetimes of 2.04 ps, 2.04 ps, and 2.10 ps were obtained at 488 nm, 529 nm, and 569 nm. These numbers remain unchanged in QOT2/AQ mixture giving 2.03 ps, 1.87 ps, and 1.98 ps at 488 nm, 529 nm, and 569 nm. This observation suggests that the ultrafast formation (<1 ps) of QOT2 TT state is unperturbed by the presence of AQ molecule, and the possibility of ET from the excited singlet state is less likely.

Furthermore, we checked the absorption spectra of ET product from the excited singlet state, $QOT2^{+}$ and $QOT2^{2+}$ in the ground state. Time-dependent density functional theory (TD-DFT) were performed to estimate the absorption spectrum of $QOT2^{+}$ and $QOT2^{2+}$ in the ground state. (!B97X-D/6-31G*) The maximum absorption wavelength was predicted to be 689 nm and 427 nm for $QOT2^{+}$ and $QOT2^{2+,}$ respectively, which are much higher energy than the observed

TT state absorption at 880 nm. The ET at the excited singlet state cannot explain the absorption at 880 nm. Transient spectrum of AQ featured excited state absorption near 450–560 nm in the very early stage (0.2 ps), and it disappears very quickly. After 1.0 ps, there are no signals observed.

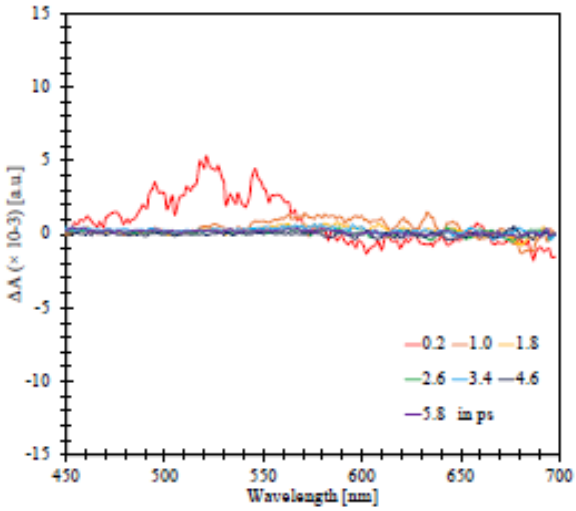

Figure 7.6.3.11. Transient absorption spectrum of AQ at selected decaying time as the function of probe wavelength. The same experimental setup and condition to obtain the spectrum of QOT2/AQ mixture is used.

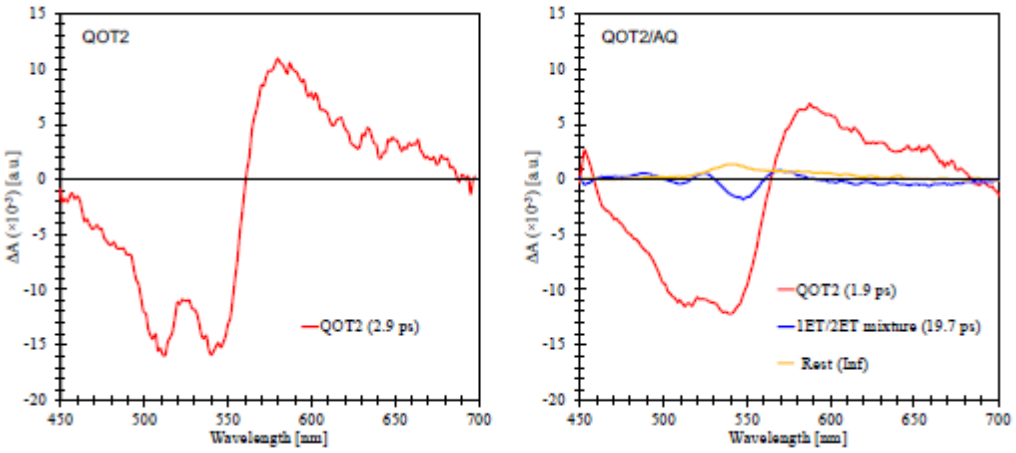

Figure 7.6.3.12. Species-associated spectra obtained from a global analysis of the transient absorption spectra of QOT2 and QOT2/AQ, respectively.

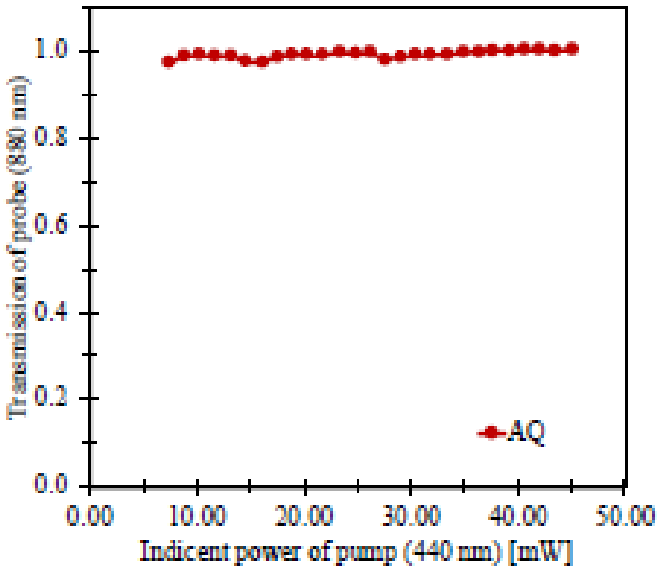

Figure 7.6.3.13. Transmission profile of pure anthraquinone (AQ, red line with filled circles) for the probe light of 880 nm as the function of the pump power at 440 nm.

Table 7.6.3.6. Assignment of ESA II, III, and IV with the Position of Peak and Oscillator Strength[a]

Bands	Wavelength [nm]	1ET	2ET
ESA II	~ 488	$QOT2^{+}$ $1^{2}B_{g}$ (498 nm, 0.29)	AQ^{2-} (470 nm, 0.36)
ESA III	~ 528	–	$QOT2^{2+}$ $1^{1}B_{u}$ (529 nm, 0.15)
ESA IV	~ 569	AQ^{-} (550 nm, 0.19)	–

a) The wavelength of corresponding transition and predicted oscillator strength are given in the parenthesis.

We have used time-dependent density functional theory (TD-DFT) simulation, PBE0/6-311++G**/PCM to obtain oscillator strength of reduced AQs (AQ□ and AQ2□). Experimental absorption peaks of reduced AQs are given together. The chemical species responsible for specific ESA and estimated oscillator strength are listed below. XMS-CASPT2 and Spin-Flip RAS results for QOT2+ TD and QOT22+ DD are also included.

References

(1) Chien, A. D.; Molina, A. R.; Abeyasinghe, N.; Varnavski, O. P.; Goodson, T.; Zimmerman, P. M. J. Phys. Chem. C 2015, 119, 28258–28268.

(2) Varnavski, O.; Abeyasinghe, N.; Arag´o, J.; Serrano-P´erez, J. J.; Ort´ı, E.; L´opez Navarrete, J. T.; Takimiya, K.; Casanova, D.; Casado, J.; Goodson, T. J. Phys. Chem. Lett. 2015, 6,1375–1384.

(3) Elfers, N.; Lyskov, I.; Spiegel, J. D.; Marian, C. M. J. Phys. Chem. C 2016, 120, 13901–13910.

(4) Kaduk, B.; Tsuchimochi, T.; Van Voorhis, T. J. Chem. Phys. 2014, 140, 18A503.

(5) Grimme, S. J. Comput. Chem. 2006, 27, 1787–1799.

(6) Zhao, Y.; Truhlar, D. G. J. Phys. Chem. A 2006, 110, 13126–13130.

(7) Zhao, Y.; Truhlar, D. G. Acc. Chem. Res. 2008, 41, 157–167.

(8) Wu, Q.; Cheng, C.-L.; Van Voorhis, T. J. Chem. Phys. 2007, 127, 164119.

(9) Newton, M. D. Chemical Reviews 1991, 91, 767–792.

(10) Shao, Y. et al. Mol. Phys. 2015, 113, 184–215.

Chapter 8

Overall Summary and Future Directions

8.1 Overall Summary

Developing efficient artificial light is an essential part of our civilization, and improvements towards more ecofriendly lightning sources are urgently required. Using organic light emitting diodes (OLEDs) represent an attractive way to address current issues, as organic materials can be used in ways that cannot be used by traditional fluorescent tubes, namely liquid crystal displays (LCD). Nowadays, multiple companies have commercially available displays based on OLEDs technologies, but their efficiencies are ways away from outcompeting the LCD leading technologies. Some of the companies involved in the OLEDs technologies are Philips, LG, Konica Minolta, among others.

In OLEDs, charges are injected from the electrodes to electrically excite the light emitting materials.[1–6] Since the spin-nature of the injected charges (electrons and holes) are uncorrelated, spin-statistic dictates that the nature of the excited state created will result in a 25%:75% singlet to triplet ratio.[6] This means that for a traditional fluorescence molecule, only 25% of the charge-to-exciton formed will potentially emit, wasting the other 75% of the triplet exciton created via non-radiative pathways. Substantial improvement of the charge-to-photon internal quantum efficiency (η_{IQE}) was made when organometallic iridium-based phosphorescence chromophores were developed and η_{IQE} ~ 100 % was reported.[2,7] The access to this previously non-emissive

triplet state is attributed to the high spin-orbit coupling (SOC) induced by the heavy atom effect in these organometallic complexes. This huge SOC promotes an electron forbidden spin flipping from singlets (S_1) to emissive triplets (T_1), arising molecules with phosphorescence nature due to the resulting faster rate of intersystem crossing (k_{ISC}) than their rate of fluorescence (k_f).[8,9] However, the use of rare elements leads to a high-cost of device fabrication. In addition to this, the high density of long-lived triplets promoted by the high SOC in these materials promotes degradation of blue phosphors by the resulting high energy singlet after the triplet-triplet annihilation (TTA) mechanism happens.[10] This mechanism is also responsible for the overall roll-off issue, which have been a well-known detrimental effect on the device operational lifetimes. Thus, efforts to develop materials that can address these problems are highly desirable.[11]

Improvements on the device's processability, cost-efficiency, operation stability, and lifetime were made when organometallic phosphors were replaced by organic chromophores with thermally activated delayed fluorescence (TADF) characteristics as the light-emitting materials.[4,12] In addition to this, these TADF-based OLED devices were able to emulates the high η_{IQE} of their phosphorescence materials counterparts.[12–14] The very high η_{IQE} was suggested as due to the conversion of non-emissive triplets (T_n) into emissive singlets (S_n) in a reverse intersystem crossing process (rISC).[6,15–17] Recently, Samanta and others have conducted quantum chemical simulations (QCS) on organic TADF to characterize the potential timescales in which this rISC process could happen. They found that the rate of rISC (k_{rISC}) could be as high as 10^8 s^{-1}, which implies that this rate could be as high as the rate of fluorescence for typical fluorescence chromophores.[18,19] The nature of these potentially fast S_n-T_n manifolds mixing on the reported systems was ascribed as due to their charge transfer nature and their minimized energy difference between the locally excited triplet state and the triplet charge transfer state.[19] These design

parameters are suggested to be rather more important for the TADF effect than the conventional design rule of focusing in the small energy gap between the singlet-triplet manifolds (ΔE_{ST}).[18,19]

Multiple studies have used primarily steady state and microsecond to millisecond spectroscopic techniques coupled with oxygen quenching experiments to characterize the TADF electronic transitions in these chromophores.[20] The steady state approach consist of pairing the fluorescence and phosphorescence spectra of these systems with their quantum yield (Φ) efficiencies before and after purging oxygen from the solution. These methods have allowed scientists to evaluate the ΔE_{st} with the former and the triplet state contribution to the emissive dynamics after purging oxygen from the solution on the Φ with the later.[4,21–24] However, a recent study has highlighted that having a small ΔE_{st} or having a Φ enhancement after the oxygen purging process is not enough evidence for claiming excited state dynamics governed by a delayed fluorescence mechanism.[20] In addition to this, recent publications have highlighted the importance of obtaining either a long-lived emissive components and/or transient triplet states as substantial evidence of excited state dynamics governed by a TADF mechanism.[5,21,25] These two excited state characteristics should be present in diluted solution or in optically-inert PMMA films.[20,25,26] Despite that these seminal findings punctuates the importance of using the appropriate spectroscopic tools to evaluate the TADF mechanism, the fundamental molecular parameters required to control and modulate the above-mentioned parameters so the desired structure-function relationships is achieved is ways away to be fully understood.[5,20,25,27]

The principles of OLED and their state-of the art current materials are discussed in detail through Chapter 1. The multiple spectroscopic tools used in this dissertation are described in detail in Chapter 2. Experimental techniques to characterize the steady state and time resolved absorption an emission properties of the investigated systems were used. In Chapter 3, the photophysical

properties of a well known TADF emitter, namely BCC-TPTA, was elucidated. This organic chromophore is believed to possess excited state dynamics governed by a TADF mechanism with a reported internal quantum efficiency (η_{IQE}) of 84 %.[4] In addition, a significant enhancement in its quantum yield ($\boldsymbol{\Phi}$) in solution after purging oxygen has been reported. The excited state dynamics of Rhodamine B and $Ir(BT)_2(acac)$ were also probed for comparison. Investigations in the absence of oxygen were also carried out. Our time-correlated single photon counting (TCSPC) measurements revealed a lack of long-lived emissive lifetime for BCC-TPTA in any of the medium tested. Our *ns* transient absorption spectroscopy (*ns* TAS) experiments revealed that BCC-TPTA does not possess triplet transient states that could be linked to a delayed fluorescence process. Instead, the evidence obtained from our spectroscopic tools suggest that BCC-TPTA has excited state dynamics that of a typical fluorescence chromophore and that just comparing the $\boldsymbol{\Phi}$ difference before and after purging oxygen from the solution is not an accurate method to claim excited state dynamics governed by a delayed fluorescence mechanism. Consequently, we believe that previous studies, in which the photo-physics of organic chromophores with TADF characteristics are reported, may have overlooked the influence of the host materials on the obtained optical properties in blended films.

In Chapter 4, a new optical approach for the direct determination of the rate of reverse intersystem crossing (k_{rISC}) in organic emitters with TADF nature was developed by using oxygen sensitized nanosecond transient absorption spectroscopy (ns TAS). The k_{rISC} values determined by our methodology are found to be in good agreement with the ones calculated by quantum chemical simulations (QCS). The obtained k_{rISC} were correlated with their device performances. A proportional relationship between the k_{rISC} and reduced external quantum efficiency (η_{EQE}) roll-off was found. We further use our methodology to evaluate the k_{rISC} of multiple TADF emitters from

the available TAS data in the literature. We found that when the k_{rISC} is $\leq 10^3$ s^{-1} the TADF chromophore becomes TADF-inactive and $\eta_{EQE} \leq 5$ % are obtained. These demarcations were not possible to be achieved by the well-known Masui methodology. Contrarily, our methodology showed consistency in obtaining high k_{rISC} with reduced η_{EQE} roll-offs and in obtaining $k_{rISC} \leq 10^3$ s^{-1} with $\eta_{EQE} < 5$ %, suggesting TADF-inactivity by the latter. This work may help to demarcate the potential top TADF emitter candidates for superior device performances before device fabrication techniques are employed.

In current societies, energy production for practical uses represent a challenge. This is because a strategical approach for a sustainable energy development is needed in order to achieve long-term practical solutions but preventing major environmental repercussions. Specifically, sustainable energy production involves three majors technological changes: saving in energy by the demand side, improvement of efficiency in energy production, and replacing fossil fuels by the implementation of renewable energy production by preventing environmental repercussion.[28] Eolic, solar, hydraulic (wave) and biomass are the main subjects under renewable energy development. With that being said, solar energy represents mankind's only constant and inexhaustible energy source.[29] Researchers have developed photovoltaic devices for the conversion of solar energy into electrical energy, but they have not been able to completely utilize the solar spectrum. Currently, the commercial photovoltaic cells are dominated by silicon-based solar cells, but the current increasing demand has led to a silicon shortage.[30] Organic materials have emerged as a possible replacement to silicon due to their advantages such as ease of tunability, ease of fabrication using low-cost solution processing techniques, and the possibility of large area films which are lightweight and flexible.[31]

The photovoltaic mechanism in the active layer of an organic material can be divided into three areas: exciton creation by light absorption, exciton diffusion splitting to produce charge carriers, and subsequent transport of these charge carriers.[32] Theoretically, these properties are tunable due to the relative ease of synthesis. These three photovoltaic abilities are mainly attributed to the morphology and hybridization of the conjugated carbons (sp_2) in the material. This hybridization leads to an unoccupied p_z-orbital for each sp_2 carbon. Therefore, each p_z-electron in a p_z-orbital have a potential π-bond interaction with neighboring carbons with the same hybridization, resulting in planar conjugated carbons with high p_z-electrons polarizability due to their delocalized nature.[32] When an organic material absorbs light, an electron from the relaxed state is promoted to an excited state and this promotion leaves an electron-hole. This new state created by the interaction of the electron and the hole is what is called exciton. Breaking this interaction is called exciton splitting. The low dielectric constant of organic materials leads to a high Coulombic interaction between the electrons and holes. This strong interaction leads to a high exciton binding energy, making the exciton splitting so challenging.[33] The excited electrons can be relaxed by radiative and non-radiative mechanisms in a process known as exciton recombination. In order to continue with the photovoltaic mechanism, the exciton splitting has to occur within the excited state relaxation time or recombination time of the exciton. If the exciton splitting occur, charge carriers mobility occur. The tunability and flexibility of organic synthesis have afforded designs that result in performance enhancements such as a relatively high molar absorptivity coefficient, but improvements to prevent the exciton recombination and enhance exciton diffusion still present difficult challenges.[34]

Recent studies suggest that the design of organic polymers based on alternating electron push-pull (donor-acceptor) moieties is an effective way to prevent exciton recombination and

facilitate exciton diffusion. The central concept behind the effectiveness in exciton splitting and exciton diffusion is the gradient created by the offset difference in chemical potential between the excites states in the Lowest Unoccupied Molecular Orbital (LUMO) of the electron donor-acceptor moieties.[35] Exciton splitting and subsequent exciton charge carrier diffusion has to happen to reach the respective electrode faster than their excitation lifetime.[36] One way to achieve this is via a triplet excited state diffusion mechanism due to their long-lived excited state. This is because of the combination of the long-lived triplet state nature with the added chemical potential between the donor-acceptor.[37] The fundamental properties of organic materials for photovoltaic applications and their device architectures are discussed in detail through chapter 1.

In Chapter 5, the influence of using heterocycles such as furan and thiophene atom as linkers on the electronic and photophysical properties of four conjugated light harvesting were investigated. The polymers were base on Benzodifuran (BDF) as the donor moiety and diketopyrrolopyrrole (DPP) as the acceptor moiety. The polymers with a furan as the linker showed higher extinction coefficients than their thiophene counterparts. Ultrafast fluorescence decay showed that the type of linker in these conjugated polymers affects the exciton relaxation process. Theoretical calculations showed that the polymers with a furan as the linker are more planar than their thiophene analogues. In addition, theoretical calculation showed that the polymers with a thiophene as the linker have larger transition dipole moments. The two-photon absorption cross-section of the polymers with a furan as the linker were larger than their thiophene polymer analogues. These results suggest that the polymers with a furan as the linker have higher charge transfer character than their thiophene polymers analogues. The photovoltaics performance for these polymers were correlated with their optical properties. These results suggest that furan-derivatives are good candidates for synthetic exploration for long-range energy transport materials

in photovoltaic applications. In Chapter 6, a new series of acceptor-donor-acceptor (A-D-A) ladder-type molecules were characterized. These molecules contain up to 25- fused rings but still show good air stability and good solubility. The photophysical properties were investigated and an intense intramolecular charge-transfer was observed. All of the molecules exhibit two-photon absorption (TPA) activity, and their TPA cross-section shows a linear relationship with increasing conjugation length of the thienoacene-PDI derivatives.

In Chapter 7, quantum chemical simulation (CQS) were coupled with ultrafast spectroscopy to characterize the feasibility of a two electron transfer between an intramolecular singlet fission chromophore (tetracyanomethylene quinoidal bithiopehene with β,β′-solubilizing groups) and multi-electron acceptor (anthraquinone). The QCS predictions are consistent with experimental observations of reduced lifetimes in time-resolved fluorescence spectroscopy, changes in transmission profile, and appearance of new absorption bands in transient absorption spectroscopy, all of which support multi-ET in the QOT2/AQ mixture. The analysis suggests 2ET is favored over 1ET by a 2.5:1 ratio.

8.2 Future Directions

Most of the excited state characterization experiments presented in this dissertation were conducted in solution phase. This approach gives the opportunity to evaluate the fundamental properties of the investigated systems in different environment just by changing the solvent. However, their optoelectronic application happens in the solid phase. In the solid state, the molecules of the organic materials are tightly packed and usually different type of host are used.[38] Therefore, solid-solid interaction must be considered if one wants to further understand the electronic transitions governing the excited state of opto-electric materials.

In the case of elucidating the fundamental electronic transitions of chromophores with TADF characteristics, it has been showed that having a quantum yield value ~ 100 % in oxygen free atmospheres is important for obtaining superior device performances.[5] This quantum yield enhancement after removing oxygen from the atmospheres and superior device performances has been explained their relatively large rate of reverse intersystem crossing ($k_{rISC} > 10^5 s^{-1}$). Therefore, the development of TADF emitters that can simultaneously achieve k_{rISC} > than $10^5 s^{-1}$ and quantum yield close to 100 % is believe to be integral for optimizing the device operational stability of TADF OLEDs.[39] This may be possible by further understanding the role of CT and LE singlet and triplet starts on the electronic transitions chromophores with TADF characteristics.[19,26,40] In addition, it has been shown how the host material may influence the obtained optical properties of the emitter.[26,41] Therefore, the full photo-physical properties of TADF emitters should be investigated in function of different host materials. Specifically, the transient absorption spectroscopic techniques, which is fully described in Chapter 2, should be a pivotal technique in the solid-state analysis. In this way, the intermediates non-emissive states responsible for the Förster resonance energy transfer (FRET) and Dexter energy transfer (DET), transition that are present in the electroluminescence mechanism, could be characterized. Consequently, correlating them with their respective device performances.

Recently, Hamze et al. developed an interesting way to achieved TADF characteristics in organometallic complex by using carbine-based ligands.[42,43] With this approach, the non-radiative transition were minimized, achieving ~ 100 % of internal quantum efficiencies. This concept was named as thermally enhanced luminescence (TEL), given that the possibility of phosphorescence cannot be completely ruled out.[42] This approach of having two potential emissive channels, namely the singlet emissive channel (due to the conversion of triplets to singlets) and the triplet emissive

channels (due to phosphorescence), could be beneficial for reducing the TTA mechanism that hampers the OLED commercialization. The TEL mechanism concept is relatively new. Therefore, fundamental studies combining QCS and multiple ultrafast spectroscopy are in need.

In the case of photovoltaics solar cells, there has been a resurgence in the use BHJ architectures with all organic materials since a PCE > 14 % was reported.[44] This was possible by engineering a wide-bandgap light harvesting polymer, so the open circuit voltage of the device was > 1 V. However, the wide-bandgap nature of this polymer may affect its absorptive properties relative to where the solar flux is. Consequently, finding ways to obtain simultaneously a high open circuit voltage with energy bandgaps were the solar flux lies needs to be developed. In addition to this, significant improvements in the design of low-bandgap materials for fullerene free solar cells has been achieved.[45–48] These recent improvements opens the possibility for further BHJ bandgap engineering so the PCE % is optimized in all organic solar cells. This could be facilitated by using QCS to demarcate between the top materials pair for the BHJ active layer fabrication. These theoretical approaches may face some trouble with systems that have many atoms in a molecule, like is the case of light harvesting polymers. This may be addressed by the further development of current methods such as configuration interaction (CI), which takes into consideration the electrons in the investigated systems.[49] The QCS could be coupled with picosecond/nanosecond time resolved spectroscopy to elucidate the transient state generated in the BHJ that may lead to the subsequent current generation in these systems.[50,51] In addition, the possibility of using the singlet exciton fission (SF) mechanism, which was introduced in Chapter 7, offers an attractive way for the further development of organic photovoltaic devices. With the SF mechanism, the extraction of two electrons per absorbed photons is possible.[52,53] With the SF mechanism, external quantum efficiencies ~ 200 % could be achieved. However, the development

of light absorbing materials with high extinction coefficient and with excited state dynamics exhibiting a SF mechanism are ways away to be understood and developed. In addition, a suitable acceptor material for the collection of two electrons is in need. As with the TADF mechanism, the combination of synthetic chemistry, QCS, photophysical characterization, and device fabrication may offer further opportunities for having a deeper understanding on the opto-electrical properties of materials for photovoltaic applications.

References

(1) Adachi, C.; Baldo, M. A.; Thompson, M. E.; Forrest, S. R. Nearly 100% Internal Phosphorescence Efficiency in an Organic Light Emitting Device. *J. Appl. Phys.* **2001**, *90* (10), 5048–5051. https://doi.org/10.1063/1.1409582.

(2) Lamansky, S.; Djurovich, P.; Murphy, D.; Abdel-Razzaq, F.; Lee, H. E.; Adachi, C.; Burrows, P. E.; Forrest, S. R.; Thompson, M. E. Highly Phosphorescent Bis-Cyclometalated Iridium Complexes: Synthesis, Photophysical Characterization, and Use in Organic Light Emitting Diodes. *J. Am. Chem. Soc.* **2001**, *123* (18), 4304–4312. https://doi.org/10.1021/ja003693s.

(3) Wu, M.-J. J.; Lin, T.-A. A.; Chung, C.-L. L.; Yi, C.-L. L.; Wu, C.-C. C.; Jiao, M.; Tsai, W.-L. L.; Pan, K.-C. C.; Wong, K.-T. T.; Lee, W.-K. K.; et al. Organic LEDs: Sky-Blue Organic Light Emitting Diode with ≈37% External Quantum Efficiency Using Thermally Activated Delayed Fluorescence from Spiroacridine-Triazine Hybrid (Adv. Mater. 32/2016). *Adv. Mater.* **2016**, *28* (32), 7029. https://doi.org/10.1002/adma.201670224.

(4) Hirata, S.; Sakai, Y.; Masui, K.; Tanaka, H.; Lee, S. Y.; Nomura, H.; Nakamura, N.; Yasumatsu, M.; Nakanotani, H.; Zhang, Q.; et al. Highly Efficient Blue Electroluminescence Based on Thermally Activated Delayed Fluorescence. *Nat. Mater.* **2015**, *14* (3), 330–336. https://doi.org/10.1038/nmat4154.

(5) Noda, H.; Nakanotani, H.; Adachi, C. Excited State Engineering for Efficient Reverse Intersystem Crossing. *Sci. Adv.* **2018**, *4* (6), eaao6910. https://doi.org/10.1126/sciadv.aao6910.

(6) Uoyama, H.; Goushi, K.; Shizu, K.; Nomura, H.; Adachi, C. Highly Efficient Organic Light-Emitting Diodes from Delayed Fluorescence. *Nature* **2012**, *492* (7428), 234–238. https://doi.org/10.1038/nature11687.

(7) Adachi, C.; Baldo, M. A.; Thompson, M. E.; Forrest, S. R. Nearly 100% Internal Phosphorescence Efficiency in an Organic Light-Emitting Device ARTICLES YOU MAY BE INTERESTED IN Electroluminescence in Organic Crystals. *J. Chem. Phys.* **2001**, *90* (10), 2042. https://doi.org/10.1063/1.1409582.

(8) Baldo, M. A.; O'Brien, D. F.; You, Y.; Shoustikov, A.; Sibley, S.; Thompson, M. E.; Forrest, S. R. Highly Efficient Phosphorescent Emission from Organic Electroluminescent Devices. *Nature* **1998**, *395* (6698), 151–154. https://doi.org/10.1038/25954.

(9) Kleinschmidt, M.; Van Wüllen, C.; Marian, C. M. Intersystem-Crossing and Phosphorescence Rates in Fac-IrIII(Ppy)3: A Theoretical Study Involving Multi-Reference Configuration Interaction Wavefunctions. *J. Chem. Phys.* **2015**, *142* (9), 094301. https://doi.org/10.1063/1.4913513.

(10) Staroske, W.; Pfeiffer, M.; Leo, K.; Hoffmann, M. Single-Step Triplet-Triplet Annihilation: An Intrinsic Limit for the High Brightness Efficiency of Phosphorescent Organic Light Emitting Diodes. *Phys. Rev. Lett.* **2007**, *98* (19), 197402.

https://doi.org/10.1103/PhysRevLett.98.197402.

(11) Bui, T. T.; Goubard, F.; Ibrahim-Ouali, M.; Gigmes, D.; Dumur, F. Recent Advances on Organic Blue Thermally Activated Delayed Fluorescence (TADF) Emitters for Organic Light-Emitting Diodes (OLEDs). *Beilstein Journal of Organic Chemistry*. Beilstein-Institut January 30, 2018, pp 282–308. https://doi.org/10.3762/bjoc.14.18.

(12) Kaji, H.; Suzuki, H.; Fukushima, T.; Shizu, K.; Suzuki, K.; Kubo, S.; Komino, T.; Oiwa, H.; Suzuki, F.; Wakamiya, A.; et al. Purely Organic Electroluminescent Material Realizing 100% Conversion from Electricity to Light. *Nat. Commun.* **2015**, *6*, 8476. https://doi.org/10.1038/ncomms9476.

(13) Kim, M.; Jeon, S. K.; Hwang, S. H.; Lee, J. Y. Stable Blue Thermally Activated Delayed Fluorescent Organic Light-Emitting Diodes with Three Times Longer Lifetime than Phosphorescent Organic Light-Emitting Diodes. *Adv. Mater.* **2015**, *27* (15), 2515–2520. https://doi.org/10.1002/adma.201500267.

(14) Sato, K.; Shizu, K.; Yoshimura, K.; Kawada, A.; Miyazaki, H.; Adachi, C. Organic Luminescent Molecule with Energetically Equivalent Singlet and Triplet Excited States for Organic Light-Emitting Diodes. *Phys. Rev. Lett.* **2013**, *110* (24), 247401. https://doi.org/10.1103/PhysRevLett.110.247401.

(15) Youn Lee, S.; Yasuda, T.; Nomura, H.; Adachi, C. High-Efficiency Organic Light-Emitting Diodes Utilizing Thermally Activated Delayed Fluorescence from Triazine-Based Donor-Acceptor Hybrid Molecules. *Appl. Phys. Lett.* **2012**, *101* (9), 093306. https://doi.org/10.1063/1.4749285.

(16) Endo, A.; Ogasawara, M.; Takahashi, A.; Yokoyama, D.; Kato, Y.; Adachi, C. Thermally Activated Delayed Fluorescence from Sn4+-Porphyrin Complexes and Their Application to Organic Light-Emitting Diodes -A Novel Mechanism for Electroluminescence. *Adv. Mater.* **2009**, *21* (47), 4802–4806. https://doi.org/10.1002/adma.200900983.

(17) Dias, F. B.; Bourdakos, K. N.; Jankus, V.; Moss, K. C.; Kamtekar, K. T.; Bhalla, V.; Santos, J.; Bryce, M. R.; Monkman, A. P. Triplet Harvesting with 100% Efficiency by Way of Thermally Activated Delayed Fluorescence in Charge Transfer OLED Emitters. *Adv. Mater.* **2013**, *25* (27), 3707–3714. https://doi.org/10.1002/adma.201300753.

(18) Chen, X. K.; Kim, D.; Brédas, J. L. Thermally Activated Delayed Fluorescence (TADF) Path toward Efficient Electroluminescence in Purely Organic Materials: Molecular Level Insight. *Acc. Chem. Res.* **2018**, *51* (9), 2215–2224. https://doi.org/10.1021/acs.accounts.8b00174.

(19) Samanta, P. K.; Kim, D.; Coropceanu, V.; Brédas, J. L. Up-Conversion Intersystem Crossing Rates in Organic Emitters for Thermally Activated Delayed Fluorescence: Impact of the Nature of Singlet vs Triplet Excited States. *J. Am. Chem. Soc.* **2017**, *139* (11), 4042–4051. https://doi.org/10.1021/jacs.6b12124.

(20) Vázquez, R. J.; Kim, H.; Zimmerman, P. M.; Goodson, T. Using Ultra-Fast Spectroscopy

to Probe the Excited State Dynamics of a Reported Highly Efficient Thermally Activated Delayed Fluorescence Chromophore. *J. Mater. Chem. C* **2019**, *7* (14), 4210–4221. https://doi.org/10.1039/c8tc05957h.

(21) Hosokai, T.; Matsuzaki, H.; Nakanotani, H.; Tokumaru, K.; Tsutsui, T.; Furube, A.; Nasu, K.; Nomura, H.; Yahiro, M.; Adachi, C. Evidence and Mechanism of Efficient Thermally Activated Delayed Fluorescence Promoted by Delocalized Excited States. *Sci. Adv.* **2017**, *3* (5), e1603282. https://doi.org/10.1126/sciadv.1603282.

(22) Thangaraju, K.; Lee, J.; Lee, J.-I.; Chu, H. Y.; Kim, Y.-H.; Kwon, S.-K. Highly Efficient Green Phosphorescent Organic Light Emitting Diodes with Improved Efficiency Roll-Off; 2015; p 060019. https://doi.org/10.1063/1.4917854.

(23) Tao, Y.; Yuan, K.; Chen, T.; Xu, P.; Li, H.; Chen, R.; Zheng, C.; Zhang, L.; Huang, W. Thermally Activated Delayed Fluorescence Materials towards the Breakthrough of Organoelectronics. *Adv. Mater.* **2014**, *26* (47), 7931–7958. https://doi.org/10.1002/adma.201402532.

(24) Yang, Z.; Mao, Z.; Xie, Z.; Zhang, Y.; Liu, S.; Zhao, J.; Xu, J.; Chi, Z.; Aldred, M. P. Recent Advances in Organic Thermally Activated Delayed Fluorescence Materials. *Chemical Society Reviews*. The Royal Society of Chemistry February 6, 2017, pp 915–1016. https://doi.org/10.1039/c6cs00368k.

(25) Kuang, Z.; He, G.; Song, H.; Wang, X.; Hu, Z.; Sun, H.; Wan, Y.; Guo, Q.; Xia, A. Conformational Relaxation and Thermally Activated Delayed Fluorescence in Anthraquinone-Based Intramolecular Charge-Transfer Compound. *J. Phys. Chem. C* **2018**, *122* (7), 3727–3737. https://doi.org/10.1021/acs.jpcc.7b11411.

(26) Chen, X. K.; Tsuchiya, Y.; Ishikawa, Y.; Zhong, C.; Adachi, C.; Brédas, J. L. A New Design Strategy for Efficient Thermally Activated Delayed Fluorescence Organic Emitters: From Twisted to Planar Structures. *Adv. Mater.* **2017**, *29* (46), 1702767. https://doi.org/10.1002/adma.201702767.

(27) Etherington, M. K.; Gibson, J.; Higginbotham, H. F.; Penfold, T. J.; Monkman, A. P. Revealing the Spin-Vibronic Coupling Mechanism of Thermally Activated Delayed Fluorescence. *Nat. Commun.* **2016**, *7* (1), 13680. https://doi.org/10.1038/ncomms13680.

(28) Lund, H. Renewable Energy Strategies for Sustainable Development. *Energy* **2007**, *32* (6), 912–919. https://doi.org/10.1016/j.energy.2006.10.017.

(29) Alonso, M. I.; Campoy-Quiles, M. Organic Solar Cells. *Springer Ser. Opt. Sci.* **2018**, *212* (3), 439–461. https://doi.org/10.1007/978-3-319-75377-5_15.

(30) Green, M. A. Thin-Film Solar Cells: Review of Materials, Technologies and Commercial Status. *J. Mater. Sci. Mater. Electron.* **2007**, *18* (S1), 15–19. https://doi.org/10.1007/s10854-007-9177-9.

(31) Liang, Y.; Xu, Z.; Xia, J.; Tsai, S.-T.; Wu, Y.; Li, G.; Ray, C.; Yu, L. For the Bright Future-

Bulk Heterojunction Polymer Solar Cells with Power Conversion Efficiency of 7.4%. *Adv. Mater.* **2010**, *22* (20), E135-8. https://doi.org/10.1002/adma.200903528.

(32) Hoppe, H.; Sariciftci, N. S. Organic Solar Cells: An Overview. *J. Mater. Res.* **2011**, *19* (07), 1924–1945. https://doi.org/10.1557/JMR.2004.0252.

(33) Bässler, H.; Köhler, A. Charge Transport in Organic Semiconductors. *Top. Curr. Chem.* **2012**, *312*, 1–65. https://doi.org/10.1007/128_2011_218.

(34) Stranks, S. D.; Eperon, G. E.; Grancini, G.; Menelaou, C.; Alcocer, M. J. P.; Leijtens, T.; Herz, L. M.; Petrozza, A.; Snaith, H. J. Electron-Hole Diffusion Lengths Exceeding 1 Micrometer in an Organometal Trihalide Perovskite Absorber. *Science* **2013**, *342* (6156), 341–344. https://doi.org/10.1126/science.1243982.

(35) Pivrikas, A.; Sariciftci, N. S.; Juška, G.; Österbacka, R. A Review of Charge Transport and Recombination in Polymer/Fullerene Organic Solar Cells. *Prog. Photovoltaics Res. Appl.* **2007**, *15* (8), 677–696. https://doi.org/10.1002/pip.791.

(36) Günes, S.; Neugebauer, H.; Sariciftci, N. S. Conjugated Polymer-Based Organic Solar Cells. *Chem. Rev.* **2007**, *107* (4), 1324–1338. https://doi.org/10.1021/cr050149z.

(37) Luhman, W. A.; Holmes, R. J. Enhanced Exciton Diffusion in an Organic Photovoltaic Cell by Energy Transfer Using a Phosphorescent Sensitizer. *Appl. Phys. Lett.* **2009**, *94* (15), 153304. https://doi.org/10.1063/1.3120566.

(38) Tirapattur, S.; Belletête, M.; Drolet, N.; Leclerc, M.; Durocher, G. Steady-State and Time-Resolved Studies of 2,7-Carbazole-Based Conjugated Polymers in Solution and as Thin Films: Determination of Their Solid State Fluorescence Quantum Efficiencies. *Chem. Phys. Lett.* **2003**, *370* (5–6), 799–804. https://doi.org/10.1016/S0009-2614(03)00178-7.

(39) Jeon, S. K.; Lee, H. L.; Yook, K. S.; Lee, J. Y. Recent Progress of the Lifetime of Organic Light-Emitting Diodes Based on Thermally Activated Delayed Fluorescent Material. *Adv. Mater.* **2019**, 1803524. https://doi.org/10.1002/adma.201803524.

(40) Gibson, J.; Monkman, A. P.; Penfold, T. J. The Importance of Vibronic Coupling for Efficient Reverse Intersystem Crossing in Thermally Activated Delayed Fluorescence Molecules. *ChemPhysChem* **2016**, *17* (19), 2956–2961. https://doi.org/10.1002/cphc.201600662.

(41) Kim, D. H.; D'Aléo, A.; Chen, X. K.; Sandanayaka, A. D. S.; Yao, D.; Zhao, L.; Komino, T.; Zaborova, E.; Canard, G.; Tsuchiya, Y.; et al. High-Efficiency Electroluminescence and Amplified Spontaneous Emission from a Thermally Activated Delayed Fluorescent near-Infrared Emitter. *Nat. Photonics* **2018**, *12* (2), 98–104. https://doi.org/10.1038/s41566-017-0087-y.

(42) Hamze, R.; Peltier, J. L.; Sylvinson, D.; Jung, M.; Cardenas, J.; Haiges, R.; Soleilhavoup, M.; Jazzar, R.; Djurovich, P. I.; Bertrand, G.; et al. Eliminating Nonradiative Decay in Cu(I) Emitters: >99% Quantum Efficiency and Microsecond Lifetime. *Science (80-.).* **2019**, *363*

(6427), 601–606. https://doi.org/10.1126/science.aav2865.

(43) Hamze, R.; Shi, S.; Kapper, S. C.; Muthiah Ravinson, D. S.; Estergreen, L.; Jung, M.-C.; Tadle, A. C.; Haiges, R.; Djurovich, P. I.; Peltier, J. L.; et al. "Quick-Silver" from a Systematic Study of Highly Luminescent, Two-Coordinate, d 10 Coinage Metal Complexes . *J. Am. Chem. Soc.* **2019**, *141* (21), 8616–8626. https://doi.org/10.1021/jacs.9b03657.

(44) Li, S.; Ye, L.; Zhao, W.; Yan, H.; Yang, B.; Liu, D.; Li, W.; Ade, H.; Hou, J. A Wide Band Gap Polymer with a Deep Highest Occupied Molecular Orbital Level Enables 14.2% Efficiency in Polymer Solar Cells. *J. Am. Chem. Soc.* **2018**, *140* (23), 7159–7167. https://doi.org/10.1021/jacs.8b02695.

(45) Cnops, K.; Rand, B. P.; Cheyns, D.; Verreet, B.; Empl, M. A.; Heremans, P. 8.4% Efficient Fullerene-Free Organic Solar Cells Exploiting Long-Range Exciton Energy Transfer. *Nat. Commun.* **2014**, *5* (1), 3406. https://doi.org/10.1038/ncomms4406.

(46) Cui, Y.; Yao, H.; Gao, B.; Qin, Y.; Zhang, S.; Yang, B.; He, C.; Xu, B.; Hou, J. Fine-Tuned Photoactive and Interconnection Layers for Achieving over 13% Efficiency in a Fullerene-Free Tandem Organic Solar Cell. *J. Am. Chem. Soc.* **2017**, *139* (21), 7302–7309. https://doi.org/10.1021/jacs.7b01493.

(47) Zhao, W.; Qian, D.; Zhang, S.; Li, S.; Inganäs, O.; Gao, F.; Hou, J. Fullerene-Free Polymer Solar Cells with over 11% Efficiency and Excellent Thermal Stability. *Adv. Mater.* **2016**, *28* (23), 4734–4739. https://doi.org/10.1002/adma.201600281.

(48) Zhang, S.; Qin, Y.; Zhu, J.; Hou, J. Over 14% Efficiency in Polymer Solar Cells Enabled by a Chlorinated Polymer Donor. *Adv. Mater.* **2018**, *30* (20), 1800868. https://doi.org/10.1002/adma.201800868.

(49) Safronova, M. S.; Kozlov, M. G.; Johnson, W. R.; Jiang, D. Development of a Configuration-Interaction plus All-Order Method for Atomic Calculations. *Phys. Rev. A - At. Mol. Opt. Phys.* **2009**, *80* (1), 012516. https://doi.org/10.1103/PhysRevA.80.012516.

(50) Yamamoto, S.; Guo, J.; Ohkita, H.; Ito, S. Formation of Methanofullerene Cation in Bulk Heterojunction Polymer Solar Cells Studied by Transient Absorption Spectroscopy. *Adv. Funct. Mater.* **2008**, *18* (17), 2555–2562. https://doi.org/10.1002/adfm.200800411.

(51) Nogueira, A. F.; Montanari, I.; Nelson, J.; Durrant, J. R.; Winder, C.; Sariciftci, N. S.; Brabec, C. Charge Recombination in Conjugated Polymer/Fullerene Blended Films Studied by Transient Absorption Spectroscopy. *J. Phys. Chem. B* **2003**, *107* (7), 1567–1573. https://doi.org/10.1021/jp027101z.

(52) Smith, M. B.; Michl, J. Recent Advances in Singlet Fission. *Annu. Rev. Phys. Chem.* **2013**, *64* (1), 361–386. https://doi.org/10.1146/annurev-physchem-040412-110130.

(53) Smith, M. B.; Michl, J. Singlet Fission. *Chem. Rev.* **2010**, *110* (11), 6891–6936. https://doi.org/10.1021/cr1002613.